

# AN IMPROVED HYPERSONIC SHOCK LAYER STAGNATION POINT FLOW WITH AND WITHOUT REAL GAS EFFECTS

by

PRADEEP KUMAR

TH  
62913206  
P8812

TH  
AE/1989/D.  
P8812

AE  
1989

D  
KUM  
IMP

DEPARTMENT OF AERONAUTICAL ENGINEERING  
INDIAN INSTITUTE OF TECHNOLOGY, KANPUR

JUNE, 1989

# **AN IMPROVED HYPERSONIC SHOCK LAYER STAGNATION POINT FLOW WITH AND WITHOUT REAL GAS EFFECTS**

A Thesis Submitted  
in partial Fulfilment of the Requirements  
for the Degree of

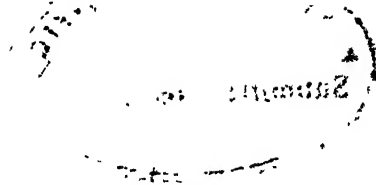
**DOCTOR OF PHILOSOPHY**

*by*

**PRADEEP KUMAR**

*to the*

**DEPARTMENT OF AERONAUTICAL ENGINEERING  
INDIAN INSTITUTE OF TECHNOLOGY, KANPUR**



AE-1989-D-KUM-IMP

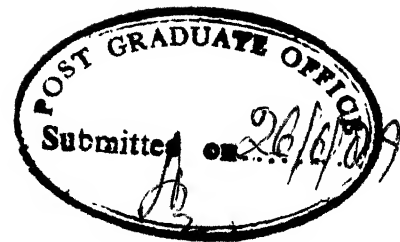
12 JUL 1990

CENTRAL LIBRARY  
I. I. T., KANPUR

Acc. No. **A** 108434

CENTRAL LIBRARY

Acc. No. **A** 108434



# CERTIFICATE

This is to certify that the work contained in the thesis entitled, "An Improved Hypersonic Shocklayer Stagnation Point Flow With And Without Real Gas Effects", submitted for Ph.D degree to the Department of Aeronautical Engineering, Indian Institute of Technology, Kanpur by Mr. Pradeep Kumar has been carried out under our supervision. This thesis has not been submitted elsewhere for a degree.

A handwritten signature in cursive script, appearing to read "V. Adimurthy".

(V. Adimurthy)  
Head, Aerodynamics Division,  
Vikram Sarabhai Space Center,  
Trivandrum

A handwritten signature in cursive script, appearing to read "A. C. Jain".

(A. C. Jain)  
Professor  
Department of Aeronautical  
Engineering,  
Indian Institute of Technology  
Kanpur



# TABLE OF CONTENT

	Page
List of Figures	vii
List of Tables	xiii
Nomenclature	xiv
Synopsis	xix
 CHAPTER 1 INTRODUCTION	 1
1.1 Introduction	1
1.2 Assessment of Existing Theories and Literature	 7
Higher Order Boundary Layer Theory	8
Two Thin Layer Theory/ Viscous Shock Layer Theory	 14
Numerical Integration through the Shock	23
Direct Simulation Monte Carlo (DSMC) Technique	 27
1.3 Surface Slip Condition	29
1.4 Scope of the Present Work	32
 CHAPTER 2 MATHEMATICAL FORMULATION	 36
2.1 Introduction	36
2.2 Governing Equations	37

2.3 Chemical Reaction Model	52
2.4 Thermodynamic and Transport Properties of Gas Mixture	56
CHAPTER 3 METHOD OF SOLUTION	74
3.1 Introduction	74
3.2 Solution Procedure	74
3.3 Numerical Scheme	78
Choice of Grid	79
Finite Difference Scheme	80
Boundary Conditions	83
3.4 Treatment of Production Term	84
3.5 Convergence of Numerical Procedure	89
CHAPTER 4 RESULTS AND DISCUSSION	127
4.1 Introduction	127
4.2 Results for Perfect Gas	128
4.3 Results for Chemically Reacting Gas	142

CHAPTER 5 CONCLUSIONS	218
5.1 Introduction	218
5.2 Extension of Validity of Shock Layer Approach with Full Navier-Stokes equations	220
5.3 Influence of Chemical Reactions in Shock Transition Zone on the Flow Field	221
5.4 Convergence of Non-Equilibrium Computational Procedure	222
5.5 Mass Conservation and Species Concentrations	223
5.6 Some Problems for Further Research	224
REFERENCES	225
APPENDIX 1 INFLUENCE OF LINEARISATION OF PRODUCTION TERM	233

# LIST OF FIGURES

Figure	Caption	Page
Fig:2.1	Coordinate System	73
Fig:3.1	Schematic for Finite Difference Scheme	98
Fig:3.2	Convergence of Flow Variables	99
Fig:3.3	Evolution of Temperature Profile	100
Fig:3.4	Evolution of Tangential Velocity Profile	101
Fig:3.5	Convergence of Concentrations	102
Fig:3.6	Convergence of Flow Variables for Shuttle	103
Fig:3.7	Convergence of Transport Property	104
Fig:3.8	Evolution of Temperature Profile	105
Fig:3.9	Evolution of Concentration Profile Of $C_{N_2}$	106
Fig:3.10	Evolution of Concentration Profile Of $CO_2$	107
Fig:3.11	Evolution of Concentration Profile Of $CO$	108
Fig:3.12	Evolution of Concentration Profile Of $C_N$	109
Fig:3.13	Convergence of u, v and T Profiles for AFE Vehicle	110
Fig:3.14	Convergence of Pressure and Heat Flux for AFE Vehicle	111
Fig:3.15	Convergence of $C_{N_2}$ , $CO_2$ and $C_{NO}$ Profiles for AFE Vehicle	112
Fig:3.16	Convergence of $CO$ , $C_N$ and $C_{NO+}$ Profiles for AFE Vehicle	113
Fig:3.17	Convergence of Shock Stand-off Distance for AFE Vehicle	114

Fig:3.18	Convergence of Heat Flux for AFE Vehicle	115
Fig:3.19	Evolution of Non-dimensional Tangential Velocity for AFE Vehicle	116
Fig:3.20	Evolution of Normal Velocity Profile for AFE Vehicle	117
Fig:3.21	Evolution of Temperature Profile for AFE Vehicle	118
Fig:3.22	Evolution of Density Profile for AFE Vehicle	119
Fig:3.23	Evolution of Pressure Profile for AFE Vehicle	120
Fig:3.24	Evolution of Concentration Profile of $N_2$ for AFE Vehicle	121
Fig:3.25	Evolution of Concentration Profile of $O_2$ for AFE Vehicle	122
Fig:3.26	Evolution of Concentration Profile of NO for AFE Vehicle	123
Fig:3.27	Evolution of Concentration Profile of O for AFE Vehicle	124
Fig:3.28	Evolution of Concentration Profile of H for AFE Vehicle	125
Fig:3.29	Evolution of Concentration Profile of $NO^+$ for AFE Vehicle	126
Fig:4.1	Shock Stand-off Distance for Cold Wall Case	159
Fig:4.2	Shock Stand-off Distance for Hot Wall Case	160

Fig:4.3 Post-Shock Pressure Variation with Reynolds	
Number	161
Fig:4.4 Post-Shock Density Variation with Reynolds	
Number	162
Fig:4.5 Base Pressure Variation with Reynolds Number	163
Fig:4.6 Wall Pressure Variation with Reynolds Number	164
Fig:4.7 Wall Pressure Variation with Reynolds	
Number with Consistent Shock Slip for VSL	165
Fig:4.8 Heat Transfer Coefficient For Cold Wall	166
Fig:4.9 Heat Transfer Coefficient For Hot Wall	167
Fig:4.10 Tangential Velocity Profile for $Re = 1$	168
Fig:4.11 Temperature Profile for $Re = 1$	169
Fig:4.12 Pressure Profile for $Re = 1$	170
Fig:4.13 Density Profile for $Re = 1$	171
Fig:4.14 Tangential Velocity Profile for $Re = 100$	172
Fig:4.15 Temperature Profile for $Re = 100$	173
Fig:4.16 Pressure Profile for $Re = 100$	174
Fig:4.17 Density Profile for $Re = 100$	175
Fig:4.18 Density Profile Comparison with Experimental	
Data of Russel for Cold Wall	176
Fig:4.19 Density Profile Comparison with Experimental	
Data of Russel for Hot Wall	177
Fig:4.20 Density Profile comparison with Monte Carlo	
Results of Vogenitz & Takata for Cold Wall	178
Fig:4.21 Temperature Profile comparison with Monte Carlo	
Results of Vogenitz & Takata for Cold Wall	179

Fig:4. 22 Comparison of Velocity Profiles of Present work with Results of Kao and HML Solution	180
Fig:4. 23 Comparison of Temperature and Pressure Profiles of Present work with Results of Kao and HML Solution	181
Fig:4. 24 Heat Transfer Coefficient Comparison with Experimental Data of Boylan	182
Fig:4. 25 Heat Transfer Coefficient Comparison with Experimental Data of Whitliff & Wilson	183
Fig:4. 26 Heat Transfer Coefficient Comparison with Experimental Data of Coleman, Metcalf & Berry	184
Fig:4. 27 Variation of Recovery Factor With Reynolds Number	185
Fig:4. 28 Influence of Surface Temperature on Heat Transfer Coefficient	186
Fig:4. 29 Influence of Surface Slip on Heat Flux	187
Fig:4. 30 Influence of Surface Slip on Temperature Gradient at Wall	188
Fig:4. 31 Variation of Heat Transfer Coefficient with Rarefaction Parameter for Shuttle	189
Fig:4. 32 Temperature Distribution for Shuttle for 92.35 Km	190
Fig:4. 33 Concentration Profile of $N_2$ for Shuttle for 92.35 Km	191
Fig:4. 34 Concentration Profile of $O_2$ for Shuttle for 92.35 Km	192

Fig:4.35 Concentration Profile of O for Shuttle for 92.35 Km	193
Fig:4.36 Concentration Profile of N for Shuttle for 92.35 Km	194
Fig:4.37 Concentration Profile of NO for Shuttle for 92.35 Km	195
Fig:4.38 Temperature Distribution for Shuttle for 104.93 Km	196
Fig:4.39 Concentration Profile of N <sub>2</sub> and O <sub>2</sub> for Shuttle for 104.93 Km	197
Fig:4.40 Influence of Transport Property Variation on Heat Flux with Armaly & Sutton Correlation	198
Fig:4.41 Influence of Transport Property Variation on Heat Flux with Wilke's Correlation	199
Fig:4.42 Influence of Mixture Property Correlation on Temperature Profile	200
Fig:4.43 Influence of Mixture Property Correlation on Concentration Profile of N <sub>2</sub>	201
Fig:4.44 Influence of Mixture Property Correlation on Concentration Profile of O <sub>2</sub>	202
Fig:4.45 Influence of Mixture Property Correlation on Concentration Profile of O	203
Fig:4.46 Influence of Mixture Property Correlation on Concentration Profile of N	204



Fig:4.47 Influence of Mixture Property Correlation on Concentration Profile of NO	205
Fig:4.48 Influence of Mixture Property Correlation on Concentration Profile of NO <sup>+</sup>	206
Fig:4.49 Influence of Mixture Property Correlation on Prandtl Number Profile	207
Fig:4.50 Influence of Freestream Velocity on Ch	208
Fig:4.51 Influence of Freestream Velocity on Ch Vs Re	209
Fig:4.52 Heat Transfer Coefficient for AFE Vehicle	210
Fig:4.53 Wall Pressure for AFE Vehicle	211
Fig:4.54 Comparison of N <sub>2</sub> Concentration for AFE vehicle	212
Fig:4.55 Comparison of O <sub>2</sub> Concentration for AFE vehicle	213
Fig:4.56 Comparison of NO Concentration for AFE vehicle	214
Fig:4.57 Comparison of O Concentration for AFE vehicle	215
Fig:4.58 Comparison of N Concentration for AFE vehicle	216
Fig:4.59 Comparison of NO <sup>+</sup> Concentration for AFE vehicle	217

## LIST OF TABLES

Title	Page
Table 1 Reaction Rate Constants	67
Table 2 Constants for Polynomial Approximation of Thermodynamic Data of Gases	68
Table 3 Molecular Constants for Transport Properties	72
Table 4 Free Stream conditions and Vehicle Parameters	155
Table 5 Influence of Property Variation on Heat Flux	156
Table 6 Wall and Post-Shock Values of Variables for Armaly & Sutton and Wilke's Correlation	157
Table 7 Trajectory Details for AFE vehicle	158

## NOMENCLATURE

$a_1, a_2 \dots a_6$	coefficient used in polynomial expansion of specific heat and enthalpy
$a_1, b_1, c_1, d_1$	terms of tri-diagonal matrix and right hand side of difference equations
$A_{1j}$	used in equation (2.4.24) and (2.4.25)
$B_{1j}$	used in equation (2.4.24) and (2.4.25)
$C_1$	mass fraction of species 1
$C_{p1}$	specific heat of species 1
$C_0, C_1, C_2$	constants defining the forward reaction rate
$Ch$	heat flux coefficient
$D_0, D_1, D_2$	constants defining the backward reaction rate
$D_{1j}$	diffusivity of species 1 into species j
$F_{1j}$	used in equation (2.4.24) and (2.4.25)
$h$	non-dimensional enthalpy, $h = h^* / U_\infty^2$
$K$	thermal conductivity
$K'$	Eucken's correction to thermal conductivity for poly-atomic gases
$K_{br}$	backward reaction rate for reaction r
$K_{fr}$	forward reaction rate for reaction r

$K_r^2$	Cheng's Rarefaction parameter
$K_r^2$	$= \frac{\gamma-1}{2\gamma} \operatorname{Re} \left[ \frac{\mu_{\text{ref}}}{T_{\text{ref}}} \frac{T_o^* + T_w^*}{\mu\{(T_o^* + T_w^*)/2\}} \right]$
$Le$	Lewis number, $Le = (C_p \rho^* D_{1j}) / K^*$
$M$	molecular weight of mixture, defined by equation (2.2.9)
$M_1$	molecular weight of species 1
$M_\infty$	free stream Mach number
$N_R$	number of reactions
$N_S$	number of species
$p$	non-dimensional pressure, $p = p^* / (\rho_\infty^* U_\infty^{*2})$
$r$	non-dimensional distance from the axis of body, $r = r^* / R_b$
$R$	universal gas constant
$R_b$	body nose radius
$Re$	Reynolds number based on reference quantities
	$Re = \frac{\rho_\infty^* U_\infty^* R_b}{\mu^*(T_{\text{ref}})}$
$Re_s, Re_2$	Reynolds number based on post shock quantities
	$Re_s = Re_2 = \frac{\rho_\infty^* U_\infty^* R_b}{\mu_2^*}$
$Re_\infty$	Reynolds number based on free stream quantities
	$Re_\infty = \frac{\rho_\infty^* U_\infty^* R_b}{\mu_\infty^*}$
$s, n$	distances along and normal to body surface
$s, n$	distances along and normal to shock

$T$	non-dimensional temperature, $T = T^* / T_{ref}$
$T_{ref}$	Reference temperature $T_{ref} = (U_{\infty}^*{}^2 / C_{p\infty})$
$T^+$	non-dimensional reduced temperature in terms of energy of attraction between molecules, defined by equations ( 2.4.8) and (2.4.14)
$u, v$	non-dimensional velocities tangential and normal to body surface
$u, v$	non-dimensional velocities tangential and normal to shock
$U_{\infty}^*$	free-stream velocity
$w_1$	mass production rate per unit volume for species 1, $w_1 = w_1^* Rb / (\rho_{\infty}^* U_{\infty}^*)$
$w_N, w_O$	total mass fraction of nitrogen and oxygen respectively in freestream
$X_1$	mole fraction of species 1
$Y$	defined by equation (2.2.14)
$Z$	defined by equation ( 2.2.15)

#### GREEK SYMBOLS

$\alpha_{1r}, \beta_{1r}$	stoichiometric coefficients for species 1 in reaction r for reactants and products respectively
$\beta$	body slope
$\beta_s$	shock slope

$\gamma$	ratio of specific heats
$\delta$	grid clustering parameter
$\epsilon$	Reynolds number parameter, $\epsilon = 1/\sqrt{Re}$
$\epsilon_1$	energy of attraction between colliding molecules of species 1
$\xi, \eta$	nondimensional distance from the body along and normal to the body
$\xi, \eta_s$	nondimensional distance from the body along and normal to the shock
$\eta_e$	shock stand-off distance
$\Theta$	momentum accommodation coefficient
$\Lambda_{1j}$	defined by equation (2.4.23)
$\mu$	coefficient of viscosity for the gas mixture $\mu = \mu^*/\mu^*_{ref}$
$\mu_1$	coefficient of viscosity for species 1 $\mu_1 = \mu_1/\mu^*_{ref}$
$\rho$	density, $\rho = \rho^*/\rho_\infty^*$
$\sigma$	thermal accommodation coefficient
$\sigma_{11}, \sigma_{1j}$	collision diameters
$\Phi_{1j}$	defined by equation ( 2.4.18 ) and (2.4.24)
$x$	defined by equation ( 2.2.13 )
$x_j$	defined by equation ( 2.2.17 )
$\Psi_{1j}$	defined by equation ( 2.4.21 ) and (2.4.25)

$\Omega_{11}^{22}$	collision integral for viscosity
$\Omega_{11}^{11}$	collision integral for thermal conductivity
$\omega_1$	catalytic body 1

### Subscripts and Superscripts

i	quantities for species i
ref	reference quantity
$\infty$	free stream quantity
b	quantities at the base of the shock layer
s	quantities at the shock
w	quantity based on wall conditions
o	quantity at Stagnation condition
*	physical quantity

equations, is numerically complex and time consuming. Also as the Reynolds number increases, it becomes increasingly difficult to capture the thin shock through the merged layer computation. One of the main aim of the present investigation is to increase the domain of the validity of the solution and to avoid the numerical instabilities associated with the integration through the shock. To achieve this, a shock layer model with full Navier-Stokes equations is proposed in this work. The domain of validity is increased because it retains all the essential terms in the equations. The numerical instabilities do not limit the solution because the integration through the shock transition zone is avoided by employing a shock layer model.

With the emergence of real gas effects at high temperatures, the problem of simulating the flow-field becomes more complex by any of these approaches due to the presence of mass production terms in the species equations. Non-linear dependence of the production term on temperature and concentrations introduces stiffness into the equations, which usually leads to non-convergence and failure of the numerical computations. Sometimes it also leads to a violation of the overall mass conservation. These problems become more severe as the Reynolds number increases. The present investigation also aims at studying these limitations and removing them to the extent possible



by a new shock layer formulation with full Navier-Stokes equations.

In the present investigation, the full Navier-Stokes equations are used to describe the hypersonic flow near the stagnation point of a blunt body both for perfect and chemically reacting gases. The equations are solved between the body and the shock. The surface slip conditions for the multi-component gas mixture are used at the wall. The mass production rates within the shock transition zone are neglected but species diffusion at the shock is accounted for in the shock conditions. Modified Rankine-Hugoniot relations are used as boundary conditions at the shock. Using the concept of local similarity, the governing equations are specialized for stagnation line flow. The resulting system of non-linear coupled ordinary differential equations with split boundary conditions is solved numerically using a special finite difference scheme called Unified Difference Representation. The equations are solved both for perfect and chemically reacting gases.

It is demonstrated that the flow field simulations using the full Navier-Stokes equations in the stagnation zone of a blunt body provide uniformly accurate results in low as well as high Reynolds number regime. At low Reynolds numbers it shows a good agreement with the experimental data. The computed results reproduce

experimentally observed features of low density flows like, increase in impact pressure and recovery temperature at stagnation point with decrease in Reynolds number, which the earlier approximate methods fail to predict even qualitatively. The computed heat transfer coefficient shows good agreement with boundary layer results at higher Reynolds numbers. The predicted profiles agree well with the available experimental measurements for density, pressure and temperature profiles across the shock layer for the low density regime.

The analysis shows that the wall temperature, in addition to the Cheng's rarefaction parameter, plays a vital role in determining the heat flux to the wall. For chemically reacting flows in addition to the Reynolds number, the free stream velocity also influences the heat transfer coefficient to the wall and needs to be accounted for explicitly. The concentration profiles are in good agreement with the merged layer predictions. This good agreement holds even at low Reynolds numbers where the shock wave is thick. The special treatment of mass production terms along with full Navier-Stokes equations in the shock layer has resulted in the increased range of Reynolds numbers for which non-equilibrium computations converge. These factors establish the superiority of present shock layer formulation with the full Navier-Stokes equations over the current viscous shock layer

## CHAPTER 1

### INTRODUCTION

#### 1.1 INTRODUCTION

The problem of hypersonic flow past a blunt axisymmetric body has attracted considerable attention due to its application to the design of re-entry vehicles. Usually, aerodynamic drag is used to slow down the vehicles entering the atmosphere with hypersonic speeds. During the atmospheric entry phase of a vehicle at hypersonic velocity, considerable work is done by the vehicle on the air surrounding it due to viscous effects. This work done by the vehicle on the surrounding atmosphere exhibits itself as thermal energy and results in increased temperature of the air surrounding the body. A part of this heat is transferred to the vehicle itself and increases the temperature of the body. In order that the vehicle survives this thermal environment, the body has to be protected against this heat load, which is quite intense. This protection is required from two considerations--(1) too much heating is likely to change the aerodynamic shape due to ablation/melting of the

vehicle's outer skin resulting in changed aerodynamic characteristics and performance of the vehicle and this increased temperature of the vehicle skin will result in change in the environment of the electronic equipments and effect their proper functioning. Thus it is essential that one has a good estimate of heat flux load coming on the vehicle, so as to be able to design an efficient protection system against this aerodynamic heating and ensure desired vehicle performance.

As vehicle descends in the atmosphere, the surrounding air changes its characteristics from the free-molecular flow regime in the upper atmosphere to the continuum regime in the lower atmosphere. The free-molecular regime is well investigated from kinetic theory considerations. The other extreme of the highly dense air, where shock wave is extremely thin and the viscous effects are confined to a narrow region near the body surface, lends itself to the classical boundary layer treatment. Between these two limits, the situation exists in which air is sufficiently rarefied resulting in breakdown of usual boundary layer approximations but at the same time mean-free path is not large enough for the free-molecular concepts to apply. This flow regime is referred to as the intermediate regime. The main features of this regime are the thickening of the boundary layer and the shock wave and their subsequent merger. Usually this regime is

further subdivided based on the different theoretical models considered necessary to describe the flow. Various authors have subdivided this intermediate regime differently depending upon the flow phenomenon and the range of validity of the regime. Hays and Probstein (1959) divided the intermediate regime into the following regimes:

- (1) First order collision regime
- (ii) Transitional regime
- (iii) Fully merged layer regime
- (iv) Incipient merged layer regime
- (v) Viscous layer regime
- (vi) Vorticity interaction regime

However, Ahouse and Bogdonoff (1969) divided this intermediate regime into following two regimes:

- (1) Transitional regime
- (ii) Merged layer regime

The transitional regime defined by Ahouse and Bogdonoff includes first order collision regime and transitional regime as defined by Hays and Probstein, while merged layer regime of Ahouse and Bogdonoff encompasses the fully merged layer regime, incipient merged layer regime, viscous layer regime and vorticity interaction regime of Hays and Probstein. In this work the classification given by Ahouse and Bogdonoff is followed.

The thickening of the boundary layer over the body

surface is associated with decreasing Reynolds number and increasing Mach number. Increased Mach number results in increased temperature in the flow-field. This increased temperature leads to higher viscosity resulting in flow-field being dominated by viscous effects. At the same time, increased Mach number results in decreased shock stand-off distance. Decreasing Reynolds number is associated with increase in viscous forces in comparison to the inertia forces. This increased viscous effect lead to increased boundary layer thickness. Thus at higher Mach number and lower Reynolds number regime, the entire flow-field is dominated by viscous effects and there is no inviscid flow region between the body and shock wave.

Another important feature of hypersonic flow is the emergence of the real gas effects, which means that the thermodynamic properties of the real air deviate from those of an ideal gas with constant specific heats. These deviations result from various physical processes occurring in the air at high temperature, namely, excitation of molecular vibration, dissociation ionization and chemical reactions. These processes occur at a finite rate, which can be characterized by relaxation time or relaxation lengths in a flow of a given velocity. If all the relevant relaxation lengths are very much smaller than the smallest flow field dimension of interest, flow may be regarded as being in thermo-chemical equilibrium. If

relaxation lengths and flow dimensions are comparable, departure from thermo-chemical equilibrium will occur. The resulting non-equilibrium flow of real gas may influence the aerodynamic characteristics. The analysis of non-equilibrium air flow requires detailed information on the mechanism and the rate of high temperature processes. If all the relevant relaxation lengths are much greater than the largest flow dimension, the flow may be regarded as frozen flow and chemical composition remain constant. These relaxation lengths are very large at higher altitudes and quite small at lower altitudes. Thus during re-entry of a vehicle, non-equilibrium flow must occur.

From continuum considerations, the existing theoretical analyses can be divided into three main categories. Firstly, there is the higher order boundary layer theory, developed systematically from the theory of singular perturbations. The classical boundary layer theory of Prandtl is the first approximation of this theory. Higher order terms provide corrections to the first approximation. This higher order theory is valid only if there is small departure from the classical boundary layer limit. The second approach to the blunt body problem is the two thin layer theory, where the flow-field is divided into two zones-(i) shock transition zone (shock structure) and (ii) shock layer that is the region between the shock and the body. In this approach, the

mass, momentum and energy fluxes tangential to the shock are assumed to be negligible in the shock transition zone. Equations similar to Prandtl's boundary layer equations are used to describe the flow field in the shock layer. These equations are uniformly valid for both inviscid flow and viscous flow. Transport effects just behind the shock wave are taken into account and consequently the classical Rankine-Hugoniot shock conditions are modified to account for the transport effects. These conditions are derived by integrating the ordinary differential equations valid in the shock transition zone. Investigations of the flow field by this model are found to be successful in predicting surface quantities such as heat transfer rate well-into the transition region, but fail to give correct behaviour of surface pressure and recovery factor at low Reynolds number regime. It also fails to describe the detailed flow-field accurately at low Reynolds numbers. It is surmised in this work that this failure to predict the correct behaviour of surface quantities at lower Reynolds number regime is due to the simplification carried out in the Navier-Stokes equations and not due to failure of shock layer model as such. From continuum theories, the last approach to the problem is the direct numerical integration of Navier-Stokes equations from the surface to the free-stream. This method is numerically complex and time consuming. Also as the Reynolds number increases, it



Becomes increasingly difficult to capture the thin shock by direct integration. Several attempts have been made to investigate non-equilibrium flow using these models. The governing equations of the non-equilibrium flow are stiff due to mass production terms in the species continuity equations. This stiffness leads to convergence problem and sometimes to violation of overall mass conservation. Currently Monte Carlo simulation is being widely used to simulate the flow field in the transition regime.

The main aim of the present dissertation is to improve the continuum solutions in the stagnation region of a blunt body under hypersonic conditions with and without the real gas effects. Improvements are required to increase the range of validity of solutions and to remove the instabilities associated with the thin shock. For chemically reacting flows improved method is required to deal with stiffness of the species continuity equations and to improve the convergence. Real gas effects include excitation of various degrees of freedom ( exhibited as variation of specific heat with temperature ) and chemical reactions. Surface slip and shock slip conditions are considered to account for rarefaction effects.

## 1.2 Assessment of Existing Theories and Literature

Existing continuum approaches to the hypersonic blunt body problem can be divided into three main categories.

There are

- (i) Higher order boundary layer theory
- (ii) Two thin layer theory/ Shock layer theory
- (iii) Merged layer theory

However, currently kinetic theory is being used to predict the flow-field well into transition regime. This approach is termed as

- (iv) Direct Simulation Monte Carlo (DSMC) technique

A survey of continuum methods was made by Cheng (1966) and Jain (1968). A critical evaluation of the work done along these approaches, leading to the motivation of the present investigation, is given below.

### Higher Order Boundary Layer Theory

The classical boundary layer theory of Prandtl is embedded as the leading approximation in a systematic asymptotic expansion of the Navier-Stokes equations in an inverse power of the Reynolds number. The method of inner and outer expansions, also called the matched asymptotic expansion ( Van Dyke 1964a ) is used here. Different types of expansions are used in different regions of the flow, depending on the order of magnitude of the thickness of the regions. So far, calculations are made up to third order boundary layer, with Prandtl's boundary layer as the leading first approximation. Exhaustive work on the second order boundary layer is done by Van Dyke (1962, 1963, 1964b), Kott and Lenard (1962) and Lenard (1962) among

others. Computations were carried out for third order boundary layer by Kao (1964a) for cold wall and by Oberai (1964) for an insulated wall.

The procedure followed in the higher order boundary layer theory is as follows. The flow quantities are expanded asymptotically for large Reynolds number in the shock wave, the inviscid region and the boundary layer. The variables are stretched appropriately for the different flow regions depending upon the thickness of the region. For proper stretching of the coordinates and variables, estimates of the thickness for the various flow regions already available from previous studies, are used. These expansions are substituted in the Navier-Stokes equations and the coefficients of like powers of the stretching parameter are collected resulting in different sets of equations valid in different regions of the flow. These equations are solved according to the following scheme:

(i) First Order Boundary Layer Approximation:- (a) first the basic inviscid flow is computed and (b) the first order boundary layer equations are solved matching with the basic inviscid flow.

(ii) Second Order Boundary Layer Approximation:- (a) The second order equations in the inviscid region are solved taking into account the displacement thickness caused by the first order boundary layer, (b) the second order

boundary layer equations are solved matching with the external inviscid flow.

(iii) Third Order Boundary Layer Approximation:- (a) The first order equations for the shock structure are solved matching with the free-stream ahead and basic inviscid flow behind, (b) the third order equations in the inviscid region are solved taking into account the modified shock conditions, which depend on the first order shock-structure solution and the shock curvature, (c) the third order boundary layer equations are solved matching with the third order inviscid flow, and finally, (d) the third order shock structure equations are solved.

For any given Reynolds number, the afore mentioned solutions for the various components can be combined to give a composite solution that is uniformly valid throughout the flow field.

The higher order boundary layer theory can describe the flow accurately only if the higher order terms are small in comparison to the basic inviscid and first order solutions. This implies that Reynolds number is moderately large and interaction between the boundary layer, inviscid flow and shock structure is not significant. This analysis allows the identification of several second order effects and calculation of their influence on the flow field individually. Van Dyke (1962) identified seven second order effects, namely, longitudinal curvature, transverse

curvature, displacement effects, external gradient of entropy, external gradient of enthalpy, slip velocity and temperature jump at the wall. The external vorticity is related to the external entropy gradient and enthalpy gradient through the Crocco's relation. All these effects, except for velocity slip and temperature jump, are not independent of each other in strict sense and thus it is better to evaluate them concurrently. Van Dyke (1963) evaluated these influences for stagnation point heat transfer rate for a sphere at  $M_\infty = 4$  for perfect gas with  $\gamma = 7/5$ , Prandtl number 0.7, viscosity proportional to temperature and surface temperature being 0.5 times stagnation temperature. He gave the following expression for heat transfer rate:

	external	curva	slip	and	displ.	
	vorticity	-ture	temp.	jump	effect	

$$\frac{q}{q_{BL}} = 1 + [ \begin{matrix} 0.57 & +0.17 & -0.39 & -0.18 & +0.17 \end{matrix} ] Re_s^{-1/2}$$

Similar expression is available for the case when surface temperature is 0.2 times stagnation temperature. Here  $Re_s$  is the Reynolds number based on the post-shock conditions and nose radius. It is seen here that the external vorticity has major influence on the stagnation point heat flux. A detailed discussion on the various second order effects can be found in the review papers by Cheng (1966), Jain (1968) and Van Dyke (1969).

The higher order boundary layer theory does not give accurate results for low Reynolds number flow, where the flow field between the body and the shock is influenced by viscous effects. The boundary layer theory envisages an essentially inviscid zone between the shock wave and the boundary layer, even though in the third order boundary layer theory viscous terms appear in this zone. In this flow regime, the departure of flow quantities from the classical boundary layer solutions is large and thus cannot be treated as a perturbation. Moreover, the method of treating the various zones in a piecewise manner is no more valid in this flow regime. Indeed, Kao (1964b) noted that for  $Re_s$  less than about 100, the heat transfer rates predicted by the third order boundary layer theory deviate appreciably from the experimental results. The failure of the higher order boundary layer to describe the low Reynolds number flow expresses itself in interesting ways. Anomalous situations such as the boundary layer overtaking the position of the shock or the thick shock wave encompassing even the body (Kao 1964b) occur during the computation of low Reynolds number flow. In such cases, it is difficult to construct any meaningful composite solution.

For the case of real gas and chemically reacting flow, most of the studies are confined to the classical boundary layer analysis and higher order boundary layer

analysis has not been developed.

Fay and Riddell (1958) analysed the influence of chemically reacting flow on the stagnation point heat flux and came out with a correlation for surface heat transfer rate for frozen and equilibrium flow. This analysis is valid for large Reynolds number, when the viscous effects are confined to the region near the wall and an inviscid flow region separates the boundary layer and the shock. The analysis is based on the assumption that air is a binary gas and that the Prandtl and Lewis numbers are constant across the boundary layer, though the concentration changes across the boundary layer due to temperature variation. This correlation expresses the stagnation point heat flux in two parts--(i) heat flux due to perfect gas and (ii) contribution due to species diffusion both for frozen and equilibrium flows. Blottner (1964) analysed the non-equilibrium boundary layer for a binary gas consisting of atoms and molecules. This analysis required the inviscid non-equilibrium flow conditions on the surface as input. The governing equations were solved numerically using a marching procedure starting from stagnation point/leading edge of the body. The analysis shows that in the non-equilibrium boundary layer the maximum temperature could be nearly 4.5 times higher than the corresponding temperature for the equilibrium boundary layer.

## Two Thin Layer Theory - viscous Shock Layer Theory:-

The main feature of this theory is to divide the entire flow field into two adjoining regions, namely the shock layer and the shock wave ( or the shock transition zone), both of which are assumed to be thin. In the shock transition zone, fluxes of mass, momentum and energy parallel to the shock are neglected. This assumption, together with the thin layer approximation, reduces the governing equations in the shock transition zone to a set of ordinary differential equations similar to that for a plane shock. The governing equations for the shock layer, that is, the region between the inner edge of the shock wave and the body, embody differential equations of both the inviscid flow and the classical boundary layer theory. These are obtained from Navier-Stokes equations by using the thin layer approximation and a high shock compression ratio assumption, by retaining the terms of the order of  $\epsilon = (\gamma-1)/2\gamma$ . These equations are parabolic in nature along the length of the body and their mathematical analysis is similar to the problem of classical boundary layer theory.

The features of the viscous shock layer theory are similar to two thin layer theory. However, in this case equations are solved in the shock layer only, that is the region between the body and the shock. The equations in the shock transition region are not solved. While deriving



the governing equations, thin shock layer assumption is made and terms of the order of  $(1/Re)$  are retained in the Navier-Stokes equations. These equations are uniformly valid in inviscid flow region and viscous flow region near the wall.

An essential feature of the two thin layer model is to preserve the viscous and energy transport effects just behind the shock. The higher order boundary layer theory failed to do it. The shock transition zone equations, when integrated across the shock, lead to modified form of Rankine-Hugoniot relations for the post-shock flow variables. According to these modified relations, the tangential velocity and the total enthalpy are not conserved across the shock but are controlled by the transport effects behind the shock, which are not small for low Reynolds number flow. These transport effects are proportional to the gradient of velocity and temperature. Being similar to surface slip conditions, these conditions are referred to as shock slip conditions (Probststein and Pan 1962).

It is interesting to note that, in the two thin layer theory, the flow in the shock layer together with the location of its outer edge (inner edge of shock transition zone or location of the shock if shock thickness is small) can be determined entirely independent of the flow in the shock transition zone. The

modified Rankine-Hugoniot conditions and the appropriate conditions at the body surface are sufficient to solve the shock layer equations completely. However, the flow in the shock transition zone depends on the shock layer solution. The shock layer solution provides the explicit boundary conditions for integrating the first order differential equations governing the shock transition zone.

With this basic formulation of the two thin layer theory, Cheng (1961) investigated analytically the shock layer flow in the stagnation region in the merged layer regime. It is noticed that the use of shock slip conditions alone ( without surface slip conditions ) lead to reduction of surface heat flux. Thus surface heat transfer rate and skin friction values tend towards the free-molecular values of heat transfer and skin friction for the case of unit accommodation coefficient. Further Cheng and Chang (1964) evaluated an analytical solution for the shock transition zone in the Newtonian ( $\gamma \rightarrow 1$ ) and the hypersonic ( $M_\infty \rightarrow \infty$ ) limit. This solution compares well with the results of Levinsky and Yoshihara (1962), where direct integration through the shock was carried out for monatomic gas. Davis (1970) solved the viscous shock layer equations on different hyperboloids. Slip conditions are incorporated as higher order terms in a perturbation scheme. The shock slip conditions have been used to account for transport effects at the shock.

However, the shock slip conditions used by Davis are inconsistent with the governing equations. These shock slip conditions do not account for change in post-shock pressure due to change in post-shock normal velocity.

Bush (1964) formulated the hypersonic viscous blunt body problem using asymptotic expansion of the variables in terms of  $(1/Re)$ ,  $(1/M_\infty^2)$  and  $\frac{\gamma-1}{\gamma+1}$ . Bush divides the shock transition zone into three subregions, namely (a) the outer region, (b) the middle region, and (c) the inner region. Including the shock layer region, Bush analyses the flow on the basis of four distinct regions as against only two used by Cheng in the two thin layer model. Cheng (1966) established that the equations governing the shock transition zone in the two layer model are equivalent to the composite equations of Bush and are uniformly valid in the entire shock transition zone.

Regarding the real gas flow with chemical reactions around blunt bodies, most of the work has been carried out in the viscous shock layer model instead of the two thin layer model. Blottner (1969) analysed the viscous shock layer flow at the stagnation region of a blunt body for chemically reacting flow. In this work, air was considered as consisting of seven species with seven chemical reactions. The analysis considered fully catalytic wall,

but did not account for either wall slip or transport effects at the shock. For evaluating the post-shock conditions, chemical composition was considered to be frozen as in the free stream. The governing equations were solved using finite difference scheme. Computations showed that this analysis predicts higher temperature at the shock than the corresponding equilibrium flow temperature. This temperature decreases as one moves towards the wall due to dissociation of gas, but the gas has not reached the equilibrium before boundary layer is reached. The computations also show that the assumption of inviscid equilibrium flow for the boundary layer is not correct even for Reynolds number corresponding to an altitude of 45.72 km. Kang and Dunn (1972) used shock layer analysis for hemisphere-cone using eleven species model with twenty six chemical reactions for simulating the real gas flow. However, the analysis followed the two thin layer model of Cheng and assumed constant Prandtl and Lewis numbers and binary diffusion. Modified Rankine-Hugoniot relations were used to account for transport effects behind the shock. These served as the initial conditions for the shock transition zone. The method of integral relations was used to obtain the solution of the governing equations. The analysis shows that, at down stream stations, the temperature profile overshoots the post-shock temperature.

Moss (1971) extended the analysis of Blottner and

analysed the chemically reacting and equilibrium flow field around  $45^\circ$  hyperboloid. This viscous shock layer analysis considers only 5 species air model and does not consider ionised species and ionisation reaction. The analysis includes the effect of multi-component diffusion and mass injection.

Computed results of Moss show that the non-equilibrium model predicts heat transfer rates which are lower than both the frozen and equilibrium predictions. Non-equilibrium heat flux predictions for the stagnation point are approximately 60% of the corresponding prediction for frozen and equilibrium flow for the cases considered in the analysis. Results also show that, for heat flux predictions, the use of variable binary diffusion coefficient ( atomic oxygen in molecular nitrogen ) compares favourably with multi-component diffusion, though there is some difference in the concentration profiles near the wall in the two cases of binary diffusion and multi-component diffusion. The computations fail to converge for the cases when the post-shock Reynolds number is 500 and above.

There have been attempts to extend this analysis of chemically reacting flow to three-dimensional bodies. Miner and Lewis (1975), Kim, Swaminathan and Lewis (1984) and Kim and Lewis (1985) are some of these studies. Miner and Lewis (1975) studied the body at angle of attack and

restricted the analysis to the windward plane of symmetry. Kim and Lewis (1985) simulated the three dimensional flow field over the Shuttle orbiter. The analysis used shock and wall slip conditions with finite wall catalyticity. These works confirm the finding of Moss (1971) regarding non-equilibrium heat flux predictions being lower than both the frozen and equilibrium flow heat flux predictions.

Prabhu, Tannehill and Marvin (1987) solved the parabolised Navier-Stokes (PNS) equations for hypersonic laminar flow of a multi-component chemically reacting gas mixture over two-dimensional/axisymmetric bodies. Space marching technique is used to evaluate the solution at the down stream stations. The equations are solved from body to the free-stream. The marching procedure requires that the local Mach number be greater than unity in the inviscid part of the flow. This implies that some other procedure is required to generate the solution in the stagnation region of the blunt body. The analysis shows higher degree of dissociation near the wall for PNS code in comparison to boundary layer results. This is due to higher pressure and density at the wall for PNS predictions.

Bhutta and Lewis (1988) solved three-dimensional PNS equations for chemically reacting gas mixture over a sphere-cone body at large angle of attack. The analysis

two seven species and seven reaction model. A new predictor-corrector scheme is devised to account for strong cross-coupling in the cross flow separated regions on the leeward side of the body. The bow-shock shape and its location are computed as the part of the solution. The fluid-mechanical equations and species continuity equations are decoupled in the solution procedure. Their coupling is accounted through an iterative procedure. However, this method can not be used to simulate the flow field in the stagnation region of the body. The analysis shows that with angle of attack, the leeward side has more dissociation of oxygen and nitrogen and formation of  $\text{NO}^+$  than on the windward side. This is due to the thicker high temperature region on the leeward side.

Park (1985) in his paper discusses the various aspects connected with the computation of the chemically reacting flow field. This work also discusses the situation when vibrational temperature and translational temperature are not in equilibrium. The influence of this phenomenon on the reaction rates is also discussed.

Park identifies the numerical problems encountered in chemical non-equilibrium flows as follows:

- (1) Violation of overall mass conservation,
- (11) Instability caused by spurious negative concentrations.

Violation of mass conservation also leads to

violation of conservation of momentum and energy. Though these problems are discussed by Park in connection with the unsteady approach, they are equally relevant to steady state solution procedures such as the viscous shock layer method.

The two thin layer model predicts the stagnation point heat transfer rates in good agreement with the experimental results and is in several respects superior to the higher order boundary layer theory. However, one should not expect the two thin layer theory to predict the detailed flow field correctly in the highly rarefied flow regime, due to several simplifying assumptions, which are not valid under rarefied conditions. These assumptions are as follows:

(i) The basic assumption of zone of disturbance being thin and thus the order of magnitude analysis is not valid under rarefied conditions, where the shock wave and shock layer are thick in comparison to body nose radius. The terms dropped based on this assumption are not negligible.

(ii) The assumption of thin one dimensional shock is not valid and the tangential transport of mass, momentum and energy across the shock can not be neglected.

(iii) The coupling between the shock layer structure and the shock structure is very weak. The shock layer solution can be obtained independent of the shock structure. In case of low density flows, there will be stronger coupling



however the shock layer structure and the shock structure, and the shock structure will influence the shock layer structure.

The failure of the two thin layer theory has been attributed by Ahouse and Bogdonoff (1969) to the failure of Navier-Stokes equations in the rarefied regime. But this is not correct as this model does not represent the full Navier-Stokes equations. It is possible that considering the full Navier-Stokes equations in this model will lead to better results and higher range of validity for this model. It is one of the aspect that is studied in detail in the present dissertation.

#### Numerical Integration through the Shock:

In this approach the governing equations, either the full Navier-Stokes equations or a simplified form, are integrated from the body surface to the free stream through the shock. Depending on the flow parameters like Mach number and Reynolds number, the position of the sharp shock or the merged profile of a thick shock wave and a thick viscous layer near the body come out as an integral part of the solution. However, the difficulties associated with the numerical integration of the Navier-Stokes equations make the computations very expensive. Also at higher Reynolds number, integration through the thin shock transition zone causes numerical instabilities.

Levinsky and Yoshihara (1962) and Kao(1964b) used this

approach in their investigation of the blunt body problem. Levinsky and Yoshihara obtained the exact numerical solution of simplified Navier-Stokes equations for insulated and cold wall cases for a monatomic gas.<sup>4</sup> In this investigation, thin layer assumption was used to simplify the Navier-Stokes equations, but this analysis contained more terms than originally used by Cheng in his thin layer model. This extended the validity of the results to much lower Reynolds number than Cheng's theory in predicting the detailed flow structure. At  $Re_{\infty} = 152$ , it is noted from this analysis that the region of disturbance is approximately 50% of the body nose radius.

Kao (1964b) used the full Navier-Stokes equations with local similarity assumption to investigate the stagnation region of a blunt body. Jain and Adimurthy (1974) extended this analysis further and obtained the solutions for various free stream conditions. These results show that the failure of the thin layer model to predict the correct behaviour of surface pressure with decreasing Reynolds number was not due to the failure of the Navier-Stokes equations, as envisaged by Ahouse and Bogdonoff (1969) and Vogenitz and Takata (1970) but was due to the simplifications introduced in the analysis by virtue of various assumptions.

Dellinger (1971) and Kumar and Jain (1975) obtained the merged layer solutions for chemically

reacting flow in the stagnation region of a blunt body. However, both these analyses assume that vibrational degree of freedom is fully excited and thus do not consider actual variation of the thermal energy of the gas as a function of the gas temperature. Also these investigations assume a simple power law variation of viscosity instead of a more realistic variation depending upon the collision cross-section. Surface slip effects are also ignored in the investigation. These studies show that the merged layer analysis predicts higher temperature in the shock layer than the thin layer theory. The higher temperature gives rise to higher reaction rates and consequently higher levels of dissociation and ionisation. Gupta and Simmonds (1986) extended this analysis by considering the actual variation of specific heat and viscosity of gases. This analysis employs the multi-component surface slip conditions. The energy equation is used in terms of temperature, thus avoiding the use of time consuming process of converting the enthalpy into temperature for use in reaction rate estimation and transport property estimation. These results show a good agreement with Direct Simulation Monte Carlo (DSMC) results of Moss and Bird (1985) for the case of shuttle orbiter.

Several authors have used unsteady approach to solve the full Navier-Stokes equations for simulating the flow field over a given body. In this approach, the unsteady

equations are solved and time marching procedure is used to get the steady state solution. MacCormack (1969) proposed his predictor-corrector scheme for solving the full Navier-Stokes equations. The scheme is second order accurate in space and time. The constraint on the time step has also been derived using stability considerations for the explicit scheme. However, due to very small time step, the time involved in the computation is very large.

Widhopf and Victoria (1972) used unsteady approach for solving the full Navier-Stokes equations for chemically reacting gas mixture past a blunt body for merged layer flow analysis. The analysis used seven species model for the air. The comparison with thin layer solution shows that thin layer model predictions for concentrations of O, N and NO are lower as compared to the merged layer model using full Navier-Stokes equations. However, this difference between the predictions by two methods decreases with increase in Reynolds number.

Li (1987) used unsteady approach to solve laminar chemically reacting flow over a blunt body under hypersonic low density conditions. The analysis used the full Navier-Stokes equations between the body and the shock. A bow shock is treated as a computational boundary. Shock slip and surface slip conditions were not considered in the analysis. In the solution procedure, fluid mechanical equations and species continuity equations were

decoupled. The approach of decoupling the two sets of equations results in faster convergence.

Candler and MacCormack (1988) solved the full Navier-Stokes equations for multi-component gas mixture in thermo-chemical non-equilibrium for a two-dimensional configuration. Implicit Gauss-Seidel line relaxation technique is used for solving unsteady Navier-Stokes equations to obtain steady state solution. The analysis uses three temperature model for energy conservation and estimation of chemical reaction rates. The analysis considers both five species and seven species model for the air. It is noted that stagnation heat transfer rates for reacting flow are nearly 50% higher than the corresponding perfect gas value. The analysis shows that electron temperature is approximately four times the free stream temperature. Translational temperature is approximately twice the vibrational temperature except near the wall, where all the temperatures are nearly equal to the wall temperature.

#### Direct Simulation Monte Carlo (DSMC) Technique

There have been attempts to simulate the flow field using Boltzmann equations. In this approach, the fluid is not considered as a continuum. Particles are considered individually or in small groups while simulating the flow. This approach is essentially valid for highly rarefied

flow regime, where the Knudsen number is of the order of unity or higher. The only closed equation that is then applicable is the Boltzmann equation. Solutions to the Boltzmann equation are readily obtained in the free molecular limit as the Knudsen number tends to infinity. However, as the Knudsen number decreases and the transition flow is encountered, it becomes difficult to solve the Boltzmann equation. Monte Carlo procedures have been developed to solve such problems. Bird (1966) used this method to evaluate heat flux and drag of a sphere in transition regime. Vogenitz and Takata (1970) computed the flow-field in the stagnation region of a blunt body. Bird (1976, 1981) has developed one such Monte Carlo technique called Direct Simulation Monte Carlo (DSMC) for simulating the transition regime flow.

In the DSMC method, molecular motion and inter-molecular collisions are simulated using appropriate probability law. The time parameter in the simulation can be identified with the physical time in the real flow, and all calculations are unsteady. For steady state flow conditions, time asymptotic limit of the unsteady solution is obtained. The computation is always started from an initial state that permits exact classification such as a vacuum or uniform equilibrium flow. The computations take advantage of flow symmetries to reduce the number of position coordinates and the dimension of cell network,

But collisions are always considered as three dimensional phenomena. For simulating the more realistic viscous behaviour of the fluid, variable hard sphere(VHS) model is used. The VHS model accounts for more realistic collisions between the molecules by modifying the hard sphere model. The chemical reactions are incorporated into the analysis by considering the reactive cross sections.

Though the DSMC model is basically developed for the transition flow regime, currently it is being used to simulate the flow for the Knudsen number of the order of 0.001. Moss and Bird (1985) used the DSMC technique to simulate the flow over Space Shuttle orbiter nose during re-entry for Knudsen number as low as 0.03. These results agree well the measured heat flux data in flight. Moss, Bird and Dogra (1988) have applied the DSMC method to simulate the flow field during the atmospheric entry of Aero-assist Flight Experiment ( AFE ) vehicle. In this analysis, apart from chemical reactions, radiation is also considered. It is seen that at an altitude of 90 km radiative heat transfer is nearly 1 percent of the convective heat flux, while at an altitude of 80 km it is as high as 15 percent. The radiative heat flux is higher at lower altitude because of the higher overall temperature in the shock layer.

### 1.3 Surface Slip Condition

In the low density flow regime, slip velocity and

temperature and density conditions are important rarefaction effects. Due to the low density in the flow, the gas particles do not suffer sufficient number of collisions so as to lose their entire momentum and thus possess a finite velocity relative to the solid surface. Similarly, the temperature of the gas adjacent to the body surface differs from that of the body. These boundary conditions become more important as the gas becomes more and more rarefied.

Several authors have derived the expressions for slip velocity and temperature jump boundary conditions using approximate solutions of the Boltzmann equation in the vicinity of the wall. These relations are derived under the assumption of small departure from local thermodynamic and chemical equilibrium conditions. The expressions given by Shidlovskiy (1967) are:

$$u = -\frac{2-\theta}{\theta} \frac{5\pi}{16} \lambda_s \left( \frac{\partial u}{\partial y} + \frac{\partial v}{\partial x} \right) + \frac{15}{32} \sqrt{\left( \frac{\pi}{2} R T \right)} \left( \frac{\lambda_s}{T} \frac{\partial T}{\partial x} \right)$$

and

$$\frac{T_s}{T_\infty} = 1 + \frac{2-\sigma}{\sigma} \frac{75\pi}{128} \left( \frac{\lambda_s}{T} \frac{\partial T}{\partial y} \right) - \frac{5\sqrt{\pi}}{48\sqrt{2}} \frac{\lambda_s}{\sqrt{RT}} \left( \frac{\partial u}{\partial x} - 2 \frac{\partial v}{\partial y} \right)$$

where  $x$  and  $y$  are the coordinates along and normal to the surface respectively, while  $u$  and  $v$  are the tangential and normal velocities.  $\theta$  and  $\sigma$  are the momentum and thermal accommodation coefficients of the surface and  $\lambda_s$  is the mean free path. It is to be noted here that even for



complete accommodation ( $\theta = \sigma = 1$ ), the slip velocity and temperature jump do not vanish. The term involving temperature gradient in the expression for velocity slip is referred to as the thermal creep. According to this term, a temperature gradient along the surface induces a flow in the direction of increasing temperature. Usually this term is neglected in the studies involving slip velocity as this term belongs to a higher order of smallness than the velocity gradient term.

In case of a multi-component gas mixture, the diffusion of species influences the slip velocity and temperature jump conditions at the wall and thus needs to be accounted for in the distribution function. Scott (1973) evaluated the wall slip conditions for a multi-component gas mixture with diffusion and wall catalysed atom recombination. These conditions were simplified by Hendricks (1974) for direct application to the fluid flow problem. However, these conditions led to an anomalous situation where temperature jump and slip velocity decreased with increasing rarefaction (Johnston and Hendricks 1978). Gupta, Scott and Moss (1985) evaluated these conditions once again for multi-component gas mixture using a distribution function, which accounted for the diffusion of the species more accurately. These conditions when applied to fluid flow problem did not exhibit anomalous behaviour. Present analysis uses these

slip conditions which are reproduced in section 2.2.

The derivation of the slip conditions assumes small departure from local thermodynamic and chemical equilibrium conditions, that is, gradients of velocity, temperature and concentration are small. The validity of these slip conditions is not established for large gradients.

#### 1.4 Scope of the Present Work

In this work, hypersonic flow in the stagnation zone of the blunt body is investigated for perfect and chemically reacting gases. In the previous sections several limitations of existing continuum approaches have been pointed out. Some of the unresolved questions in this regard are as follows:

- (i) Is it possible to extend the range of validity of the shock layer method by use of full Navier-Stokes equations?
- (ii) How do the chemical reactions within the shock transition zone influence the shock layer flow-field at low Reynolds numbers, where the shock wave is thick?
- (iii) Is it possible to extend the range of Reynolds number for which non-equilibrium computations converge?
- (iv) How to overcome the violation of mass conservation law normally occurring in numerical studies of chemically reacting flow?
- (v) Is it possible to overcome the numerical instability

caused by spurious negative concentrations?

The aim of the present investigation is to find out the answers to questions posed above. In the present analysis full steady state Navier-Stokes equations with species continuity equations are assumed to be valid for describing the hypersonic rarefied flow field past a blunt body. The region of interest is the stagnation region, which is most crucial for thermal protection system design considerations. In this region, the non-dimensionalised governing equations are reduced to a set of ordinary differential equations with split boundary conditions under the assumption of local similarity. Post-shock transport effects are accounted for by using modified Rankine-Hugoniot conditions. Surface slip conditions for multi-component gas mixture are used at the wall. The analysis considers a real gas with variable specific heat. Transport properties are evaluated using available correlations for multi-component gas mixture. The numerical solution to the governing equations adapted to the stagnation region is obtained using a finite difference procedure.

As a result of present studies, it is observed that the use of the full Navier-Stokes equations within the viscous shock layer approach provides uniformly accurate results both for high as well as low Reynolds number. At high Reynolds number, heat transfer results approach the

boundary layer values while at low Reynolds number it gives correct behaviour of surface pressure and adiabatic wall temperature. It is seen that wall pressure and adiabatic wall temperature increase with decreasing Reynolds number as observed experimentally. The present study shows that the use of full Navier-Stokes equations within shock layer model increases the range of validity of the solution without having to solve fully merged layer equations from the body to the free stream.

For the case of a real gas, the flow-field obtained from present computations agrees well with merged layer and DSMC results. It is also observed that in addition to the Reynolds number, free stream velocity influences the heat flux to the wall for the real gas flow. It is also observed that chemical reactions within the shock transition zone do not appreciably influence the shock layer flow field. The proper treatment of the production terms in the species continuity equations has improved the convergence characteristics of the solution procedure. It is also observed that non-equilibrium computations capture equilibrium concentrations in most of the shock layer region at higher Reynolds number.

The mathematical formulation of the problem is presented in Chapter 2. The solution procedure is discussed in Chapter 3. In this chapter, details about finite difference scheme, grid clustering and treatment of

mass production terms due to chemical reactions are presented. At higher Reynolds number, grid clustering plays an important role in resolving the details of the flow-field. Treatment of the production terms also plays a crucial role in the evolution of various profiles in the flow-field.

Chapter 4 presents the detailed results obtained from the computations and their comparison with available theoretical and experimental results. The results are computed for a wide range of Reynolds number extending from the boundary layer regime on one side to the transition regime on the other. Detailed flow profiles as well as surface characteristics are presented.

In Chapter 5, the important conclusions drawn from the present study are reiterated and summed up. Thus, this chapter focuses the contribution of the present study to hypersonic, chemically reacting, rarefied blunt body problem. A brief statement on the further research that can be carried out is also included.

## CHAPTER 2

### MATHEMATICAL FORMULATION

#### 2.1 INTRODUCTION

In the present study, the full steady Navier-Stokes equations for chemically reacting flows are employed for the analysis of the flow field in the stagnation zone of a blunt body. The equations are specialised for stagnation zone by expanding the flow variables about their stagnation line values using flow field symmetry in the stagnation zone of a blunt body. In order to account for the rarefaction effects present at low Reynolds numbers, surface slip conditions for multi-component gas are employed. Similarly at the shock, transport effects are considered while evaluating post-shock conditions. Section 2.2 describes the governing equations and boundary conditions as applicable to the stagnation zone.

For chemically reacting flows it is necessary to consider various reactions occurring in the flow field and their influence on the flow field through the mass production terms. The mass production terms depend on the reaction rate constants for various reactions. Section 2.3 describes the different reactions considered in the analysis of the flow field and their reaction rate

constants.

The analysis of real gas flow field requires the estimation of thermodynamic and transport properties of the gas mixture as function of local composition pressure and temperature. Section 2.4 describes the method used for estimating the thermodynamic and transport properties of individual gases. It also describes the method for evaluating the properties of the gas mixture from those of the individual gases.

## 2.2 GOVERNING EQUATIONS

The equations employed in the present analysis for the simulation of flow field in the stagnation region of a blunt body are the steady Navier-Stokes equations for compressible reacting mixture. The governing equations for laminar flow of a multi-component gas in chemical non-equilibrium are available in various references namely, Hirschfelder, Curtiss and Bird(1954), Bird, Stewart and Lightfoot(1960) and Williams(1965). Recently these equations have been derived by Lee(1986) accounting for thermal non-equilibrium between various temperatures. The various assumptions used in the present analysis are as follows:

1. Flow is steady, laminar and axially symmetric.
2. There is only one temperature, that is, there is thermal equilibrium.
3. Radiative heat transfer has been neglected.

4. Mass diffusion is binary and due to concentration gradient only. Mass diffusion due to temperature and pressure gradients is neglected.
6. The influence of production rates for various species in the shock transition zone on the post-shock conditions is neglected. The post-shock transport effects are accounted for.
7. Ambi-polar diffusion is considered for the charged species.

The governing equations have been written in surface oriented coordinate system ( Fig 2.1 ). In case of flow around blunt bodies, the flow field is symmetric about the stagnation line. The flow variables have been non-dimensionalised as follows:

$$\begin{aligned}
 u &= u^* / U_{\infty}^* & v &= v^* / U_{\infty}^* \\
 \xi &= s / R_b & \eta &= n / R_b \\
 \rho &= \rho^* / \rho_{\infty}^* & p &= p^* / (\rho_{\infty}^* U_{\infty}^{*2}) & (2.2.1) \\
 T &= T^* / T_{ref}^* & h &= h^* / U_{\infty}^{*2} \\
 \mu &= \mu^* / \mu^*(T_{ref}^*) & T_{ref}^* &= U_{\infty}^{*2} / C_{p_{\infty}} \\
 Re &= \rho_{\infty}^* U_{\infty}^* R_b / \mu^*(T_{ref}^*)
 \end{aligned}$$

The governing equations in terms of these non-dimensional variables can be expressed as follows, with  $\beta$  denoting the body slope and subscripts  $\xi$  and  $\eta$  denoting differentiation with respect to  $\xi$  and  $\eta$  respectively:



### Global Continuity Equation

$$(\rho r u)_\xi + \{\rho r (1 + \eta) v\}_\eta = 0$$

( 2.2.2 )

### Tangential Momentum Equation

$$\begin{aligned} & \frac{\rho u u_\xi}{(1+\eta)} + \rho v u_\eta + \frac{\rho u v}{(1+\eta)} + \frac{p_\xi}{(1+\eta)} = \\ & \frac{1}{r(1+\eta) Re} \left[ r \left[ \frac{4}{3} \frac{\mu}{(1+\eta)} u_\xi + \frac{2}{3} \frac{\mu v}{(1+\eta)} \right. \right. \\ & \quad \left. \left. - \frac{2}{3} \frac{\mu u \sin \beta}{r} - \frac{2}{3} \mu v_\eta \right] \right]_\xi \\ & + \frac{1}{r(1+\eta) Re} \left[ \mu r (1+\eta) \left[ u_\eta + \frac{v_\xi}{(1+\eta)} - \frac{u}{(1+\eta)} \right] \right]_\eta \\ & + \frac{\mu}{Re(1+\eta)} \left[ u_\eta + \frac{v_\xi}{(1+\eta)} - \frac{u}{(1+\eta)} \right] \\ & - \frac{\mu \sin \beta}{r Re} \left[ \frac{4}{3} \frac{u \sin \beta}{r} + \frac{2}{3} \frac{v}{(1+\eta)} - \frac{2}{3} \frac{u_\xi}{(1+\eta)} - \frac{2}{3} v_\eta \right] \end{aligned}$$

( 2.2.3 )

### Normal Momentum Equation

$$\begin{aligned}
 & \frac{\rho u v_{\xi}}{(1+\eta)} + \rho v v_{\eta} - \frac{\rho u^2}{(1+\eta)} + p_{\eta} = \\
 & \frac{1}{\text{Re } r (1+\eta)} \left[ \mu r \left( \frac{u}{\eta} + \frac{v_{\xi}}{(1+\eta)} - \frac{u}{(1+\eta)} \right) \right]_{\xi} \\
 & + \frac{1}{\text{Re } (1+\eta) r} \left[ \mu r (1+\eta) \left[ \frac{4}{3} \frac{v}{\eta} - \frac{2}{3} \frac{u \sin \beta}{r} - \frac{2}{3} \frac{u_{\xi} + 2 v}{(1+\eta)} \right] \right]_{\eta} \\
 & - \frac{\mu}{\text{Re}(1+\eta)} \left[ \frac{4}{3} \frac{u \sin \beta}{r} + \frac{2}{3} \frac{v - u_{\xi}}{(1+\eta)} - \frac{2}{3} \frac{v}{\eta} \right] \\
 & - \frac{\mu}{\text{Re}(1+\eta)} \left[ \frac{2}{3} \frac{2 u_{\xi} + v}{(1+\eta)} - \frac{2}{3} \frac{u \sin \beta}{r} - \frac{2}{3} \frac{v}{\eta} \right]
 \end{aligned}
 \tag{2.2.4}$$

### Energy Equation

$$\begin{aligned}
 & \rho C_p \left( \frac{u}{(1+\eta)} T_{\xi} + v T_{\eta} \right) - \left( \frac{u}{(1+\eta)} p_{\xi} + v p_{\eta} \right) = \\
 & \frac{1}{\text{Re } r (1+\eta)} \left[ \left( \frac{\mu r}{\text{Pr } (1+\eta)} C_p T_{\xi} \right)_{\xi} + \left( \frac{\mu r (1+\eta)}{\text{Pr}} C_p T_{\eta} \right)_{\eta} \right] \\
 & + \frac{\mu}{\text{Re}} \left[ \left( \frac{u_{\xi} + v}{1+\eta} \right) \left( \frac{2}{3} \frac{2 u_{\xi} + v}{(1+\eta)} - \frac{2}{3} \frac{u \sin \beta}{r} - \frac{2}{3} \frac{v}{\eta} \right) \right. \\
 & \left. + \left( u_{\eta} + \frac{v_{\xi} - u}{(1+\eta)} \right) \left( \frac{2}{3} \frac{v}{\eta} - \frac{2}{3} \frac{u \sin \beta}{r} - \frac{2}{3} \frac{u_{\xi} + 2 v}{(1+\eta)} \right) \right. \\
 & \left. + \frac{2}{3} \left( \frac{u \sin \beta}{r} + \frac{v}{1+\eta} \right) \left( \frac{2}{3} \frac{u \sin \beta}{r} + \frac{v - u_{\xi}}{1+\eta} - \frac{v}{\eta} \right) \right] \\
 & + \sum_{i=1}^{N_s} \left[ \frac{\mu \text{Le}_i C_{p_i}}{\text{Re Pr}} \left\{ \frac{C_{1\xi}}{(1+\eta)^2} T_{\xi} + C_{1\eta} T_{\eta} \right\} \right]
 \end{aligned}$$

Species Continuity Equation

$$\frac{\rho u}{1+\eta} C_{1\xi} + \rho v C_{1\eta} = w_1$$

$$+ \frac{1}{Re \, r(1+\eta)} \left[ \left( \frac{\mu Le \, r}{Pr (1+\eta)} C_{1\xi} \right)_{\xi} + \left( \frac{\mu Le \, r(1+\eta)}{Pr} C_{1\eta} \right)_{\eta} \right]$$

for  $i = 1, 2, \dots, N_s$ .

( 2.2.6 )

Equation of State

$$p = \frac{\rho \, T \, R}{C_{p\infty} \, M}$$

( 2.2.7 )

here the specific heat  $C_p$  of the gas mixture is given by

$$C_p = \sum_{i=1}^{N_s} C_i \, C_{p_i}$$

( 2.2.8 )

and molecular weight  $M$  of the gas mixture is given by

$$M = \left[ \sum_{i=1}^{N_s} \frac{C_i}{M_i} \right]^{-1}$$

( 2.2.9 )

Boundary Conditions:

The governing equations ( 2.2.2 -- 2.2.6 ) along with supplementary equations ( 2.2.7 -- 2.2.9 ) require boundary conditions which are to be used while solving

these equations. In the present case, as the solution is being sought between body and shock, conditions need to be prescribed at the body and at the shock. Usually no slip conditions are applied at the body surface. However, in low Reynolds number regime, sufficient number of collisions do not occur so as to make the gas stick to the body and the flow slips at the body. The flow velocity and temperature of the gas at the body are not the same as those of the body. The surface slip conditions used in the present study for multi-component gas mixture have been derived by Gupta, Scott and Moss (1985) and are given by:

At the surface  $\eta = 0$

### Normal Velocity

$$v = 0 \quad (2.2.10)$$

### Tangential Velocity

$$u = \frac{1}{\text{Re} \sum_{i=1}^{\text{Ns}} \frac{C_i}{\sqrt{M/M_1}}} \left[ \mu \frac{2-\theta}{\theta} \sqrt{\left(\frac{\pi}{2}\right)} \frac{u_\eta - u + v_\xi}{(\rho p)} \right. \\ + \frac{T_\xi}{5p} \sum_{i=1}^{\text{Ns}} \frac{\mu_i C_i}{\text{Pr}_i} \left( \frac{\text{CP}_i}{\text{CP}_\infty} \right) \sqrt{\left(\frac{M}{M_1}\right)} \\ \left. + \frac{\text{Le} \mu}{\text{Pr} \rho} \sum_{i=1}^{\text{Ns}} \sqrt{\left(\frac{1}{M}\right)} \left\{ C_{1\xi} + (1-C_1) \sum_{j=1}^{\text{Ns}} \frac{M}{M_j} C_{j\xi} \right\} \right] \quad (2.2.11)$$

### Surface Temperature

$$\begin{aligned}
 T_s = & \frac{T_w}{Z} \left[ 1 + \frac{\mu}{Re \, p} (u_\xi - 2 v_\eta) \right] \\
 & + \sqrt{\left(\frac{\pi}{2}\right)} \frac{2-\sigma}{2\sigma} \frac{\mu}{Re \, Pr} \sqrt{\left(\frac{\rho}{p}\right)} \frac{T}{p} \left(\frac{C_p}{C_{p\infty}}\right) \frac{T_\eta}{Y \, Z} \\
 & - \sqrt{\left(\frac{\pi}{2}\right)} \frac{\mu}{Re \, Pr} \frac{x}{(p\rho)} \frac{1}{Y \, Z} \left[ T_w + \frac{2-\theta}{\theta} \frac{5}{4} T \right]
 \end{aligned}
 \tag{2.2.12}$$

where

$$x = \sum_{i=1}^{Ns} Le_i \sum_{\substack{j=1 \\ j \neq i}}^{Ns} \{ C_{j\eta} - C_j \sum_{k=1}^{Ns} \frac{M}{M_k} C_{k\eta} \}
 \tag{2.2.13}$$

$$Y = \sum_{i=1}^{Ns} \left( \frac{M}{M_i} \right)^{1.5} C_i
 \tag{2.2.14}$$

and

$$Z = 1 + 1.5 \frac{\mu}{Re \, p} (u_\xi - 2 v_\eta)
 \tag{2.2.15}$$

### Species Concentration

$$C_1 = \frac{C_1 \left(\frac{\rho_w}{\rho}\right) \sqrt{\left(\frac{T}{T_w}\right)} + \frac{\mu}{Re \, Pr} \frac{1}{\sqrt{(p\rho)}} \left(\frac{M_1}{M}\right)^{1.5} \sum_{j=1, j \neq 1}^{Ns} Le_j x_j}{1 + \frac{\mu}{Re \, p} (u_\xi - 2 v_\eta)}
 \tag{2.2.16}$$

with

$$x_j = C_{j\eta} - C_j \sum_{k=1}^{Ns} \frac{M}{M_k} C_{k\eta} \quad (2.2.17)$$

### Wall Pressure

$$P_w = - \frac{2}{3} \frac{\mu}{Re} (u_\xi - 2 v_\eta) + \frac{2}{5} \frac{2-\theta}{\theta} \frac{T_\eta}{Re} \sqrt{\left(\frac{2\rho}{p}\right)} \sum_{i=1}^{Ns} \frac{\mu_1 C_1 C_{p1}}{Pr_1 C_{p\infty}} \sqrt{\left(\frac{M}{M_1}\right)} \\ + p \left[ 1 - \frac{4}{\sqrt{\pi}} \frac{Le}{Pr} \frac{2-\theta}{Re\theta} \frac{1}{\sqrt{(2p\rho)}} \sum_{i=1}^{Ns} \sqrt{\left(\frac{M}{M_1}\right)} \{ C_{i1\eta} + (1-C_{i1}) \sum_{j=1}^{Ns} \frac{M}{M_1} C_{j\eta} \} \right] \quad (2.2.18)$$

However, though equation (2.2.16) is valid for general species concentration slip condition, for a non-catalytic wall one has

$$C_{i\eta} = 0 \quad (2.2.19)$$

while for a fully catalytic wall

$$C_i = C_{i\infty} \quad (2.2.20)$$

The slip conditions taken from Gupta et al. have been adapted so as to avoid derived quantities such as  $\gamma$ . These conditions reduce to no slip conditions as the Reynolds number increases to infinity.

### Shock Slip Conditions

The conditions at the shock, which is being fitted in the present analysis, are normally given by Rankine-Hugoniot relations. However, these relations are modified to account for transport effects down stream of the shock at low Reynolds number. These shock slip conditions are given by

$$\rho \tilde{v} = -\sin \beta_s \quad (2.2.21)$$

$$\tilde{u} \sin \beta_s + \frac{\mu}{Re} \tilde{u}_{\eta} = \cos \beta_s \sin \beta_s \quad (2.2.22)$$

$$p - \tilde{v} \sin \beta_s - \frac{4\mu}{3Re} \tilde{v}_{\eta} = \frac{p_{\infty}^*}{\rho_{\infty}^* U_{\infty}^{*2}} + \sin^2 \beta_s \quad (2.2.23)$$

$$\sin \beta_s \left\{ h + \frac{\tilde{u}^2 + \tilde{v}^2}{2} \right\} + \frac{\mu}{Re Pr} C_p T_{\eta} =$$

$$\sin \beta_s \left( 0.5 + \frac{h_{\infty}^*}{U_{\infty}^{*2}} \right) + \frac{\mu}{Re} \left( \tilde{u} \tilde{u}_{\eta} + \frac{4}{3} \tilde{v} \tilde{v}_{\eta} \right)$$

$$+ \sum_{i=1}^{Ns} \frac{\mu Le_i}{Re Pr} C_{i\eta} h_i$$

$$(2.2.24)$$

and

$$C_1 + \frac{\mu Le}{Re Pr} C_{1\eta} = C_{1\infty}$$

( 2.2.25 )

Here  $\tilde{u}$  and  $\tilde{v}$  are velocity components tangential and normal to the shock and  $\tilde{\eta}$  is the outward normal to the shock.  $\beta_s$  is the shock slope.

These shock slip conditions have been derived from Navier-Stokes equations under the assumption of thin one-dimensional shock. Under the assumption of thin shock, there is no contribution of mass production term to shock slip condition on the species continuity equation. These shock slip conditions reduce to usual conservation laws applied across the oblique shock with slope  $\beta_s$  as the Reynolds number increases indefinitely.

### Series Expansion

The governing equations (2.2.2 - 2.2.9) and boundary conditions (2.2.10 - 2.2.25) presented above can not be used directly to solve for the flow field at stagnation line. This is due to the term  $r$ , the distance from the axis of symmetry which is zero along the stagnation line, occurring in the equations. In order to specialise these equations along the stagnation line, the concept of local similarity is used and all the flow variables are expanded in terms of  $\xi$  about the stagnation line. It is further assumed that there is no influence of higher order terms on the behaviour of lower order terms.



Considering the symmetry of the flow field about the stagnation line, the following series expansion is used:

$$\rho = \rho_0 + \rho_2 \xi^2 + \dots \quad (2.2.26)$$

$$P = P_0 + P_2 \xi^2 + P_4 \xi^4 + \dots \quad (2.2.27)$$

$$T = T_0 + T_2 \xi^2 + \dots \quad (2.2.28)$$

$$u = u_1 \xi + u_3 \xi^3 + \dots \quad (2.2.29)$$

$$v = v_0 (1 - \xi^2/2) + v_2 \xi^2 + \dots \quad (2.2.30)$$

$$C_1 = C_{10} + C_{12} \xi^2 + \dots \quad (2.2.31)$$

$$h = h_0 + h_2 \xi^2 + \dots \quad (2.2.32)$$

$$Pr = Pr_0 + Pr_2 \xi^2 + \dots \quad (2.2.33)$$

$$Le = Le_0 + Le_2 \xi^2 + \dots \quad (2.2.34)$$

$$\mu = \mu_0 + \mu_2 \xi^2 + \dots \quad (2.2.35)$$

$$\sin \beta = \sin \beta_s = 1 - \xi^2/2 + \dots \quad (2.2.36)$$

$$r = (1 + \eta) \{ \xi - \xi^2/2 + \dots \} \quad (2.2.37)$$

$$\cos \beta = \xi - \xi^2/2 + \dots \quad (2.2.38)$$

Here the flow variables  $\rho_0$ ,  $\rho_2$ ,  $P_0$ ,  $P_2$ ,  $P_4$  etc. are functions of  $\eta$  alone. It has been tacitly assumed here that the shock and the body are parallel to each other in the neighbourhood of the stagnation line.

The series expansions (2.2.26 - 2.2.38) is substituted in the governing equations (2.2.2 - 2.2.9). Collecting the coefficients of like powers of  $\xi$ , one gets the governing equations which are applicable for the stagnation line. However, due to the elliptic nature of

the Navier-Stokes equations, higher order terms appear in the equations governing the lower order terms. All higher order terms except  $p_2$  are dropped under the assumption that higher order terms do not effect the behaviour of lower order terms appreciably. This assumption has been verified by Kao(1964b) in the context of merged layer solution. Dropping the subscripts 0 and 1, one gets the following set of equations governing the stagnation line flow:

### Continuity Equation

$$2 \rho (u+v) + (1+\eta) (\rho v)_\eta = 0$$

( 2.2.39 )

### Tangential Momentum Equation

$$\begin{aligned} & \frac{\rho u (u+v)}{1+\eta} + \rho v u_\eta + \frac{2 p_2}{1+\eta} = \\ & \frac{\mu}{Re} \left[ u_{\eta\eta} + \frac{2 u_\eta}{1+\eta} - \frac{8}{9} \frac{u - 3v}{(1+\eta)^2} - \frac{v_\eta}{3(1+\eta)} \right. \\ & \left. + \frac{\mu_\eta}{\mu} \left\{ u_\eta - \frac{u+v}{1+\eta} \right\} \right] \end{aligned}$$

( 2.2.40 )

### Normal Momentum Equation

$$\begin{aligned}
 P_{\eta} + \rho v v_{\eta} = & \frac{4 \mu}{3 Re} \left[ \frac{\mu_{\eta}}{\mu} \left\{ v_{\eta} - \frac{u+v}{1+\eta} \right\} \right. \\
 & \left. + v_{\eta\eta} + \frac{2 v_{\eta} + 0.5 u_{\eta}}{1+\eta} - \frac{7 (u+v)}{2 (1+\eta)^2} \right]
 \end{aligned}
 \quad (2.2.41)$$

### Equation for $P_2$

$$P_{2\eta} - \frac{\rho u(u+v)}{1+\eta} - \rho v v_{\eta} = 0
 \quad (2.2.42)$$

### Energy Equation

$$\begin{aligned}
 \rho v C_p T_{\eta} - v P_{\eta} = & \frac{1}{Re} \left[ \frac{\mu C_p}{Pr} T_{\eta\eta} + \frac{2 \mu C_p}{Pr(1+\eta)} T_{\eta} \right. \\
 & \left. + \left\{ \frac{\mu_{\eta} C_p + \mu C_{p\eta}}{Pr} - \frac{\mu C_p Pr_{\eta}}{Pr^2} \right\} T_{\eta} \right] \\
 & + \sum_{i=1}^{Ns} \frac{\mu Le_i}{Re Pr} C_{p_i} C_{1\eta} T_{\eta i} - \sum_{i=1}^{Ns} h_i w_i \\
 & + \frac{2\mu}{Re} v_{\eta}^2 + \frac{4 \mu}{Re} \frac{(u+v)^2}{(1+\eta)^2} - \frac{2 \mu}{3 Re} \left[ \frac{2(u+v)}{1+\eta} + v_{\eta} \right]^2
 \end{aligned}
 \quad (2.2.43)$$

### Species Continuity equation

$$\rho \tilde{V} C_{1\tilde{\eta}} = w_1 + \frac{\mu Le}{Re Pr} [ C_{1\tilde{\eta}\tilde{\eta}} + \frac{2}{1+\eta} C_{1\tilde{\eta}} + ( \frac{\mu\tilde{\eta}}{\mu} + \frac{Le\tilde{\eta}}{Le} - \frac{Pr\tilde{\eta}}{Pr} ) C_{1\tilde{\eta}} ]$$

$$i = 1, 2, \dots, N_s \quad (2.2.44)$$

The use of series expansions ( 2.2.26 - 2.2.38 ) into the boundary conditions ( 2.2.10 - 2.2.25 ) gives the following boundary conditions:

At the Surface  $\eta = 0$

$$v = 0 \quad (2.2.45)$$

$$u = \frac{\mu}{Re} \sqrt{\left(\frac{\pi}{2}\right)} \frac{2-\theta}{\theta} \frac{1}{\sum_{i=1}^{Ns} \sqrt{\left(\frac{M}{M_1}\right)} C_1} \left( \frac{u_\eta - u}{\sqrt{(p\rho)}} \right) \quad (2.2.46)$$

$$T = T_w \frac{1 + \frac{\mu}{Re p} (u - 2 v_\eta)}{Z_0}$$

$$+ \sqrt{\left(\frac{\pi}{2}\right)} \frac{2-\sigma}{\sigma} \frac{\mu}{Re Pr Y Z_0} \sqrt{\left(\frac{\rho}{p}\right)} T \frac{C_p}{C_{p\infty}} T_\eta - \sqrt{\left(\frac{\pi}{2}\right)} \frac{\mu}{Re Pr} \frac{x}{\sqrt{(p\rho)} Y Z_0} \left( T_w + \frac{5}{4} \frac{2-\sigma}{\sigma} T \right)$$

$$(2.2.47)$$

Post- Shock Conditions

$$\text{At } \eta = \eta_e$$

$$\rho v = -1 \quad (2.2.51)$$

$$u + \frac{\mu}{Re} u_\eta = 1 \quad (2.2.52)$$

$$p - v - \frac{4\mu}{3Re} v_\eta = 1 + \frac{p_\infty^*}{\rho_\infty^* U_\infty^{*2}} \quad (2.2.53)$$

$$h + \frac{v^2}{2} + \frac{\mu C_p}{Re Pr} T_\eta = 1 + \frac{h_\infty^*}{U_\infty^{*2}} + \frac{4\mu}{3Re} v v_\eta$$

$$+ \sum_{i=1}^N \frac{\mu Le_i}{Re Pr} C_{1\eta} h_i \quad (2.2.54)$$

$$C_1 + \frac{\mu Le}{Re Pr} C_{1\eta} = C_{1\infty} \quad (2.2.55)$$

$$P_2 = -1 - v - \frac{2\mu}{3Re} v_\eta \quad (2.2.56)$$

2.3 CHEMICAL REACTION MODEL

In the present analysis, a seven species and seven reaction model as proposed by Blottner (1969) is considered. The species considered as constituents of air are  $N_2$ ,  $O_2$ ,  $NO$ ,  $O$ ,  $N$ ,  $NO^+$  and  $e^-$ . The model accounts for

a single ionisation reaction only, namely, the ionisation of NO. Eleven species model of Kang and Dunn(1972) involving twenty six reaction was not considered in this study as it would involve more computation without significant improvement in the computed results as already noted by Swaminathan, Kim and Lewis(1983).

### FINITE RATE CHEMISTRY

When the relaxation lengths associated with the chemical reactions are comparable with the flow dimensions, the rates of production of various species  $w_i$  are required to be evaluated. These terms appear in the energy conservation equation and the species continuity equation. For a multi-component gas mixture with  $N_s$  chemical species and  $N_R$  chemical reactions, the chemical balance equation describing the overall change from reactants to products may be written as follows:

$$\sum_{i=1}^{N_j} \alpha_{ir} X_i \quad \begin{matrix} K_{fr} \\ <=====> \\ K_{br} \end{matrix} \quad \sum_{i=1}^{N_j} \beta_{ir} X_i$$

$$r = 1, 2, \dots, N_R$$

( 2.3.1 )

Here  $N_j$  is equal to the sum of the number of the species and the catalytic bodies. The quantities  $\alpha_{ir}$  and  $\beta_{ir}$  are the stoichiometric coefficients for the reactants

and the products respectively for the reaction  $r$ , whereas  $K_{fr}$  and  $K_{br}$  are the forward and backward reaction rate constants. Also, the quantities  $X_1$  denote the concentration of various species and catalytic bodies in moles per unit volume.

The rate of change of concentration of any species as a result of given reaction  $r$  is given by:

$$\left(\frac{\partial X}{\partial t}\right)_r = (\beta_{1r} - \alpha_{1r}) \left[ K_{fr} \prod_{j=1}^{N_j} X_j^{\alpha_{jr}} - K_{br} \prod_{j=1}^{N_j} X_j^{\beta_{jr}} \right] \quad (2.3.2)$$

This equation is written in terms of  $X_1$ , that is, the molar concentration per unit volume for various species. Writing it in terms of mass fractions  $C_1$  of various species with the help of relations:

$$X_1 = \rho^* C_1 / M_1 \quad (2.3.3)$$

and

$$w_1^* = M_1 \left( \frac{\partial X_1}{\partial t} \right) = \frac{\partial \rho^*}{\partial t} \quad (2.3.4)$$

one gets

$$w_{1r}^* = M_1 (\beta_{1r} - \alpha_{1r})$$

$$\left[ K_{fr} \prod_{j=1}^{N_j} \left( \frac{C_j \rho^*}{M_j} \right)^{\alpha_{jr}} - K_{br} \prod_{j=1}^{N_j} \left( \frac{C_j \rho^*}{M_j} \right)^{\beta_{jr}} \right] \quad (2.3.5)$$

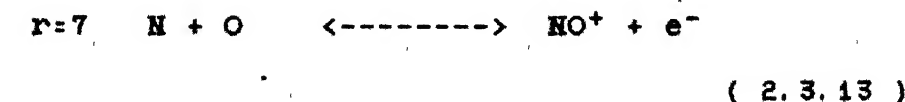
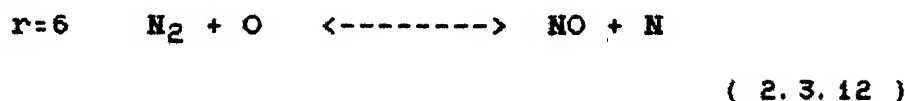
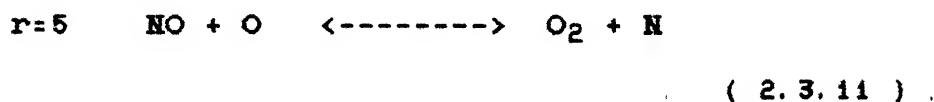
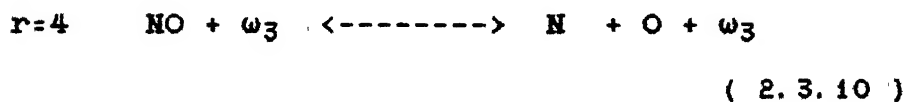
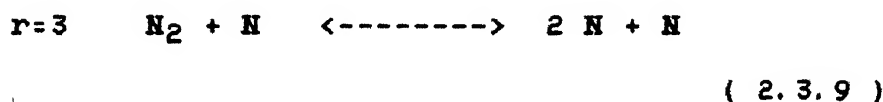
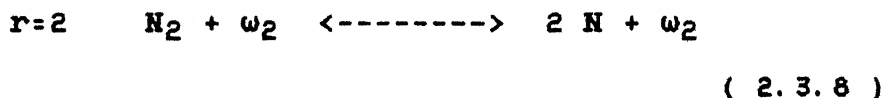
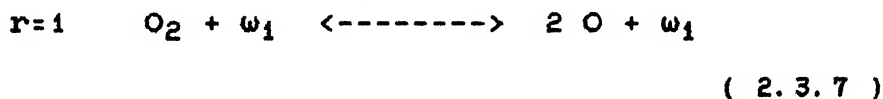
This equation gives the mass rate of production per unit volume of the species  $i$  due to the reaction  $r$ . The overall mass rate of production per unit volume for the species  $i$  is obtained by summing  $w_{ir}^*$  over all the reactions, that is:

$$w_i^* = \sum_{r=1}^{Nr} M_i ( \beta_{ir} - \alpha_{ir} )$$

$$\left[ K_{fr} \prod_{j=1}^{Nj} \left( \frac{C_j \rho^*}{M_j} \right)^{\alpha_{jr}} - K_{br} \prod_{j=1}^{Nj} \left( \frac{C_j \rho^*}{M_j} \right)^{\beta_{jr}} \right]$$

( 2.3.6 )

The seven chemical reactions considered in the present analysis are as follows:



here  $w_1$ ,  $w_2$  and  $w_3$  are the catalytic bodies.



The reaction rates for these reactions are expressed in the modified Arrhenius form and are given by

$$K_{fr} = C_{Or} T^{*C_{1r}} \exp( - C_{2r} / T^{*} ) \quad ( 2.3.14 )$$

and

$$K_{br} = D_{Or} T^{*D_{1r}} \exp( - D_{2r} / T^{*} ) \quad ( 2.3.15 )$$

The constants occurring in these equations have been taken from Blottner (1969) and are given in Table 1. This table also gives the third body efficiency for the gases considered in the analysis.

## 2.4 THERMODYNAMIC AND TRANSPORT PROPERTIES OF GAS MIXTURE

Thermodynamic properties, specific heat  $C_{p1}$  and enthalpy  $h_1^*$ , are functions of temperature for the species considered in the analysis. These are required for estimation of post-shock conditions and estimation of heat flux due to diffusion of the species. Various transport properties like molecular viscosity  $\mu_1^*$ , thermal conductivity  $K_1^*$  and diffusivity  $D_{1j}$  are also functions of temperature and pressure. These are required for estimation of overall mixture viscosity, thermal conductivity and diffusivity. Since the multi-component

gas mixtures are considered to be mixtures of thermally perfect gases, the thermodynamic and transport properties for each species are computed using local temperature and pressure. The individual properties of these species are then used to evaluate overall properties of the gas mixture. The following two sections describe the procedure for evaluating the individual and mixture thermodynamic and transport properties.

### THERMODYNAMIC PROPERTIES

The value of specific heat  $C_{p1}$  and enthalpy  $h_1$  are obtained as function of temperature by using a fourth order polynomial curve-fit for specific heat  $C_{p1}$  for each chemical species. The polynomial for enthalpy is derived from the expression for the specific heat. The polynomial for specific heat for species 1 is given by

$$\frac{C_{p1}}{R} = a_1 + a_2 T + a_3 T^2 + a_4 T^3 + a_5 T^4 \quad (2.4.1)$$

and for enthalpy one has

$$\frac{h_1}{R} = a_1 T^* + \frac{a_2 T^{*2}}{2} + \frac{a_3 T^{*3}}{3} + \frac{a_4 T^{*4}}{4} + \frac{a_5 T^{*5}}{5} + a_6 \quad (2.4.2)$$

where  $R$  is the universal gas constant. The values of the different constants of the polynomial ( $a_1$  to  $a_6$ ) are taken from Gupta (1987). These constants have been

evaluated for each species for different temperature range. These expressions give specific heat and enthalpy per mole. The constants used in the present study for each species are given in Table 2.

### TRANSPORT PROPERTIES

The gas mixture is considered to be a mixture of thermally perfect gases. The transport properties of each species as a function of temperature are evaluated using kinetic theory and later mixture properties are evaluated.

To a first approximation ( first order kinetic theory) the viscosity of a perfect gas( Hirschfelder, Curtiss and Bird 1964) is given by

$$\mu_1^* = \frac{2.6693 \times 10^{-5} \sqrt{(T^* M_1)}}{\sigma_1^2 \Omega_{11}(22)}$$

( 2.4.3 )

and the thermal conductivity for mono-atomic gases species is given by

$$K_{1 \text{ mono}}^* = \frac{1.9891 \times 10^{-4} \sqrt{(T^*/M_1)}}{\sigma_1^2 \Omega_{11}(22)}$$

( 2.4.4 )

or

$$K^*_{1 \text{ mono}} = \frac{15}{4} \frac{\mu_1}{M_1} R \quad (2.4.5)$$

However, the thermal conductivity for a polyatomic gas has an additional contribution due to the transfer of energy between the translational and internal degrees of freedom. This contribution to the thermal conductivity is given by

$$K'^* = 0.88 \left( \frac{2}{5} \frac{Cp_1}{R_1} - 1 \right) K^*_{1 \text{ mono}} \quad (2.4.6)$$

and thus

$$K_1^* = \frac{15}{4} \frac{\mu_1}{M_1} R \left\{ 1 + 0.88 \left( \frac{2}{5} \frac{Cp_1}{R_1} - 1 \right) \right\} \quad (2.4.7)$$

Here the different variables have the following units

$T^*$  -- temperature (°K)

$M_1$  -- Molecular weight of the species 1

$\sigma_1$  -- collision diameter of the species 1 (Å)

$\mu_1^*$  -- molecular viscosity of the species 1 (gm/cm sec)

$K_1^*$  -- thermal conductivity of species 1 (cal/sec °K)

$\Omega_{11}^{22}$  -- collision integral for viscosity

The collision integral  $\Omega_{11}^{22}$  is a function of the non-dimensional reduced temperature

$$T^+ = \frac{T^*}{(\epsilon_1/k)} \quad (2.4.8)$$

where  $\epsilon_1$  is the maximum energy of attraction between the colliding molecules and  $k$  is the Boltzmann constant. The collision integral  $\Omega_{11}^{22}$  is approximated by White (1974) as

$$\Omega_{11}^{22} = 1.147 (T^+)^{-0.145} + (T^+ + 0.5)^{-2} \quad (2.4.9)$$

The binary diffusion coefficient  $D_{1j}$  is given by

$$D_{1j} = \frac{2.628 \times 10^{-3} T^{*1.5} \sqrt{\frac{M_1 + M_j}{2 M_1 M_j}}}{p^* \sigma_{1j}^2 \Omega_{1j}^{(11)}} \quad (2.4.10)$$

where

$\Omega_{1j}^{11}$  -- collision integral for diffusion

$p^*$  ----- pressure in atmosphere

$\sigma_{1j}$  ---- collision diameter for combination of species (A<sup>0</sup>)

$M_1, M_j$  -- molecular weights of species  $i$  and  $j$

$D_{1j}$  ---- diffusion coefficient (  $\text{cm}^2 / \text{sec}$  )

Here for estimating the diffusion coefficient, the parameters  $\sigma_{ij}$  and  $\epsilon_{ij}$  are evaluated as follows:

$$\sigma_{ij} = \frac{\sigma_i + \sigma_j}{2} \quad (2.4.11)$$

and

$$\epsilon_{ij} = \sqrt{(\epsilon_i \epsilon_j)} \quad (2.4.12)$$

and the collision integral  $\Omega_{ij}^{11}$  is approximated by

$$\Omega_{ij}^{11} = (T^+)^{-0.145} + (T^+ + 0.5)^{-2} \quad (2.4.13)$$

with

$$T^+ = T^* / (\epsilon_{ij}/K) \quad (2.4.14)$$

The data regarding collision diameter  $\sigma_1$  and energy of attraction  $(\epsilon_1 / K)$  are given in Table 3 for the species considered in the present analysis.

## MIXTURE PROPERTIES

The mixture specific heat and enthalpy are given by

$$C_p = \sum_{i=1}^{N_s} C_i C_{p_i} \quad (2.4.15)$$

and

$$h^* = \sum_{i=1}^{N_s} C_i h_{i,1}^* \quad (2.4.16)$$

where  $C_1$  is the mass fraction for species 1 and  $Cp_1$  and  $h_1$  are specific heat and enthalpy respectively for the species 1.

The expression for viscosity and thermal conductivity for the multi-component gas mixture are given by Hirschfelder, Curtiss and Bird (1964) according to kinetic theory. However, these expressions are cumbersome and computationally time consuming. Therefore, most of the studies use an approximate technique for estimating the mixture viscosity and thermal conductivity.

According to semi-empirical formula of Wilke ( from Brokaw 1958, 1961), the mixture viscosity is given by:

$$\mu^*_{mix} = \sum_{i=1}^{Ns} \frac{x_i \mu^*_i}{\sum_{j=1}^{Ns} \phi_{1j} x_j} \quad (2.4.17)$$

where

$$\phi_{1j} = \frac{\left[ 1 + \left( \frac{\mu^*_1}{\mu^*_j} \right)^{0.5} \left( \frac{M_1}{M_j} \right)^{0.25} \right]^2}{2\sqrt{2} \left[ 1 + \frac{M_1}{M_j} \right]^{0.5}} \quad (2.4.18)$$

Here  $\mu^*_1$ ,  $M_1$  and  $x_1$  are viscosity, molecular weight and mole fraction respectively for species 1. These relations, though developed empirically, have been justified by

rigorous kinetic theory ( Brokaw 1958).

The thermal conductivity of a mixture of polyatomic gases can be divided into two portions

$$K^*_{mix} = K^*_{mix \text{ mono}} + K'^*_{mix} \quad ( 2.4.19 )$$

here  $K^*_{mix \text{ mono}}$  represents the monatomic thermal conductivity of the mixture and  $K'^*_{mix}$  gives the correction due to transfer of energy between translational and internal degrees of freedom.

Monatomic mixture conductivity is given by

$$K^*_{mix \text{ mono}} = \sum_{i=1}^{Ns} \frac{K^*_i x_i}{\sum_{j=1}^{Ns} \psi_{ij} x_j} \quad ( 2.4.20 )$$

where

$$\psi_{ij} = \frac{\left[ 1 + \left( \frac{K^*_{i \text{ mono}}}{K^*_{j \text{ mono}}} \right)^{0.5} \left( \frac{M_i}{M_j} \right)^{0.25} \right]^2}{2\sqrt{2} \left[ 1 + \frac{M_i}{M_j} \right]^2} \times \left[ 1 + 2.41 \frac{(M_i - M_j)(M_i - .142 M_j)}{(M_i + M_j)^2} \right] \quad ( 2.4.21 )$$



and correction to the mixture conductivity

$$K'^{*}_{mix} = \sum_{i=1}^{Ns} \frac{K'^{*}_i x_i}{\sum_{j=1}^{Ns} \Lambda_{1j} x_j} \quad (2.4.22)$$

where

$$\Lambda_{1j} = \frac{\left[ 1 + \left( \frac{K^*_{1 \text{ mono}}}{K^*_{j \text{ mono}}} \right)^{0.5} \left( \frac{M_1}{M_j} \right)^{0.25} \right]^2}{2\sqrt{2} \left[ 1 + \frac{M_1}{M_j} \right]^{0.5}} \quad (2.4.23)$$

However, in recent studies it has been noticed that various assumptions regarding the interaction between molecules in the analysis of Wilke for mixture properties are not valid for temperatures above 10000 °K. Armaly and Sutton (1980,1981) considered these interactions at these higher temperatures and suggested an alternative relationship for mixture viscosity and thermal conductivity. These modifications in the correlations are as follows:

For viscosity  $\phi_{1j}$  is given by

$$\phi_{1j} = \frac{\left[ 1 + \frac{5}{3} \frac{M_1}{M_1 A_{11}} \right]}{2\sqrt{2} \left[ 1 + \frac{M_1}{M_j} \right]^{1.5}} \left[ F_{1j} + B_{1j} \frac{\sqrt{\frac{\mu^*}{(\frac{M_1}{M_j})^{0.25}}}}{\left( \frac{M_1}{M_j} \right)^{0.25}} \right]$$

( 2.4.24 )

where

$A_{1j} = 1.1$  for atom interacting with their own ion  
 $= 1.25$  for all other interactions

$F_{1j} = 1.0$

$B_{1j} = 0.2$  for atom and molecules interacting with  
 electrons

$= 0.15$  for atom and molecules interacting  
 with ions

$= 0.78$  for atom and molecules interacting  
 with atoms and molecules

$= 1.0$  for all other interactions

It is worth noting here that this correlation of  
 Armaly and Sutton becomes identical to the correlation  
 given by Wilke if one has  $A_{1j} = 5/3$  ,  $F_{1j} = B_{1j} = 1$ .

The correlation parameter  $\psi_{1j}$  for mixture thermal conductivity is given by

$$\psi_{1j} = \frac{1}{4\sqrt{2} A_{1j}} \frac{\left[ \frac{5}{2} + 4 \frac{M_1}{M_j} A_{1j} + \frac{15}{2} \left( \frac{M_1}{M_j} \right)^2 \right]}{\left( 1 + \frac{M_1}{M_j} \right)^{2.5}} \times$$

$$\left[ F_{1j} + \left( \frac{K_{1 \text{ mono}}^*}{K_{j \text{ mono}}^*} \right)^{0.5} \left( \frac{M_1}{M_j} \right)^{0.25} B_{1j} \right]$$

( 2.4.25 )

Here the values of constants  $A_{1j}$  ,  $B_{1j}$  and  $F_{1j}$  are same as given in the viscosity model.

TABLE 1  
REACTION RATE CONSTANTS

Reaction r	C <sub>Or</sub>	C <sub>1r</sub>	C <sub>2r</sub>	D <sub>Or</sub>	D <sub>1r</sub>	D <sub>2r</sub>
1	3.61x10 <sup>18</sup>	59400.	-1.0	3.01x10 <sup>15</sup>	0	-0.5
2	1.92x10 <sup>17</sup>	113100.	-0.5	1.06x10 <sup>16</sup>	0	-0.5
3	4.15x10 <sup>22</sup>	113100	-1.5	2.32x10 <sup>21</sup>	0	-1.5
4	3.97x10 <sup>20</sup>	75600.	-1.5	1.01x10 <sup>20</sup>	0	-1.5
5	3.18x10 <sup>9</sup>	19700.	1.0	9.63x10 <sup>11</sup>	3600	0.5
6	6.75x10 <sup>13</sup>	37500.	0	1.50x10 <sup>11</sup>	0	0
7	9.03x10 <sup>9</sup>	32400.	0.5	1.80x10 <sup>19</sup>	0	-1.0

THIRD BODY EFFICIENCY RELATIVE TO ARGON

Catalytic Bodies	Efficiency relative to argon of				
	O	O <sub>2</sub>	N	N <sub>2</sub>	NO
ω <sub>1</sub>	25	9	1	2	1
ω <sub>2</sub>	1	1	-	2.5	1
ω <sub>3</sub>	20	1	20	1	20

TABLE 2

CONSTANTS FOR POLYNOMIAL APPROXIMATION OF THERMODYNAMIC DATA OF GASES

DATA FOR N<sub>2</sub>

Temp.	a <sub>1</sub>	a <sub>2</sub>	a <sub>3</sub>	a <sub>4</sub>	a <sub>5</sub>	a <sub>6</sub>
300	.36748E01	-.12081E-02	.23240E-05	-.63217E-09	-.22577E-12	-.10611E04
1000	.28963E01	.15154E-02	-.57235E-06	.99807E-10	-.65223E-14	-.90586E03
6000	.37270E01	.46840E-03	-.11400E-06	.11540E-10	-.32930E-15	-.10430E04
15000	.96376E01	-.25728E-02	.33019E-06	-.14314E-10	.20332E-15	-.10430E04
25000	-.51680E01	-.23336E-02	-.12953E-06	.27872E-11	-.21359E-16	-.10430E04

DATA FOR O<sub>2</sub>

Temp.	a <sub>1</sub>	a <sub>2</sub>	a <sub>3</sub>	a <sub>4</sub>	a <sub>5</sub>	a <sub>6</sub>
300	.36256E01	-.18782E-02	.70554E-05	-.67635E-08	-.21556E-11	-.10475E04
1000	.36219E01	.73618E-03	-.19652E-06	.36201E-10	-.28945E-14	-.12019E04
6000	.37210E01	.42540E-03	-.28350E-07	.60500E-12	-.51860E-17	-.10440E04
15000	.34866E01	.52384E-03	-.39123E-07	.10093E-11	-.88714E-17	-.10440E04
25000	.39619E01	.39445E-03	-.29505E-07	.73974E-12	-.64209E-17	-.10440E04

TABLE 2 Continued

## DATA FOR NO

Temp.	a <sub>1</sub>	a <sub>2</sub>	a <sub>3</sub>	a <sub>4</sub>	a <sub>5</sub>	a <sub>6</sub>
300	.40459E01	-.34181E-02	.79819E-05	-.61139E-08	.15919E-11	.97453E04
1000	.31890E01	.13382E-02	-.52899E-06	.95919E-10	-.64847E-14	.98283E04
6000	.38450E01	.25210E-03	-.26580E-07	.21620E-11	-.63810E-16	.97640E04
15000	.43308E01	-.58086E-04	.28059E-07	-.15694E-11	.24103E-16	.97640E04
25000	.23507E01	.58643E-03	-.31316E-07	.60495E-12	-.40556E-17	.97640E04

## DATA FOR O

Temp.	a <sub>1</sub>	a <sub>2</sub>	a <sub>3</sub>	a <sub>4</sub>	a <sub>5</sub>	a <sub>6</sub>
300	.29464E01	-.16381E-02	.24210E-05	-.16028E-08	.38907E-12	.29147E05
1000	.25420E01	-.27550E-04	-.31028E-08	.45510E-11	-.43680E-15	.29230E05
6000	.25460E01	-.59520E-04	.27010E-07	-.27980E-11	.93800E-16	.29150E05
15000	-.97871E-02	.12449E-02	-.16154E-06	.80379E-11	-.12624E-15	.29150E05
25000	.16428E02	-.39313E-02	.29839E-06	-.81612E-11	.75004E-16	.29150E05

TABLE 2 Continued

## DATA FOR N

Temp.	a <sub>1</sub>	a <sub>2</sub>	a <sub>3</sub>	a <sub>4</sub>	a <sub>5</sub>	a <sub>6</sub>
300	.25030E01	-.21800E-04	.54205E-07	-.56475E-10	.20999E-13	.56098E05
1000	.24502E01	.10661E-03	-.74653E-07	.18796E-10	-.10259E-14	.56116E05
6000	.27480E01	-.39090E-03	.13380E-06	-.11910E-10	.33690E-15	.56090E05
15000	-.12279E01	.19268E-02	-.24370E-06	.12193E-10	-.19918E-15	.56090E05
25000	.15520E02	-.38857E-02	.32288E-06	-.96052E-11	.95472E-16	.56090E05

DATA FOR NO<sup>+</sup>

Temp.	a <sub>1</sub>	a <sub>2</sub>	a <sub>3</sub>	a <sub>4</sub>	a <sub>5</sub>	a <sub>6</sub>
300	.36685E01	-.11544E-02	.21755E-05	-.48227E-09	-.27848E-12	.11803E06
1000	.28885E01	.15217E-02	-.57531E-06	.10051E-09	-.66044E-14	.11819E06
6000	.22141E01	.17760E-02	-.43038E-06	.41737E-10	-.12828E-14	.11819E06
15000	-.33240E01	.24419E-02	-.19057E-06	.66580E-11	-.99112E-16	.11819E06
25000	-.43487E01	.24012E-02	-.14459E-06	.33813E-11	-.28255E-16	.11819E06

TABLE 2 Continued

DATA FOR  $e^-$ 

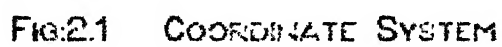
Temp.	$a_1$	$a_2$	$a_3$	$a_4$	$a_5$	$a_6$
300	.25000E01	0.	0.	0.	0.	-.74537E03
1000	.25000E01	0.	0.	0.	0.	-.74537E03
6000	.25080E01	-.63320E-05	.13640E-08	-.10940E-12	.29340E-17	-.74500E03
15000	.25001E01	-.31128E-09	.35720E-13	-.16036E-17	.25070E-22	-.74500E03
25000	.25001E01	.30157E-09	-.22620E-13	.66734E-18	-.68916E-23	-.74500E03



TABLE 3

## MOLECULAR CONSTANTS FOR TRANSPORT PROPERTIES

Species	$\epsilon/k$ °K	$\sigma$ Å°	M g/g-mole
O	106.7	3.050	16.00
O <sub>2</sub>	106.7	3.467	32.00
N	71.4	3.298	14.00
N <sub>2</sub>	71.4	3.798	28.00
NO	116.7	3.492	30.00
NO <sup>+</sup>	116.7	3.492	30.00



**FIG:2.1 COORDINATE SYSTEM**

## CHAPTER 3

### METHOD OF SOLUTION

#### 3.1 Introduction

In order to get the surface characteristics and the detailed flow structure, one has to solve the equations governing the flow field. This chapter describes the solution procedure adopted to obtain the numerical solution of the governing equations. The numerical solution involves the use of proper numerical scheme to ensure the convergence of solution. Moreover, in the present case the nonlinear production term becomes important and needs to be treated carefully for numerical convergence of the solution. Section 3.2 describes the overall solution procedure, while sections 3.3 and 3.4 describe the numerical scheme and treatment of the production term respectively.

#### 3.2 SOLUTION PROCEDURE

The governing equations adapted for the stagnation flow field were solved numerically by a finite difference

scheme.

The set of governing equations contains  $N_S$  species continuity equations. However, three of these equations can be replaced by algebraic relations using the condition of charge neutrality and elemental mass conservation. The condition of charge neutrality is used to obtain the electron concentration and elemental mass conservation is used to find the concentration of molecular nitrogen and oxygen. Thus only  $(N_S-3)$  species continuity equations need be solved.

The set of equations involves  $N_S$  second order equations namely, tangential momentum equation, normal momentum equation, energy equation and  $(N_S-3)$  species continuity equations. Also it has 2 first order equations namely, global continuity equation and the equation for  $p_2$ . There are  $(2 N_S+2)$  boundary conditions namely, tangential velocity, normal velocity, temperature (or enthalpy) and  $(N_S-3)$  species concentrations at the wall and also at the shock, and post shock values of pressure (or density) and  $p_2$ . Thus it is seen that all the  $(2 N_S + 2)$  conditions are required for solving the equations.

However, in order to determine the shock stand-off distance one more condition is needed. As already noted by Ho and Probst (1960) and Kao (1964b), this condition is obtained by the application of global continuity equation

at the wall. At an impermeable wall, the global continuity equation reduces to:

$$2 u + v_{\eta} = 0$$

( 3.2.1 )

This equation provides the extra condition needed for the determination of the shock stand-off distance  $\eta_e$ . However, the application of normal momentum equation at the wall results into:

$$p_{\eta} = \frac{4}{3} \frac{\mu}{Re} \left[ \frac{\mu}{\mu} (v_{\eta} - u) + v_{\eta\eta} + 2v_{\eta} - \frac{u}{2} - 3.5 u \right]$$

( 3.2.2 )

If the normal momentum equation is solved for normal velocity  $v$ , it is imperative that the normal momentum equation be solved in such a manner that it satisfies not only two usual boundary conditions at the wall and at the shock but also the condition ( 3.2.1 ) at the wall. At the same time, it is necessary that when continuity equation is solved for density ( or pressure through use of equation of state 2.2.7 ), it should satisfy the additional condition ( 3.2.2 ) at the wall. Thus it appears that a second order differential equation is to be solved using three boundary conditions and a first order differential equation is to be solved using two boundary

conditions.

In order to avoid the difficulty of imposing these additional conditions, it was decided to solve the global continuity equation for normal velocity  $v$  and normal momentum equation for the pressure  $p$ . This avoids the apparent problem of imposing the additional constraints. Strictly speaking, these conditions have already been satisfied because these conditions were derived from the equations themselves. In this approach, the normal momentum equation, being first order in pressure, requires only one condition and thus releases one condition ( post-shock normal velocity ) which can be used for determining the shock stand-off distance. An additional advantage of this scheme is that the solution approaches the boundary layer solution when Reynolds number is very high.

Once the free-stream conditions and the nose radius of the body are specified, initial profiles for all the dependent variables are assumed along with a guess value for shock stand-off distance.

A unified finite difference representation of the governing equations is generated as described in the next section, and the initial profiles are substituted into the finite difference form of the governing equations. The governing equations are solved in the order described below.

- (i) Species Continuity Equations -- for mass concentrations of various species.
- (ii) Energy Equation -- for temperature .
- (iii) Equation of State -- for density using old values of pressure and new values of temperature and mass concentrations of various species.
- (iv) Evaluation of thermodynamic and transport properties
- (v) Tangential Momentum Equation -- for tangential velocity
- (vi) Global Continuity Equation -- for normal velocity and shock stand-off distance.
- (vii) Normal Momentum Equation -- for pressure
- (viii)  $p_2$  Equation -- for  $p_2$

The solution of the finite difference equations gives improved profiles for the flow variables. This completes an iteration. These improved profiles are substituted into the governing equations once again yielding new profiles. This iterative procedure is repeated till all the profiles converge to a prescribed accuracy.

### 3.3 Numerical Scheme

The tangential momentum equation, energy equation and species continuity equation are solved for tangential velocity, temperature and mass concentration of different species. All these equations are of second order with

split boundary conditions. Usually in these equations each derivative is replaced by corresponding finite difference representation. Thus these differential equations reduce to a set of difference equations which are to be solved for profiles of various flow variables.

### Choice of Grid

In order to get realistic behaviour of the flow variables in the shock layer, it is necessary that there are grid points at close intervals, wherever there are sharp gradients in the flow variables. If the grid is chosen to be uniform, large number of grid points will be needed to simulate the flow field and it will require large amount of computation time. In order to avoid large number of grid points and large amount of computation time, it is necessary that grid points are chosen to be at un-equal intervals. In this way, one can have reasonable number of grid points( and less computational time) and at the same time get sufficiently accurate profiles for flow variables.

In the present analysis, the grid chosen was geometrically stretched, with each succeeding grid spacing being  $\delta$  times the previous spacing as one proceeds from the body to the shock. The first grid spacing is the function of  $\delta$  and number of grid intervals in the shock layer. The grid stretching parameter  $\delta$  was chosen in such



a way that first grid point next to the wall was approximately 0.5 percent of the boundary layer thickness away from the wall.

However, if value of  $\delta$  is very large, then the grid spacing may be quite large near the shock. It is likely to lead to the breakdown of the solution procedure in the sense that the conditions at the shock may not have any influence on the solution near the wall. In order to avoid such a possibility, an upper limit for  $\delta$  has been prescribed for present analysis. This upper limit is a function of number of grid points employed in the analysis.

### Finite Difference Scheme

For achieving smooth behaviour of the solution it is necessary that the system of difference equations be diagonally dominant. This condition is equivalent to local cell Reynolds number being less than 2 (Leonard 1979). This implies that the step size is quite small. This will result in large number of steps and thus large computation time.

One way to overcome the large number of steps is to introduce one-sided difference for first order derivatives resulting in diagonally dominant difference equations. This ensures smooth behaviour of the solution variable, but it is at the cost of increased truncation error due to first order accuracy of one-sided difference

representation. In order to overcome this problem, in the present analysis Unified Difference Representation (UDR) for differential terms was used. In this approach both second and first order terms in a given equation are treated together and not as the sum of two terms (Roach 1982). The difference form is evaluated for both the terms combined together. With the notations of the Figure 3.1, the difference form is given by:

$$A f_{\eta\eta} + B f_{\eta} = C_1 f_{i-1} + C_2 f_i + C_3 f_{i+1}$$

( 3.3.1 )

where

$$C_1 = \frac{B [ 1 - \exp(-B\Delta_2/A) ]}{\Delta_2 [ \exp(B\Delta_1/A) - 1 ] - \Delta_1 [ 1 - \exp(-B\Delta_2/A) ]}$$

$$C_3 = \frac{B [ \exp(B\Delta_1/A) - 1 ]}{\Delta_2 [ \exp(B\Delta_1/A) - 1 ] - \Delta_1 [ 1 - \exp(-B\Delta_2/A) ]}$$

$$C_2 = -C_1 - C_3$$

This form is always diagonally dominant for all values of A, B,  $\Delta_1$  and  $\Delta_2$ . For the case B=0, this expression 3.3.1 reduces to the usual central difference form for second order derivative for unequal steps. Use of this scheme to second order differential equation results in a

set of tridiagonal difference equations which can be represented for a grid point  $i$  as

$$a_i z_{i-1} + b_i z_i + c_i z_{i+1} = d_i$$

( 3.3.2 )

where  $z_i$  is either tangential velocity, temperature or mass concentration at the grid point  $i$ . This set of tridiagonal system of difference equations was solved by forward and backward substitution scheme of Thomas algorithm.

Global continuity equation, normal momentum equation and  $p_2$  equations are solved for normal velocity, pressure and  $p_2$  respectively. These are first order initial value problems. These equations were integrated using trapezoidal rule.

Continuity equation is also used to determine shock stand-off distance  $\eta_e$ . The continuity equation can be integrated to give

$$\rho v \left( \frac{1}{\eta_e} + \xi \right)^2 = -2 \int_0^\xi \rho u \left( \xi + \frac{1}{\eta_e} \right) d\xi$$

( 3.3.3 )

where  $\xi$  is the distance from the wall non-dimensionalised with respect to shock stand-off distance  $\eta_e$ , that is

$$\xi = \eta / \eta_e$$

using boundary condition at the shock

$$\text{at } \xi = 1 \quad \rho v = -1$$

one has

$$\left(1 + \frac{1}{\eta_e}\right)^2 = \frac{2}{\eta_e} \int_0^1 \rho u d\xi + 2 \int_0^1 \rho u \xi d\xi$$

( 3.3.4 )

This equation is quadratic in  $\eta_e$  and can be solved for  $\eta_e$ . It is noticed that for all the cases, one values of the  $\eta_e$  is positive and another negative. Thus there was no ambiguity in choosing  $\eta_e$ .

### Boundary Conditions

The governing equations are to be solved with the boundary conditions 2.2.45-2.2.50 at the wall. These conditions are mixed type, that is these involve both the variable and its derivative. In these equations, the derivatives are to be replaced by their finite difference form and the resultant equations are used instead of governing equations at the wall. The condition 2.2.50 is used to evaluate the wall pressure from the pressure at the base of shock layer after solving the normal momentum equation for pressure. Equations 2.2.51-2.2.56 provide the boundary conditions at the shock. These conditions are also mixed type and need replacement of derivatives by their finite difference equivalent.

However, when formulation is in terms of temperature, the post shock condition given by equation (2.2.54) in terms of enthalpy is not in suitable form. It has to be rewritten in terms of temperature. The equation (2.2.54) can be rewritten as follows:

$$h_0 + C_p (T - T_0) + \frac{\mu}{Re Pr} C_p T_\eta = 1 + \frac{h_\infty^*}{U_\infty^*{}^2} - \frac{v^2}{2} + \frac{4\mu}{3 Re} v v_\eta + \sum_{i=1}^{Ns} \frac{\mu Le_i}{Re Pr} C_{i\eta} h_i$$

( 3.3.5 )

Here  $h_0$  and  $T_0$  are the known post shock enthalpy and temperature at the previous iteration.  $T$  is the new post shock temperature to be evaluated. This equation ( 3.3.5 ) is used in place of condition ( 2.2.54 ).

### 3.4 Treatment of Production Term

It is observed from equations ( 2.3.6 ) that  $w_1^*$  and hence  $w_1$  is a strong nonlinear function of  $C_1$ . This appears as a source term in the species continuity equation and in the energy equation formulated in terms of temperature. However, from the considerations of numerical convergence it is desirable to express  $w_1$  as a linear function of  $C_1$ . This can be achieved by linearisation of term  $w_1$  about the present value of  $C_1$ . Thus it is written in the form

$$w_1 = w_1^0 - w_1^1 C_1$$

( 3.4.1 )

Similarly for energy equation also it is desirable to express the term  $\sum h_1 w_1$  as a linear function of temperature. It is written by expanding it about the current value of temperature in the following manner:

$$\sum_{i=1}^{N_s} h_1 w_1 = \sum_{i=1}^{N_s} (h_1 w_1)^k + (T_{k+1} - T_k) \sum_{i=1}^{N_s} h_1 \left( \frac{\partial w_1}{\partial T} \right)_k$$

( 3.4.2 )

Here  $k$  denotes the iteration at which approximate profile is known and  $(k+1)$  is the iteration for which improved profile is being sought. Blottner (1969) has discussed the need for splitting these terms in this form. Essentially this is required for getting the convergence of the numerical solution. If this expansion is not carried out then one uses only the first term of this expansion while evaluating the expression numerically and thus it amounts to neglecting the variation of this term with respect to  $C_1$  or  $T$  during a particular iteration.

If sufficient care is not exercised in the computation of chemically reacting flow, the net mass production rate of all the species may not vanish (Park 1985). Apart from the numerical errors, it also occurs

because of the linearisation of the production terms( Appendix 1). In order to avoid this problem, mass conservation for elemental species was used to evaluate the mass concentration of oxygen and nitrogen (  $C_{O_2}$  and  $C_{N_2}$  ). It was also used to evaluate the production rate of oxygen and nitrogen (  $w_{O_2}$  and  $w_{N_2}$  ) and their temperature derivatives as well.

For elemental mass conservation one has

$$C_{O_2} + C_O + \frac{M_O}{M_{NO}} ( C_{NO} + C_{NO+} ) = W_O$$

( 3.4.3 )

and

$$C_{N_2} + C_N + \frac{M_N}{M_{NO}} ( C_{NO} + C_{NO+} ) = W_N$$

( 3.4.4 )

Since production rate  $w_1$  is related to mass concentration by

$$w_1 = \rho \frac{dC_1}{dt}$$

one gets

$$w_{O_2} = - w_O - \frac{M_O}{M_{NO}} ( w_{NO} + w_{NO+} )$$

( 3.4.5 )

and

$$w_{N2} = -w_N - \frac{M_N}{M_{NO}} (w_{NO} + w_{NO+}) \quad (3.4.6)$$

In the present work equations ( 3.4.5 ) and ( 3.4.6 ) are used to evaluate the production rate  $w_{O2}$  and  $w_{N2}$  for use in equation ( 3.4.2 ) for energy equation solution. This ensures that at every iteration net mass production for all species is zero and thus total mass is conserved.

In order to evaluate terms  $\partial w_{O2}/\partial T$  and  $\partial w_{N2}/\partial T$  for use in equation ( 3.4.2 ), differentiating equations (3.4.5) and ( 3.4.6 ) one gets,

$$\frac{\partial w_{O2}}{\partial T} = - \frac{\partial w_O}{\partial T} - \frac{M_O}{M_{NO}} \left( \frac{\partial w_{NO}}{\partial T} + \frac{\partial w_{NO+}}{\partial T} \right) \quad (3.4.7)$$

and

$$\frac{\partial w_{N2}}{\partial T} = - \frac{\partial w_N}{\partial T} - \frac{M_N}{M_{NO}} \left( \frac{\partial w_{NO}}{\partial T} + \frac{\partial w_{NO+}}{\partial T} \right) \quad (3.4.8)$$

Use of the equations ( 3.4.7 ) and ( 3.4.8 ) ensures that rate of change of overall mass is zero with temperature.

One more aspect of chemically reacting flows which needs attention is the oscillations of profiles from one



reversion to another. This is possibly due to conversion of energy from translational mode to chemical mode and vice versa (Park 1986). Some times it may lead to one particular concentration becoming negative and this will further amplify and lead to other concentrations becoming negative, if unchecked. Finally, it will lead to breakdown of the solution procedure. It has been taken care of in the following manner:

It is assumed that at any given point in the flow field, the various concentrations must lie between free-stream value and maximum permissible values.

$$C_{10} \leq C_1 \leq C_1 \text{ max}$$

for the species which do not have significant concentrations in the free stream, namely O, N, NO, NO<sup>+</sup> and e<sup>-</sup>, usually referred to as minor species. The maximum permissible values can be evaluated from free stream conditions. In case concentrations during iterative procedure are outside these bounds, then they are forced to the nearest bound. This ensures that none of the concentrations become negative during iterative solution procedure and eliminates problem associated with negative concentrations and unrealistically high values of concentration. Elemental mass conservation procedure is applied after all the above minor species have been evaluated.

### 3.5 Convergence of Numerical Procedure

The procedure described above was coded in FORTRAN IV and was run on CDC Cyber 170/730 at VSSC Trivandrum for evaluating the flow field and surface characteristics for various free stream conditions. The parameters used in connection with numerical solution procedure are as follows:

Number of intervals : 100

Grid stretching parameter :  $1.01 \leq \delta \leq 1.05$

Convergence criterion : 1%

The convergence criterion of 1 percent means that all the variables over the entire shock layer are within 1 percent of their respective values in previous iteration.

The computations were performed both for perfect gas and for chemically reacting non-equilibrium flow. For the perfect gas case, the free stream and fluid property parameters are given by:

$$Re = 100$$

$$M_{\infty} = 10$$

$$Pr = 0.7$$

$$\gamma = 1.4$$

$$\mu \propto \sqrt{T}$$

Figures 3.2 - 3.3 show the convergence of various profiles for the perfect gas case. Figure 3.2 shows the maximum fractional change for a flow variable over the entire profile. It is observed that maximum fractional

change in  $u$ ,  $v$  and  $T$  decreases to a value less than convergence criteria by fifth iteration.

Figure 3.3 shows the evolution of temperature profile as iterations progress. It is noted that at iteration 2, there is an increase in shock stand-off distance which decreases as the profiles evolve with the iterations. It is observed that the profiles are more or less identical at iteration 3 and iteration 4. Similar behaviour is noted in Figure 3.4 which shows the evolution of tangential velocity profile.

For chemically reacting flow, the free stream conditions used correspond to the Shuttle flight conditions. These are as follows:

Altitude = 92.35 km

Free Stream Velocity  $U_{\infty}$  = 7.5 km/s

Nose radius  $R_b$  = 1.296 m

Wall Temperature = 1043 °K

Wall Catalyticity : Non-catalytic

The thermodynamic and transport properties of the air were evaluated by the method described in section 2.4. For mixture properties estimation, correlation proposed by Armaly and Sutton (1980, 1981) has been used.

Figures 3.5-3.7 shows the maximum fractional changes in concentration profiles, flow variables and transport property with iteration count. The solution based on convergence criterion was obtained at twelfth iteration.

Figure 3.5 shows the fractional change in the concentration profiles with iteration count. It is observed that maximum changes occur in concentration of atomic oxygen and therefore atomic oxygen profile is the last one to converge. This figure does not show the changes in electron concentration, molecular oxygen, and nitrogen. The fractional changes in electron concentration is identical to fractional changes in  $\text{NO}^+$  concentration. The changes in concentration of molecular oxygen and nitrogen are related to the changes in other concentrations by elemental mass conservation.

Figure 3.6 shows the convergence of flow variables. It is observed from this figure that pressure is the first variable to converge, while tangential velocity gradient is the last one to converge. Figure 3.7 shows the convergence of transport properties. It is seen that Prandtl number converges to the prescribed accuracy at iteration 2, while viscosity converges at iteration 3.

Figure 3.8 shows the evolution of temperature profile with iteration count. It is seen that at iteration 1, there is a sudden decrease in shock stand-off distance. This is due to fact that initial guess value of shock stand-off distance correspond to the perfect gas conditions. It is seen that both post shock temperature and gas temperature at the wall evolve with the iterations and attain the final converged values.

Figures 3.9-3.12 show the convergence of concentration profiles with iteration count. Figure 3.9 shows the evolution of concentration of molecular nitrogen. It is observed that with each iteration, level of concentrations decrease continuously and convergence is achieved without oscillations in profiles. Similar behaviour is noticed in figure 3.10, which shows the evolution of concentration of molecular oxygen. It is seen that near the wall molecular oxygen is almost fully dissociated at about 2000 °K. This is because near the wall, diffusion of species dominates over the chemical kinetics. Figure 3.11 and 3.12 show the evolution of concentration profiles for atomic oxygen and nitrogen respectively.

In order to assess the convergence characteristics of the present formulation and the computer code at higher Reynolds number, the flow field was computed for conditions corresponding to atmospheric entry of Aero-Assist Flight Experiment (AFE) vehicle. These conditions are as follows:

Altitude = 78.90 km

Free Stream Velocity  $U_\infty$  = 9.365 Km/s

Nose radius  $R_b$  = 2.530 m

Wall Temperature = 1111 °K

Wall Catalyticity : Non-catalytic

The thermodynamic and transport properties of the air

were evaluated by the method described in section 2.4. For mixture properties estimation, correlation proposed by Armaly and Sutton (1980, 1981) has been used.

In this case the post-shock Reynolds number  $Re_s$  is 1760, while Moss (1971) reported the failure of convergence of numerical computations for post-shock Reynolds number greater than 500. Moreover, in order to check whether the numerical solution has any tendency for divergence at later stages of the computations, the computations were carried upto 100 iterations, when solution satisfied the convergence criterion at about 48 iterations.

Figures 3.13 to 3.18 show the convergence of various flow variables with iteration count. It is observed that the maximum change in all the variables over the entire shock layer decreases continuously after first 10 iterations. Figure 3.13 shows the maximum fractional change for both tangential and normal velocities and temperature. It is observed that these variables converged to the prescribed accuracy by about 30 iterations and there is monotonic decrease in the fractional change thereafter. Figure 3.14 shows the maximum fractional change in the pressure and fractional change in the heat flux to the wall. It is noticed that pressure profile converges to the prescribed accuracy by about 30 iterations while heat flux values satisfy this test after

about 10 iterations. This accuracy test has not been prescribed for heat flux value. Nevertheless the heat flux to the body is found to have converged very fast. The convergence of heat flux by about 10 iterations implies that after 10 iterations, there are no significant changes in the flow variables near the wall.

Figure 3.15 shows the maximum fractional change in the concentration of  $N_2$ ,  $O_2$  and  $NO$ . It is observed that after initial sudden changes for about 10 iterations, the changes in the concentrations decrease monotonically with iterations. It is seen that concentration of  $N_2$  converges last at about 50 iterations. Figure 3.16 shows the maximum fractional changes in the concentration of  $O$ ,  $N$  and  $NO^+$ . The changes in the concentration of  $e^-$  is identical to that of  $NO^+$ . It is noted that in this case also fractional changes decrease continuously with iterations and concentration of  $NO^+$  is last to converge. The fractional changes in the flow variable do not show any tendency of increasing with iteration except in the beginning when the flow variables are adjusting to the boundary conditions. Figure 3.17 shows the convergence of shock stand-off distance with iterations. It is observed that shock stand-off distance converges by about 25 iterations and then it remains steady. Figure 3.18 shows the convergence of the wall heat flux. Heat flux converges by about 10 iterations and then remains

constant.

Figures 3.19 to 3.29 show the evolution of the various profiles with number of iterations. Figures 3.19 and 3.20 show the evolution of the tangential and normal velocity profiles. It is seen that velocity profiles converge by about 30 iterations and after 30 iterations, there are no appreciable changes in the profiles. It is observed that profiles at different iterations terminate at different distance from the wall as shock stand-off distance evolves with the iterations. The profiles after 60 iterations have not been plotted.

Figures 3.21 - 3.23 show the evolution of temperature, density and pressure profiles respectively. In this case also it is noted that the profiles converge by 30 iterations. It is seen that temperature first increases with distance from the wall and later temperature remains constant. Near the shock, the temperature suddenly increases. This sudden increase in the temperature is due to post-shock boundary condition.

Figures 3.24-3.29 show the evolution of various concentration profiles. It is seen that profiles evolve to the converged profiles without oscillations. Figure 3.24 shows the evolution of  $N_2$  concentration profile. It is observed that near the wall, initially concentration decreases due to dissociation of  $N_2$  as temperature increases. After some distance, the concentration remains



constant and then near the shock, the concentration of  $N_2$  increases sharply. This sharp increase in the concentration is due the boundary conditions at the shock. Similar behaviour is noticed in Figure 3.25, which shows the evolution of  $O_2$  concentration profile. It is seen that at the wall  $O_2$  is completely dissociated, while  $N_2$  is not fully dissociated. This is due to the wall temperature being low for  $N_2$  dissociation to take place.

Figure 3.26 shows evolution of the concentration profile of the NO. In this case it is observed that near the wall NO concentration is nearly zero and the concentration increases with the distance from the wall as the temperature increases. Near the shock, there is sudden decrease in NO concentration due the boundary condition. Figure 3.27 shows the evolution of the concentration profile of O with iterations. It is observed that near the wall, concentration of O is large indicating complete dissociation of  $O_2$ . This is due to fact that near the wall concentration is dominated by diffusion and not by chemical kinetics. Near the shock, concentration of O decreases suddenly due to the boundary condition. Similar phenomenon is observed in Figures 3.28 and 3.29, which show the evolution of concentration profiles of H and  $NO^+$  respectively.

The computations were carried out for higher number of intervals also, namely 200 and 500 for a few sample

cases. It was observed that the final converged profiles were identical with the converged profiles obtained for 100 intervals. In view of the computation time involved, rest of the computation were performed for 100 intervals only.

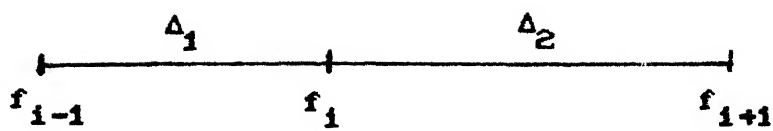


FIG: 3.1 SCHEMATIC FOR FINITE DIFFERENCE SCHEME

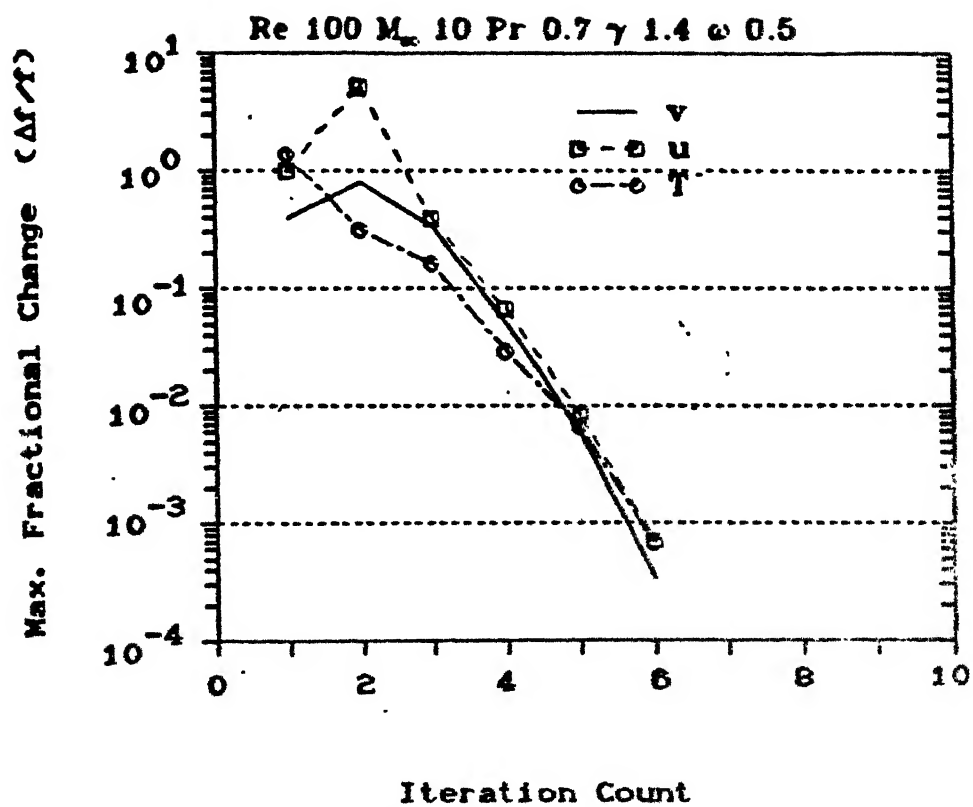


FIG. 3.2. CONVERGENCE OF FLOW VARIABLES

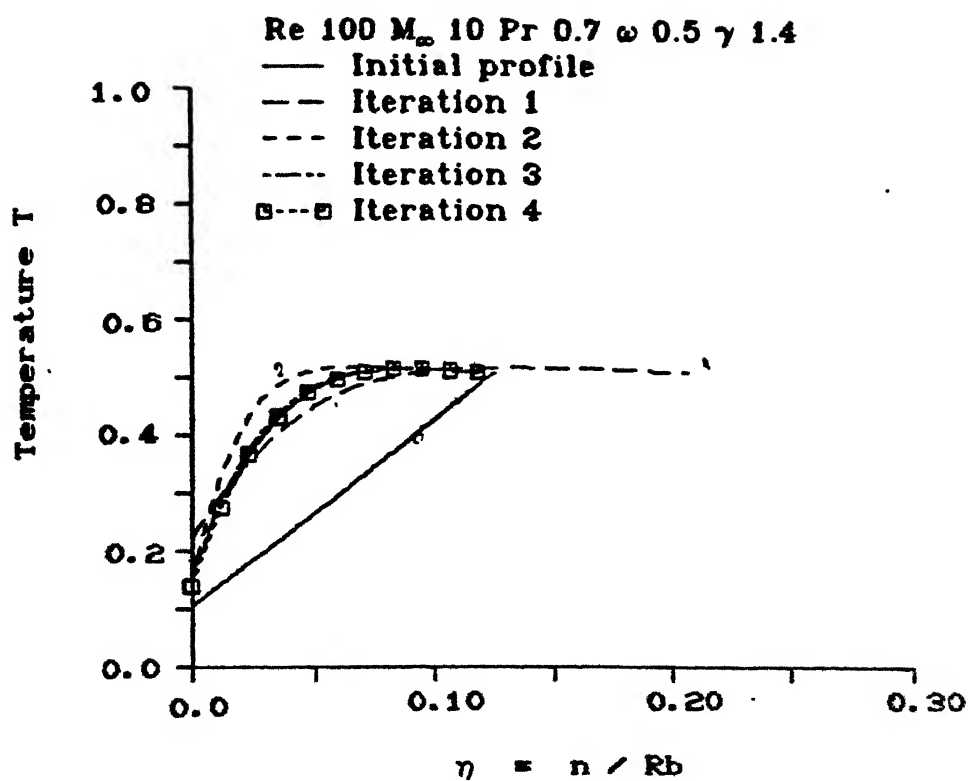


FIG. 3.3 EVOLUTION OF TEMPERATURE PROFILE

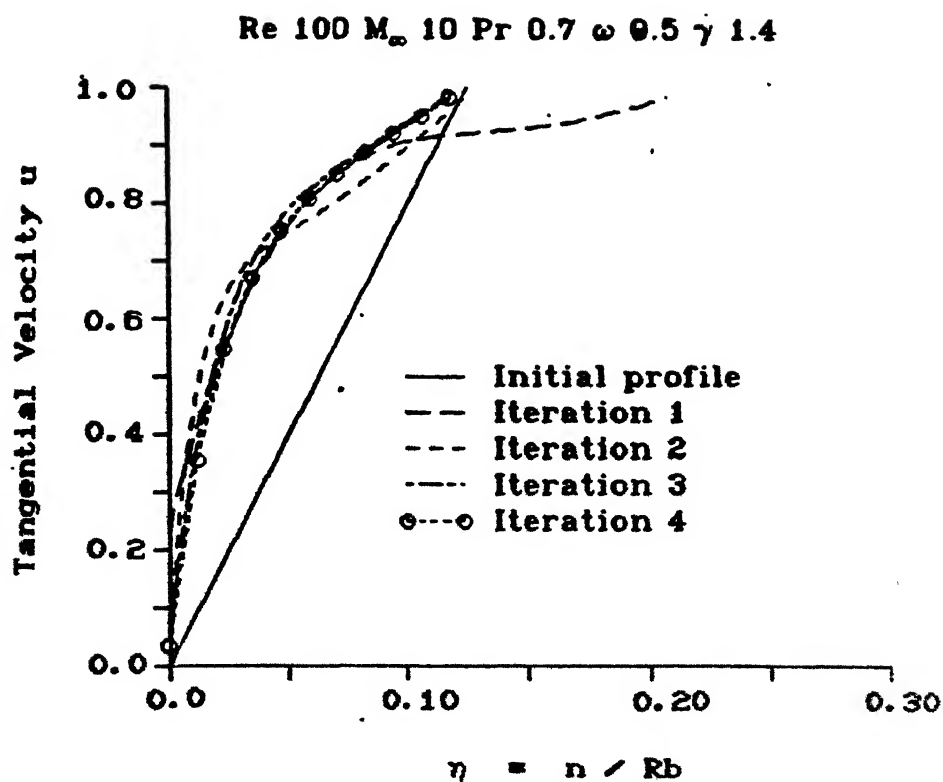


FIG. 3.4 EVOLUTION OF TANGENTIAL VELOCITY PROFILE

Shuttle Non-equilibrium Flow  
Alt 92.35 Km  $U_\infty$  7.5 Km/sec  
 $R_p$  1.296 m  $T_w$  1043°K

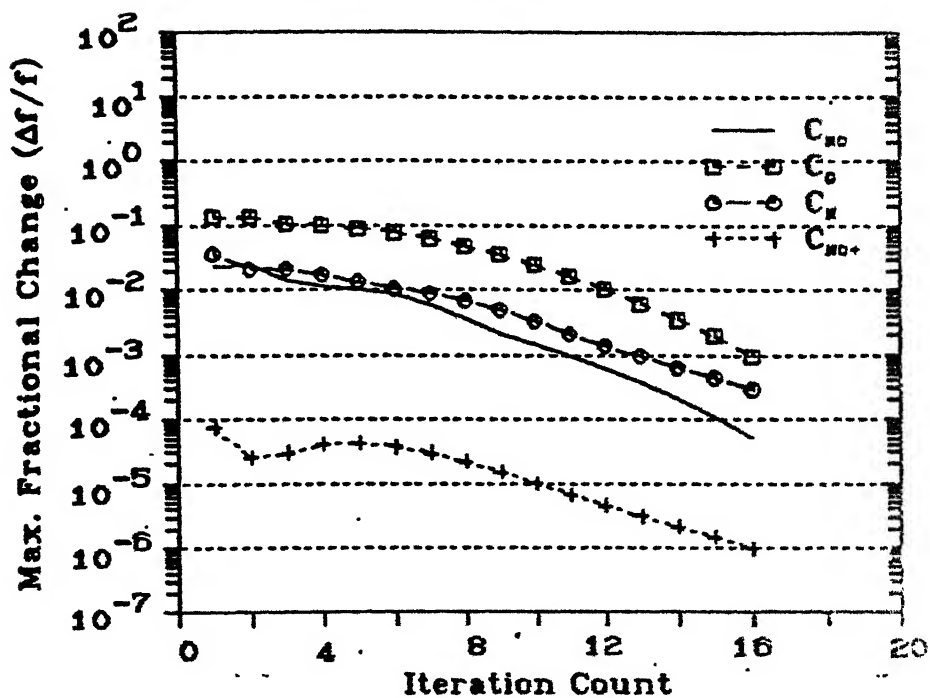


Fig:3.5 Convergence of Concentrations

Shuttle Non-equilibrium Flow  
 Alt 92.35 Km  $U_\infty$  7.5 Km/sec  
 $R_b$  1.296 m  $T_w$  1043°K

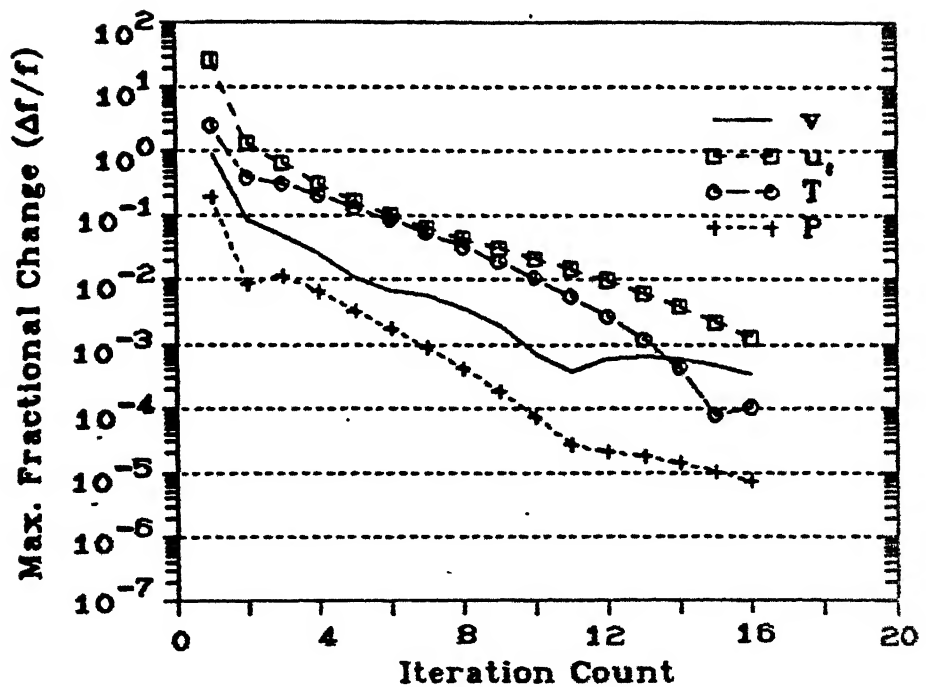


Fig.3.6 Convergence of Flow Variables  
 for Shuttle



Shuttle Non-equilibrium Flow  
Alt 92.35 Km  $U_\infty$  7.5 Km/sec  
 $R_b$  1.296 m  $T_w$  1043°K

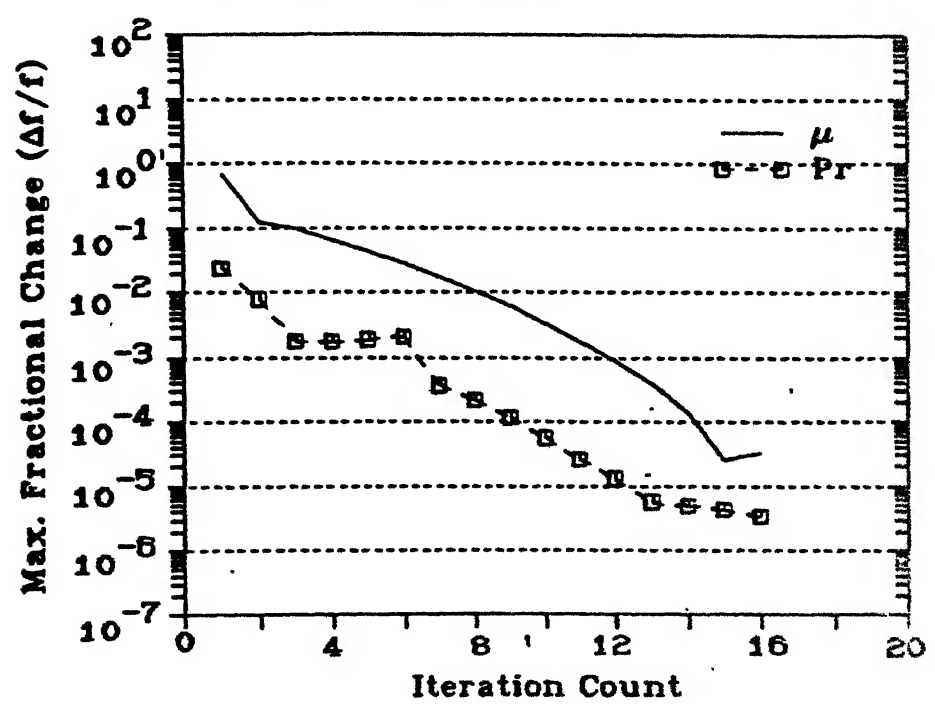


Fig:3.7 Convergence of Transport Property

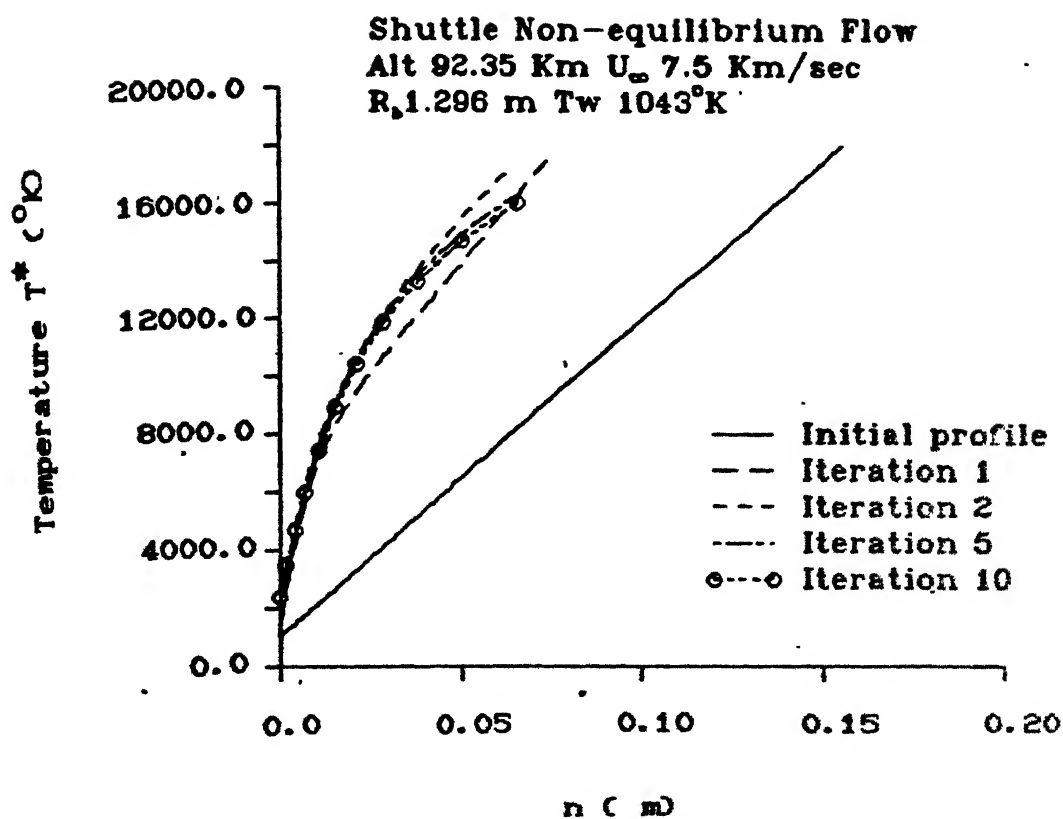


FIG: 3.8 EVOLUTION OF TEMPERATURE PROFILE

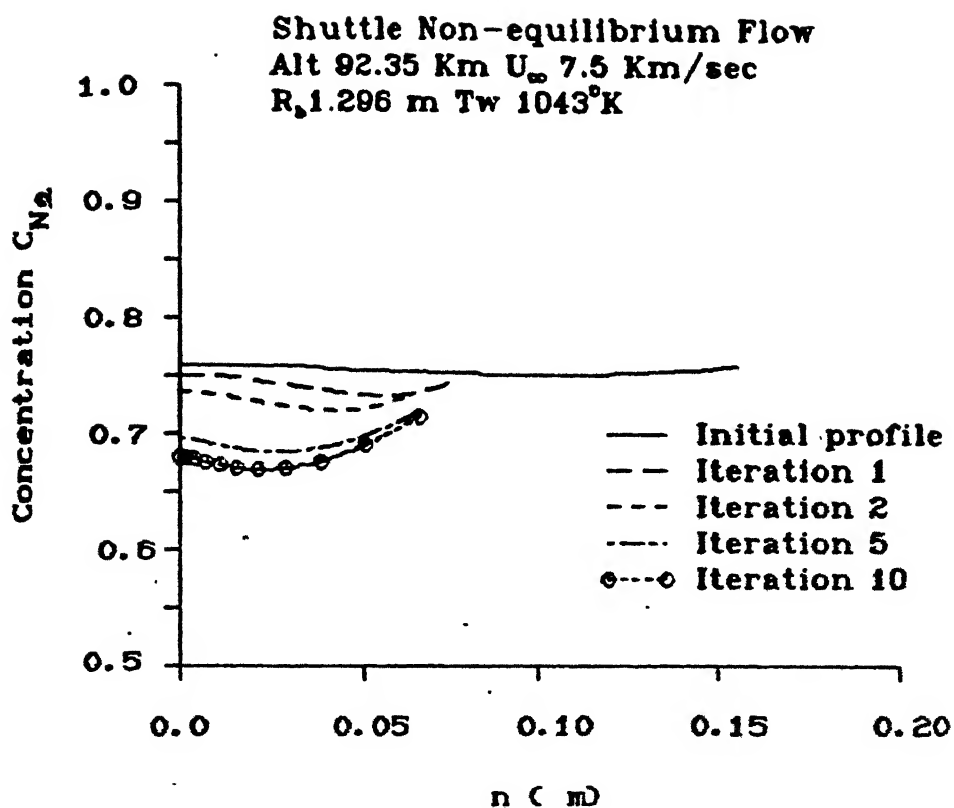
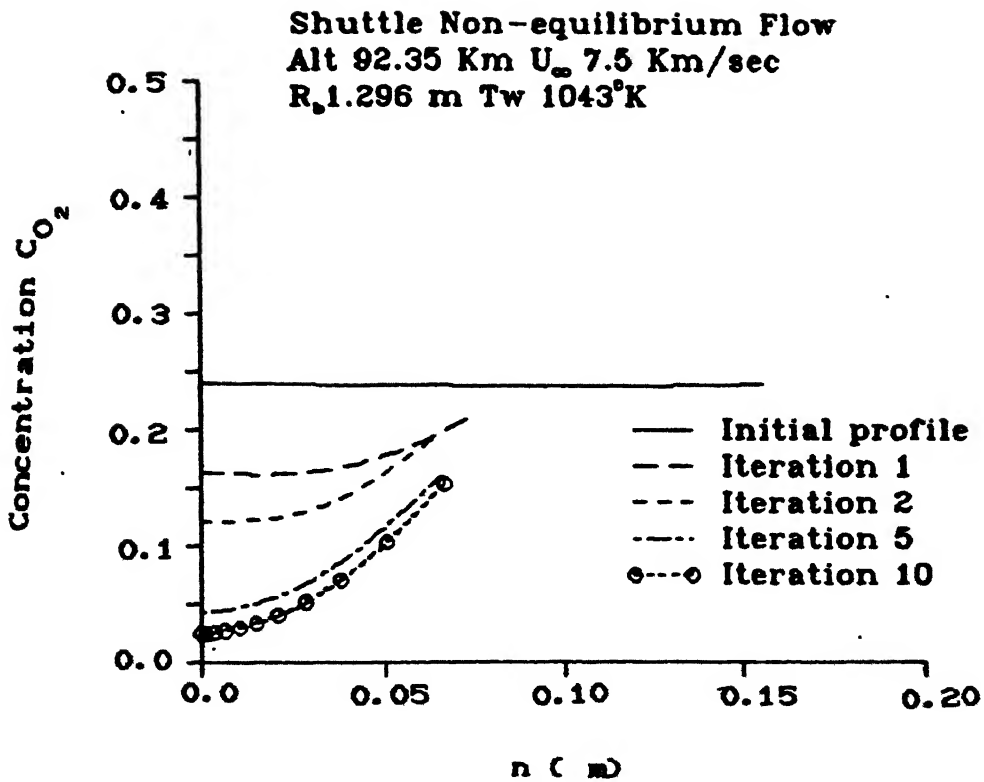


FIG. 3.9 EVOLUTION OF CONCENTRATION PROFILE OF  $C_{N_2}$



**FIG: 3.10 EVOLUTION OF CONCENTRATION PROFILE OF  $CO_2$**

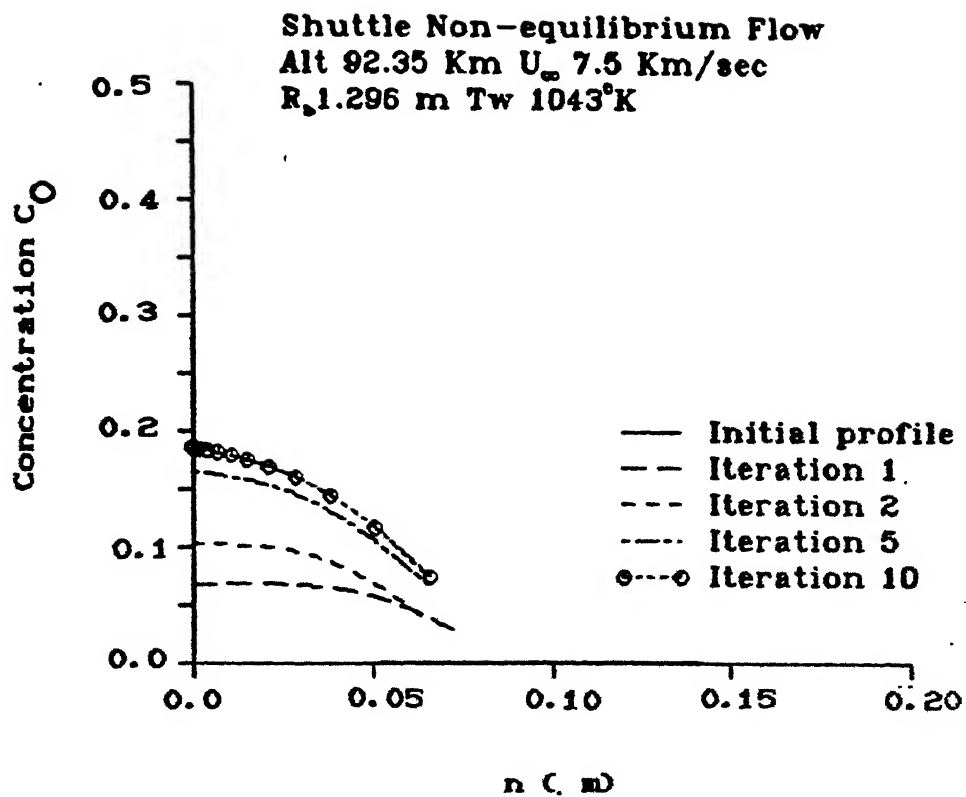


FIG. 3.11 EVOLUTION OF CONCENTRATION PROFILE OF  $C_O$

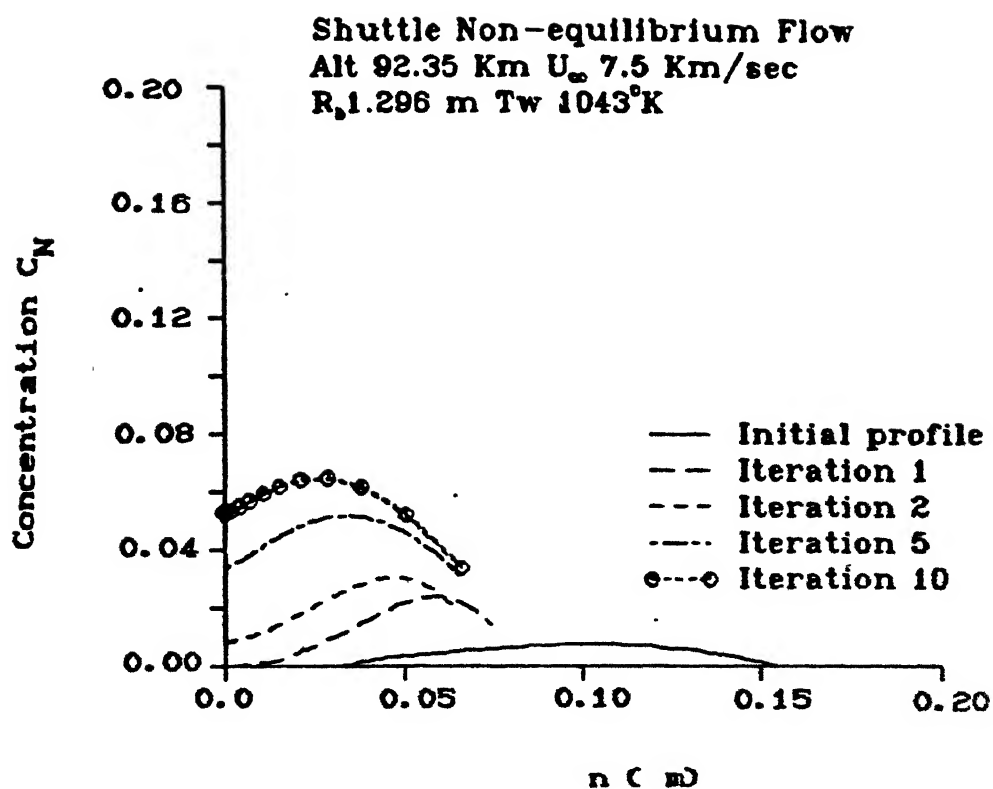


FIG: 3.12 EVOLUTION OF CONCENTRATION PROFILE OF  $C_N$

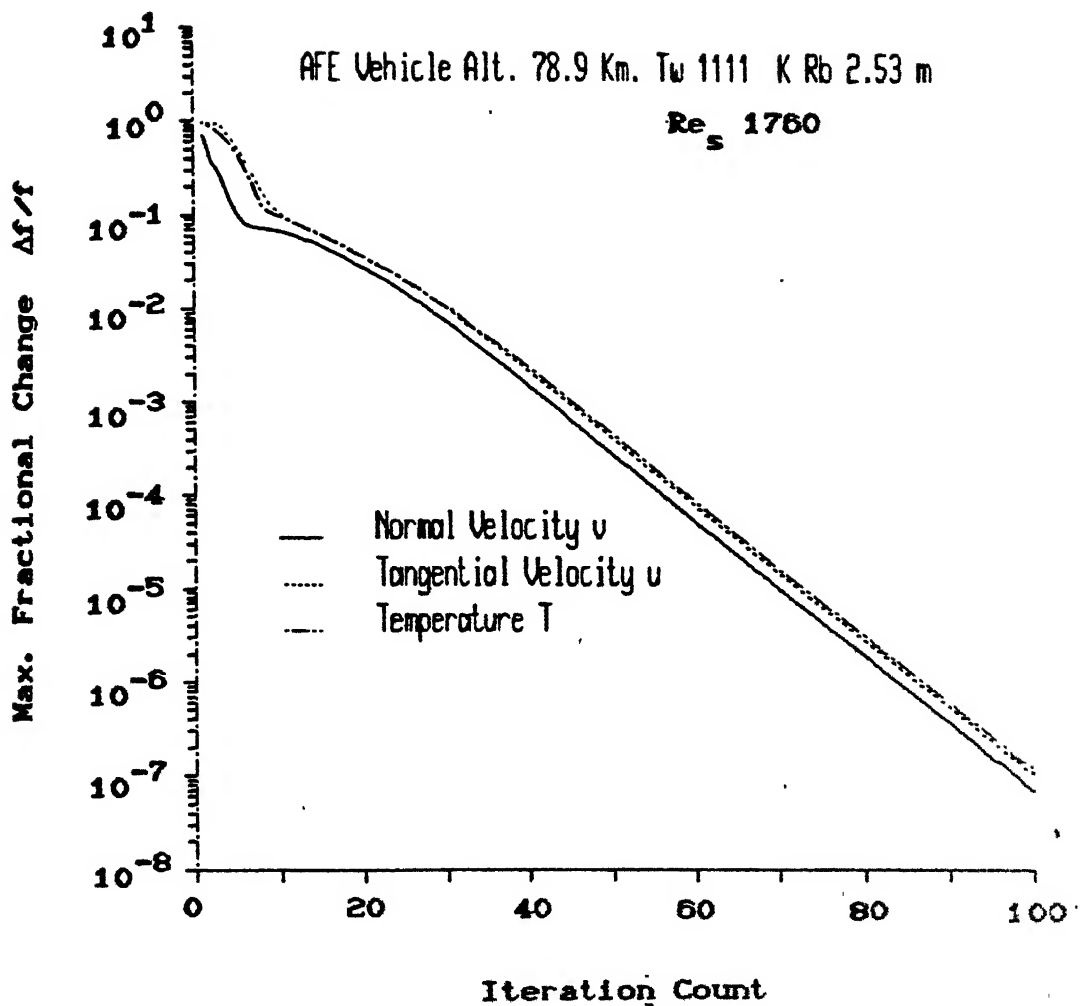


FIG.3.13 CONVERGENCE OF U, V AND T PROFILES  
FOR AFE VEHICLE

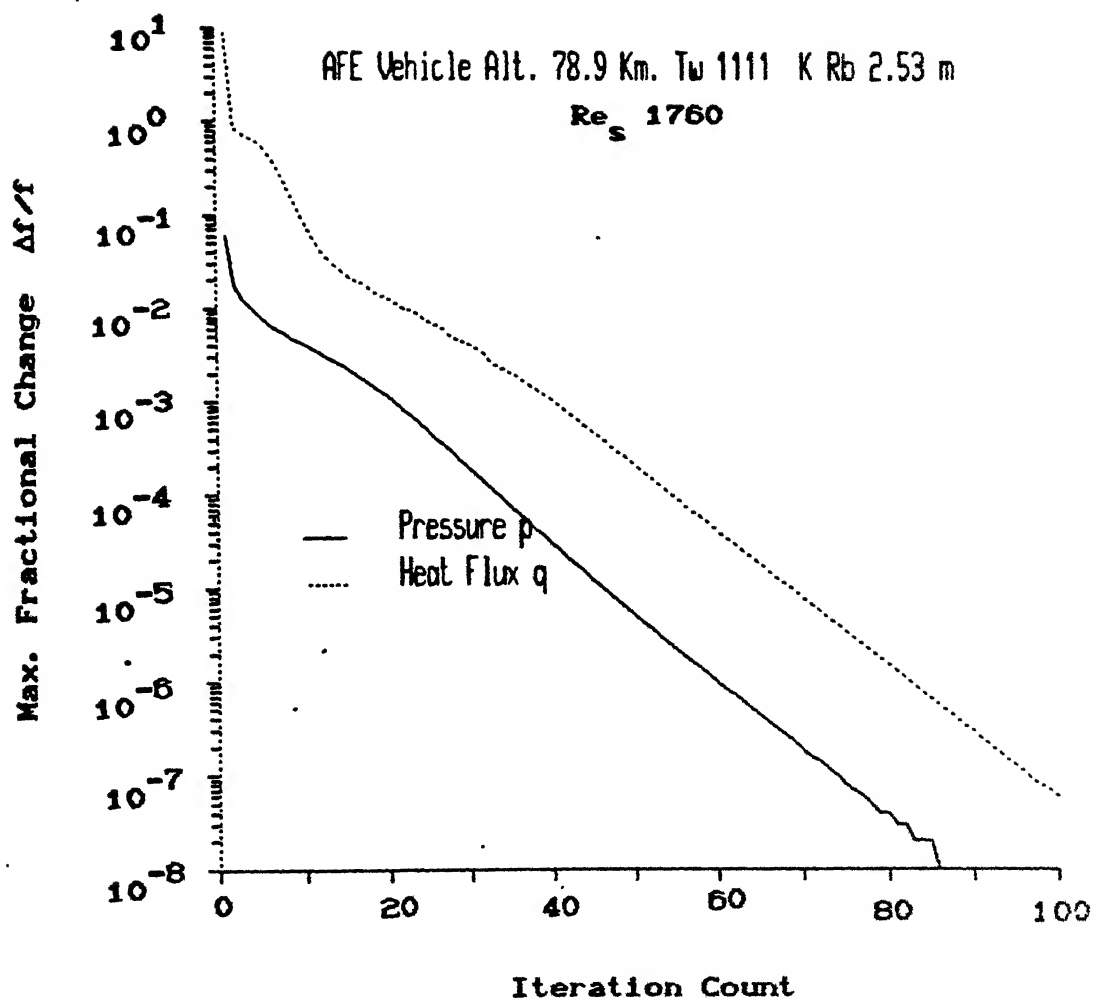


FIG.3.14 CONVERGENCE OF PRESSURE AND HEAT FLUX FOR AFE VEHICLE



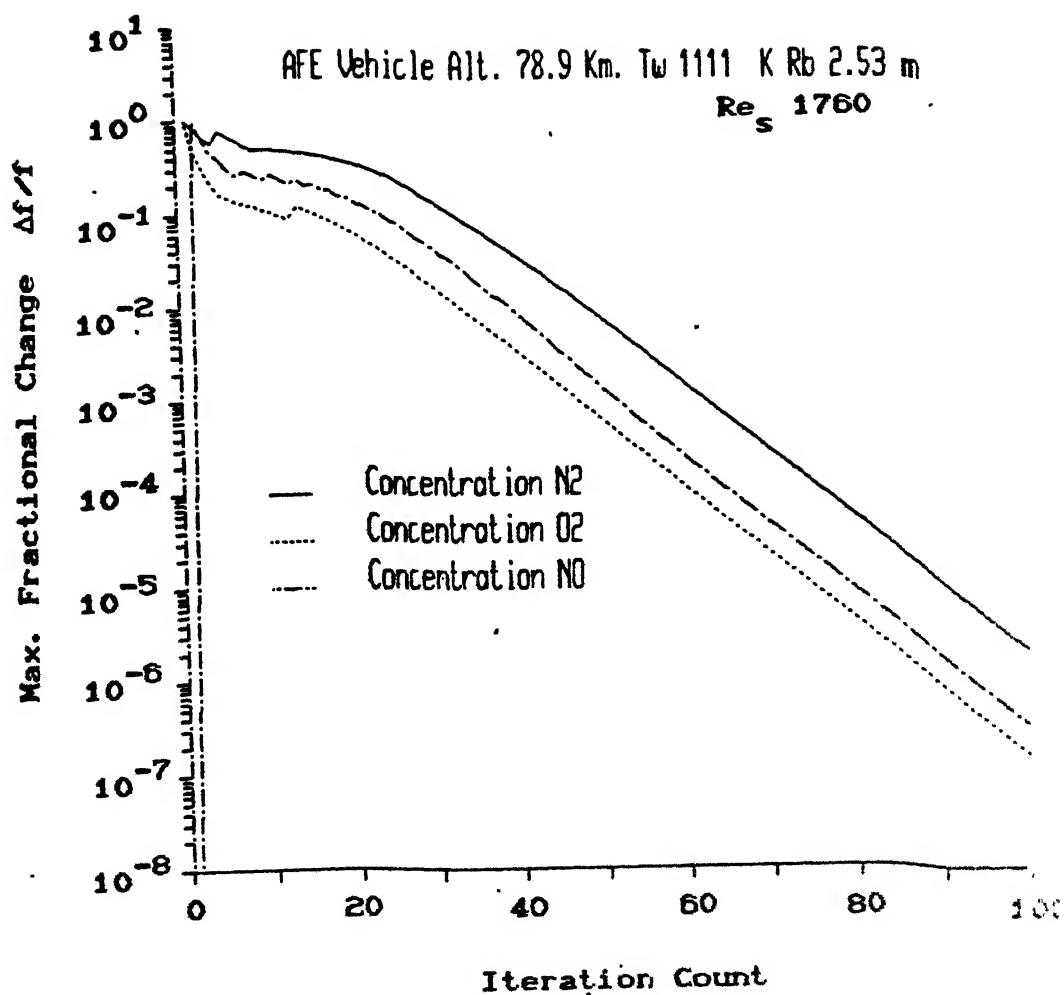


FIG.3.15 CONVERGENCE OF  $C_{N_2}$ ,  $C_{O_2}$  AND  $C_{NO}$  PROFILES  
 FOR AFE VEHICLE

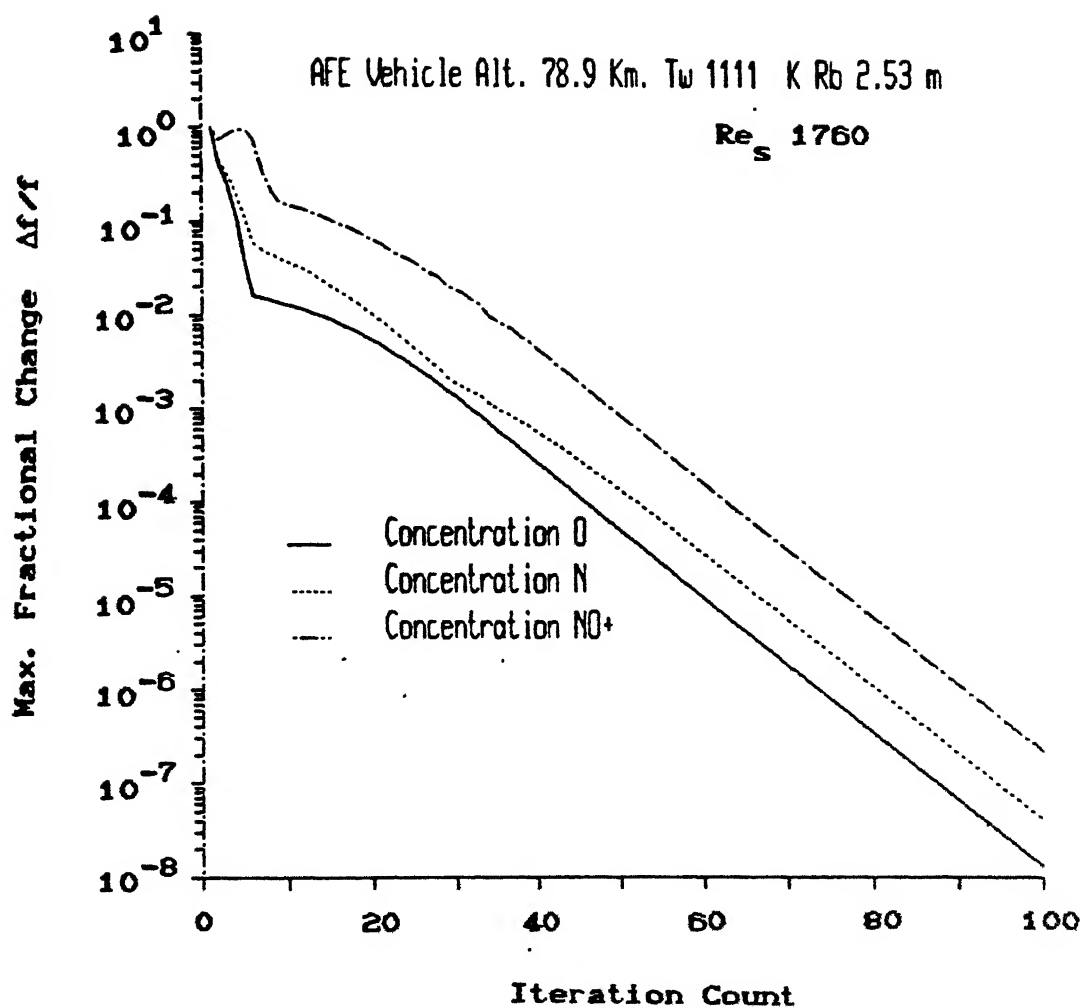


FIG.3.16 CONVERGENCE OF  $C_O$ ,  $C_N$  AND  $C_{NO^+}$  PROFILES  
 FOR AFE VEHICLE

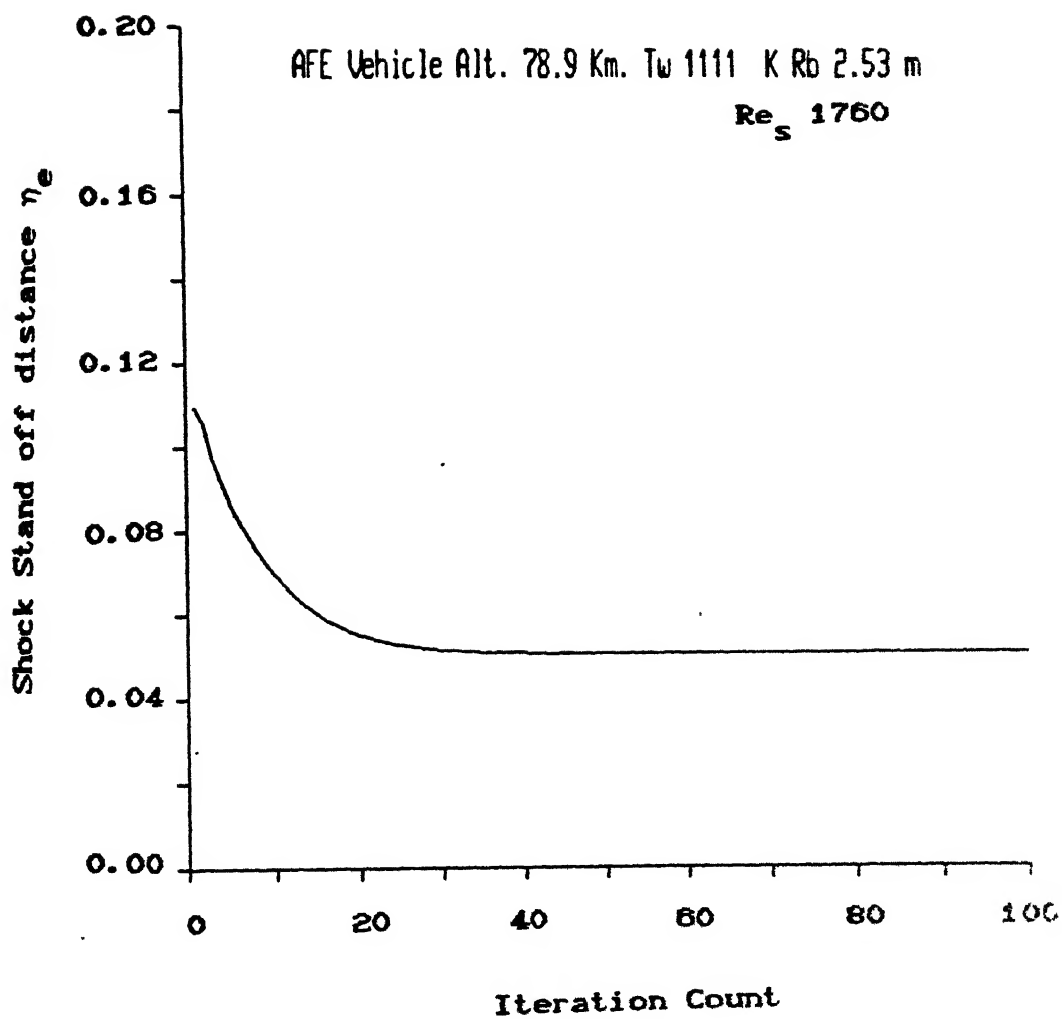


FIG.3.17 CONVERGENCE OF SHOCK STAND-OFF DISTANCE  
FOR AFE VEHICLE

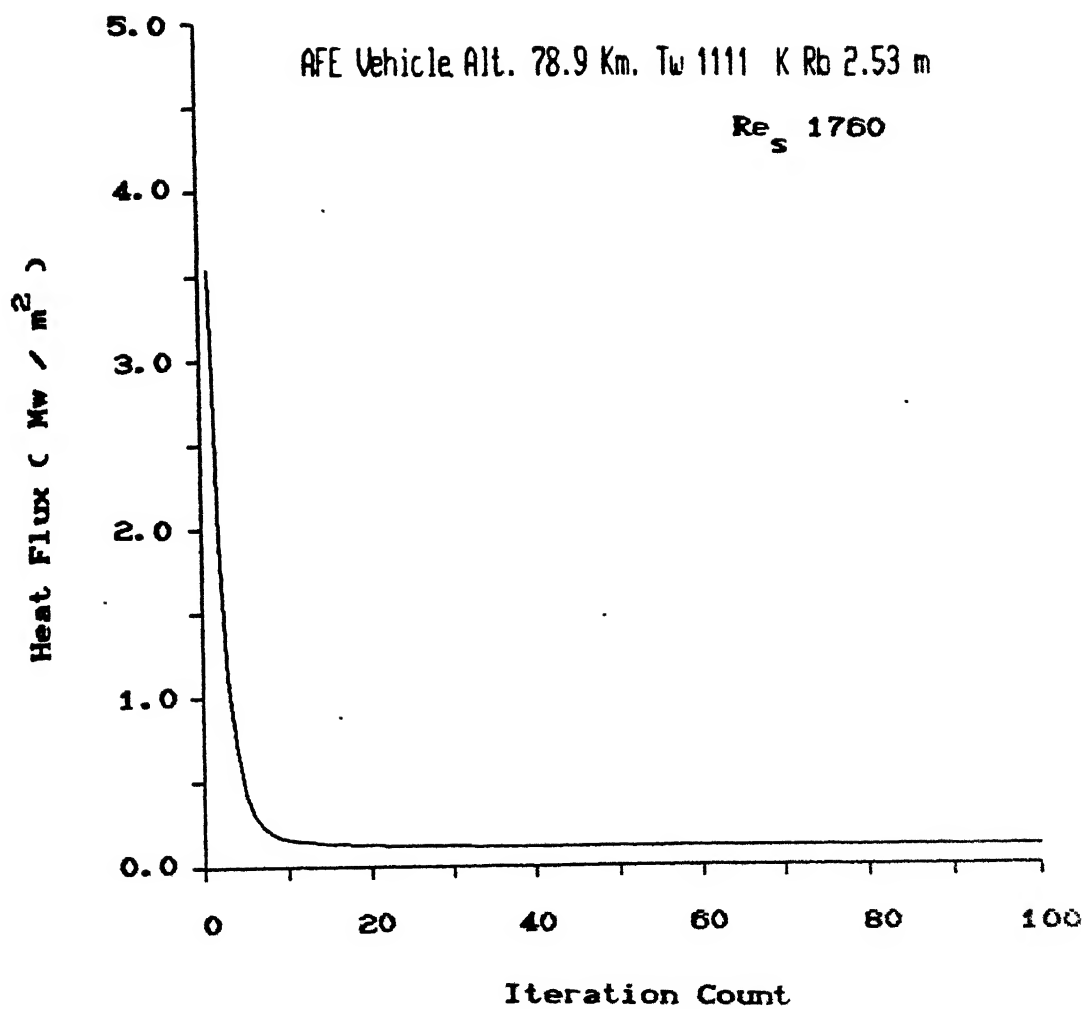


FIG:3.18 CONVERGENCE OF HEAT FLUX FOR AFE VEHICLE

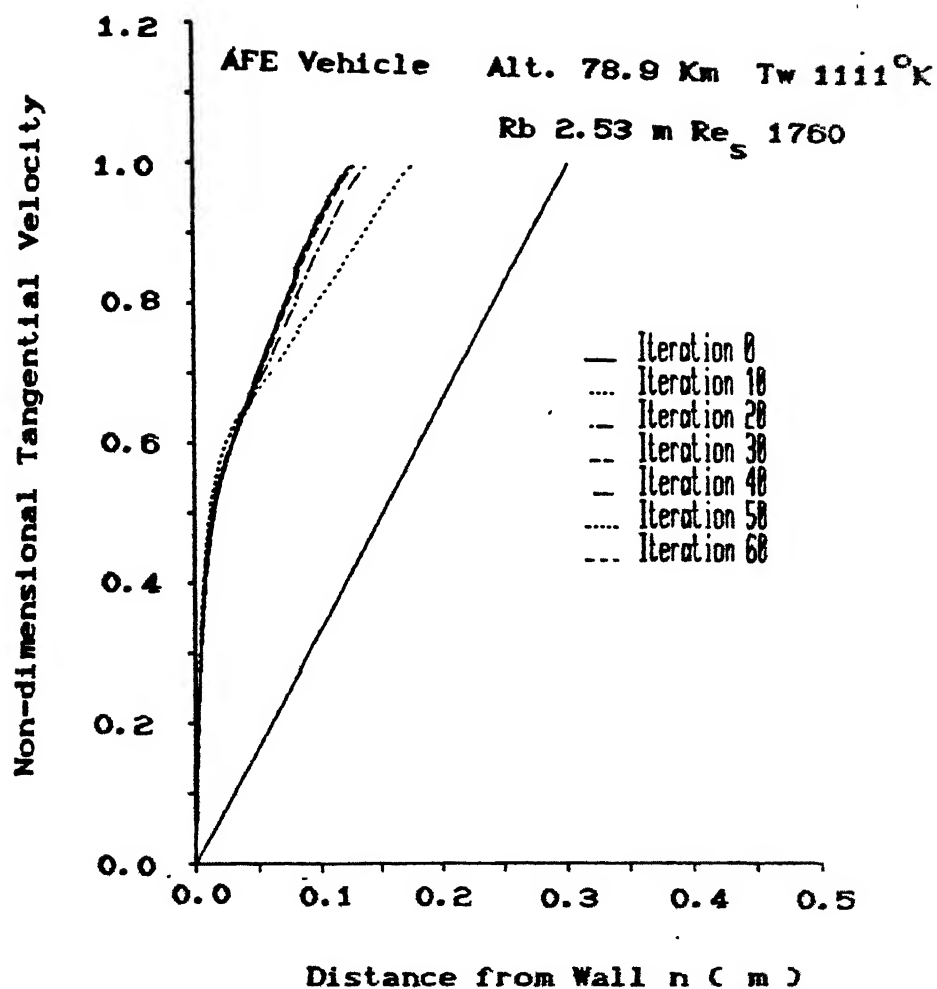


FIG.3.19 EVOLUTION OF NON-DIMENSIONAL TANGENTIAL VELOCITY FOR AFE VEHICLE

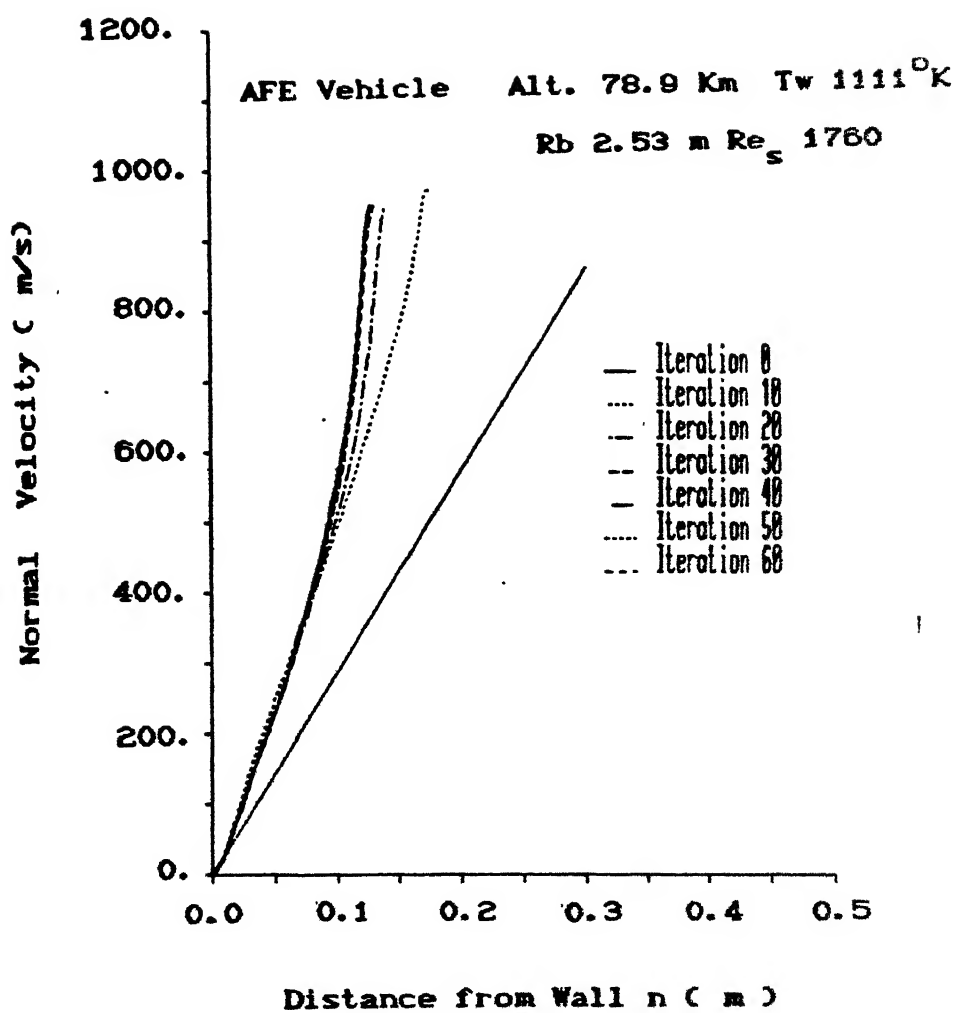


FIG:3.20 EVOLUTION OF NORMAL VELOCITY PROFILE  
 FOR AFE VEHICLE

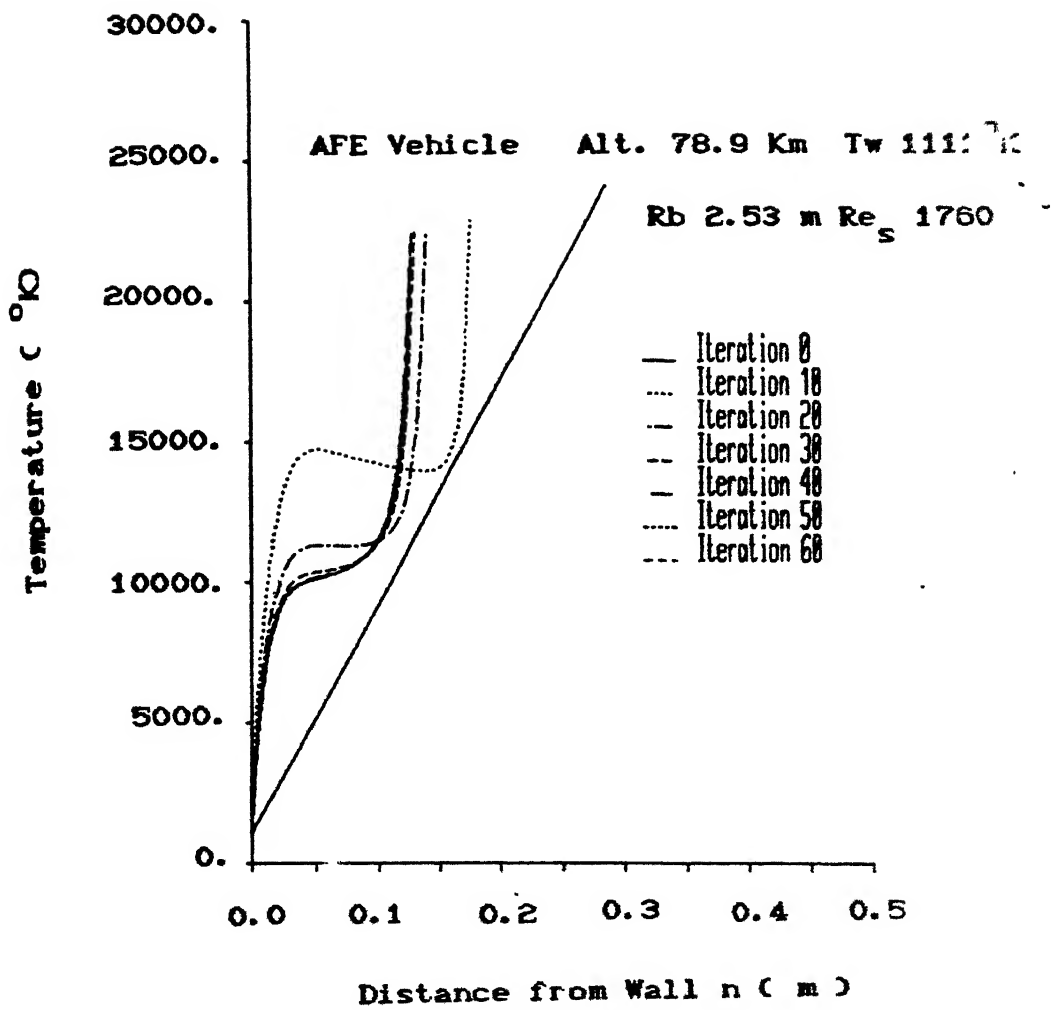


FIG.3.21 EVOLUTION OF TEMPERATURE PROFILE  
FOR AFE VEHICLE

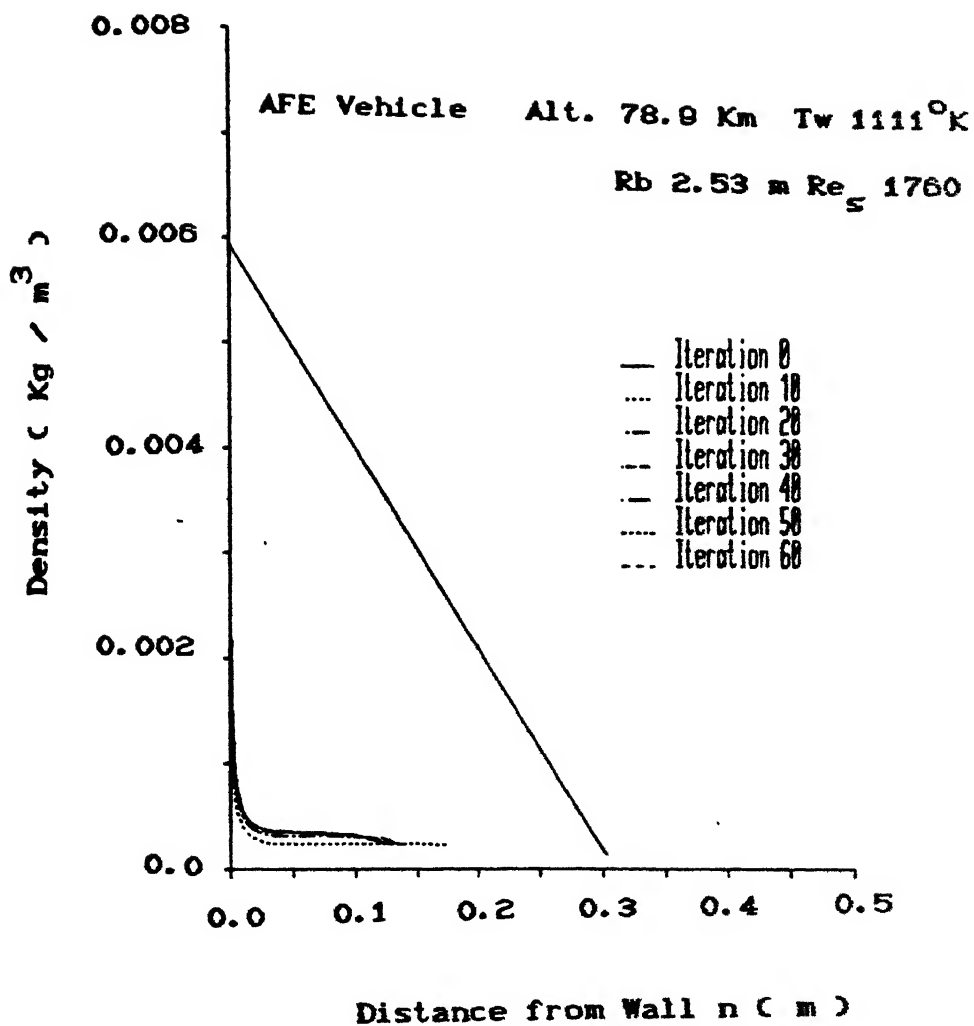


FIG:3.22 EVOLUTION OF DENSITY PROFILE  
FOR AFE VEHICLE



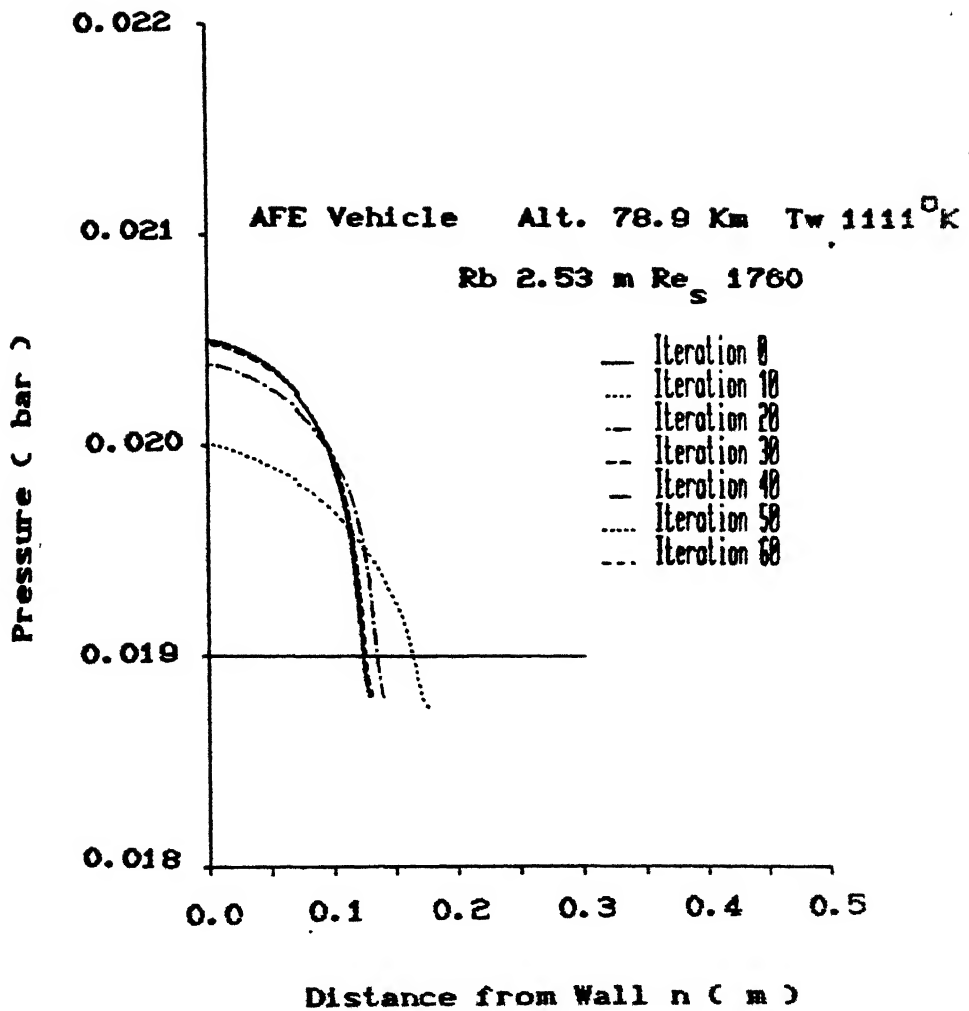


FIG:3.23 EVOLUTION OF PRESSURE PROFILE  
 FOR AFE VEHICLE

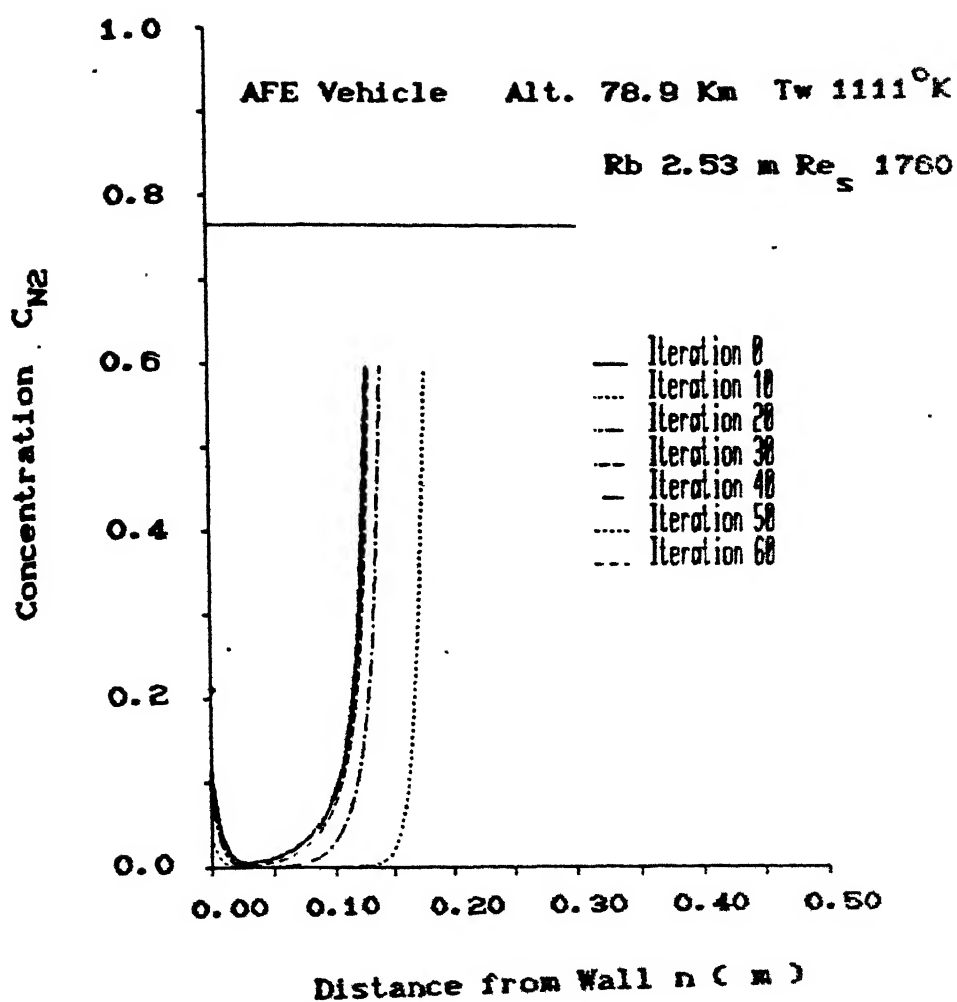


FIG.3.24 EVOLUTION OF CONCENTRATION PROFILE  
OF  $N_2$  FOR AFE VEHICLE

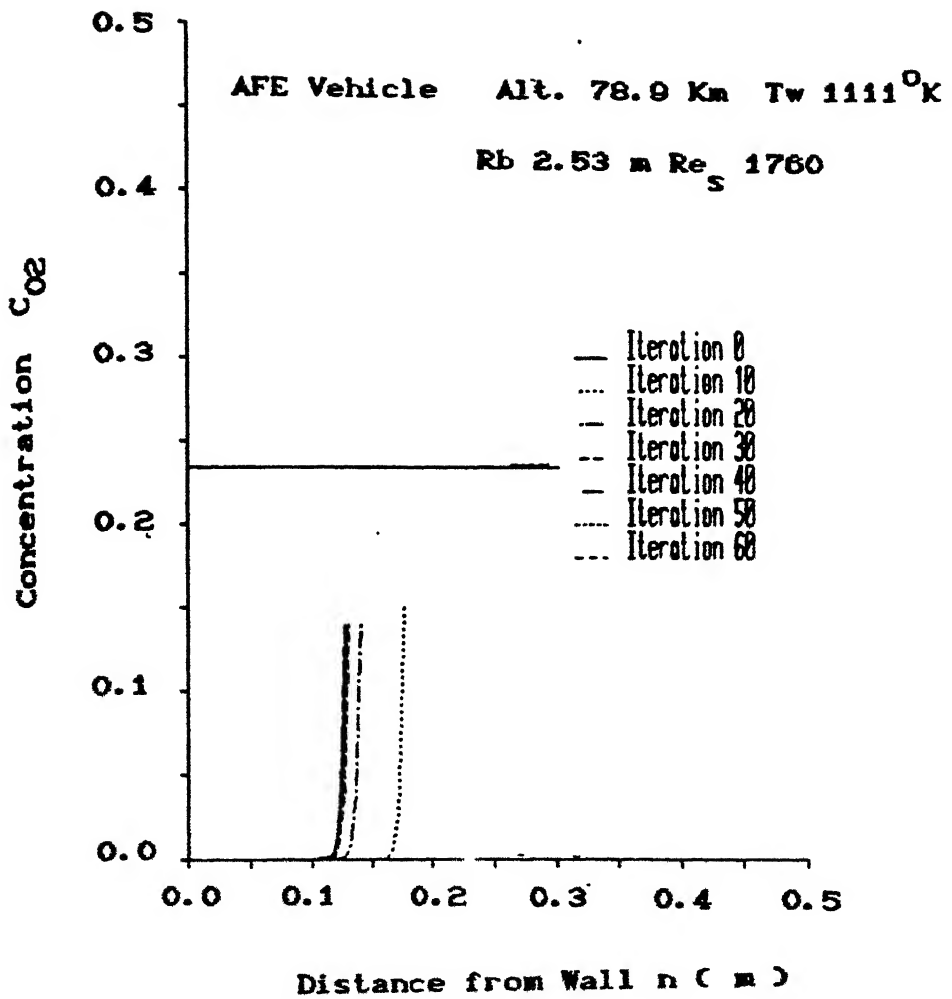


FIG:3.25 EVOLUTION OF CONCENTRATION PROFILE OF  $O_2$  FOR AFE VEHICLE

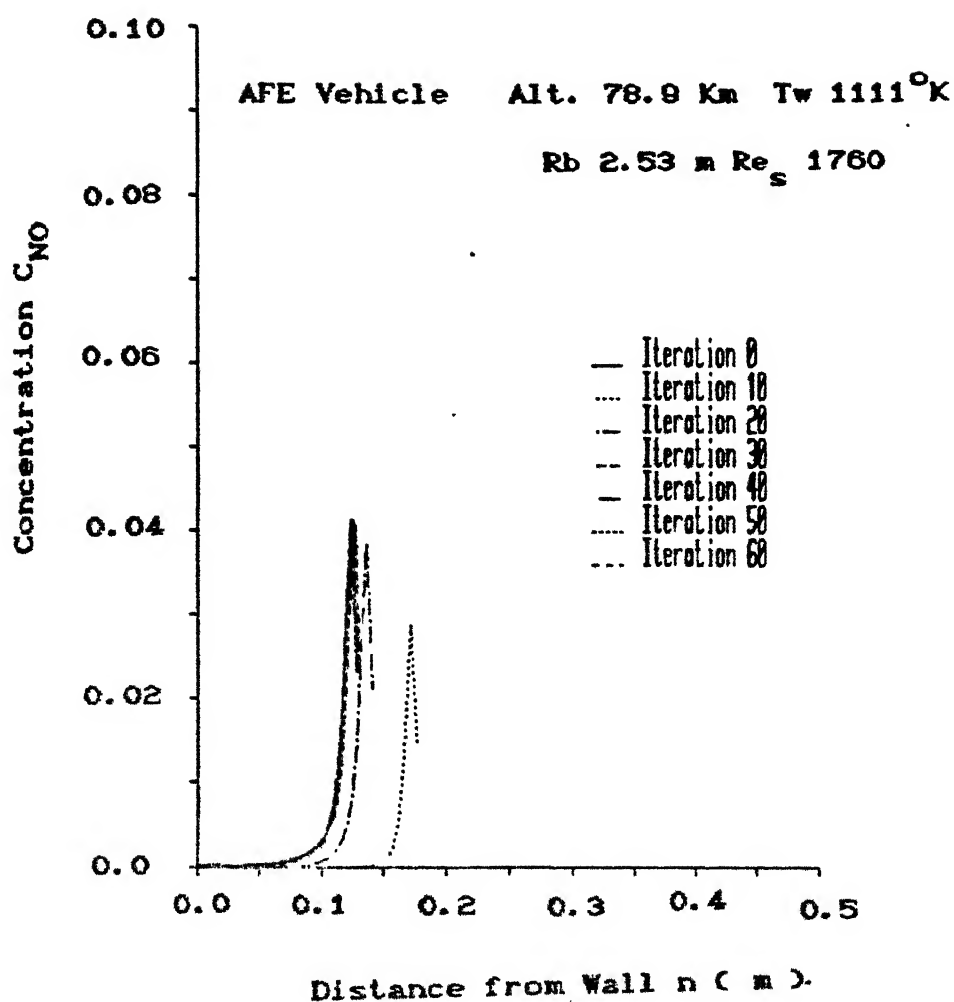


FIG.3.26 EVOLUTION OF CONCENTRATION PROFILE  
OF NO FOR AFE VEHICLE

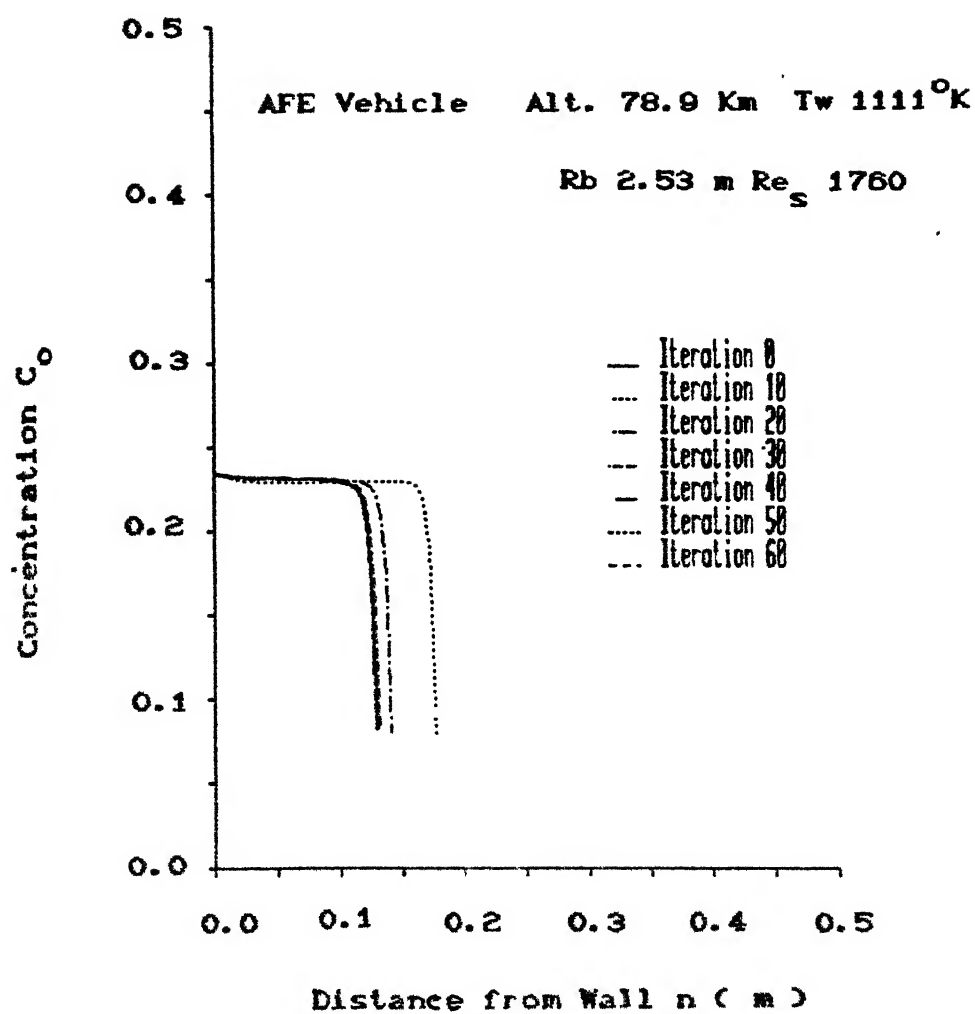


FIG.3.27 EVOLUTION OF CONCENTRATION PROFILE  
OF O FOR AFE VEHICLE

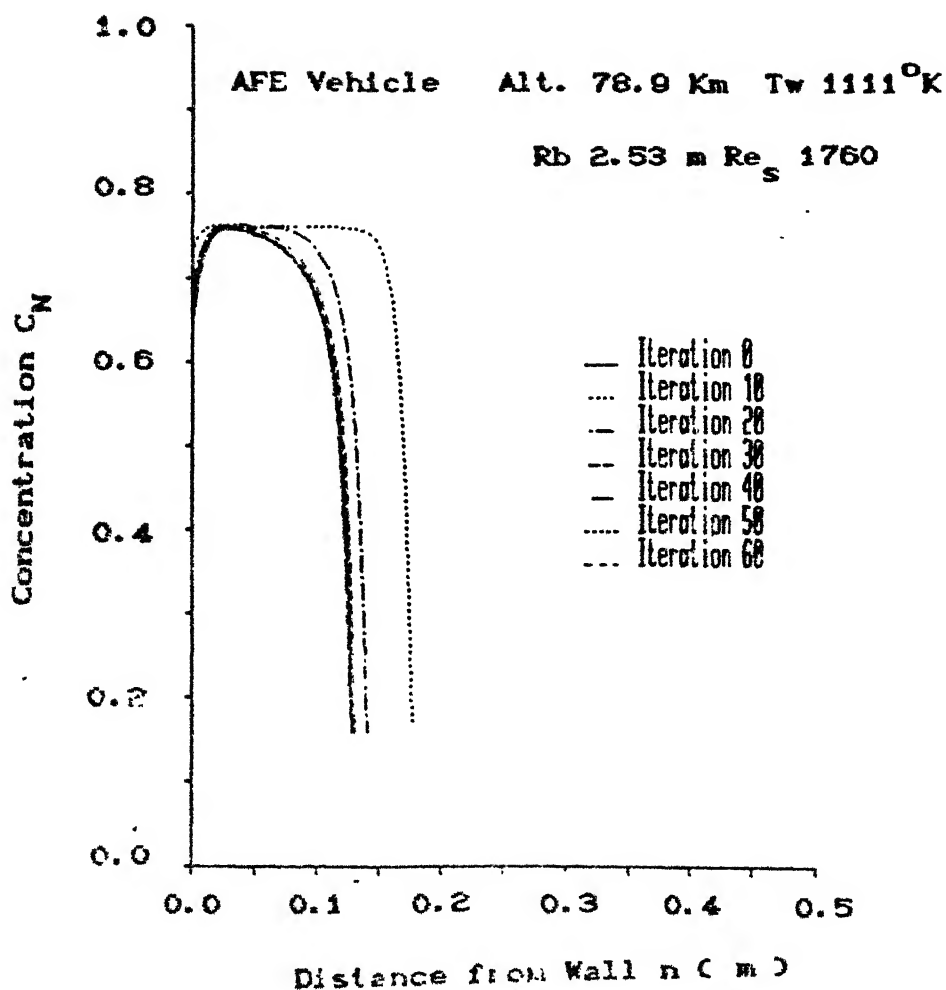


FIG.3.28 EVOLUTION OF CONCENTRATION PROFILE  
OF N FOR AFE VEHICLE

## CHAPTER 4

### RESULTS AND DISCUSSION

#### 4.1 Introduction

Based on the formulation given in Chapter 2 and the numerical procedure described in Chapter 3, a number of computations were performed both for perfect gas and real gas for various free-stream and body conditions. These are discussed in the present Chapter. The basic purpose of these studies was:

- (i) To verify the conjecture regarding the failure of shock layer approach, that is, failure is due to neglecting the terms in the governing equations and not due to the shock layer approach,
- (ii) To compare and bring out the differences between results from full Navier-Stokes equation solution and Shock Layer model ( Davis 1970 ) with truncated Navier-Stokes equations and
- (iii) To address to the problem of numerical problem of numerical convergence of chemically reacting flow solution procedure including the violation of overall mass conservation.

The results are being presented in two parts. Section 4.2 discusses the results for the perfect gas case while section 4.3 presents results for the real gas case.

#### 4.2 Results for Perfect Gas

The computations were performed for both the Shock Layer model ( Davis 1970 ) and for the present model of solving the full Navier-Stokes equation within shock layer. The free stream conditions were as follows:

$$M_{\infty} = 10$$

$$T_w / T_0 = 0.2$$

$$Pr = 0.7$$

$$\gamma = 1.4$$

$$\mu \propto \sqrt{T}$$

$$\theta = \sigma = 1.0$$

The Reynolds number based on reference conditions was varied between 100 and 1. These parameter were chosen so that it is easier to compare the results with reported results of Davis (1970).

#### Comparison of Overall Characteristics

The computations were performed for the freestream conditions described above. For these conditions it is noticed that the two approaches, namely, the present approach of using full Navier-Stokes equations and the Davis-approach of using truncated Navier-Stokes equations, differ both in overall characteristics and detailed flow



field. These are discussed below.

Figure 4.1 presents the variation of shock stand-off distance as a function of Reynolds number for the two methods. It is seen that the behaviour of shock stand-off distance is similar in the two methods. It is noted that initially with decrease in the Reynolds number, the shock stand-off distance is nearly constant, but with further decrease in the Reynolds number, the shock stand-off distance increases. In the beginning, at higher Reynolds number, the viscous effects are confined to the region near the wall and do not influence the shock stand-off distance. Later with the decrease in Reynolds number, viscous effects encompass the entire flow field and result in an increase of shock stand-off distance. It is to be noted here that the shock stand-off distance predictions by full Navier-Stokes equations are lower than the corresponding predictions of the Viscous Shock Layer (VSL) model of Davis (1970). It was expected that the prediction of shock stand-off distance from the full Navier-Stokes equations will be higher than the VSL predictions. The very assumption that the viscous effects are dominant in the region near the body (argument used in order of magnitude analysis) implies that actually viscous effects encompass larger region though the viscous influence may be small in this extra region. The higher prediction of shock stand-off distance by the VSL model is partly the

result of the shock slip condition as applied in the VSL model. The shock slip conditions as applied in the VSL model are inconsistent with the governing equations of the VSL model. Under the shock slip conditions used by Davis, post shock pressure is same as predicted by Rankine-Hugoniot relations. With shock slip conditions, the post shock temperature is lower than the temperature predicted by Rankine-Hugoniot relations, which results in higher post shock density and lower post shock velocity. This lower post shock velocity will result in lower shock stand-off distance. Lower post shock velocity will in actual case result in higher post shock pressure and thus higher post shock density. This will result in further decrease in the shock stand-off distance. The VSL approach of Davis(1970) does not account for this change in the post-shock pressure due to the shock slip conditions and thus predicts higher shock stand-off distance.

Figure 4.2 gives the variation of shock stand-off distance for the case of hot wall ( $T_w = T_0$ ) with free stream conditions remaining the same. It is noted here that there is a continuous increase in shock stand-off distance with decrease in Reynolds number. In this case due to higher wall temperature, the viscosity is higher and viscous effects influence a larger region of the flow field even at higher Reynolds number.

Figure 4.3 and 4.4 show the variation of post shock pressure and post shock density respectively with the Reynolds number. It is noted that the present computations predict higher values of post shock pressure and post shock density as compared to the VSL computations. This behaviour is the outcome of the use of incorrect shock slip condition in case of the VSL solution as explained earlier.

Figure 4.5 shows the variation of pressure at the base of the shock layer, that is pressure of gas at the surface of the body, with the Reynolds number. It is noticed that at higher Reynolds number, present computations predict nearly constant base pressure with decreasing Reynolds number, but with further decrease in the Reynolds number base pressure increases. This phenomenon is not observed in case of the VSL solutions where the base pressure continuously decreases with decrease in Reynolds number. However, wall pressure initially decreases with Reynolds number and with further decrease in Reynolds number, the wall pressure increases (Figure 4.6). Wall pressure is computed from the base pressure using the shock slip condition for the pressure. This phenomenon of increasing wall and base pressure with decreasing Reynolds number is noticed in case of the Navier-Stokes solution only and not in case of the VSL solution. However, from experimental results (Potter and

Bailey 1964, Sherman 1953) it is known that wall pressure does initially decrease with decreasing Reynolds number and later increases with further decrease in Reynolds number. This clearly shows that full Navier-Stokes equation solution procedure is superior to the VSL model in the low Reynolds number regime.

It was stated earlier that the shock slip conditions used in case of the VSL solution are inconsistent with the governing equations and use of proper shock slip conditions will lead to increased post shock pressure and thus overall higher pressure in the shock layer. In order to determine whether the continuous decrease in wall pressure is due to inconsistent shock slip condition or it is inherent in the governing equations, computations were performed for VSL model with shock slip conditions consistent with the governing equations of the VSL model. Figure 4.7 shows the variation of wall pressure with Reynolds number as obtained from solution of Navier-Stokes equations and VSL equations with consistent shock slip conditions. This figure also shows that wall pressure continuously decreases with decreasing Reynolds number for VSL solution even with correct shock slip conditions. This shows that correct behaviour of wall pressure can not be predicted within the framework of VSL model and it is necessary to make use of full Navier-Stokes equations within the shock layer model to get the correct behaviour

of the wall pressure with Reynolds number.

Figure 4.8 and 4.9 show the variation of heat transfer coefficient with Reynolds number for cold wall case ( $T_w = 0.2 T_0$ ) and hot wall case ( $T_w = T_0$ ) respectively. For the case of cold wall case usual definition of the heat transfer coefficient based on temperature differential has been used while for the case of hot wall heat flux is nondimensionalised with respect to kinetic energy of the free stream as the temperature differential is zero. Figure 4.8 shows that the Navier-Stokes equations predict higher heat flux as compared to the VSL model. This is basically due to smaller shock stand-off distance leading to higher temperature gradient at the wall and difference in the temperature profile itself. This figure also shows the results of Fay and Riddell (1958) and Lees (1956). It is seen that for higher Reynolds number all the methods give results close to one another except Lees' method which does not account for variation of transport properties of the gas due to change in the wall temperature. With reduction in Reynolds number, both the numerical methods namely the present method of solving full Navier-Stokes equations and the VSL model predict higher heat flux than Fay and Riddell's method. This increase in heat flux can be attributed to the influence of the post-shock vorticity. Later on with further decrease in Reynolds number, the surface slip

dominates and heat flux predictions by numerical methods are lower in comparison to Fay and Riddell (1958) predictions. Figure 4.9 shows the variation of heat transfer coefficient with Reynolds number for the case of hot wall. It is noticed that Navier-Stokes equations predict positive heat flux to the wall that is heating of the wall for lower Reynolds number while VSL model predicts negative heat flux that is cooling of the wall for the entire range of Reynolds number. This implies that according to the solution of the Navier-Stokes equations the recovery temperature is greater than the stagnation temperature of the free stream. In case of VSL model, as heat flux is always negative, it implies that recovery temperature is always less than stagnation temperature. It has been noted from experimental data (Hickman and Giedt 1963) that at low Reynolds numbers, the recovery factor increases beyond unity. This shows that in order to get the correct behaviour of heat flux with Reynolds number, it is necessary to consider the full Navier-Stokes equations instead of the truncated Navier-Stokes equations.

#### Comparison of Structure of Flowfield

Figures 4.10 through 4.13 show the profiles of the tangential velocity, temperature, pressure and density respectively for the low Reynolds number case. These

figures also give the corresponding profiles for VSL model. It is seen from Figures 4.10 and 4.11 that the variation of tangential velocity and temperature across the shock layer are similar in nature, but gradient at the wall is higher in the case of Navier-Stokes equations solution. This results in higher skin friction and higher value of heat flux.

Figure 4.12 shows the variation of pressure across the shock layer. It is seen that apart from quantitative difference in pressure, there is a qualitative difference in the variation of pressure in the shock layer. Navier-Stokes equations not only predict higher post-shock pressure but also show continuous increase in pressure as one moves closer to the wall while in case of the VSL model, pressure is almost constant across the shock layer. This feature of pressure being almost constant across the shock layer is essentially a feature of the boundary layer and results from the fact that in the VSL equations all the viscous terms have been dropped from the normal momentum equation. Figure 4.13 shows the variation of density across the shock layer. As expected, the behaviour of the density is different in the two models in view of the difference in the pressure profiles.

Figures 4.14 through 4.17 show the profiles of tangential velocity, temperature, pressure and density respectively at Reynolds number of 100. It is seen from

Figures 4.14 and 4.15 that at this higher Reynolds number, tangential velocity and temperature profiles are almost identical for the present computations and the VSL model. It is due to the fact that at higher Reynolds number the terms neglected in VSL model contribute very little. However, Figure 4.16 shows that even at this Reynolds number, pressure profiles are different in the vicinity of the wall. This is due to the viscous terms dropped in case of the VSL model in the normal momentum equation. The difference in the density profile near the wall is not visible due to the scale (Figure 4.17). At this Reynolds number, post-shock pressure, temperature and tangential velocity and shock stand-off distance are the same from the two approaches.

#### Comparison with Experimental and other Theoretical Results

Computations were carried out for the VSL model and the present method in order to compare them with available experimental and other theoretical results. Russel (1968) measured the density profiles in a rarefied stream. Figure 4.18 shows the comparison of density profiles from these two methods with the experimental data of Russel for the cold wall case ( $T_w = 0.26 T_o$ ). It is noticed that the density profile computed from the full Navier-Stokes equations is in much better agreement with experimental data of Russel than the profile from VSL equations. Figure



4.19 shows density profile for the case of hot wall ( $T_w = T_o$ ). Once again it is seen that the density profile as predicted by the Navier-Stokes equations is much closer to the experimental results.

Figures 4.20 and 4.21 show the comparison of density and temperature profiles with Monte Carlo results of Vogenitz and Takata (1970). For this analysis, Prandtl number of the gas has been taken to be  $2/3$  which is consistent with the hard sphere model used for the Monte Carlo simulation. Figure 4.20 shows the comparison of the density profiles. The figure also includes the results of Levinsky and Yoshihara (1962). It is seen that the present computations agree well with Monte Carlo results while Levinsky and Yoshihara underpredict the density in comparison to the Monte Carlo results. However, Figure 4.21 shows that present results are closer to results of Levinsky and Yoshihara and both predict higher temperature in comparison to Monte Carlo results.

Kao (1964b) computed the hypersonic flow in the stagnation region of a blunt body using the concept of local similarity. Figures 4.22 and 4.23 show the comparison of profiles for the case studied by Kao. It is seen from Figure 4.22 that the present computations predict smaller value of shock stand-off distance in comparison to results of Kao. This figure also shows the hypersonic merged layer profile (Jain and Prabha 1983). It

is seen that though the normal velocity profiles are reasonably close to one another from three approaches, the behaviour of tangential velocity is quite different in case of the merged layer solution. It is due to the fact that in case of merged layer, the boundary condition is being applied at the freestream while in other two methods it is being applied at the shock. In case of tangential velocity, the boundary condition is same in all the three methods, namely  $u = 1$ , while for normal velocity, temperature et cetera, it is different in these methods. Figure 4.23 shows the variation of temperature and pressure in the flow field. It is seen that temperature profile agrees well from these three methods, but pressure profiles differ. This difference in the pressure profile is because Kao has used inviscid pressure distribution to evaluate second order derivative of pressure for integrating the continuity equation. In case of merged layer solution, this difference in the pressure profile is due to the effect of shock transition zone. It seems that the influence of the shock transition zone is more pronounced on pressure than on temperature or normal velocity.

Computations were performed for the conditions used by Boylan (1971) in the experimental measurement of heat transfer coefficient. Figure 4.24 shows the variation of heat transfer coefficient with parameter  $\epsilon = 1/\sqrt{Re}$  and

comparison with experimental data of Boylan. VSL results for the same conditions are also presented. It is seen that present heat transfer predictions are closer to the experimental data even for lower Reynolds number, while VSL results deviate from the experimental data in the lower Reynolds number regime. This again shows that the full Navier-Stokes equation model is better than VSL model for heat transfer predictions.

Figure 4.25 shows the influence of rarefaction on the heat transfer coefficient. In this case, computations were performed for  $M_\infty = 20$ . The data is compared against the experimental data of Whittliff and Wilson, as given by Vidal and Whittliff(1963). It is seen that for rarefaction parameter as low as 0.1, the present computations yield results which are quite close to the experimental data. Figure 4.26 shows the similar comparison against more recent experimental data of Coleman et al. (1977). In this case also it is seen that the present computations give good results for rarefaction parameter even below 0.1.

Figure 4.27 shows the variation of the recovery factor with post shock Reynolds number. This has been compared with the experimental data of Hickman and Giedt (1963). This figure also shows the recovery factor as computed from VSL model. It is seen that the recovery factor computed from present model reflects the actual behaviour quite accurately while the recovery factor

computed from VSL model does not give even the qualitative behaviour correctly.

### Influence of Surface Temperature on Heat Flux

Computations were performed to estimate the heat transfer coefficient using the present approach for  $M_\infty = 5, 10, 15$  and  $20$  and for wall temperature ratio  $T_w/T_o = 0.2, 0.4, 0.6$  and  $0.8$ . Figure 4.28 shows the variation of heat transfer coefficient as function of Cheng's rarefaction parameter  $K_r^2$ . The figure shows that, for a given surface temperature, Mach number variation from  $5$  to  $20$  has negligible effect on the heat transfer coefficient. This is an expected behaviour in view of the Mach number independence principle applicable for hypersonic flow. However, it is noticed that there are distinct curves for different wall temperatures. These curves tend to collapse into single curve at higher values of  $K_r^2$ . From this it can be concluded that Cheng's rarefaction parameter fails to completely correlate the heat transfer behaviour as the level of rarefaction increases. Temperature of the surface also needs to be taken into account as already noted by Jain and Kumar (1986). This is despite the fact that rarefaction parameter  $K_r^2$  is a function of wall temperature through the viscosity and Chapman-Rubisen constant.

Usually surface slip results in reduction of heat flux to the surface. Davis (1970) has shown the influence

of both surface slip and shock slip on the heat transfer coefficient using VSL equations. Both of these effects tend to decrease the heat flux to the surface. Jain and Adimurthy (1974), who used a full Navier-Stokes merged layer model reported the increase in heat flux due to surface slip. In order to find out whether this phenomenon of increasing heat flux is associated with Navier-Stokes equations, computations were performed for the free stream and surface conditions used by Davis. It was found that influence of surface slip was to decrease the heat flux even in the present model of Navier-Stokes solution. In order to resolve this problem, computations were performed for different surface temperatures because surface temperature conditions were different in case of Jain and Adimurthy. Figure 4.29 shows the variation of heat transfer coefficient with and without surface slip for two different Reynolds numbers against wall temperature. It is seen that surface slip increases the heat flux for lower surface temperatures. But at relatively higher surface temperatures, surface slip leads to reduction in heat flux. Surface slip reduces the temperature gradient at the wall (Figure 4.30), but at the same time increases the temperature at the base of shock layer leading to increased thermal conductivity. At lower surface temperatures this increase in thermal conductivity in combination with the reduction in temperature gradient

results in an increase in the heat flux. At higher surface temperatures this increase in thermal conductivity is not sufficient to compensate for the reduction in temperature gradient.

#### 4.3 Results for Chemically Reacting Gas

Computations were performed for a chemically reacting gas with variable specific heat. The free stream conditions and vehicle parameters are representative of Shuttle orbiter nose during re-entry. These conditions and parameters are given in Table 4. The computed results are compared with the merged layer results ( Gupta and Simmonds 1986) and DSMC results ( Moss and Bird 1985). In these computations Prandtl number and Lewis number were taken to be constant as in case of the merged layer analysis. The computations were performed for non-catalytic wall case which is more realistic physical situation for Shuttle.

Figure 4.31 shows the comparison of heat transfer coefficient variation with Cheng's rarefaction parameter. It is seen that present results agree well with the merged layer results and DSMC results except for 109 km altitude case. This difference in the heat transfer rates between present formulation and merged layer formulation at higher altitude is possibly due to the neglect of tangential transport effects in the shock transition zone which is

approximately 70% of the shock layer thickness even at 92.35 Km altitude according to the merged layer computations. Earlier, similar results (Jain and Kumar 1987) were computed for these conditions for perfect gas. It was noticed that the computed results deviated from the DSMC results at an altitude of 104 Km. For present computations the agreement is good upto 109 Km. For 104 Km altitude, the flow is frozen and it was expected that perfect gas results will hold good. This deviation is caused by variable specific heat of the gas which is not accounted for in the perfect gas computations.

Figure 4.32 shows the variation of temperature across the shock layer for 92.35 Km altitude case. The profile has been compared with merged layer profile and DSMC profile. It is seen that within the shock layer, the profiles are in good agreement with one another.

Figures 4.33 through 4.37 show the variation of mass concentration across the shock layer for various species. The profiles have been compared with corresponding profiles for merged layer and DSMC results. It is seen that in general, present profiles are in better agreement with merged layer profile.

Figure 4.33 shows the variation of mass concentration of molecular nitrogen. It is seen that at the edge of the shock layer the concentration is same for both the present method and the merged layer solution. There is good

agreement in the profile across the shock layer between present predictions and merged layer predictions. The continuum methods predict higher concentration of molecular nitrogen as compared to DSMC results.

Figure 4.34 shows the variation of mass concentration of molecular oxygen across the shock layer. Once again it is noticed that there is a good agreement in the profiles predicted by present computations and merged layer solution and these concentrations are higher than the concentrations predicted by DSMC. One noticeable aspect of this figure is that at the wall the concentration of molecular oxygen is 0.025 for continuum methods while for DSMC it is virtually zero. This implies that there is complete dissociation of molecular oxygen at about 2000°K. This is because near the wall, the concentration is controlled by diffusion and not by chemical reaction.

Figures 4.35, 4.36 and 4.37 show the variation of mass concentration of atomic oxygen, atomic nitrogen and nitric oxide respectively. It is seen that there is good agreement between present results and merged layer results while DSMC predictions are higher than these concentrations. This difference in concentration levels of various species as predicted by continuum methods and DSMC method can be attributed to difference in dependence of viscosity and chemical reaction rates on temperature as used in two different methods. It is also to be noted that



DSMC results predict higher concentrations of atomic species and lower concentrations of molecular species. Possibly it is due to inadequate accounting of multi-body collision processes, which are mainly responsible for recombination reactions.

It is noticed from figures 4.33 to 4.37 that various concentrations from the two continuum methods, namely the shock layer solution using full Navier-Stokes equations and merged layer solution are in good agreement. For this altitude, the merged layer computations show that shock transition zone is approximately 70% to 80% of the shock layer thickness. Even though, this thickness is comparable to the shock layer thickness, still there is a good agreement in the post shock concentrations for the two methods. It shows that the effect of chemical reactions in the shock transition zone on the mass concentrations of various species is not very significant.

Figures 4.38 and 4.39 show the temperature and mass concentration profiles for the free stream conditions corresponding to 104 Km altitude. It is observed from Figure 4.38, showing the temperature profile, that present method predicts higher temperature across the shock layer in comparison to the merged layer and DSMC results. This higher temperature prediction by present method is possibly due to shock conditions, which assume thin shock and thus neglect transfer of momentum and energy parallel

to the shock. This effect can be significant here as the shock transition zone is approximately 6 times the shock layer thickness according to the merged layer computations. Figure 4.39 shows the concentration profile of the molecular nitrogen and molecular oxygen. It is noticed that the concentrations are constant across the shock layer. This implies that flow is frozen at this altitude for the conditions used in the analysis.

#### Influence of Variable Transport Properties

In the results presented so far, Prandtl number and Lewis number were assumed to be constant. In order to study the influence of the variation of Prandtl number and Lewis number on the behaviour of the flow parameters, computations were carried out for Shuttle conditions considering variable Prandtl number and Lewis number. For Lewis number estimation, binary diffusion of atomic oxygen into molecular nitrogen was considered as suggested by Moss (1971). Figure 4.40 shows the variation of heat flux with Cheng's parameter for different flight conditions. The mixture properties were evaluated using Armaly and Sutton (1980,1981) correlation. It is seen that the use of variable Lewis number in the shock layer as a function of temperature and composition does not affect the heat flux appreciably. On the other hand, use of variable Prandtl number in the shock layer has significant effect on the heat flux. For 92.35 Km altitude case the heat flux

increases by approximately 20% . Similar computations were carried out using Wilke's correlation also for the mixture properties. Figure 4.41 shows the variation of heat flux with Cheng's parameter for this case. In this case it is noticed that the use of variable Prandtl number and Lewis number in the shock layer has no appreciable effect on the heat flux to the wall. Table 5 shows the heat flux values for the various cases considered in this study. In case Armaly and Sutton correlation is used, the increase in heat flux is associated with the increased value of thermal conductivity.

Figures 4.42 through 4.49 show the variation of different flow variables across the shock layer for the two mixture property correlations. The profiles agree well for the two cases except for marginal quantitative changes in the values of the flow variables. Figure 4.42 shows the variation of the temperature across the shock layer. It is seen that use of Armaly and Sutton correlation predicts higher temperature at the wall and lower temperature at the shock in comparison to the corresponding predictions for Wilke's correlations. This is because Armaly and Sutton correlation predict higher values of thermal conductivity at higher temperature and thus causes more thermal diffusion in the post shock region leading to lower temperature there. This heat transfer leads to higher temperature near the wall.

Figure 4.43 shows the concentration profile for molecular nitrogen. This figure shows that use of Armaly and Sutton correlation predicts the higher concentration of molecular nitrogen in the shock layer than the corresponding predictions for Wilke's correlation. This is due to lower temperature predictions in case of Armaly and Sutton correlation and thus lower rate of dissociation. Near the wall, where the gas temperature is not high enough for dissociation to take place, and flow is controlled by diffusion resulting in significant concentration of N and lower concentration of  $N_2$ . Figure 4.44 shows the concentration profile for molecular oxygen. Here it is noticed that use of Armaly and Sutton and Wilke's correlation give similar values of molecular oxygen concentration. This is due to fact that in the entire shock layer except near the wall, the temperature is high enough for oxygen molecules to dissociate. Thus both the methods give similar values of concentration of O and  $O_2$ . Near the wall, the concentration is governed by the diffusion.

Figures 4.45, 4.46, 4.47 and 4.48 show the concentration profiles for atomic oxygen, atomic nitrogen, nitric oxide and ionised nitric oxide. It is seen that use of Wilke's correlation in the computations leads to prediction of higher concentration of N and  $NO^+$  than the corresponding predictions for Armaly and Sutton

correlation. This is the consequence of higher temperature in the shock layer for the case when Wilke's correlation is used.

Figure 4.49 shows the variation of Prandtl number in the shock layer. It is seen that use of Wilke's correlation leads to higher values of Prandtl number throughout the shock layer. This is mainly due to underprediction of thermal conductivity when Wilke's correlation is used and partly due to change in local concentration of various species. This change in thermal conductivity causes increase in heat flux to the surface when Armaly and Sutton correlation is used. Table 6 gives the comparison of wall values and post shock values of different flow variables for the two cases.

#### Influence of Mach Number on Heat Transfer to Wall

In hypersonic flow, according to Mach number independence principle, the heat transfer coefficient is independent of Mach number. It is true for the case of perfect gas as already observed in figure 4.28. However, in case of chemically reacting gas flows, Mach number independence principle may not hold. Higher free stream velocity implies higher post shock temperature and thus higher temperature in the shock layer. The reaction rates being dependent on the actual temperature, chemical reactions (dissociation, ionisation et cetera) will proceed at different rates for different free stream

velocities and thus result in different heat flux levels. This variation of velocity will not result in any change in Reynolds number based on post shock temperature or based on reference conditions used in the present work if the square-root viscosity law is used. However, in actual case, Reynolds number based on reference conditions or based on post shock conditions will not be constant but change slightly with velocity as square-root viscosity law is not strictly valid.

In order to study the influence of free stream velocity on heat transfer coefficient, computations were carried out for Shuttle conditions with free stream velocity varying between 6 Km/sec to 10 Km/sec. It should be noted here that for higher free-stream velocity, the seven species air model may not be appropriate and better model may be necessary. Figure 4.50 shows the variation of heat transfer coefficient against free stream velocity for different altitudes. It is seen that for altitude of 104.93 Km and 109.75 Km, where flow is frozen, heat transfer coefficient decreases with increase in free stream velocity. Heat transfer coefficient decreases with increase in free stream velocity for 92.35 Km altitude while for altitude 99.49 Km heat transfer coefficient increases with increase in free stream velocity. In case of 104.93 Km and 109 Km altitude, the flow is frozen and one might expect that heat transfer coefficient will

remain constant with free stream velocity as Mach number independence principle should apply in these cases. The variation in heat transfer coefficient is due to the temperature dependence of specific heat. The variable specific heat leads to lower non-dimensional temperature in the shock layer and thus lower heat transfer coefficient. Figure 4.51 shows the variation of heat transfer coefficient against Reynolds number based on reference conditions. It is seen that heat transfer coefficient varies very sharply with Reynolds number as there is not much change in Reynolds number with change in free stream velocity. This leads one to conclude that free stream velocity and thus the actual temperature in the shock layer should be accounted for while considering the Reynolds number parameter in case of chemically reacting flows.

In order to estimate the range of the Reynolds number for which present scheme converges for chemically reacting flow, computations were carried out for AFE trajectory. The trajectory details are given in Table 7. It should be noted here that at these high free-stream velocities, seven species model for the air is not likely to represent the actual situation for non-equilibrium flow. Moreover radiation is likely to influence the flow-field significantly. Nevertheless, the computations were performed to assess the capability of the present scheme.

Figure 4.52 shows the variation of stagnation point heat transfer coefficient with post shock Reynolds number for AFE vehicle. The computations converged without any problem for the entire trajectory range, which corresponds to

$$3 \leq Re_s \leq 1760$$

This upper limit of  $Re_s$  1760 is achieved for the present scheme as against of  $Re_s$  500 for VSL scheme (Moss 1971). The details regarding the convergence of various surface quantities and profiles for higher Reynolds number case have already been discussed in Chapter 3.

Figure 4.52 shows the variation of stagnation point heat transfer coefficient with post shock Reynolds number for AFE vehicle. This figure shows the heat transfer coefficient for frozen flow and both for catalytic and non-catalytic wall in case of non-equilibrium flow. It is observed that heat flux is lowest in case of non-catalytic wall while it is highest for catalytic wall. In case of non-equilibrium flow, higher temperature induces dissociation and ionisation of various species. This process absorbs heat and lowers the temperature of the gas in the shock layer. This lower temperature results in lower heat flux. However, in case of catalytic wall, all the ionised and dissociated species combine to give molecular species near the wall and release the energy



associated with dissociation and ionisation. This leads to increased heat flux to the wall.

Figure 4.53 shows the variation of wall pressure with post shock Reynolds number for AFE vehicle. It is observed that non-equilibrium flow predicts higher wall pressure in comparison to frozen flow. Due to chemical reactions, various species dissociate and ionise. This reduces the molecular weight of the gas resulting in increased pressure in case of non-equilibrium flow.

It was stated earlier that present computations converged for AFE vehicle trajectory at an altitude of 78.9 Km corresponding to post shock Reynolds number of 1760. As this Reynolds number is reasonably high, it was expected that flow may be in chemical equilibrium. In order to check whether or not present computations capture the equilibrium composition, the same was estimated corresponding to the pressure and temperature profiles obtained from the non-equilibrium computations. Figures 4.54 to 4.59 show the concentration profiles of  $N_2$ ,  $O_2$ ,  $NO$ ,  $O$ ,  $N$  and  $NO^+$  respectively as obtained by non-equilibrium computations and their comparison with corresponding equilibrium concentration for the pressure and temperature of the non-equilibrium flow. It is observed that in most of the shock layer region, equilibrium and non-equilibrium concentrations are identical. These concentrations differ near the wall and

near the shock. At the wall, non-equilibrium computations give higher values of atomic species and lower values of molecular species concentrations in comparison to equilibrium values. This is due to the fact that in case of non-equilibrium computations, concentrations near the wall are controlled by diffusion while in case of equilibrium, concentrations are controlled by chemical kinetics. Near the shock, the difference in concentrations is due to the boundary conditions to be satisfied by the concentrations at the shock. The difference in the concentration profile near the wall contributes to the heat flux to wall. It is due to energy transport associated with diffusion of species. It implies that even if the flow is mostly in chemical equilibrium and non-equilibrium computations do capture equilibrium concentration profiles as seen in figures 4.54 to 4.59, the equilibrium and non-equilibrium heat flux to the wall will differ. This difference in the heat flux will grow with increase in the Reynolds number as it will result in sharper temperature gradient and therefore concentration gradient near the wall. Moreover, when equilibrium code is run, this difference in concentrations near the wall and the shock will influence flow field in the entire shock layer and the heat flux to the wall.

TABLE 4

Free Stream Conditions and Vehicle Parameter

## Free Stream Conditions

Alt. Km	Density Kg/m <sup>3</sup>	U <sub>∞</sub> <sup>*</sup> Km/sec	T <sub>∞</sub> <sup>*</sup> °K	Mole Fractions		
				XN <sub>2</sub>	XO <sub>2</sub>	XO
92.35	2.184e-6	7.50	180.0	.783	.217	.000
99.49	5.906e-7	7.50	190.0	.783	.217	.000
104.93	2.457e-7	7.47	223.0	.782	.153	.065
109.75	1.146e-7	7.47	249.0	.771	.123	.106

## Vehicle Parameter with Altitude

Altitude Km	Nose Radius R <sub>b</sub> m	Wall Temperature °K
92.35	1.296	1043.0
99.49	1.362	800.0
104.93	1.362	560.0
109.75	1.362	420.0

TABLE 5

Influence of Property Variation on Heat Flux

## (a) Use of Armaly and Sutton Correlation

Heat Flux in Kw/m<sup>2</sup>

Pr	Le	Altitude (Km)			
		92.35	99.49	104.39	109.0
0.7	1.4	92.92	47.65	30.08	19.20
0.7	Le(T)	92.10	47.64	30.08	19.21
Pr(T)	1.4	110.00	51.00	32.80	19.70
Pr(T)	Le(T)	109.28	51.46	32.80	19.73

## (b) Use of Wilke's Correlation

Heat Flux in Kw/m<sup>2</sup>

Pr	Le	Altitude (Km)			
		92.35	99.49	104.39	109.0
0.7	1.4	90.20	47.10	29.86	19.10
0.7	Le(T)	89.80	47.17	29.86	19.10
Pr(T)	1.4	90.56	47.20	30.16	19.11
Pr(T)	Le(T)	90.20	47.20	30.20	19.12

TABLE 6

Wall and Post Shock Values of VariablesArmaly & Sutton and Wilke's Correlation

Correlation		
	Armaly & Sutton	Wilke
Wall Values		
Temperature ( $^{\circ}\text{K}$ )	2386.0	2043.0
$C_{\text{N}_2}$	0.6804	0.6780
$C_{\text{O}_2}$	0.0251	0.0243
$C_{\text{NO}}$	0.0553	0.0524
$C_{\text{O}}$	0.1859	0.1880
$C_{\text{N}}$	0.0532	0.0569
$C_{\text{NO}+}$	0.000126	0.00013
Pr	0.5711	0.6876
Post Shock Values		
Temperature ( $^{\circ}\text{K}$ )	15999.0	16267.0
Normal Velocity (m/sec)	752.67	768.35
$C_{\text{N}_2}$	0.7153	0.7133
$C_{\text{O}_2}$	0.1536	0.1539
$C_{\text{NO}}$	0.0215	0.0213
$C_{\text{O}}$	0.0754	0.0752
$C_{\text{N}}$	0.0341	0.0361
$C_{\text{NO}+}$	0.000062	0.000064
Pr	0.6210	0.7200

**TABLE 7**  
**TRAJECTORY DETAILS FOR APF VEHICLE**

Alt. Km	Density Kg/m <sup>3</sup>	U <sub>∞</sub> <sup>*</sup> Km/sec	T <sub>∞</sub> <sup>*</sup> °K	Mole Fractions		
				X <sub>N2</sub>	X <sub>O2</sub>	X <sub>O</sub>
114.3	5.306e-8	9.905	285.8	.7571	.1011	.1418
110.5	9.669e-8	9.909	251.2	.7695	.1205	.1100
107.2	1.661e-7	9.911	230.8	.7773	.1405	.0822
103.9	2.876e-7	9.913	214.4	.7832	.1581	.0587
100.6	5.309e-7	9.915	203.7	.7848	.1740	.0412
97.7	9.056e-7	9.912	196.8	.7865	.1864	.0271
94.8	1.513e-6	9.909	191.7	.7870	.1977	.0153
92.3	2.392e-6	9.898	188.4	.7873	.2049	.0078
89.9	3.712e-6	9.886	186.7	.7880	.2120	.0000
87.7	5.350e-6	9.863	189.5	.7880	.2120	.0000
85.6	7.615e-6	9.832	191.5	.7880	.2120	.0000
83.9	1.015e-5	9.785	193.0	.7880	.2120	.0000
82.4	1.354e-5	9.539	194.0	.7880	.2120	.0000
81.2	1.614e-5	9.653	194.4	.7880	.2120	.0000
80.1	1.927e-5	9.569	195.5	.7880	.2120	.0000
79.4	2.188e-5	9.471	195.6	.7880	.2120	.0000
78.9	2.386e-5	9.365	196.2	.7880	.2120	.0000

Wall Temperature : 1111 °K

Nose Radius : 2.53 m

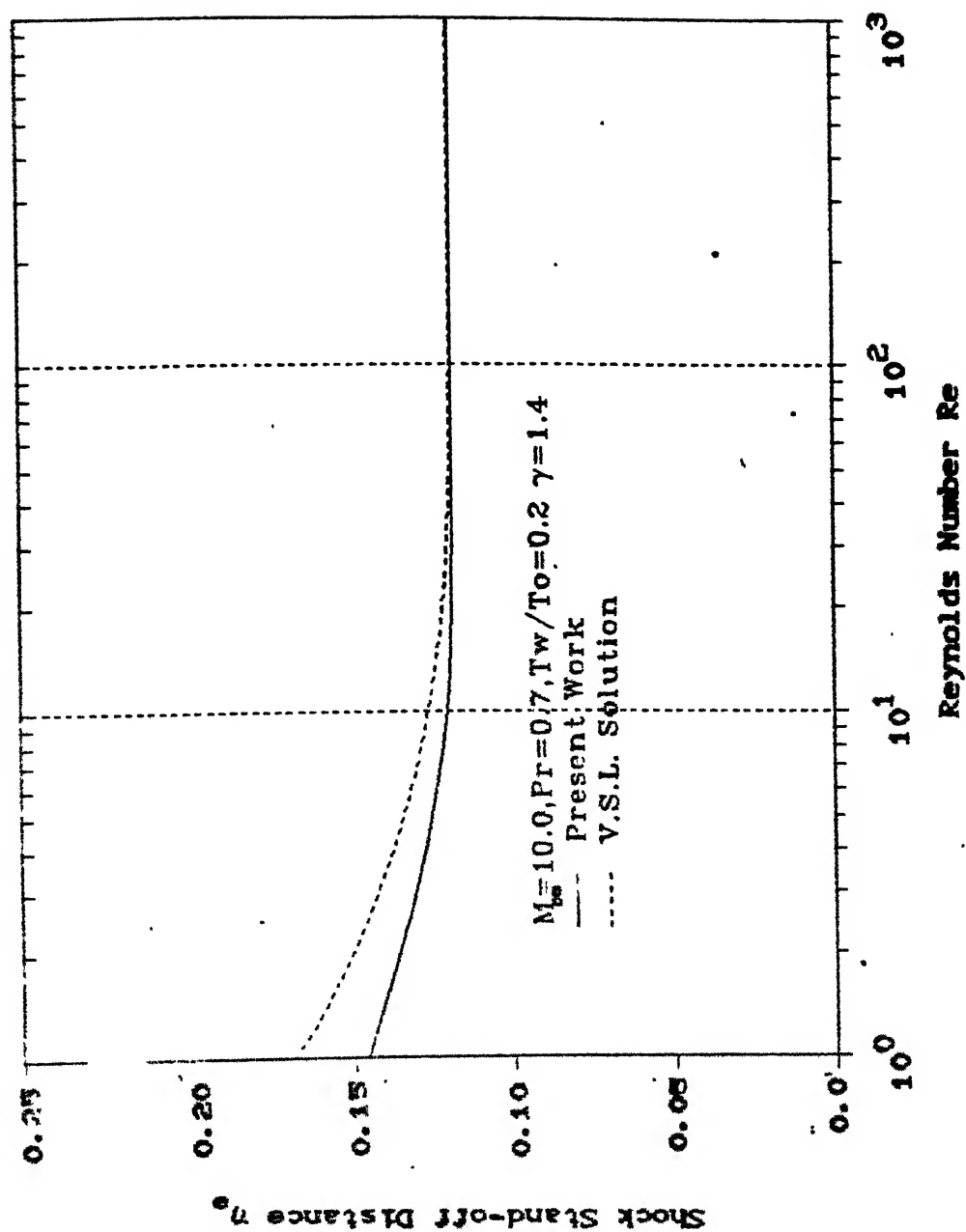


FIG. 4.1 SHOCK STAND-OFF DISTANCE FOR COLD WALL CASE

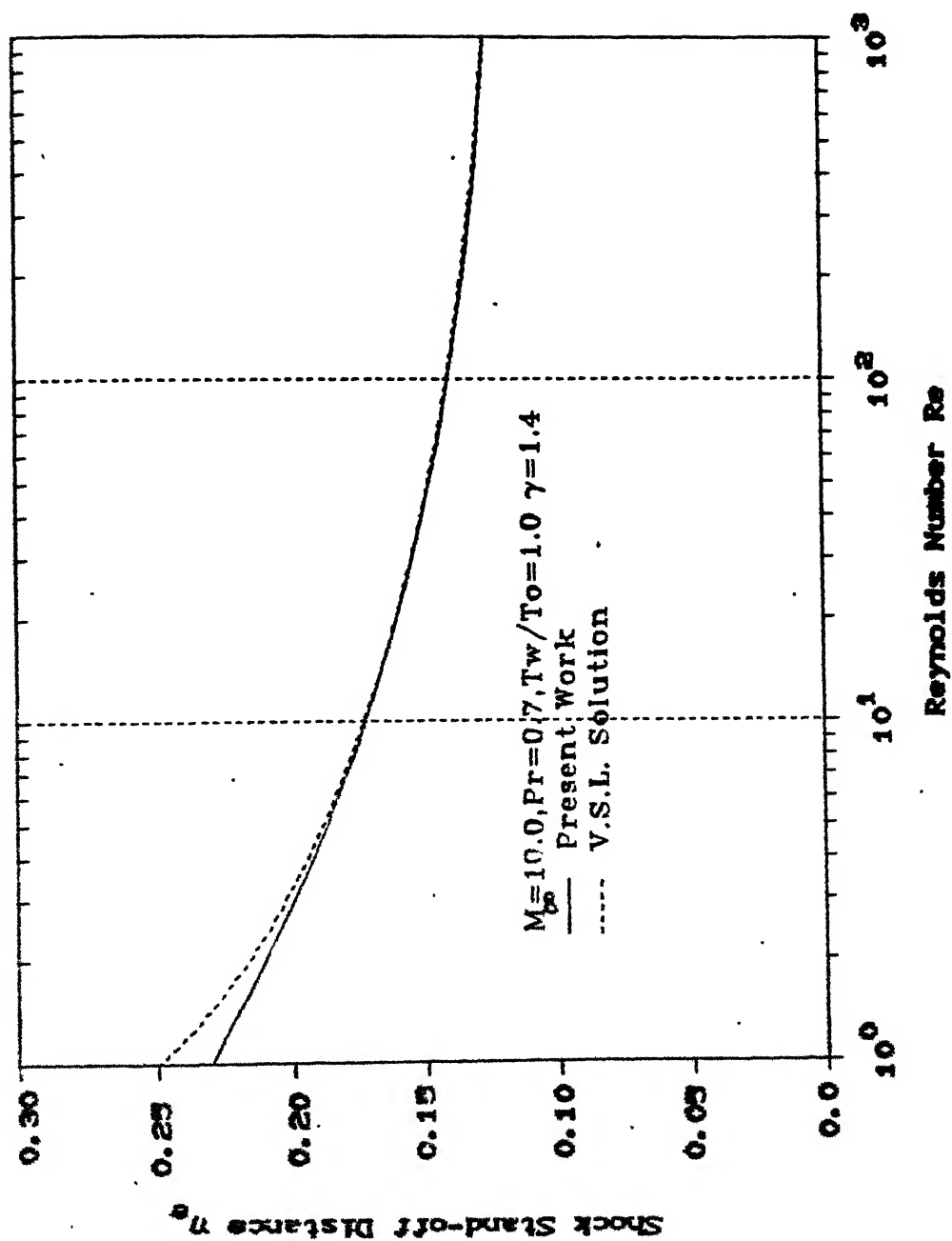


FIG. 4.2 SHOCK STAND-OFF DISTANCE FOR HOT WALL CASE



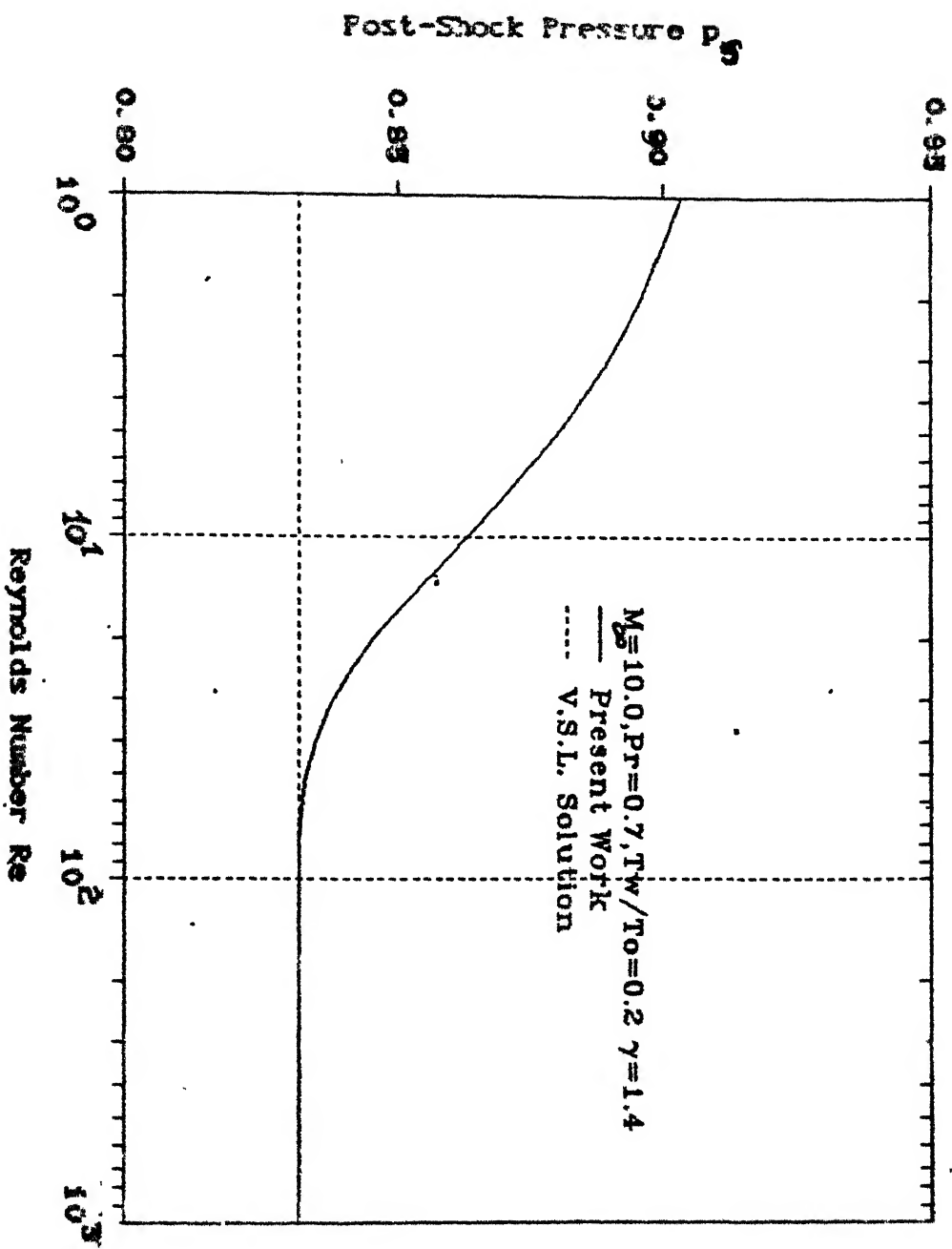
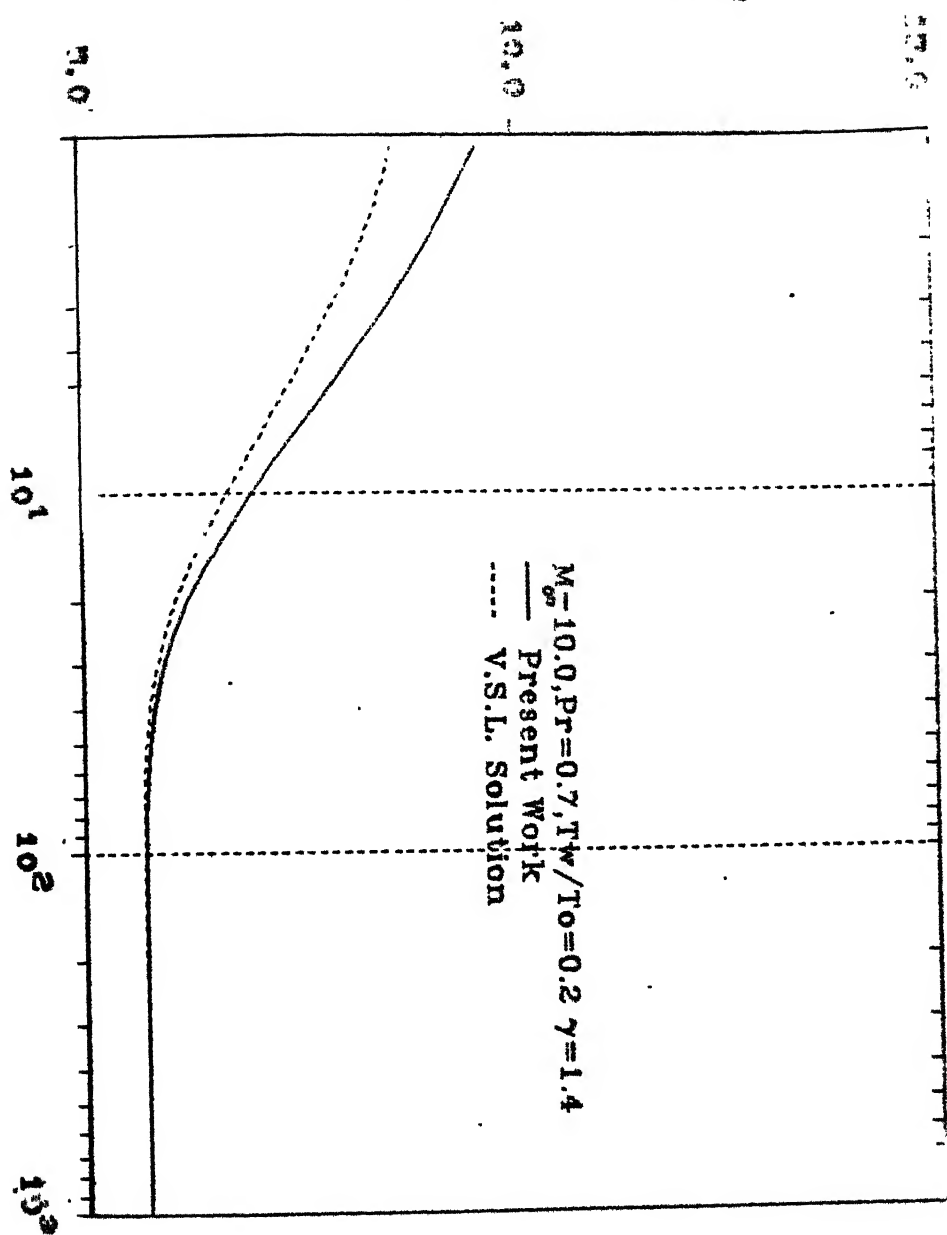
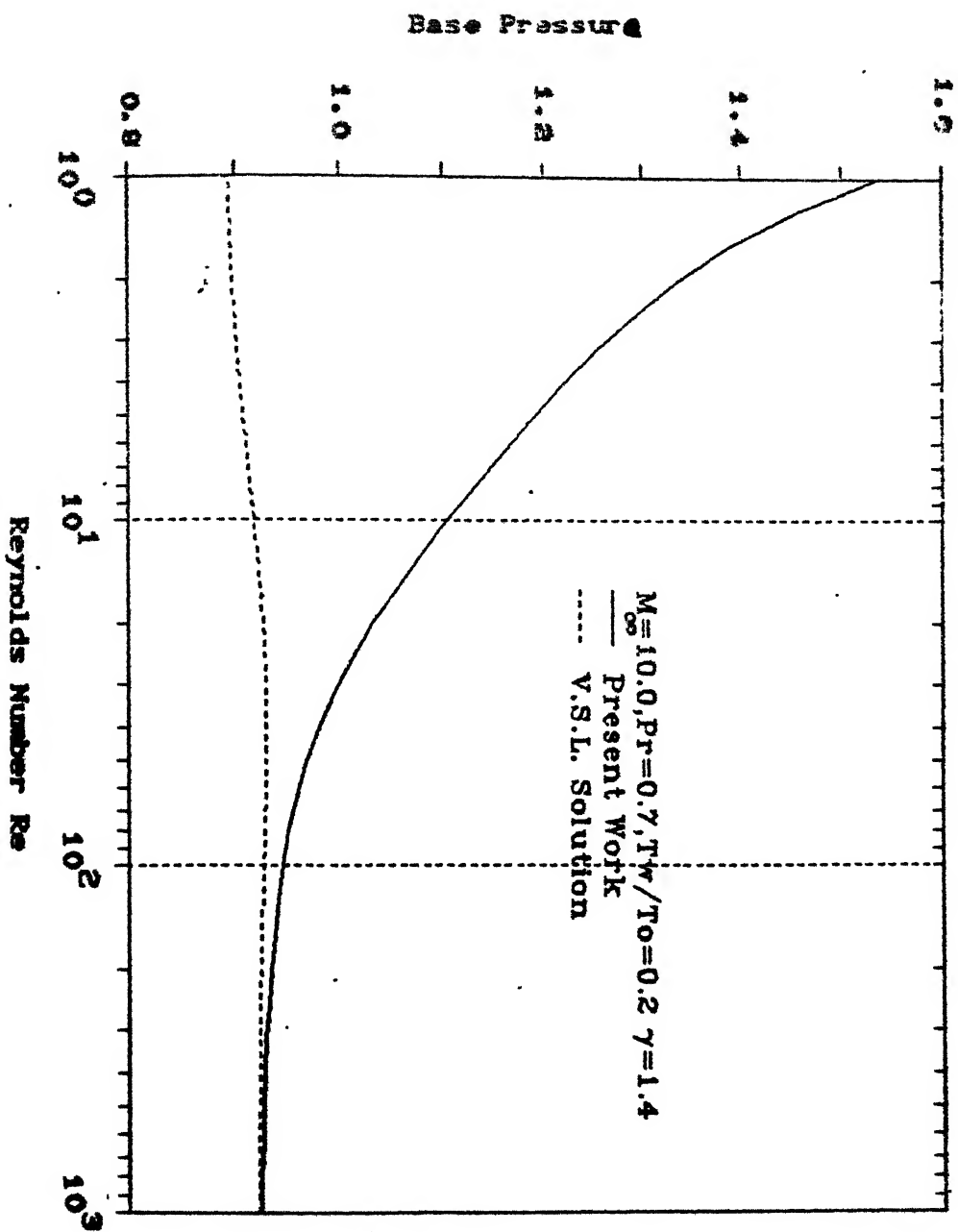


FIG. 4.3 POST-SHOCK PRESSURE VARIATION WITH REYNOLDS

Post-Shock Density  $\rho_2$





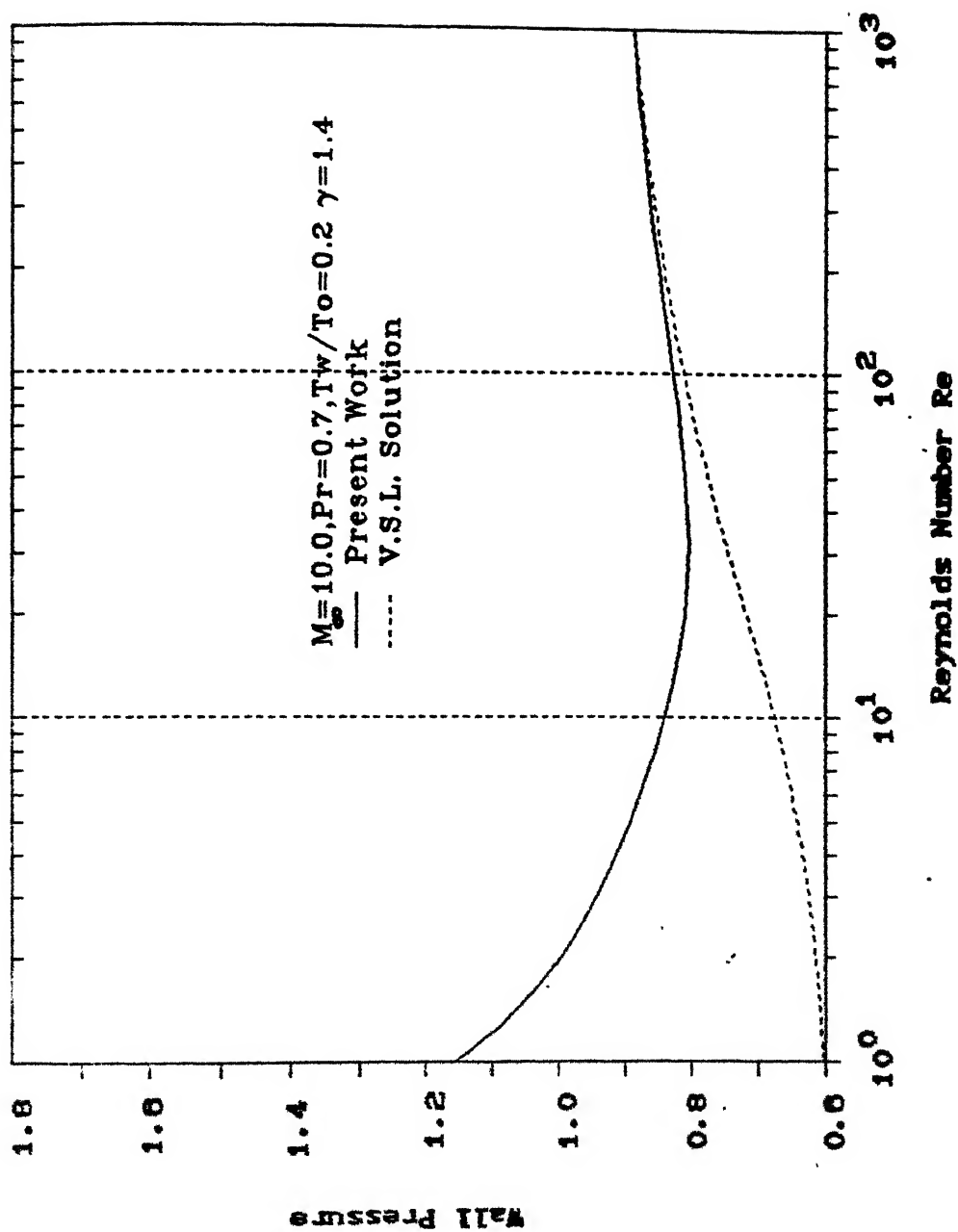


FIG: 4.6 WALL PRESSURE VARIATION WITH REYNOLDS NUMBER

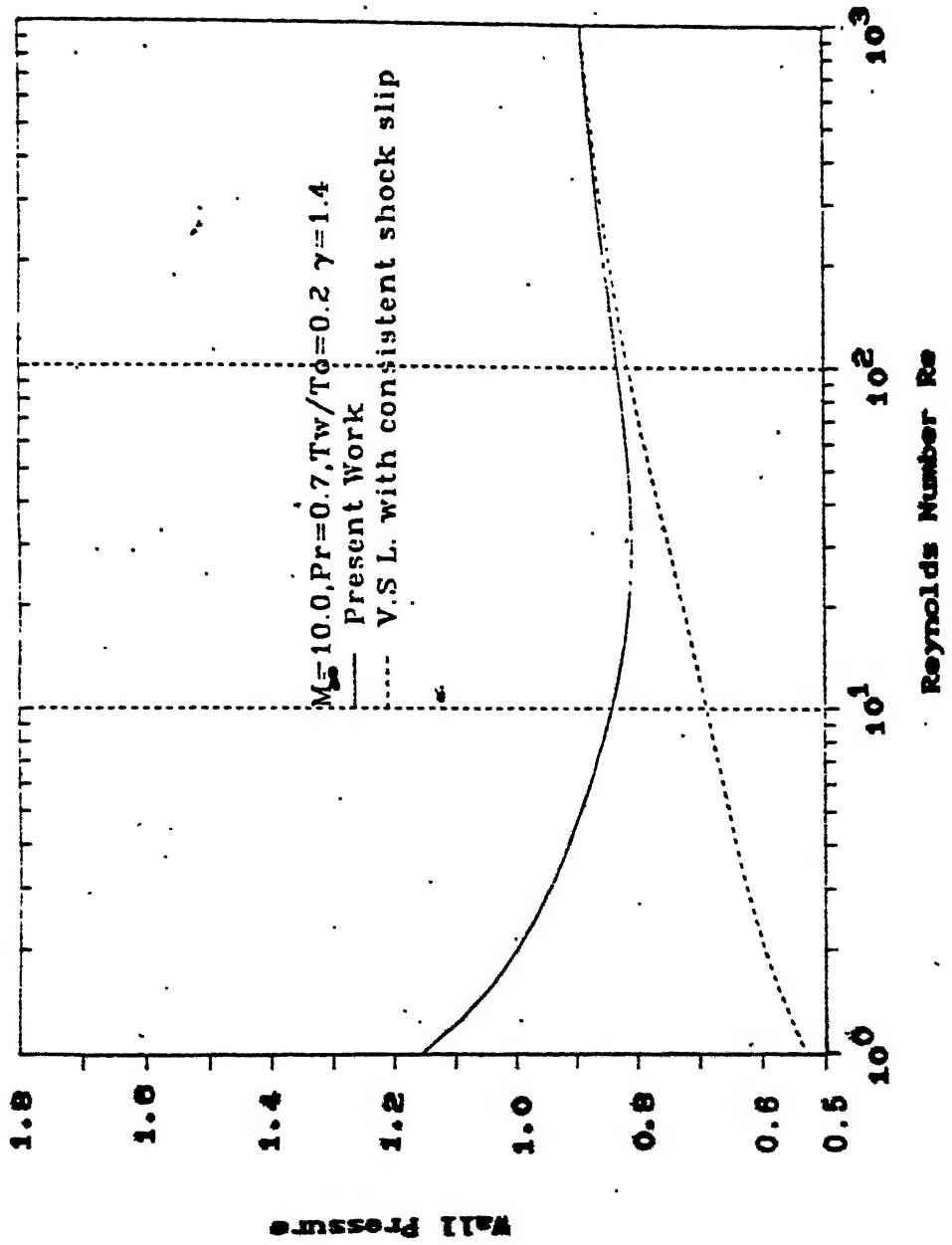


FIG: 4.7 WALL PRESSURE VARIATION WITH REYNOLDS

NUMBER WITH CONSISTENT SHOCK SLIP FOR VSI

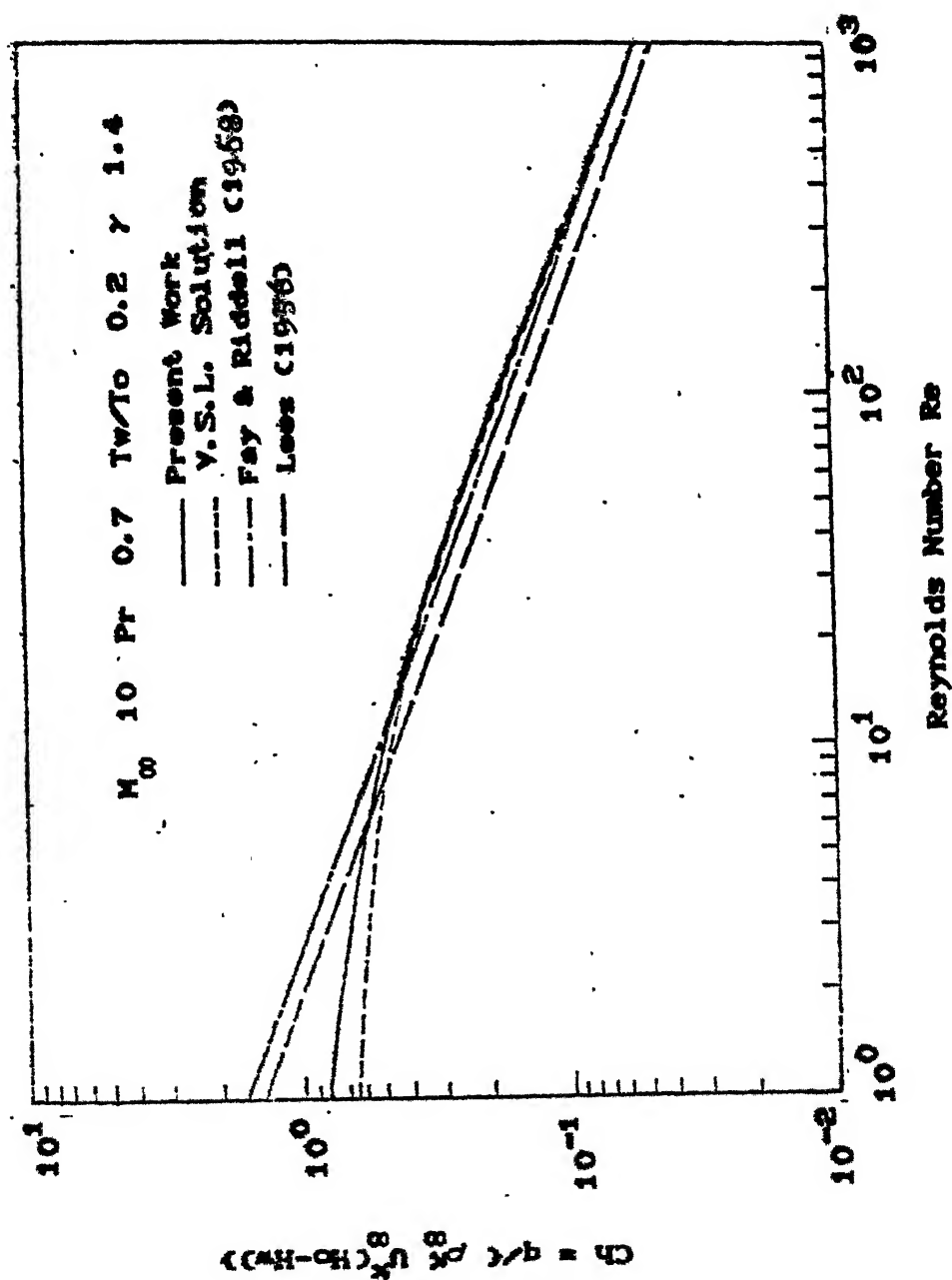


FIG. 4.8 HEAT TRANSFER COEFFICIENT FOR COLD WALL

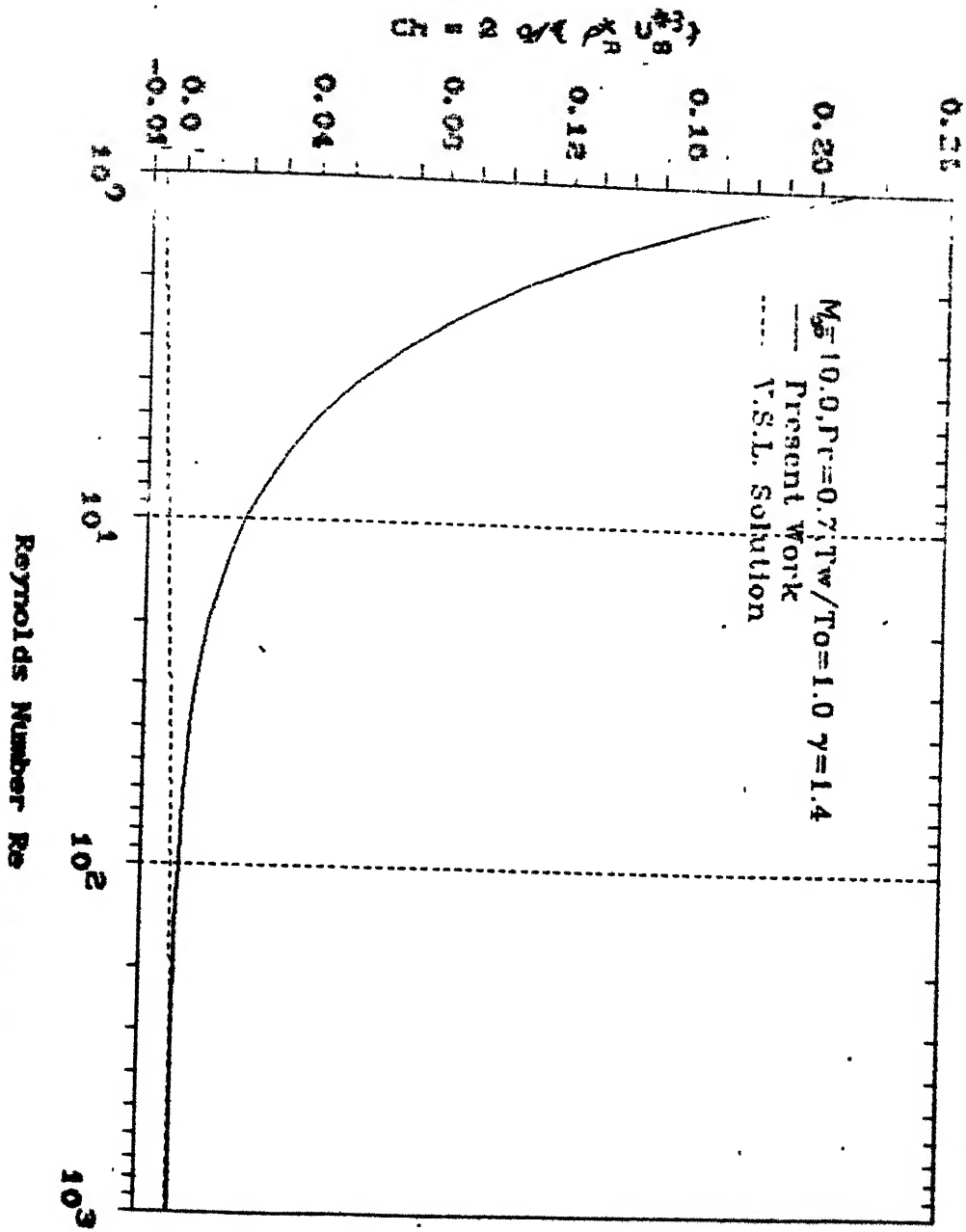


FIG. 4.9 HEAT TRANSFER COEFFICIENT FOR HOT WALL

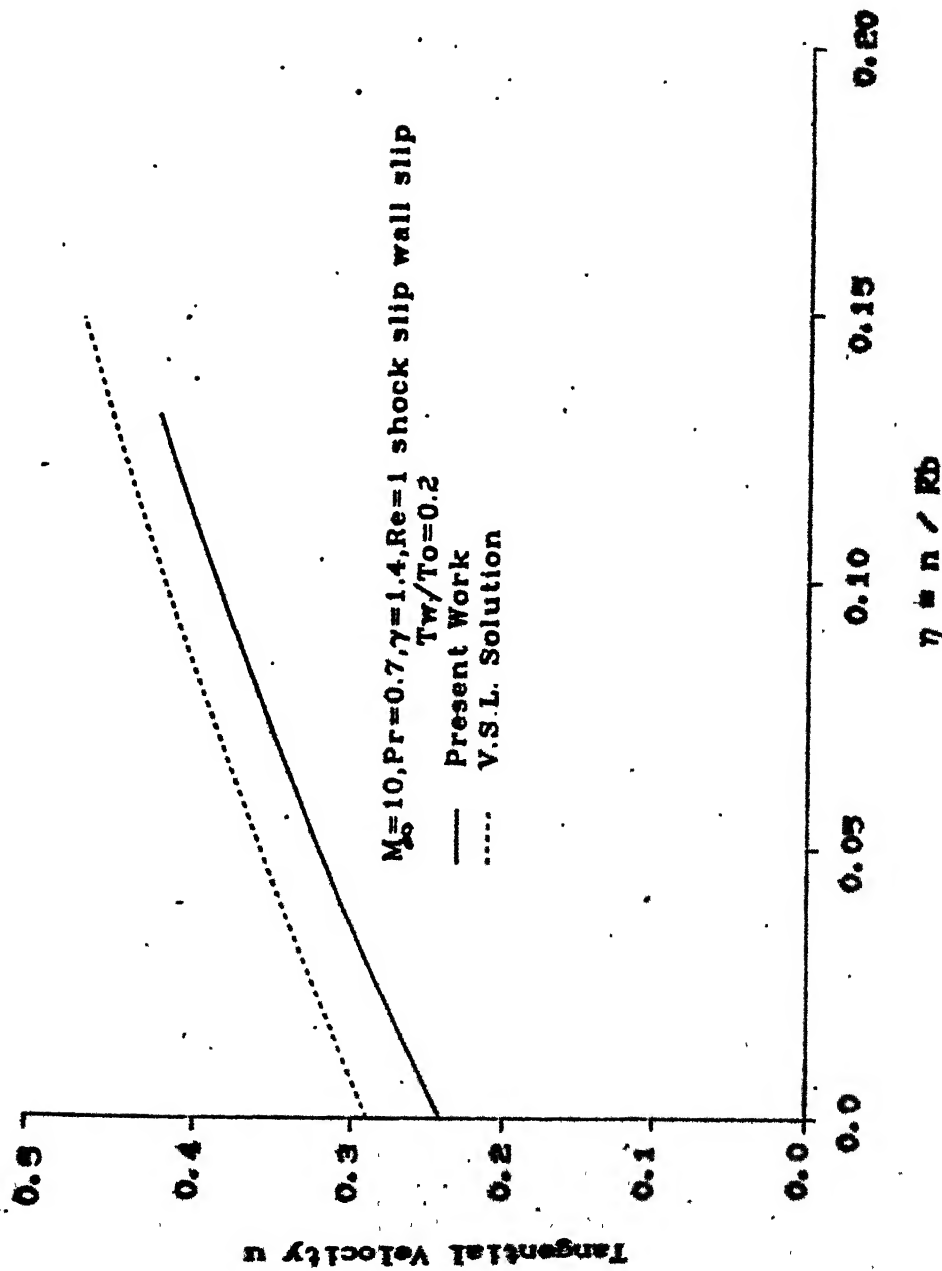


FIG. 4.10 TANGENTIAL VELOCITY PROFILE FOR  $Re = 1$



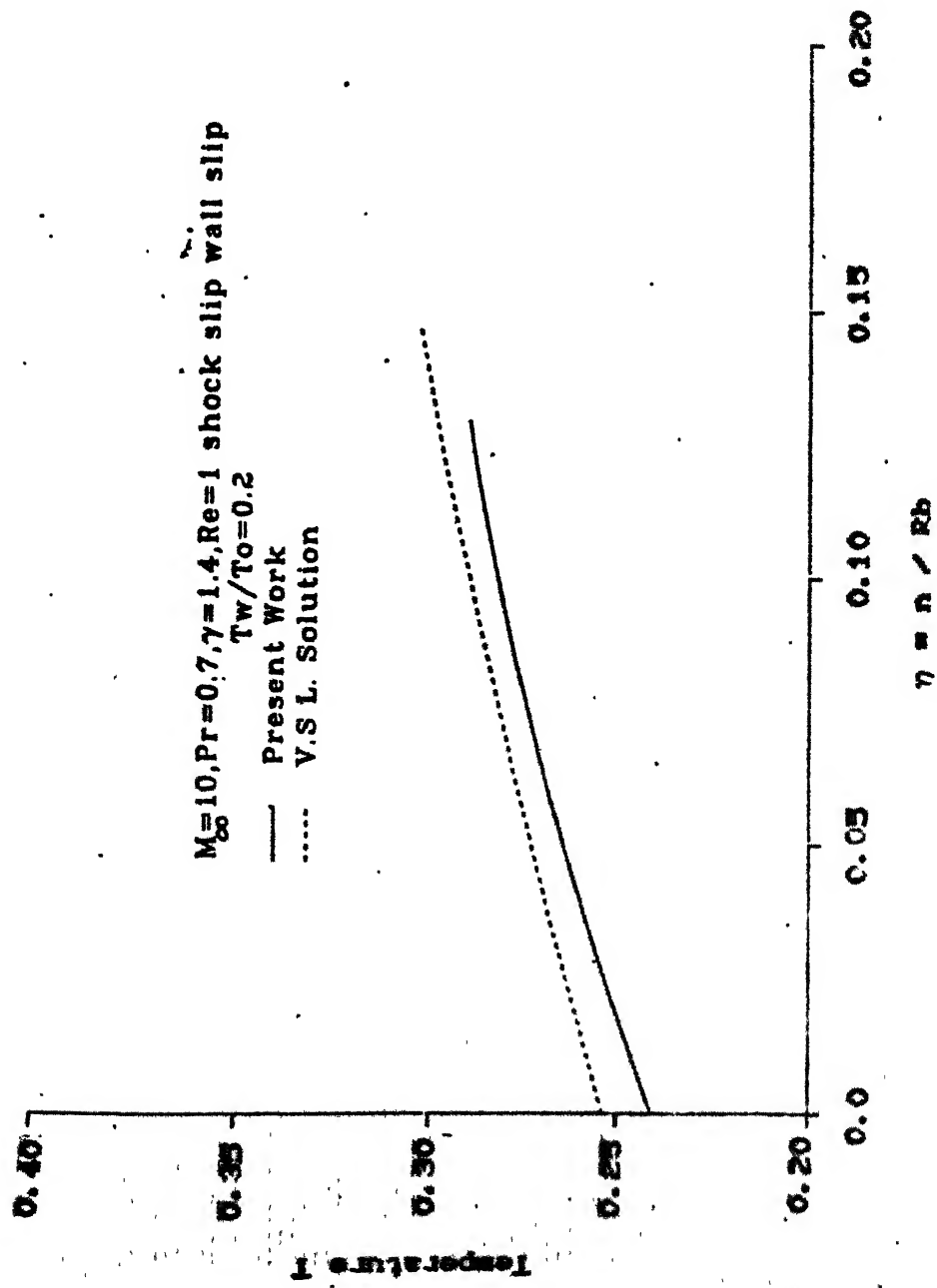


FIG: 4.11 TEMPERATURE PROFILE FOR  $Re = 1$

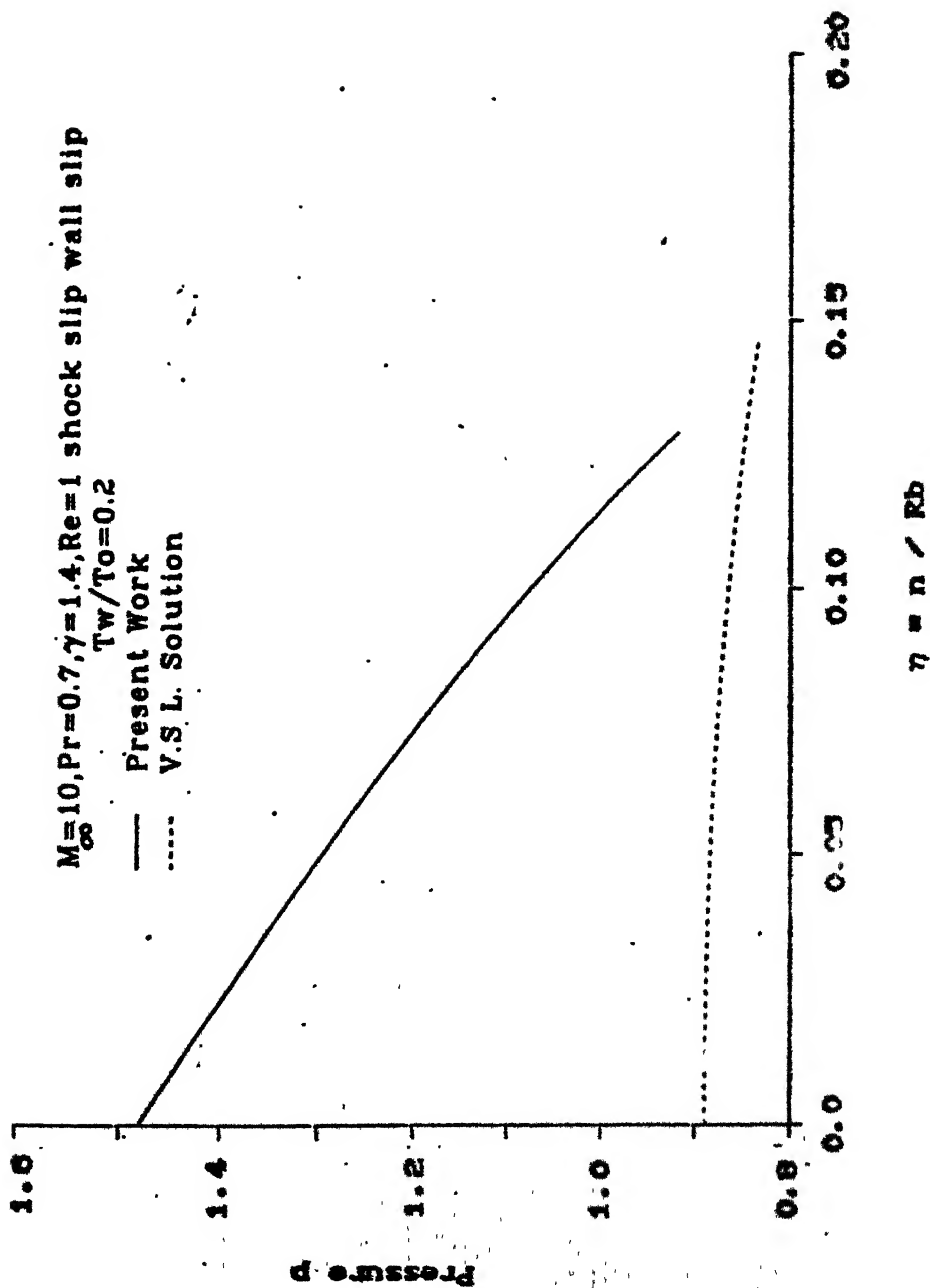
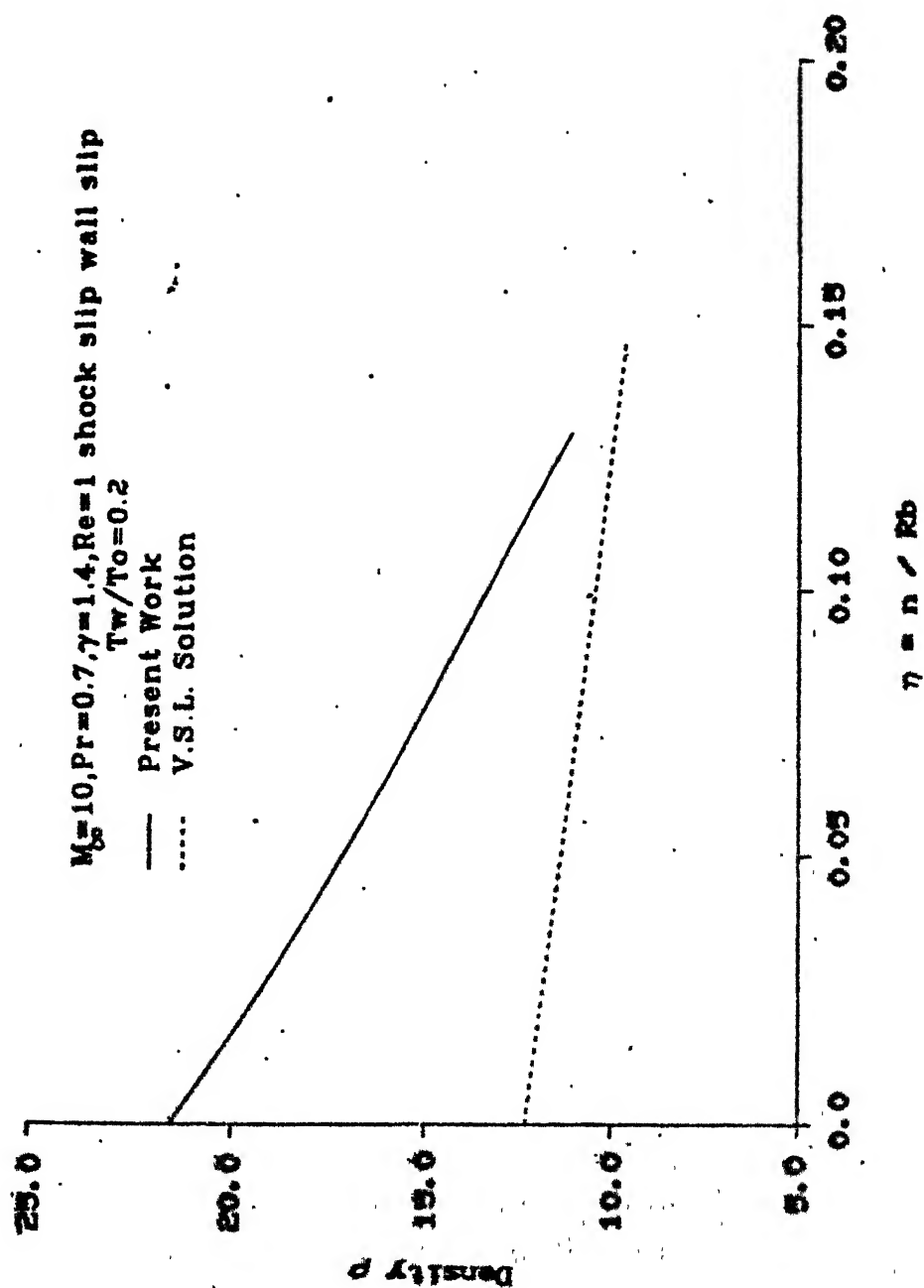


FIG: 4.12 PRESSURE PROFILE FOR  $Re = 1$

FIG. 4.13 DENSITY PROFILE FOR  $Re = 1$

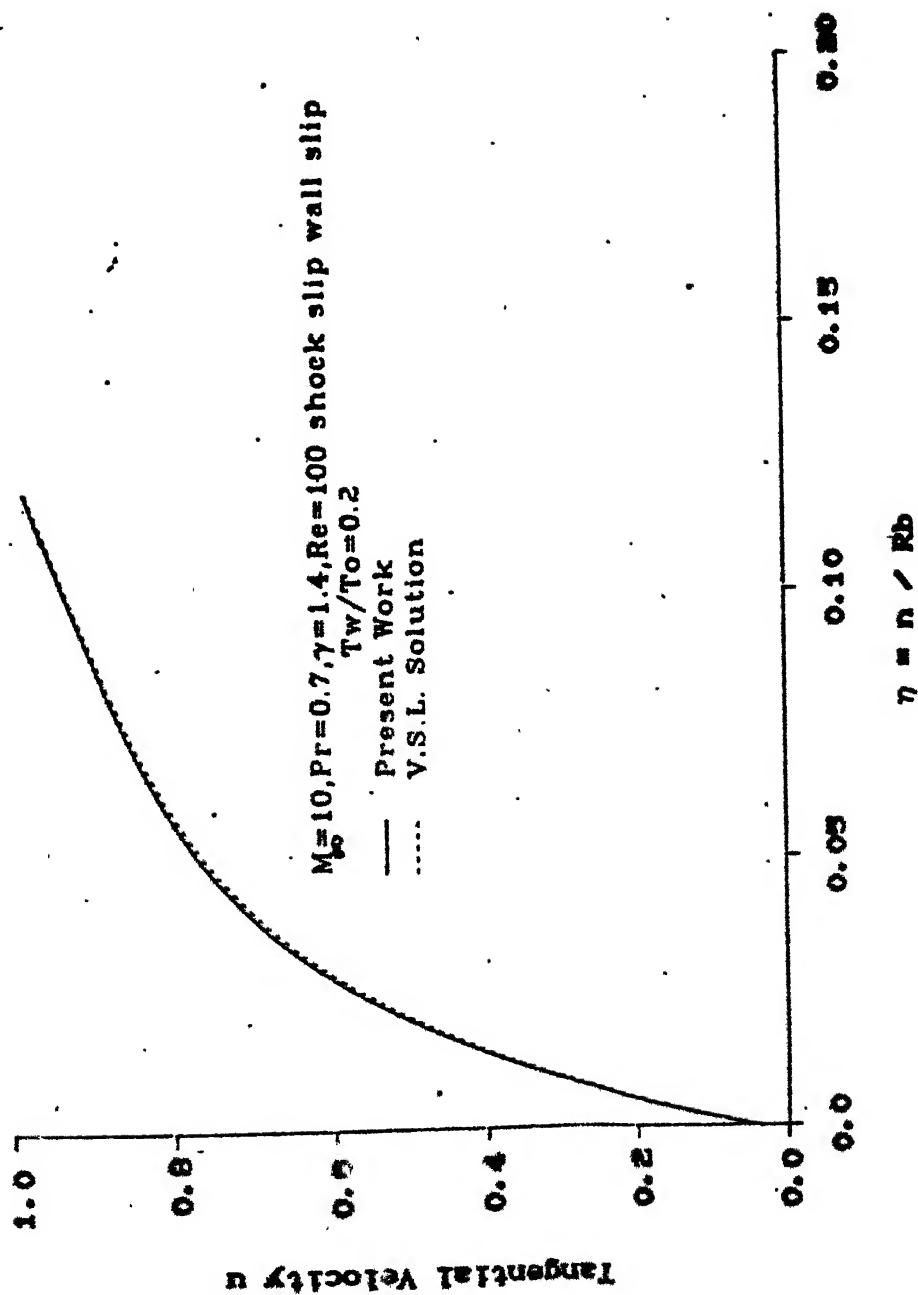
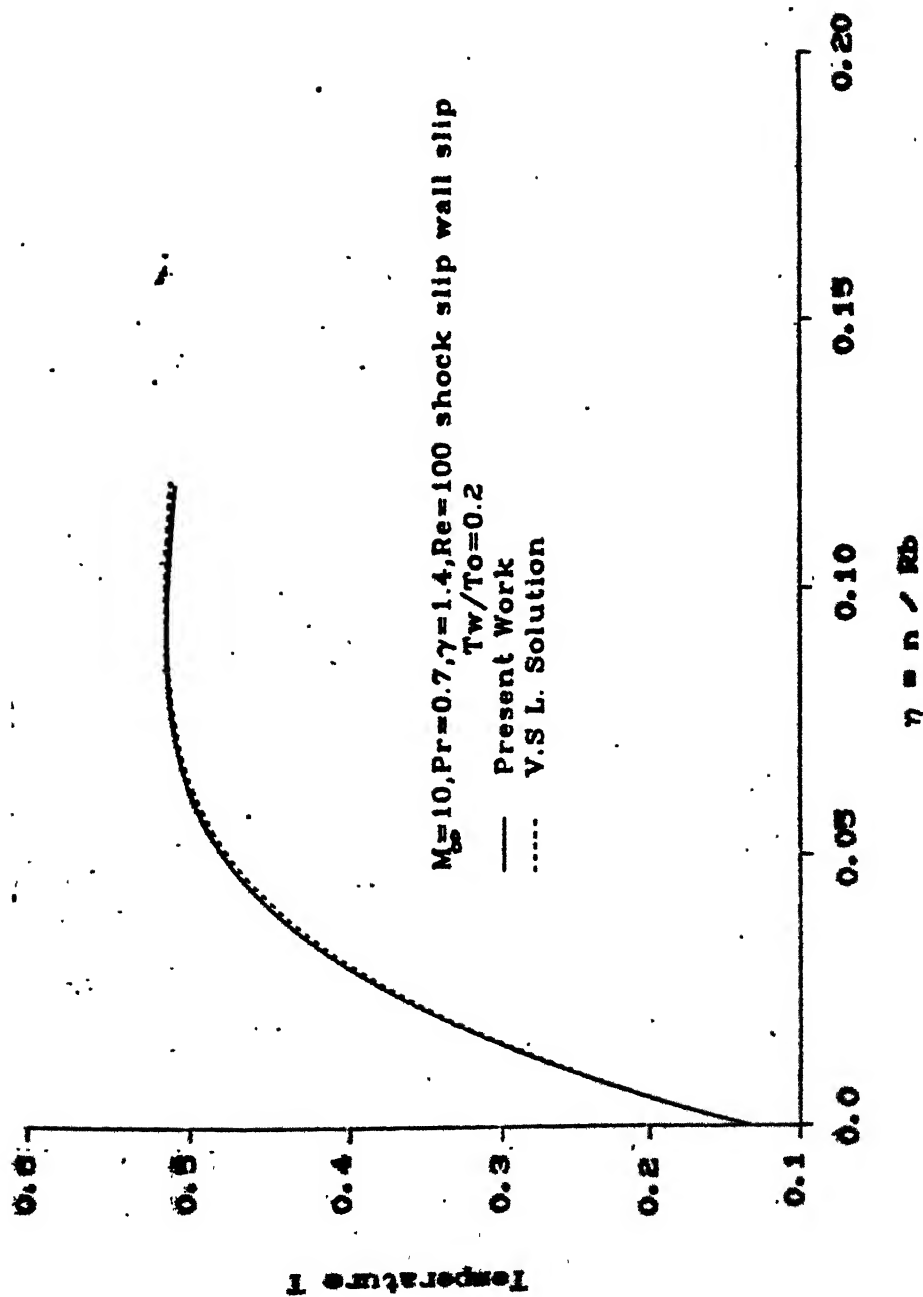
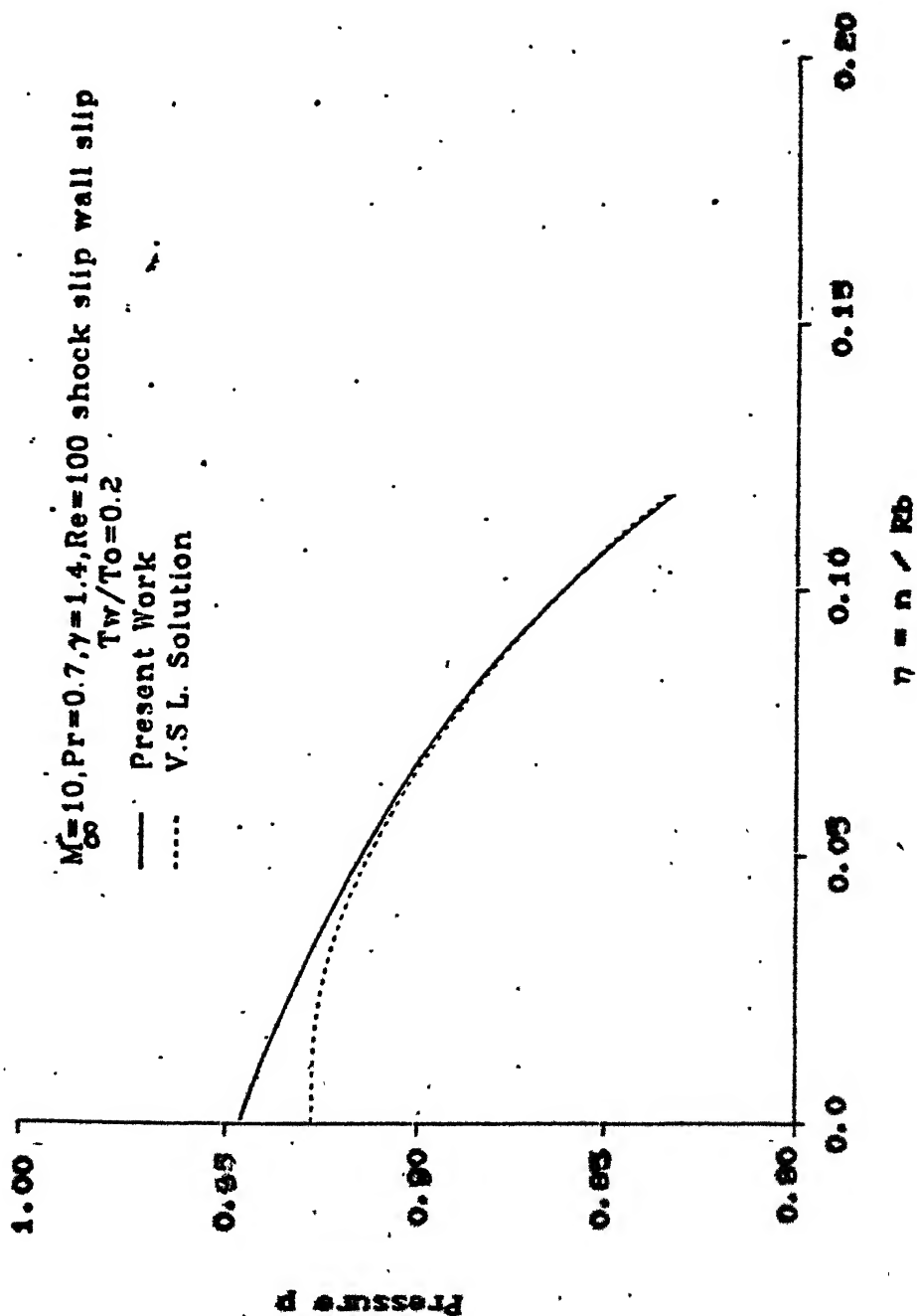
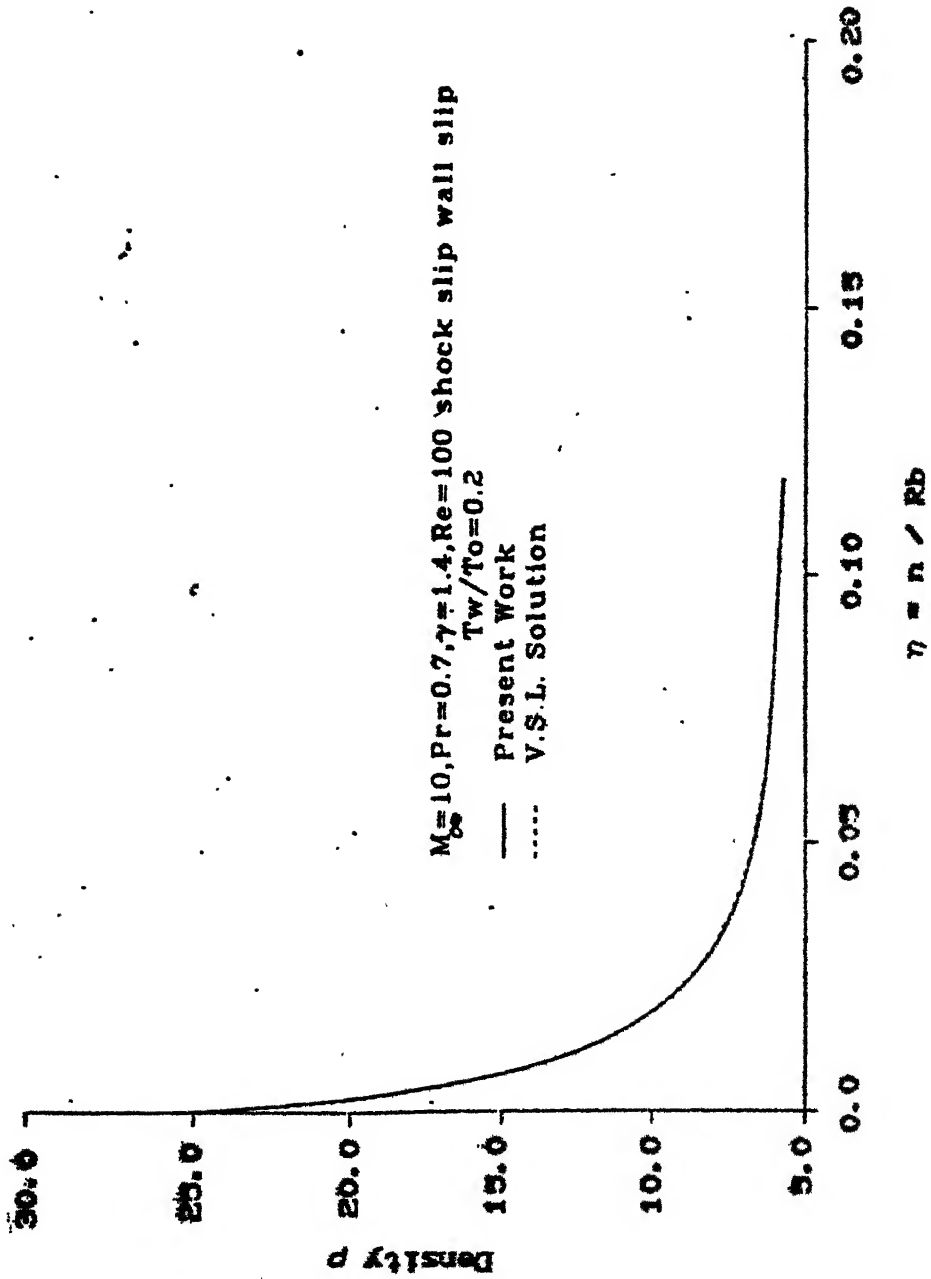


FIG. 4.14 TANGENTIAL VELOCITY PROFILE FOR  $Re = 100$

FIG. 4.15 TEMPERATURE PROFILE FOR  $Re = 100$

FIG. 4.16 PRESSURE PROFILE FOR  $Re = 100$

FIG. 4.17 DENSITY PROFILE FOR  $Re = 100$

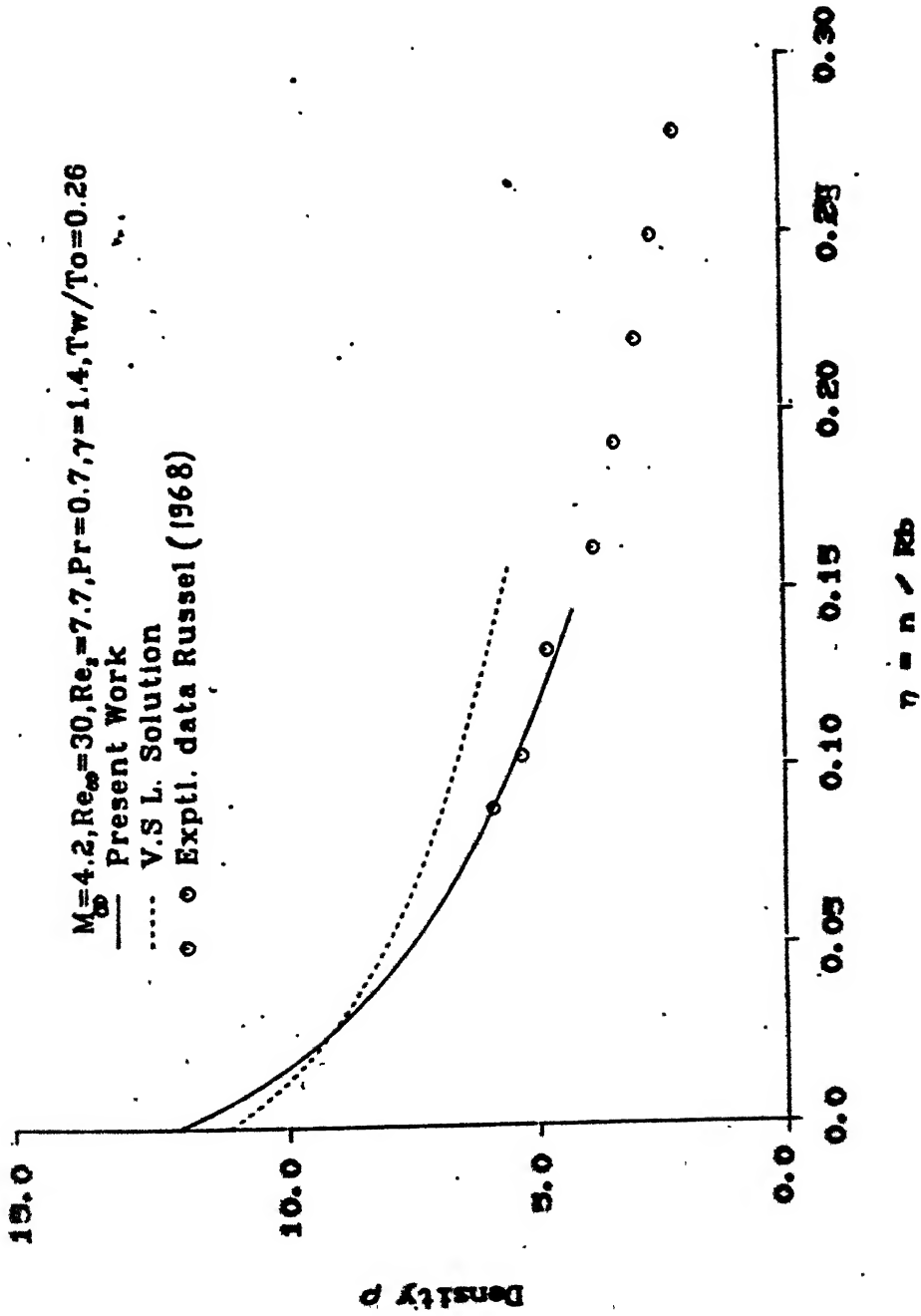


FIG: 4.18 DENSITY PROFILE COMPARISON WITH EXPERIMENTAL  
DATA OF RUSSEL FOR COLD WALL



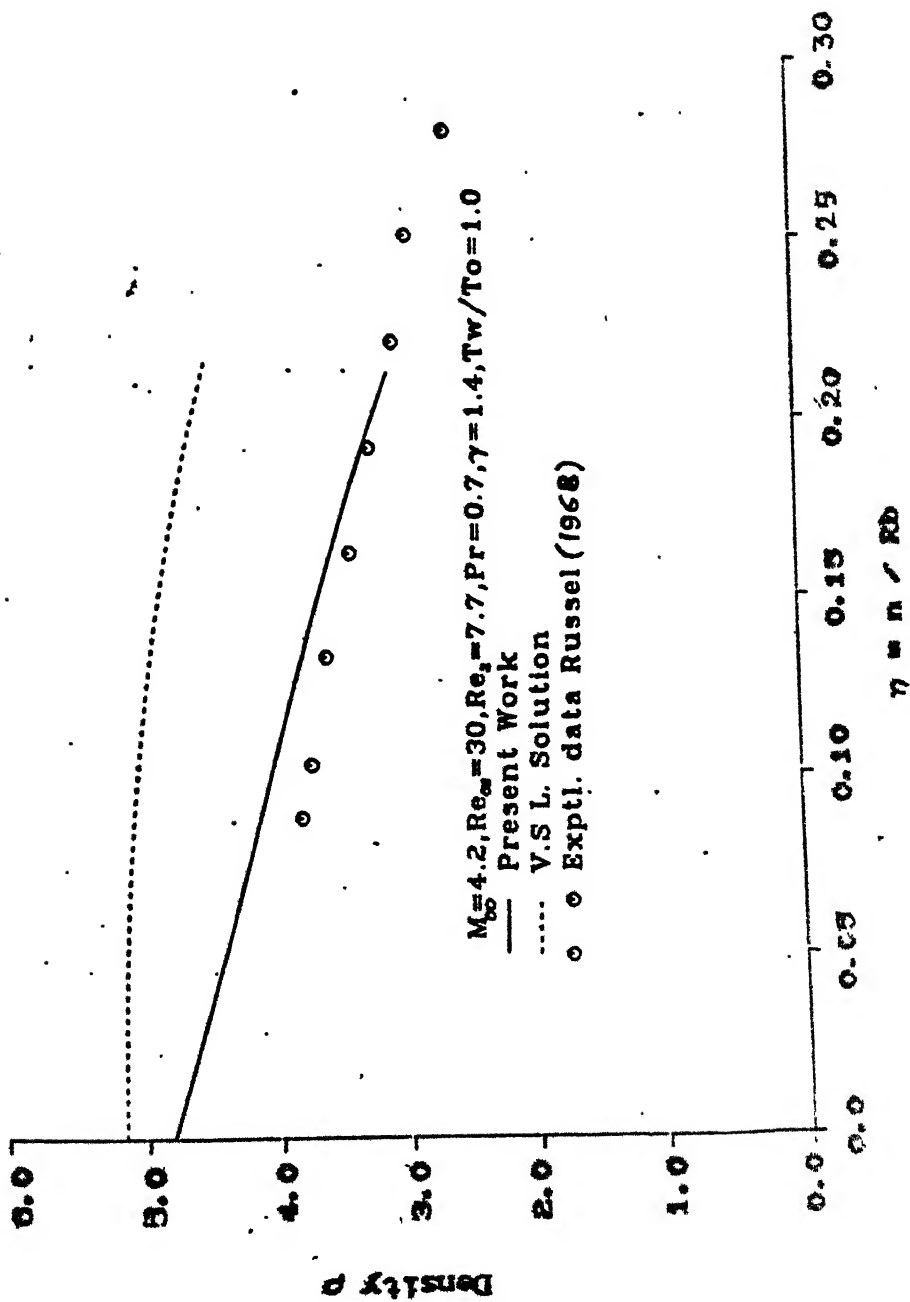


FIG. 4.23 DENSITY PROFILE COMPARISON WITH EXPERIMENTAL

DATA OF RUSSEL FOR HOT WALL

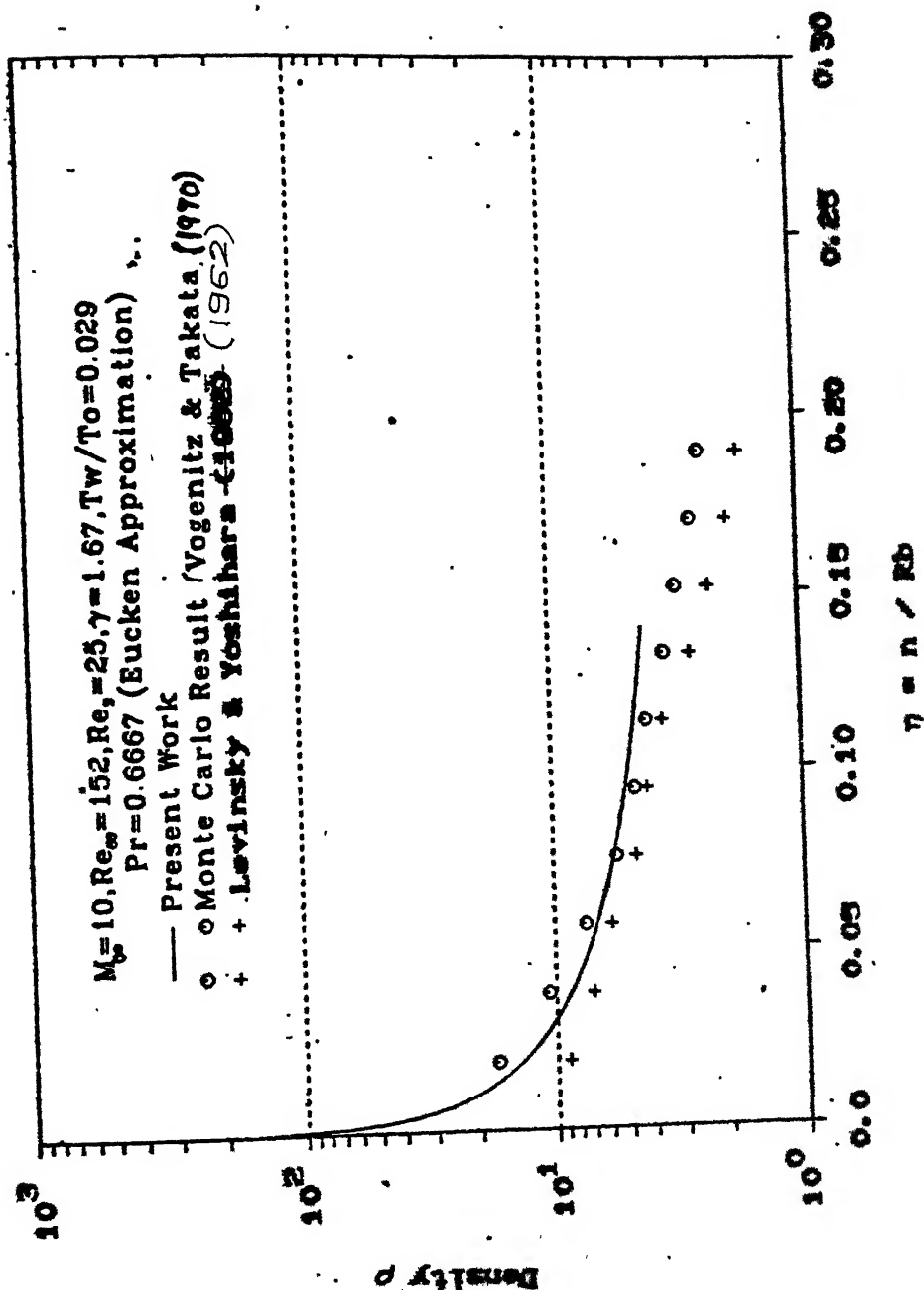


FIG. 4.20 DENSITY PROFILE COMPARISON WITH MONTE CARLO RESULTS OF VOGENTZ & TAKATA FOR COLD WALL

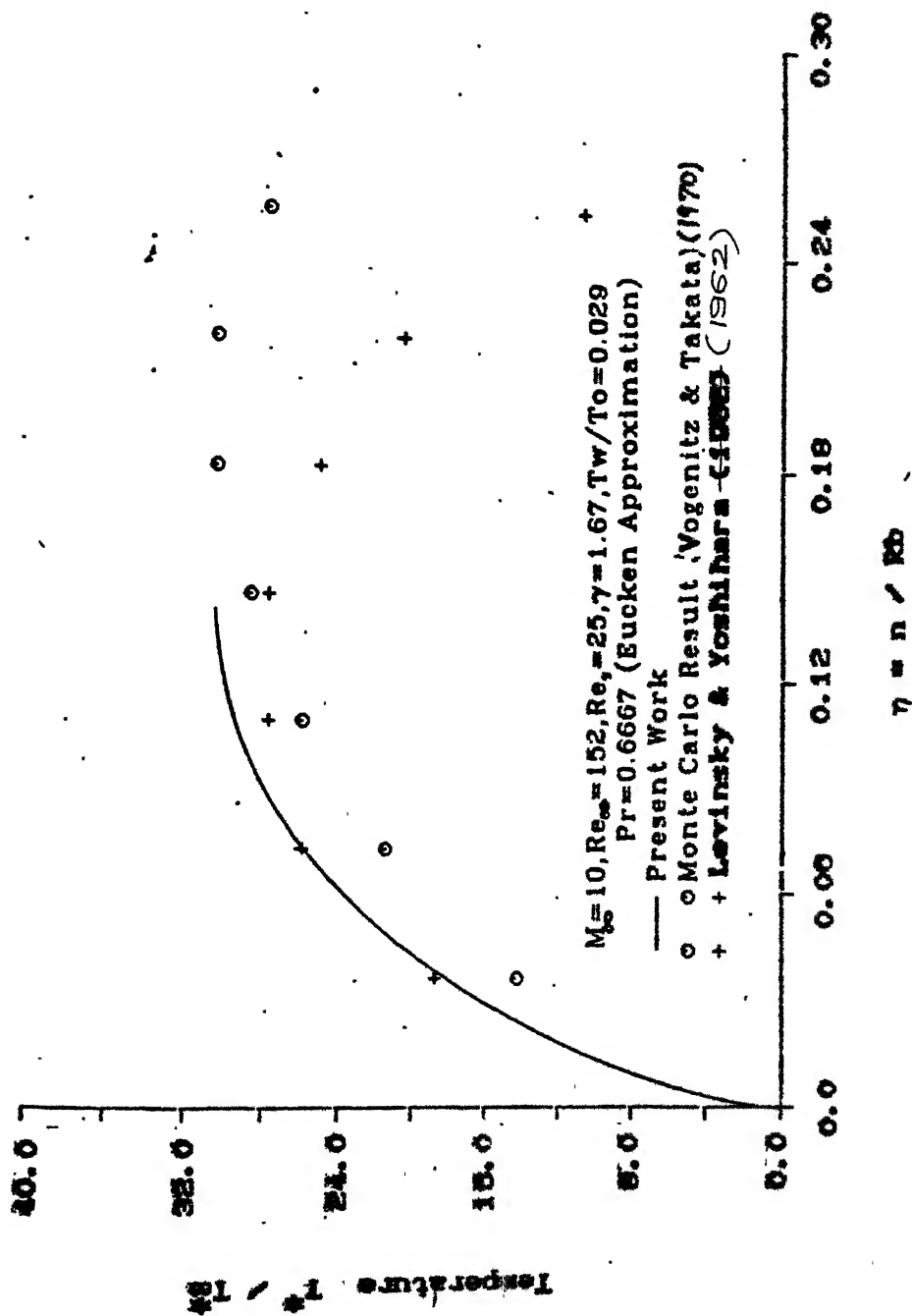
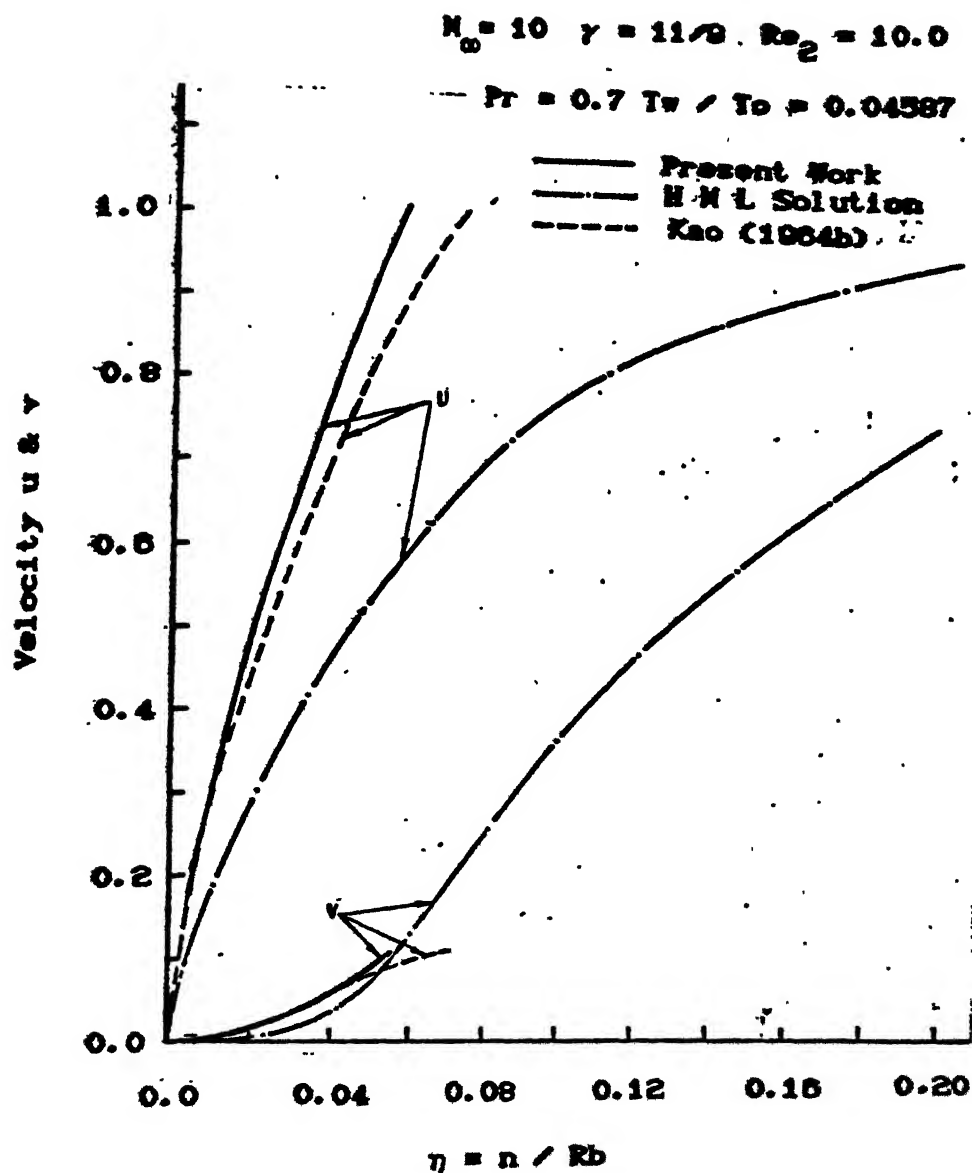


FIG. 4.21 TEMPERATURE PROFILE COMPARISON WITH MONTE CARLO RESULTS  
OF VOGENTZ & TAKATA FOR COLD WALL



**FIG: 4.22 COMPARISON OF VELOCITY PROFILES OF PRESENT WORK WITH RESULTS OF KAO AND HML SOLUTION**

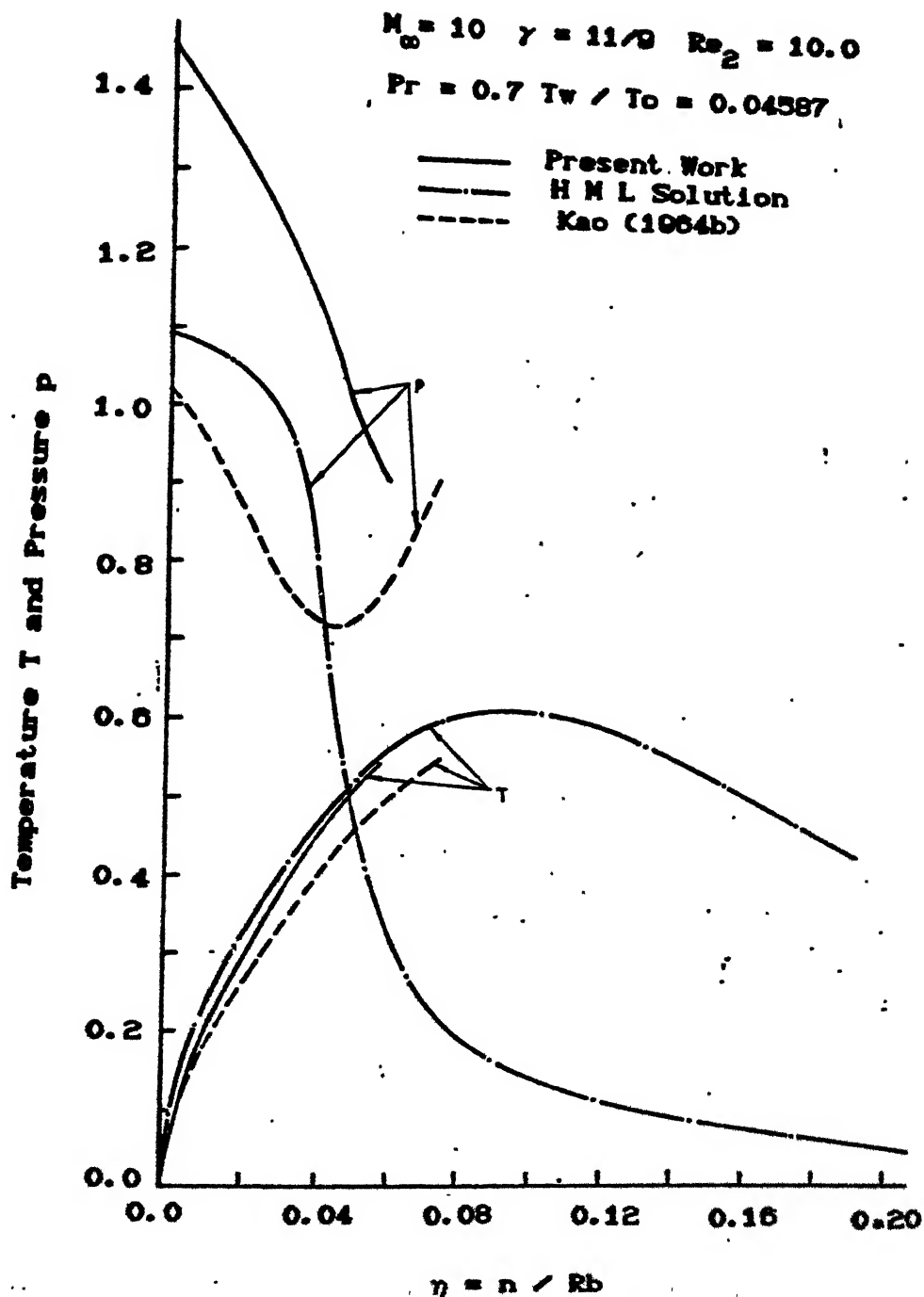


FIG. 4.23 COMPARISON OF TEMPERATURE AND PRESSURE PROFILES OF PRESENT WORK WITH RESULTS OF KAO AND H M L SOLUTION

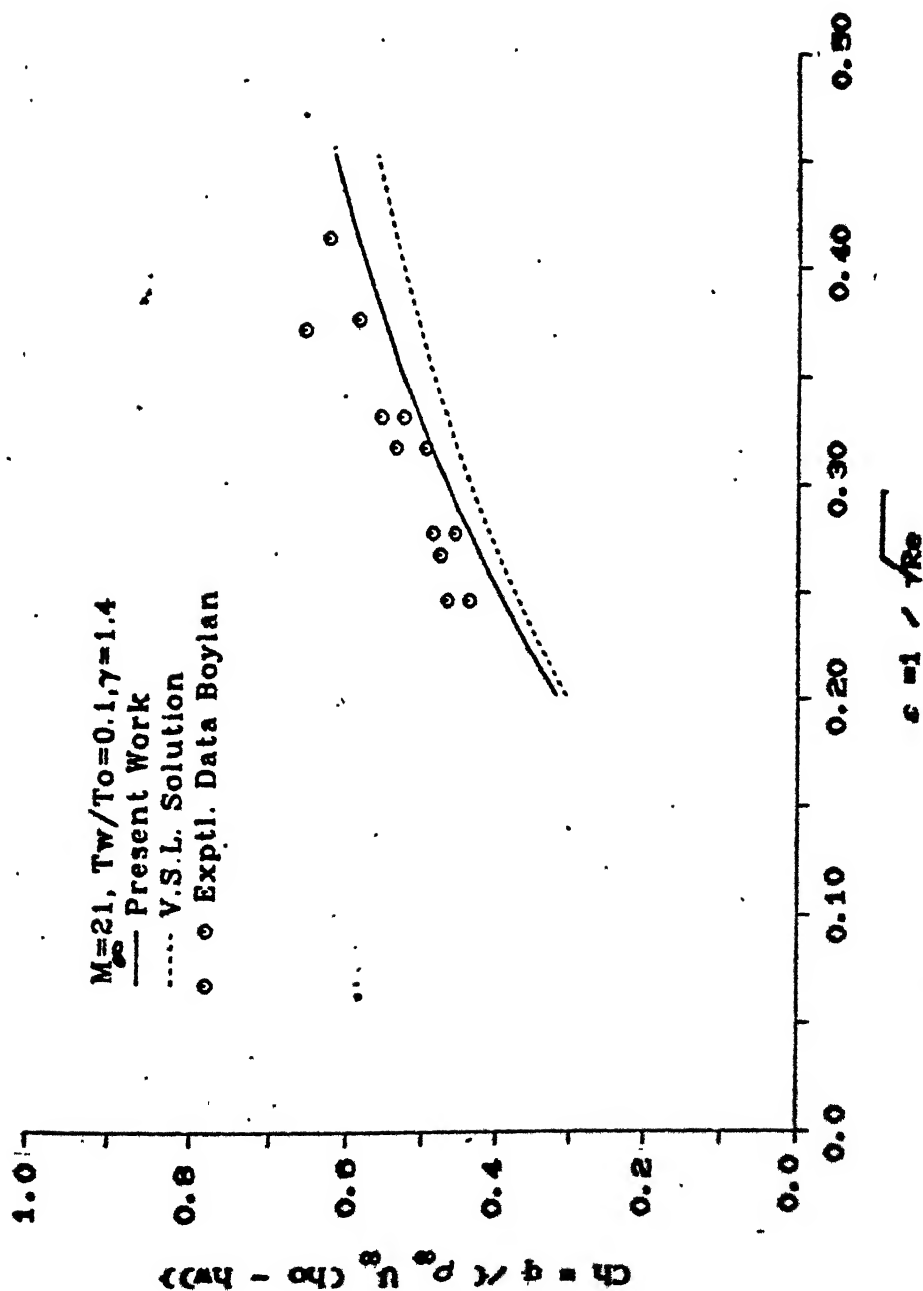


FIG. 4.24 HEAT TRANSFER COEFFICIENT COMPARISON WITH  
EXPERIMENTAL DATA OF BOYLAN

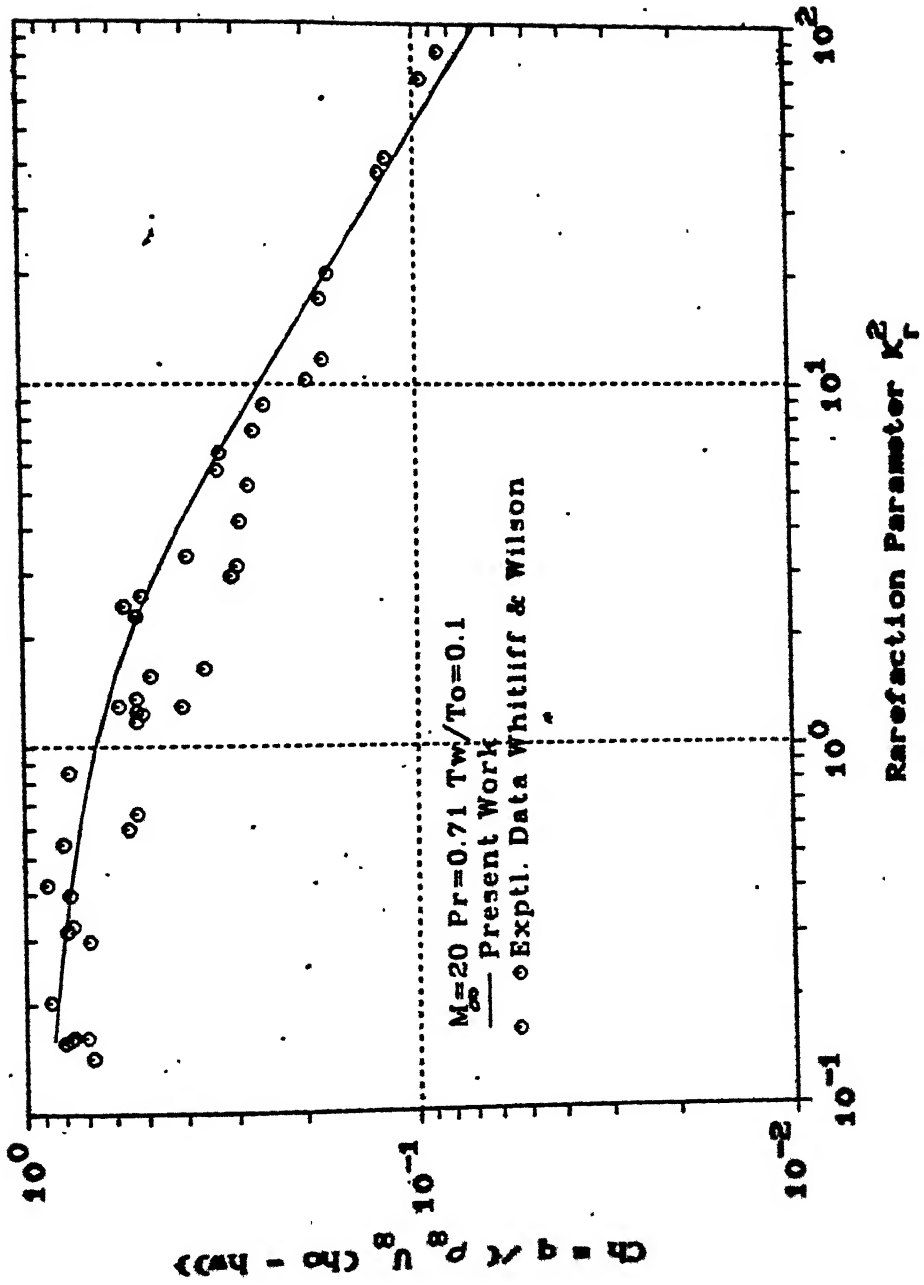


FIG.4.25 HEAT TRANSFER COEFFICIENT COMPARISON WITH  
EXPERIMENTAL DATA OF WHITLIFF & WILSON

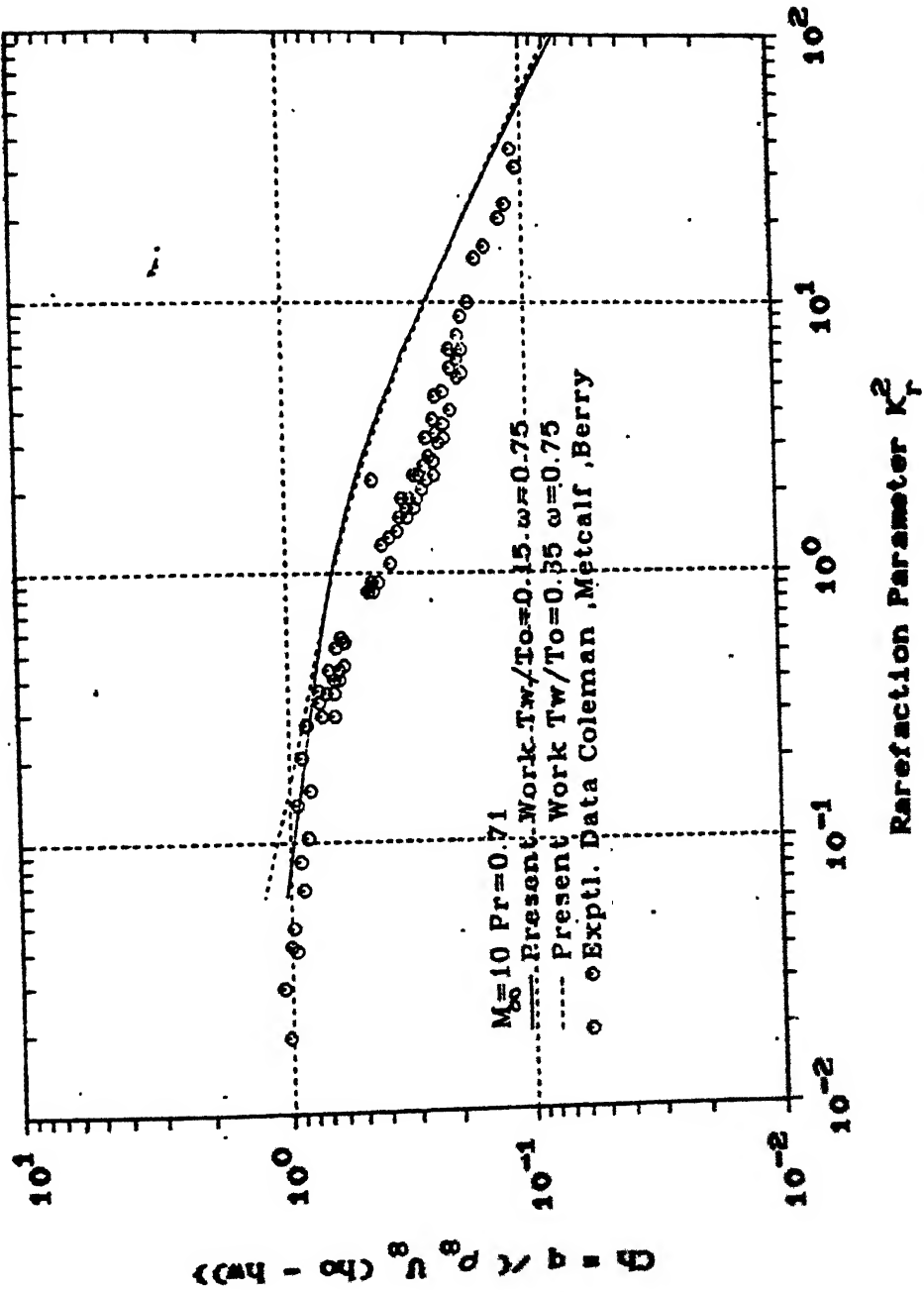


FIG.4.26 HEAT TRANSFER COEFFICIENT COMPARISON WITH  
EXPERIMENTAL DATA OF COLEMAN, METCALF & BERRY



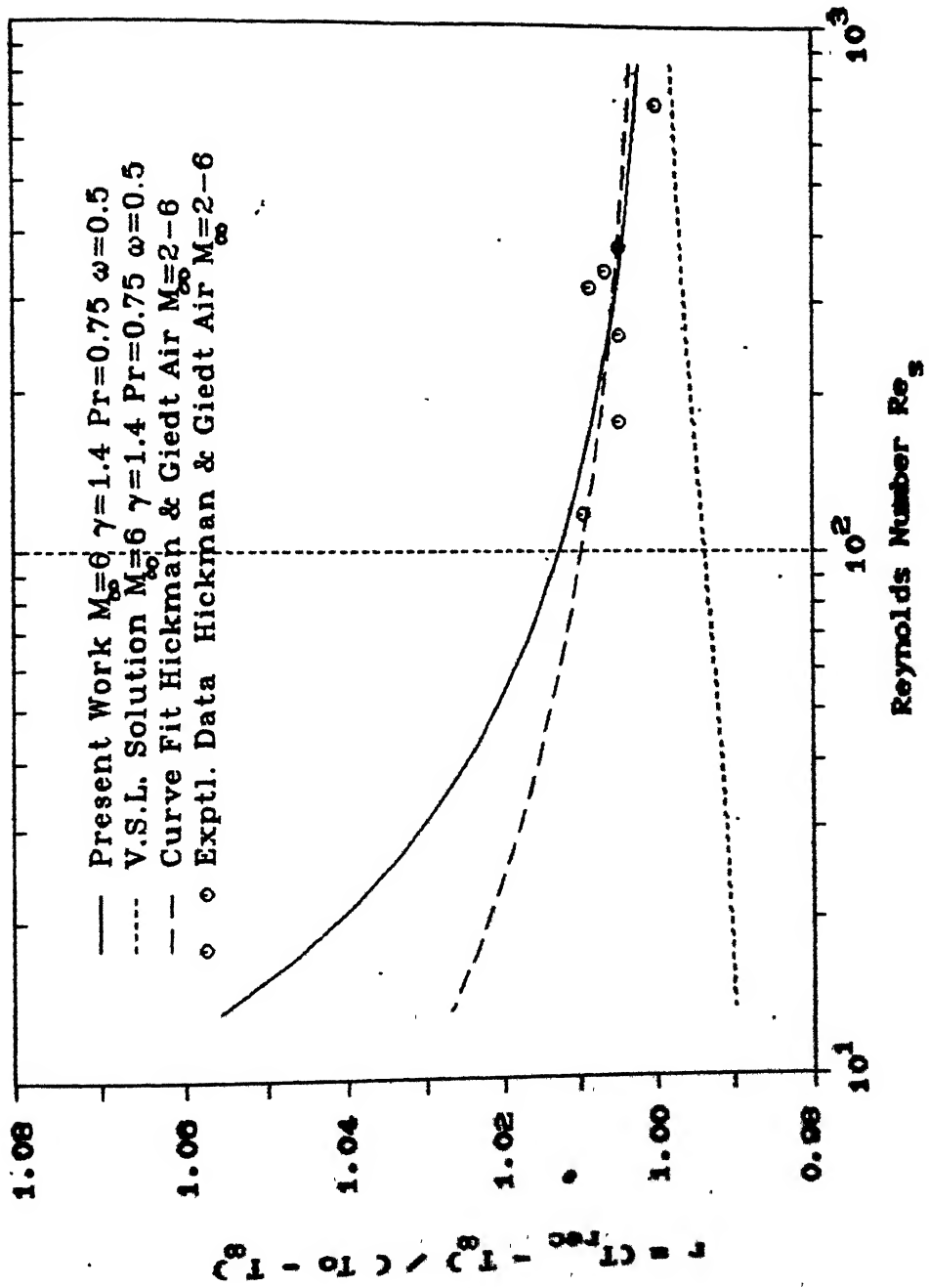


FIG. 4.27 VARIATION OF RECOVERY FACTOR WITH REYNOLDS NUMBER

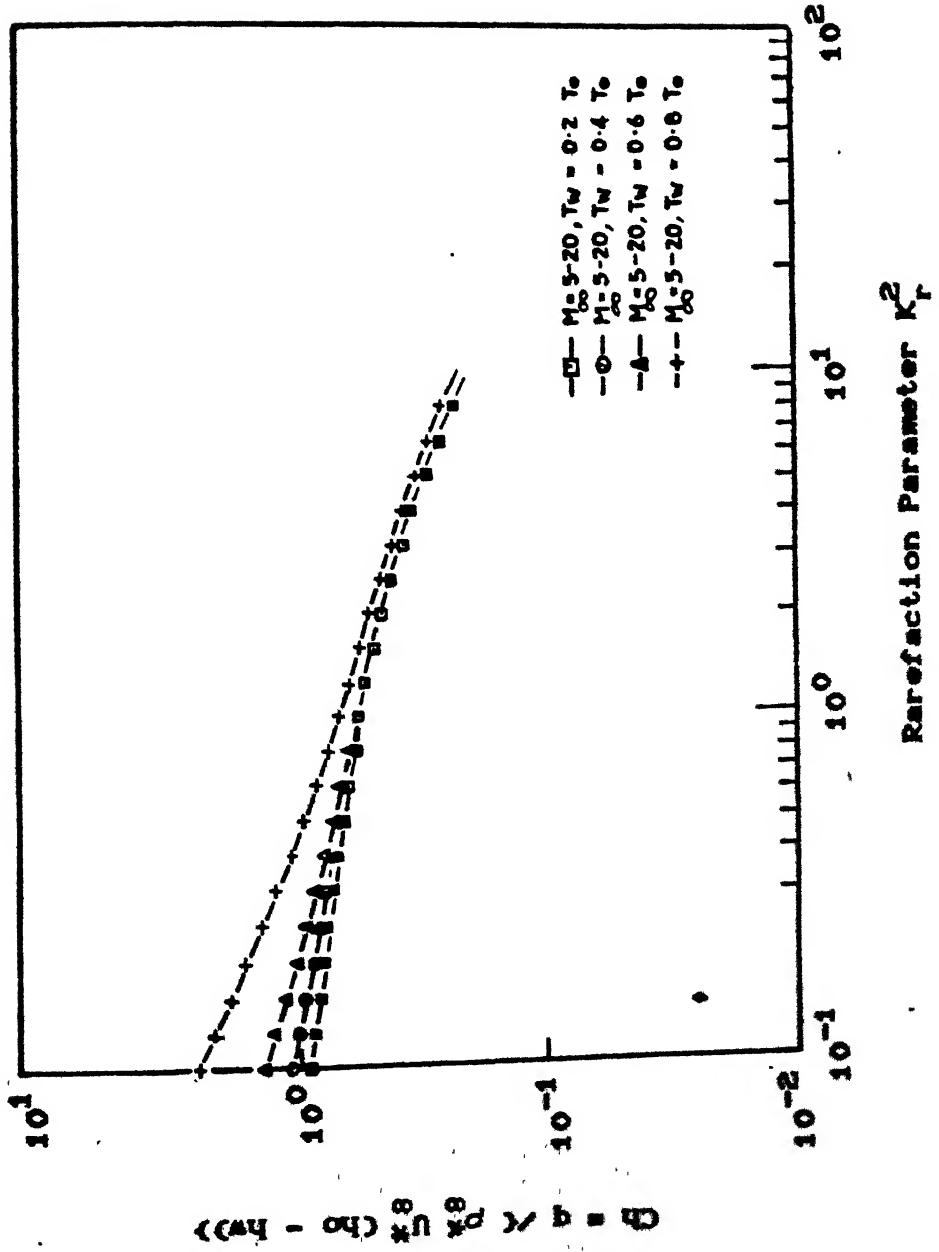


Fig: 4.28 INFLUENCE OF SURFACE TEMPERATURE ON HEAT  
TRANSFER COEFFICIENT

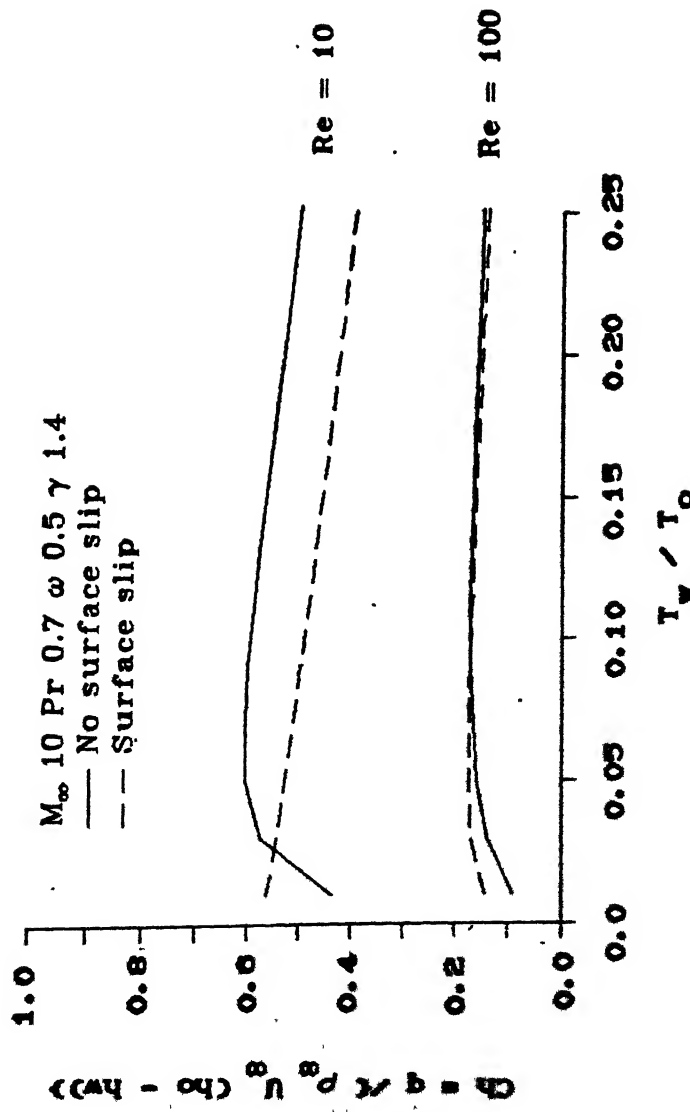


FIG: 4.29 INFLUENCE OF SURFACE SLIP ON HEAT FLUX

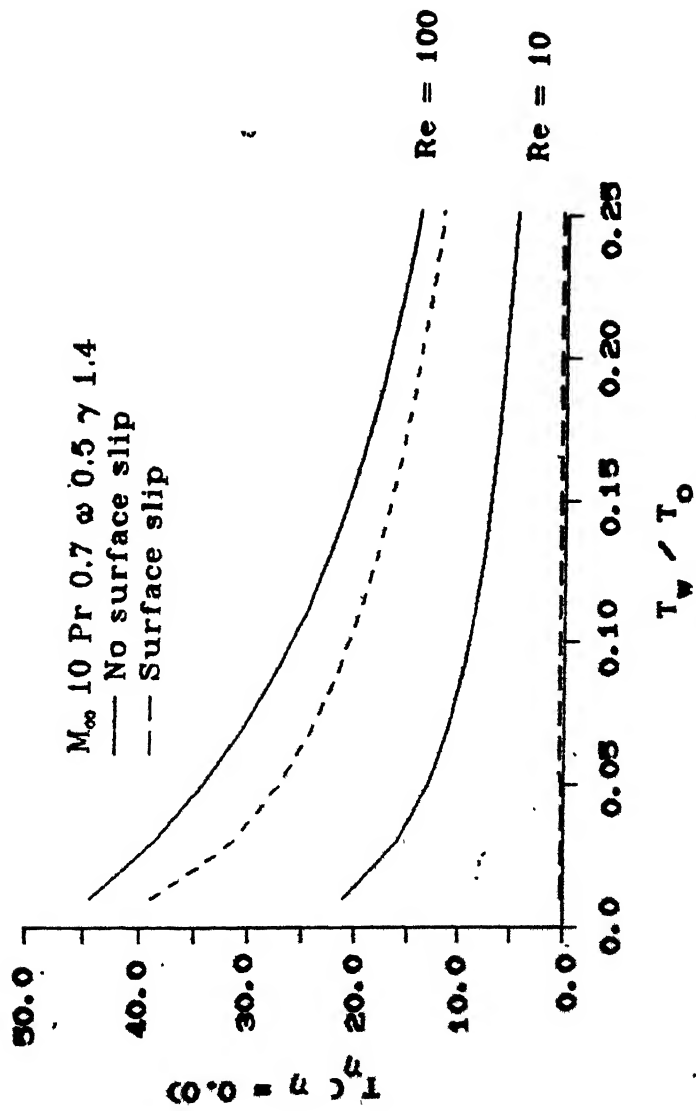


FIG. 4.30 INFLUENCE OF SURFACE SLIP ON TEMPERATURE GRADIENT AT WALL

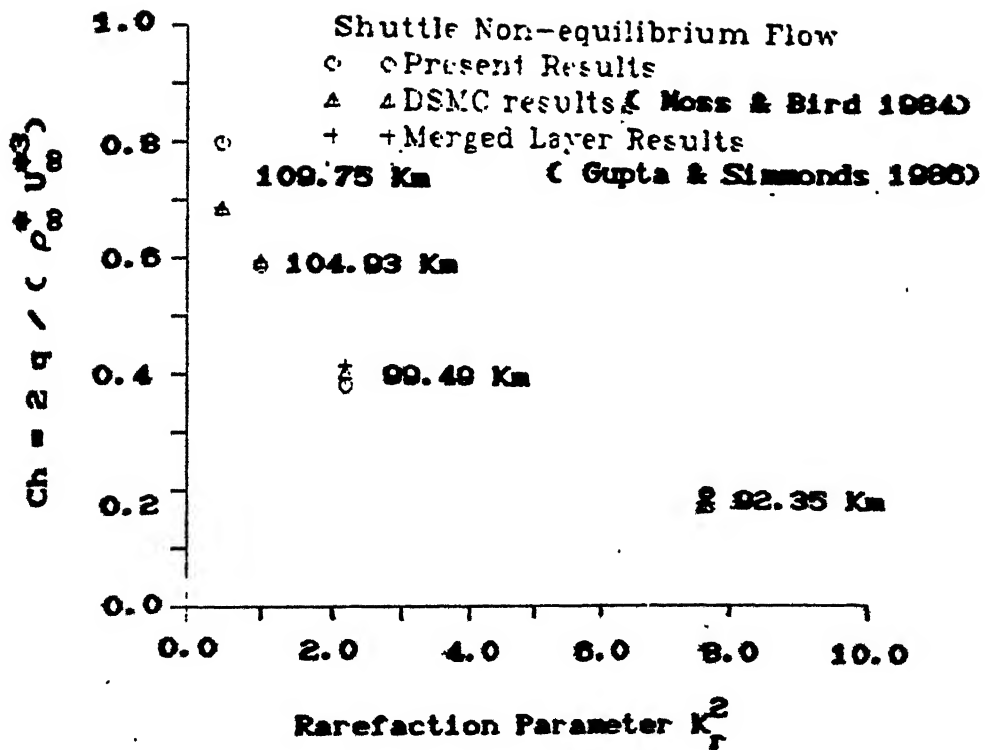
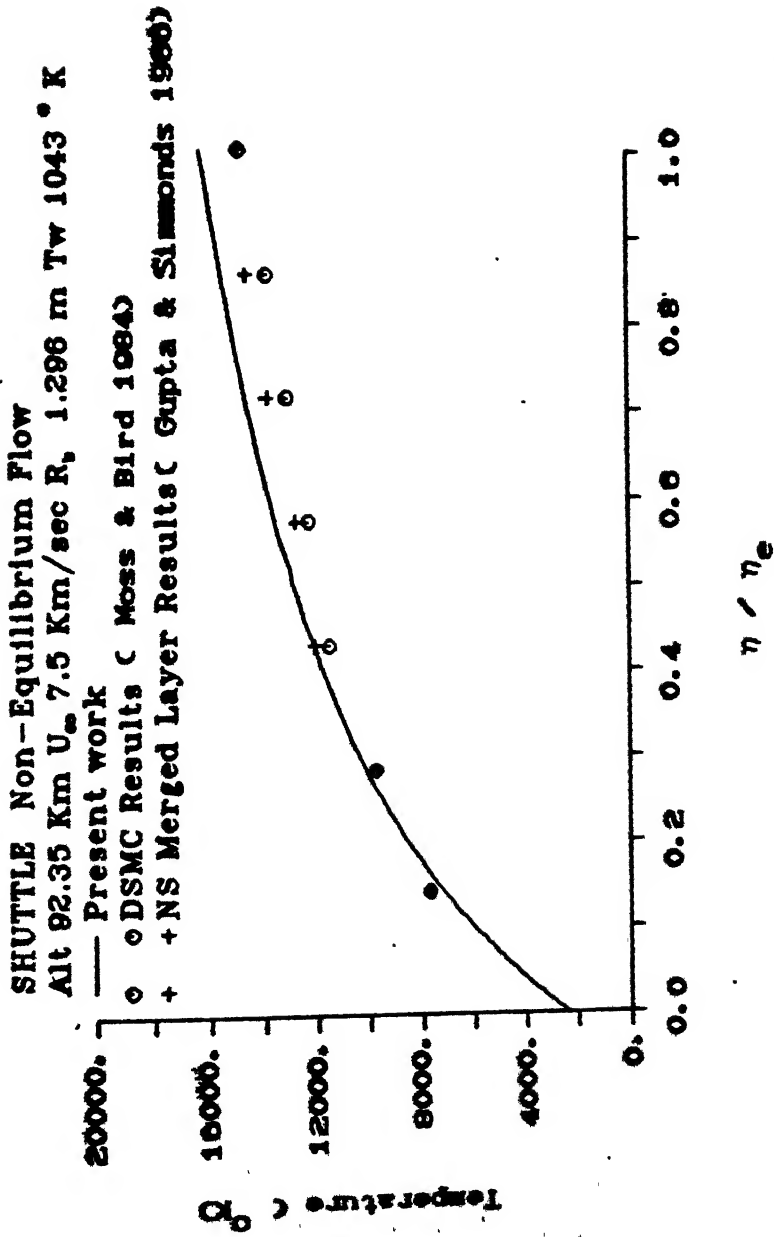


FIG: 4.31 VARIATION OF HEAT TRANSFER COEFFICIENT WITH  
 RAREFACTION PARAMETER FOR SHUTTLE



**FIG. 4.32 TEMPERATURE DISTRIBUTION FOR SHUTTLE FOR 92.35 Km**

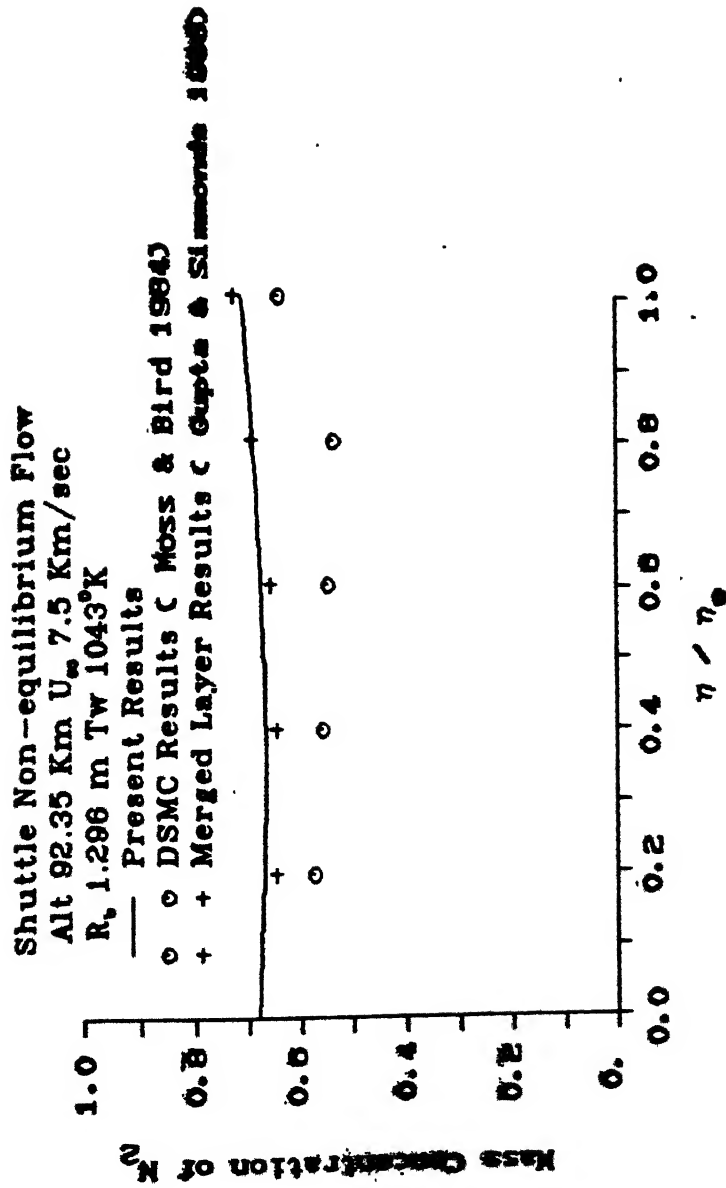


FIG: 4.33 CONCENTRATION PROFILE OF  $N_2$  FOR SHUTTLE

FOR 92.35 KM

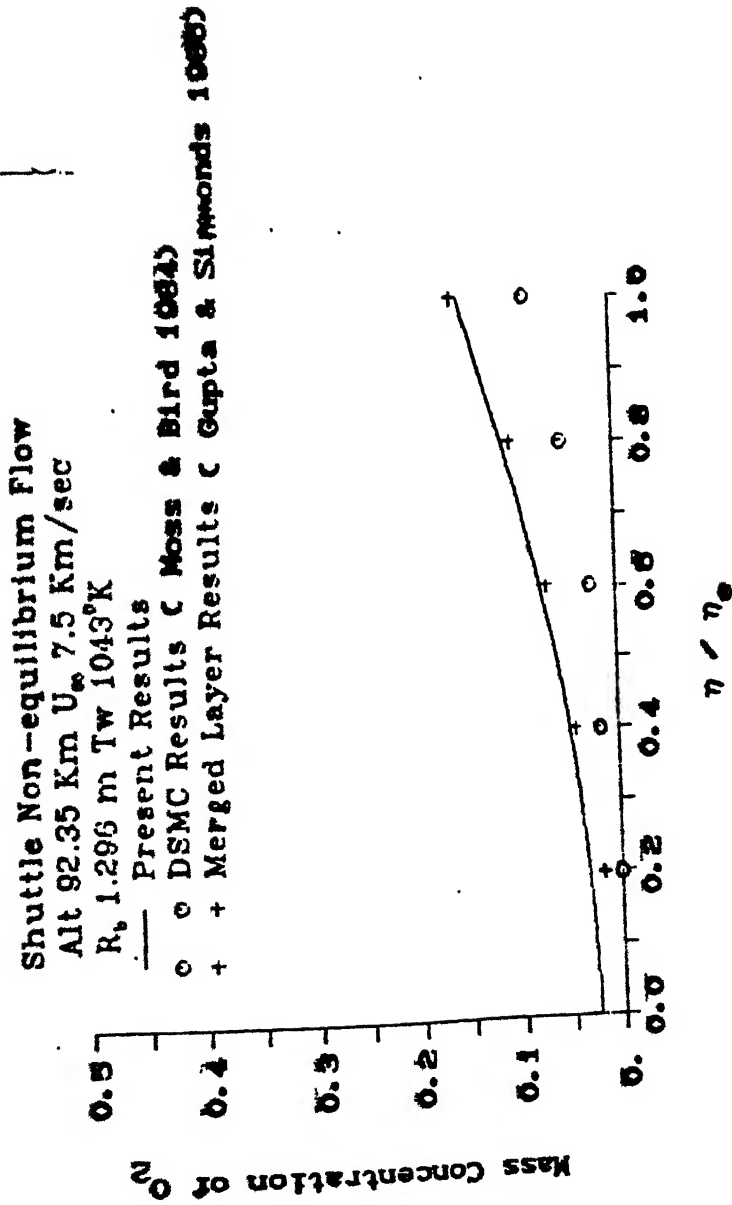


FIG. 4.34 CONCENTRATION PROFILE OF  $O_2$  FOR SHUTTLE  
 FOR 92.35 KM



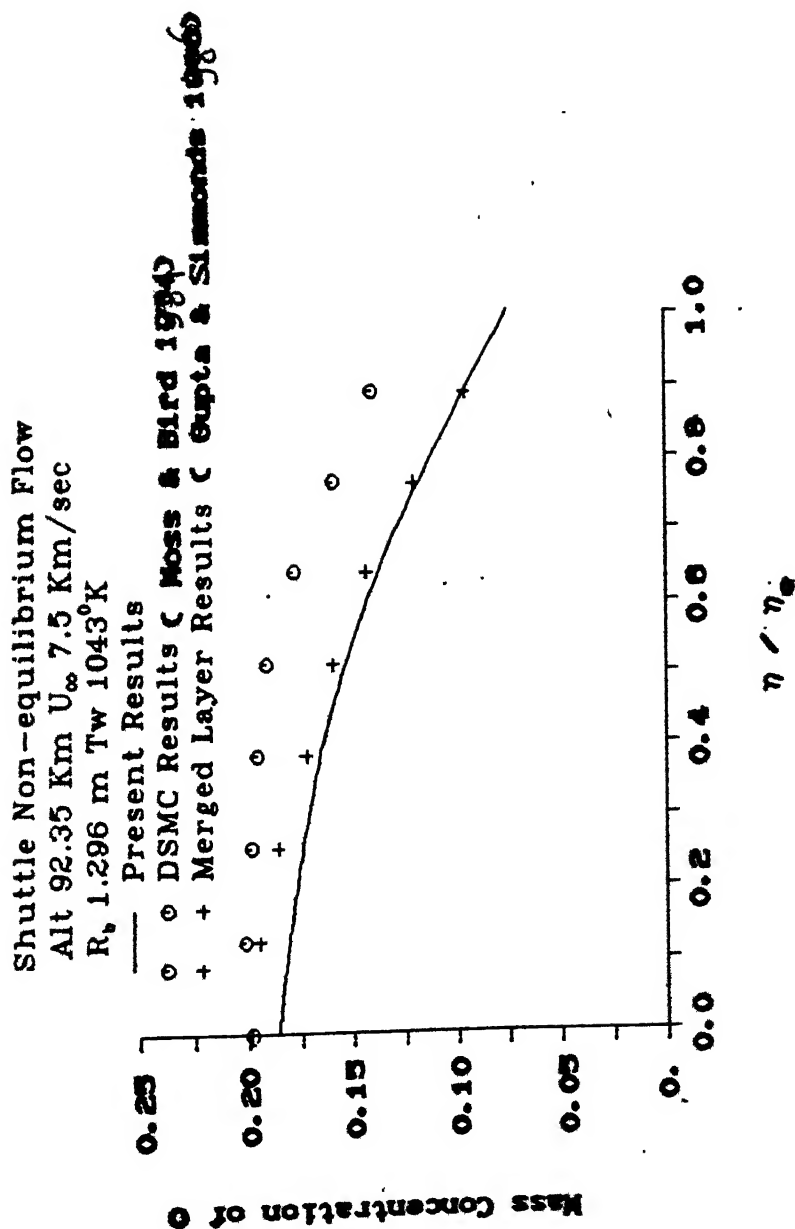


FIG: 4.35 CONCENTRATION PROFILE OF O FOR SHUTTLE FOR

92.35 KM

Shuttle Non-equilibrium Flow  
 Alt 92.35 Km  $U_\infty$  7.5 Km/sec  
 $R_e$  1.296 m Tw 1043°K  
 — Present Results  
 ○ DSMC Results C Moss & Bird 1980  
 + Merged Layer Results C Gupta & Srinivasan 1986

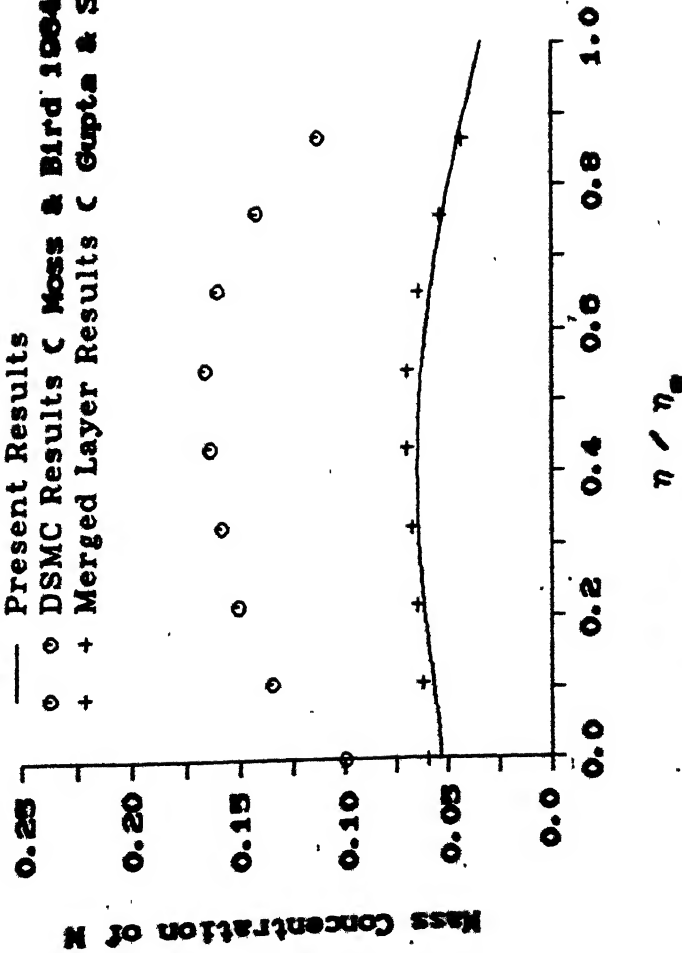


FIG. 4.36 CONCENTRATION PROFILE OF N FOR SHUTTLE  
 FOR 92.35 KM

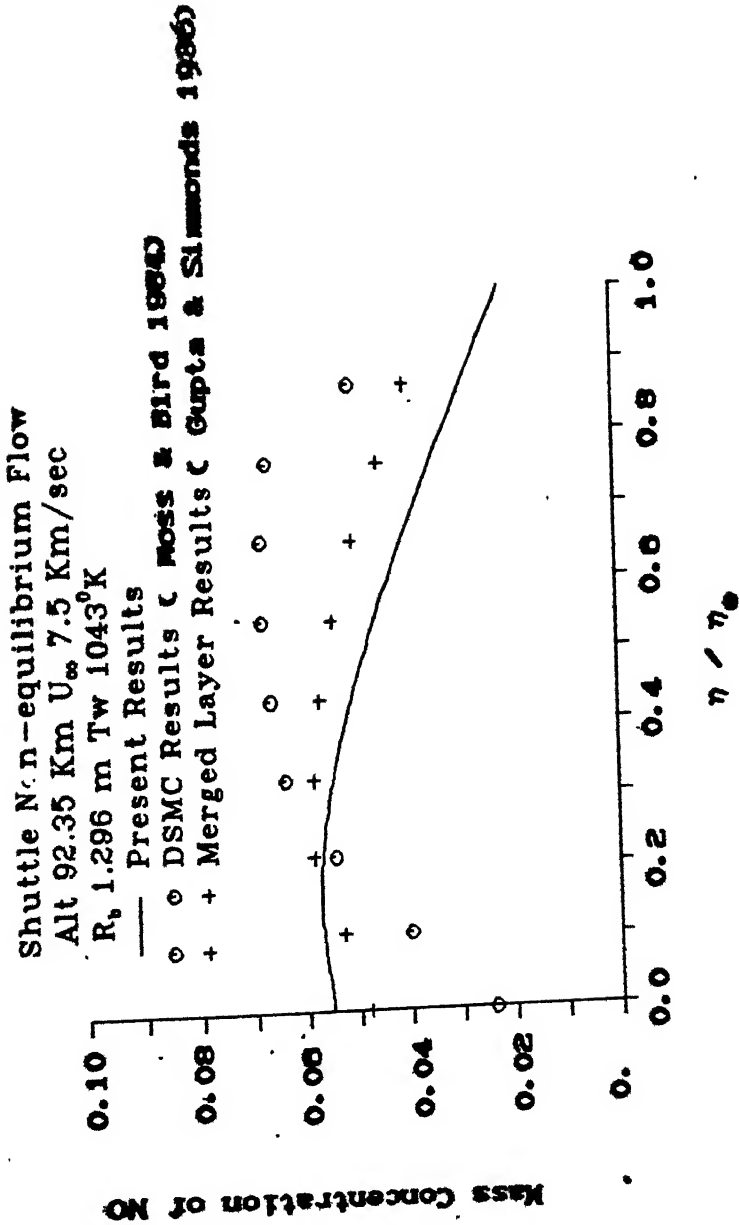


FIG: 4.37 CONCENTRATION PROFILE OF NO FOR SHUTTLE  
FOR 92.35 KM

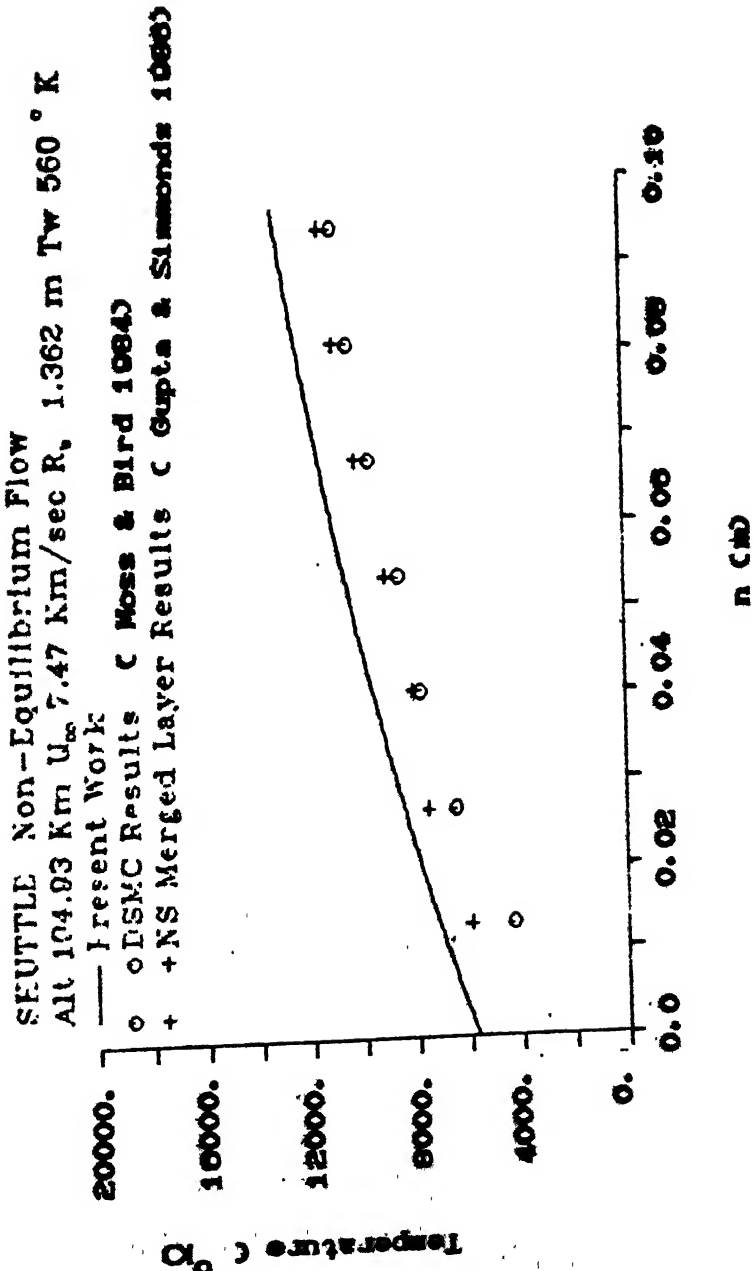
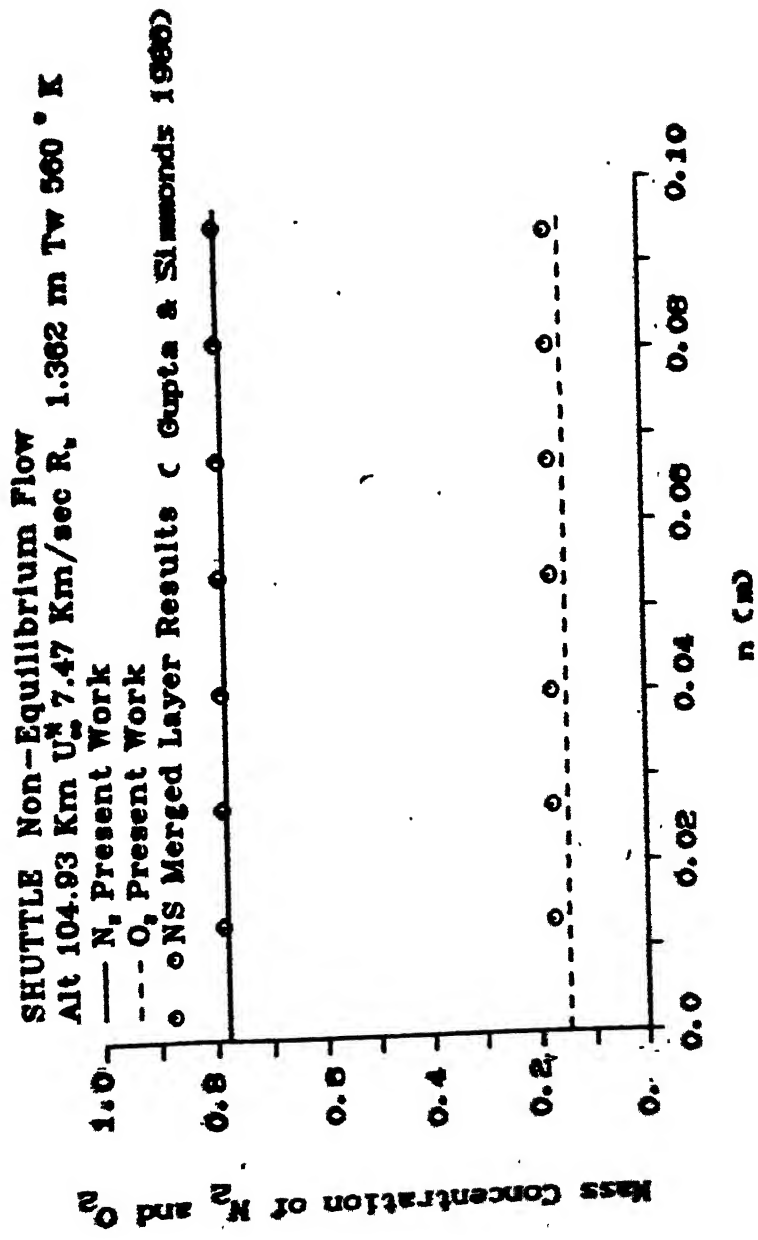


FIG: 4.38 TEMPERATURE DISTRIBUTION FOR SHUTTLE FOR 104.93 Km



**FIG: 4.39 CONCENTRATION PROFILE OF  $N_2$  AND  $O_2$  FOR SHUTTLE FOR 104.93 KM**

Shuttle Non-equilibrium Flow  
Armaly & Sutton Correlation

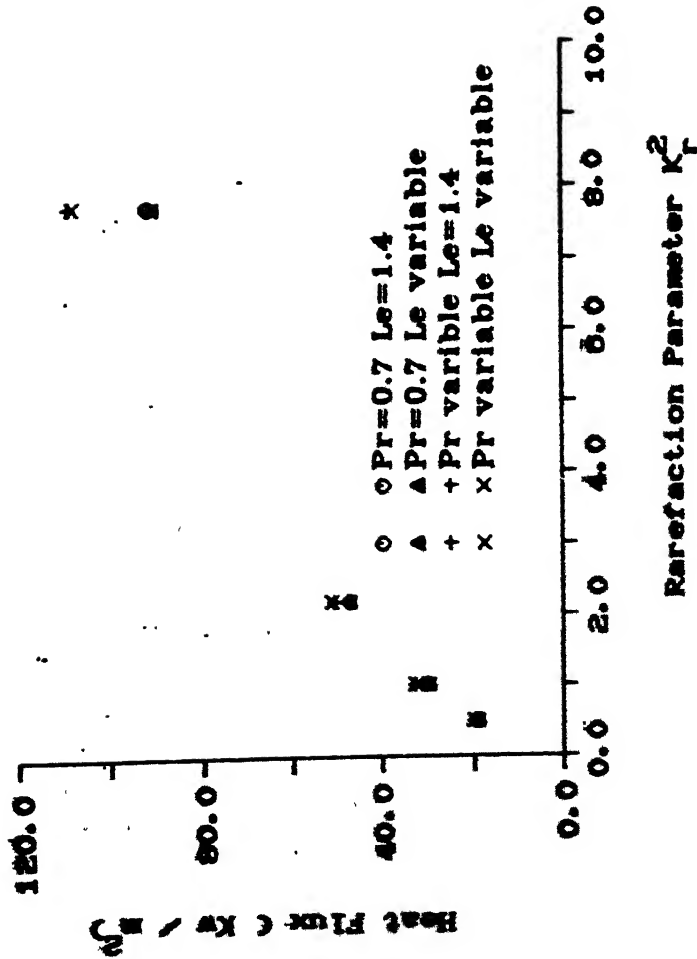


FIG.4.10 INFLUENCE OF TRANSPORT PROPERTY VARIATION ON HEAT  
FLUX WITH ARMALY & SUTTON CORRELATION

Shuttle Non-equilibrium Flow  
Wilke's Correlation

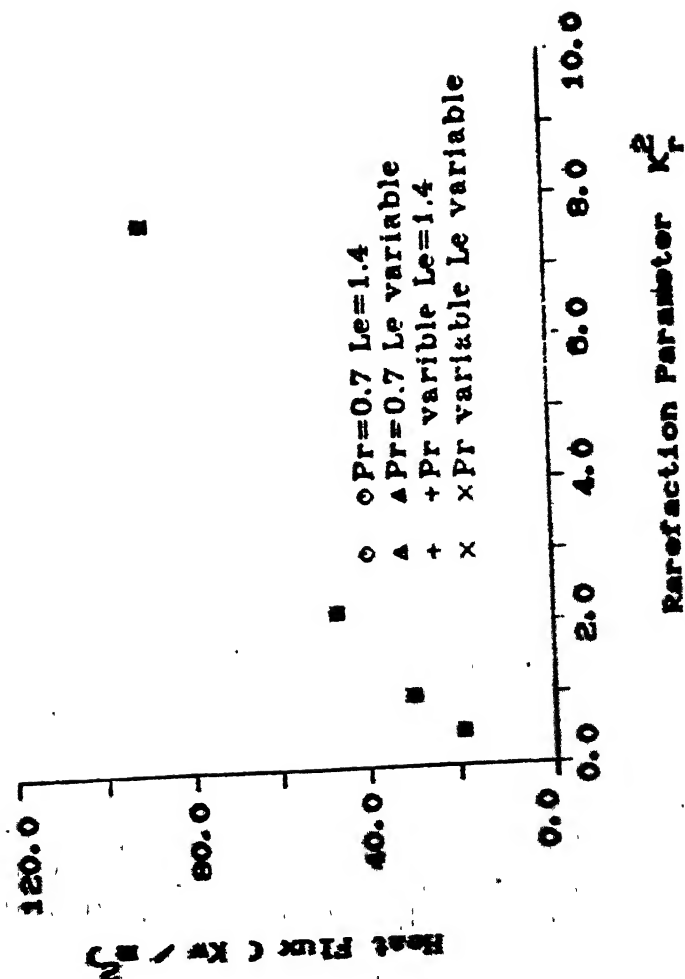


FIG.4.1 INFLUENCE OF TRANSPORT PROPERTY VARIATION ON HEAT  
FLUX WITH WILKE'S CORRELATION

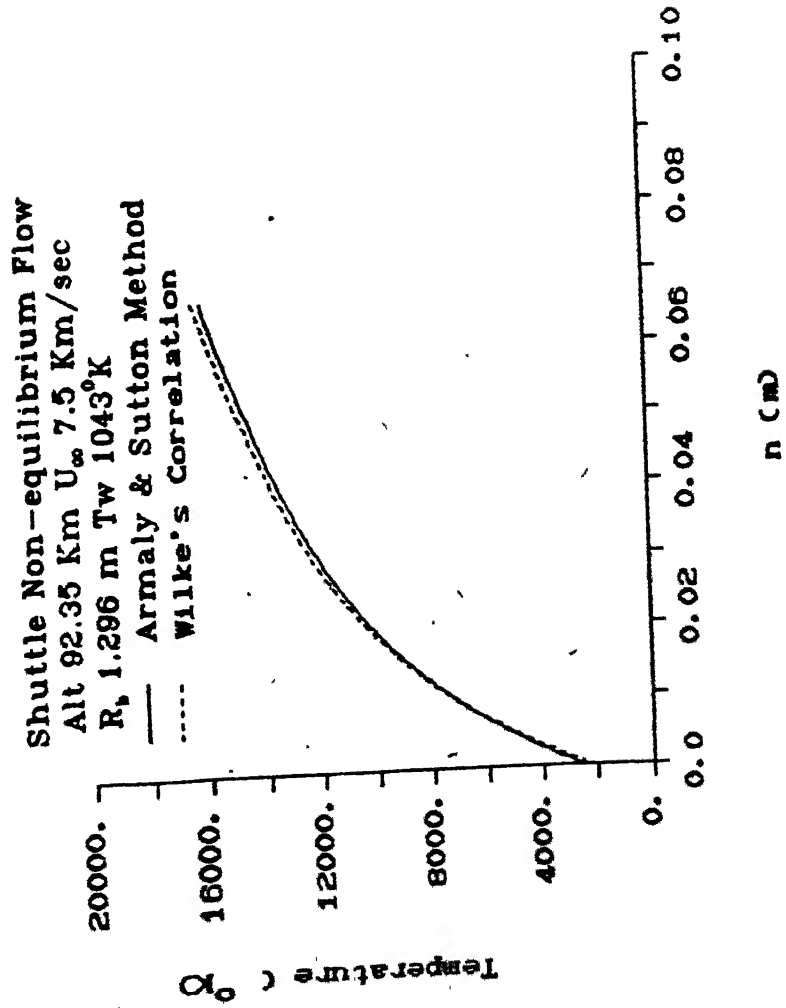


FIG: 4.42 INFLUENCE OF MIXTURE PROPERTY CORRELATION ON TEMPERATURE PROFILE



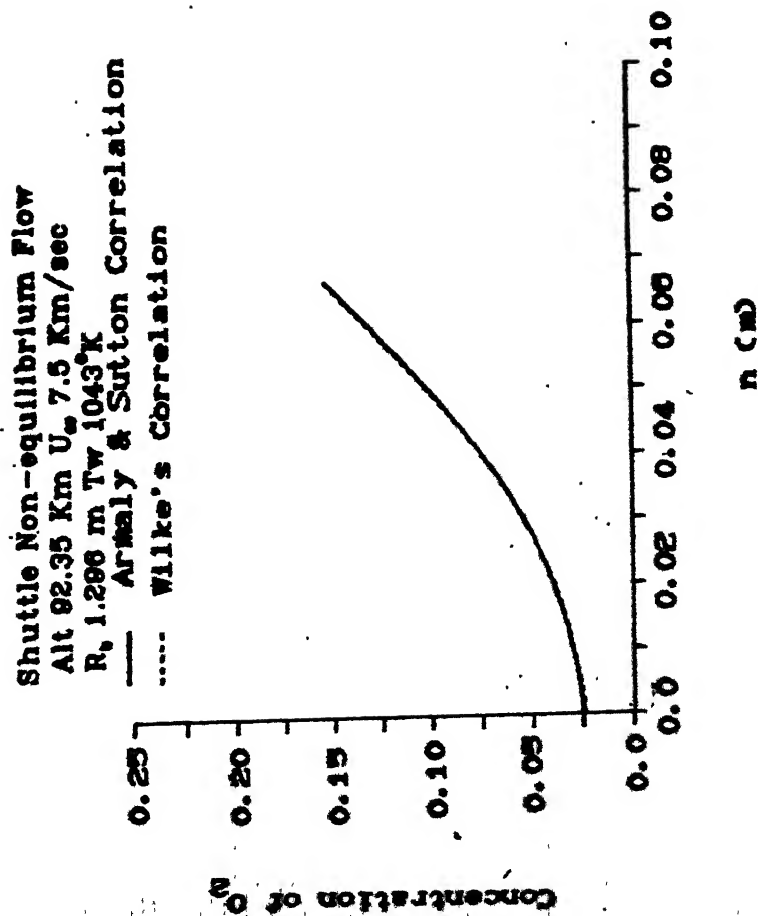


FIG. 4.44 INFLUENCE OF MIXTURE PROPERTY CORRELATION ON  
 CONCENTRATION PROFILE OF O<sub>2</sub>

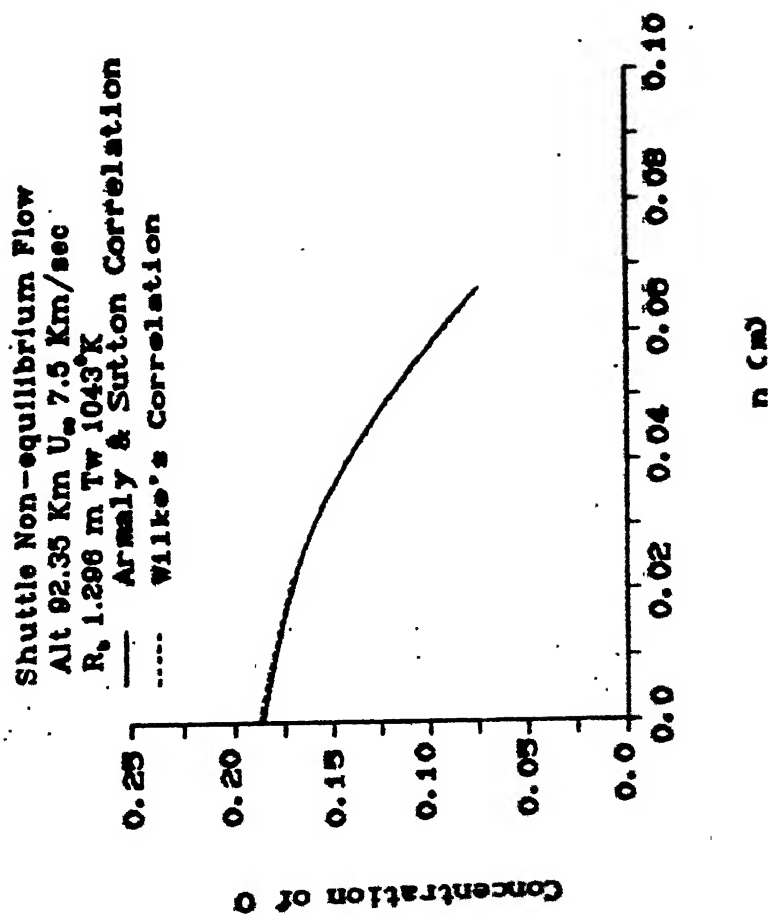


FIG: 4.45 INFLUENCE OF MIXTURE PROPERTY CORRELATION ON  
 CONCENTRATION PROFILE OF O

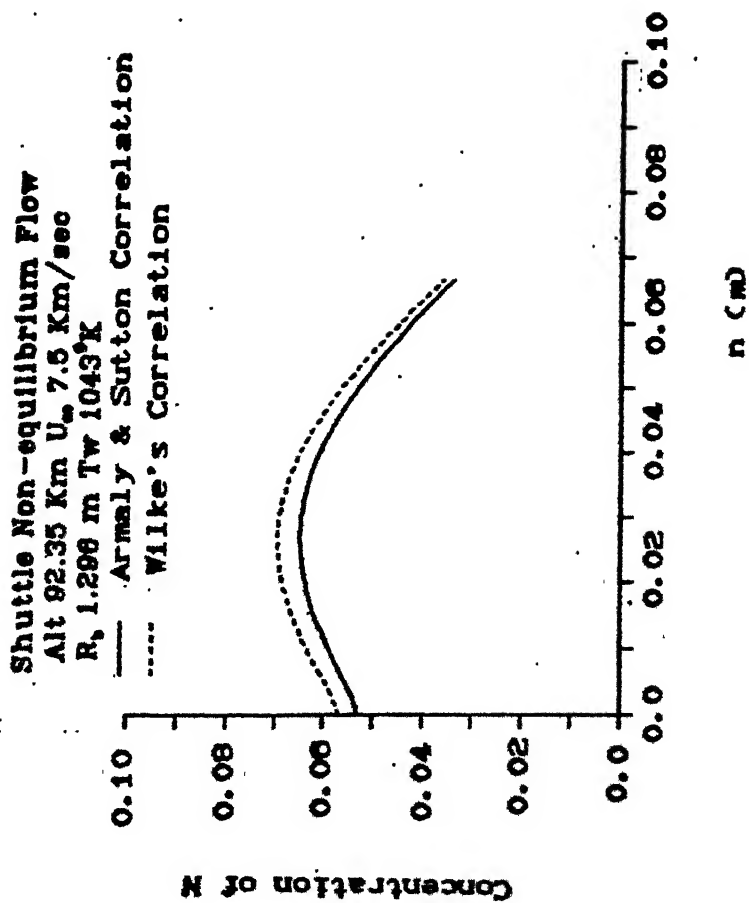


FIG. 4.46 INFLUENCE OF MIXTURE PROPERTY CORRELATION ON  
 CONCENTRATION PROFILE OF N

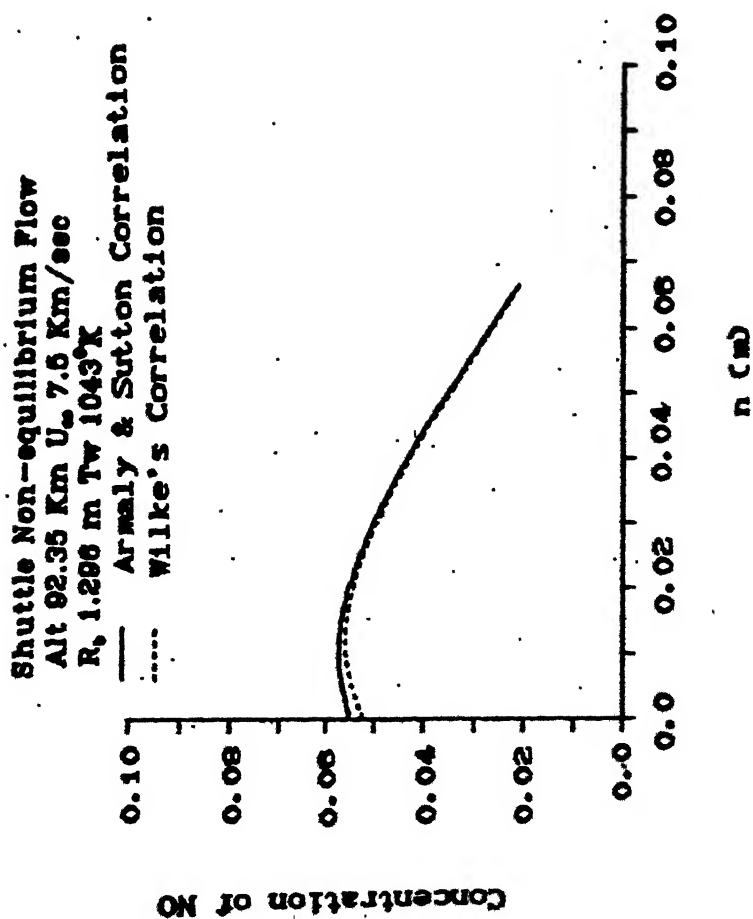


FIG: 4.47 INFLUENCE OF MIXTURE PROPERTY CORRELATION ON  
 CONCENTRATION PROFILE OF NO

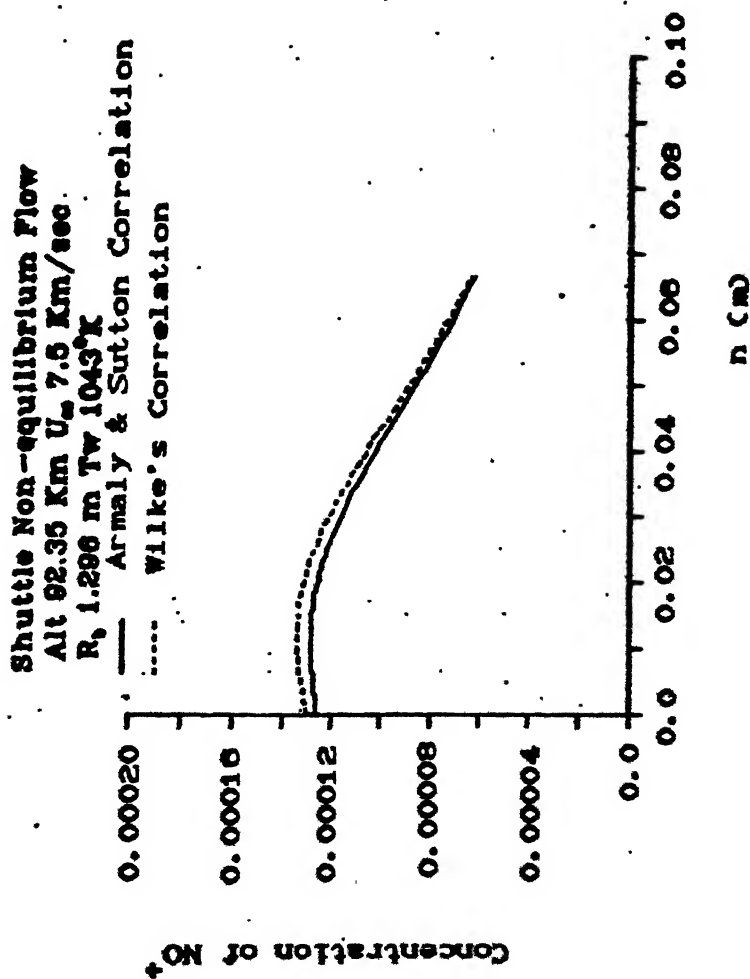


FIG: 4.48 INFLUENCE OF MIXTURE PROPERTY CORRELATION ON  
 CONCENTRATION PROFILE OF  $\text{NO}^+$

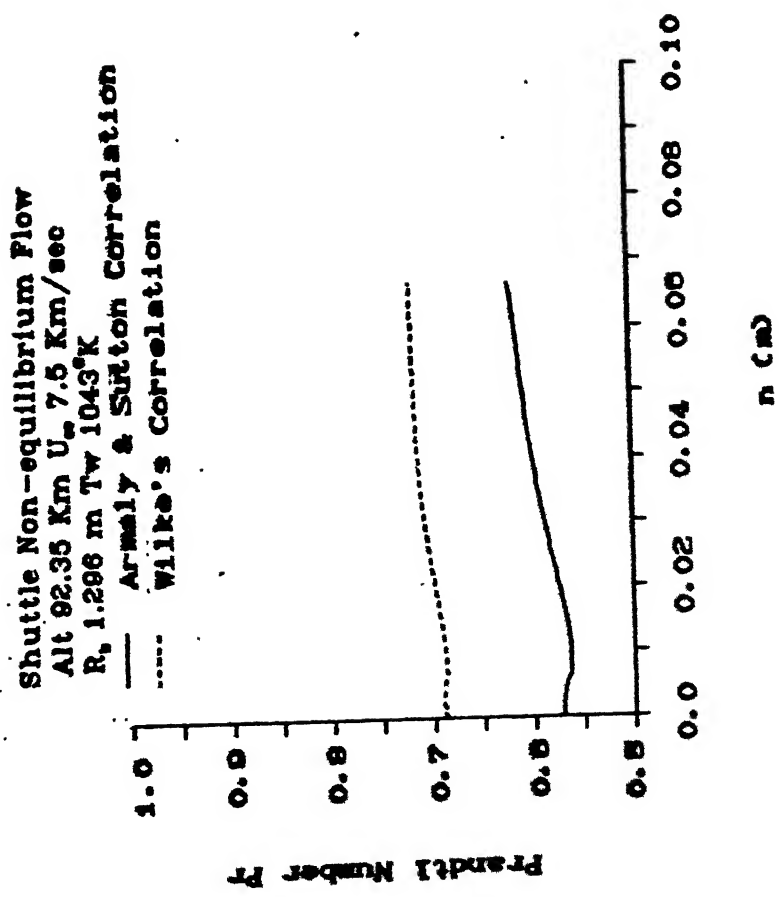
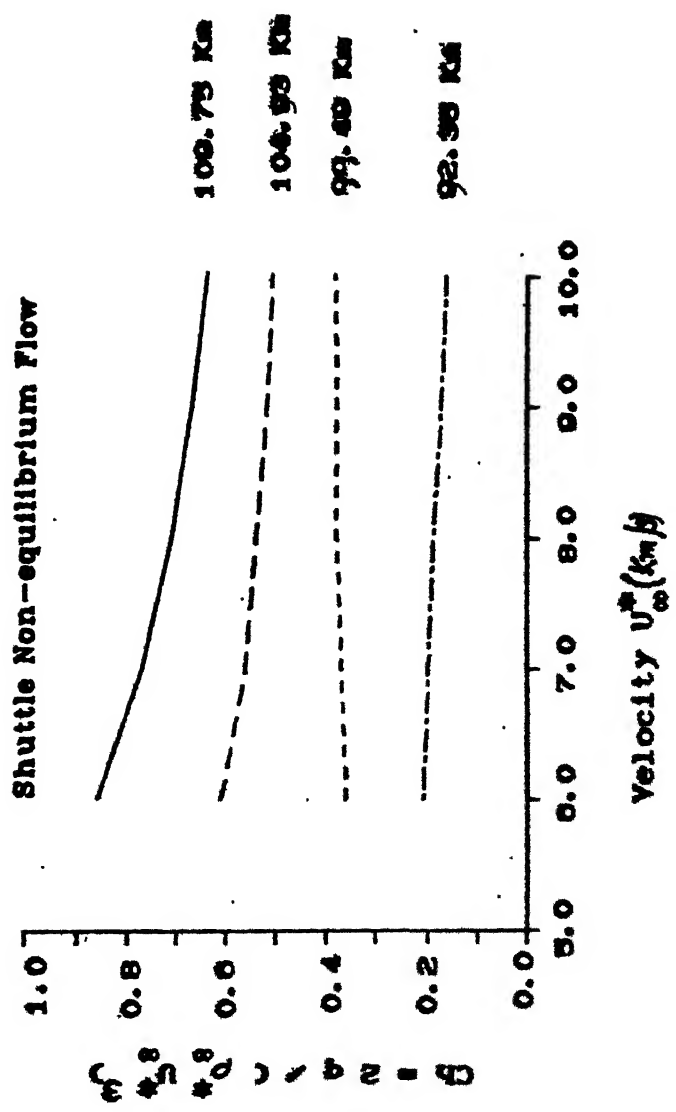
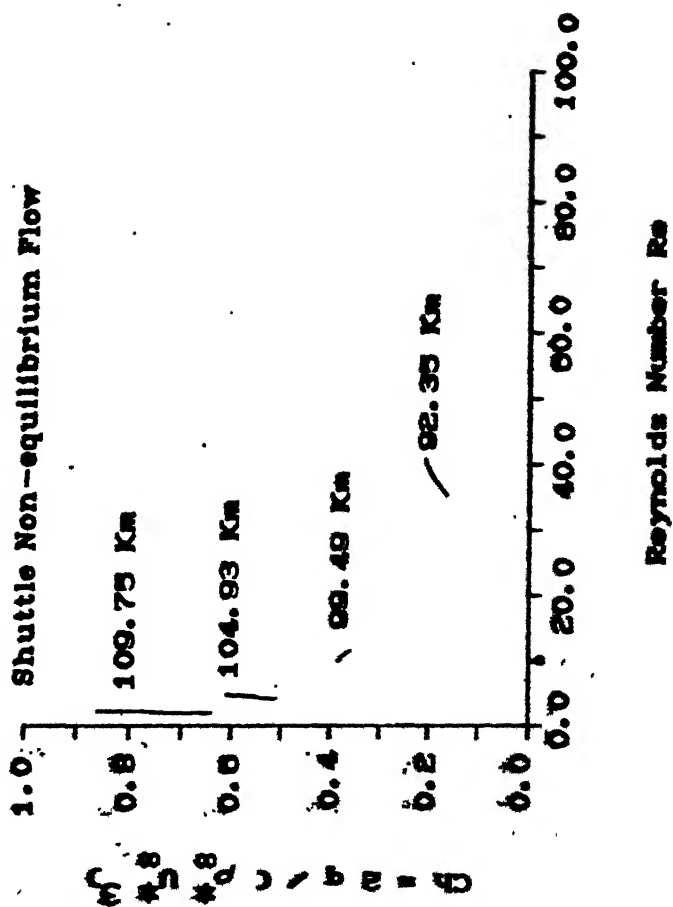


FIG. 4.49 INFLUENCE OF MIXTURE PROPERTY CORRELATION ON PRANDTL NUMBER PROFILE



**FIG: 4.50 INFLUENCE OF FREESTREAM VELOCITY ON CH**



**FIG. 4.51 INFLUENCE OF FREESTREAM VELOCITY ON  $C_H$  VS  $Re$**



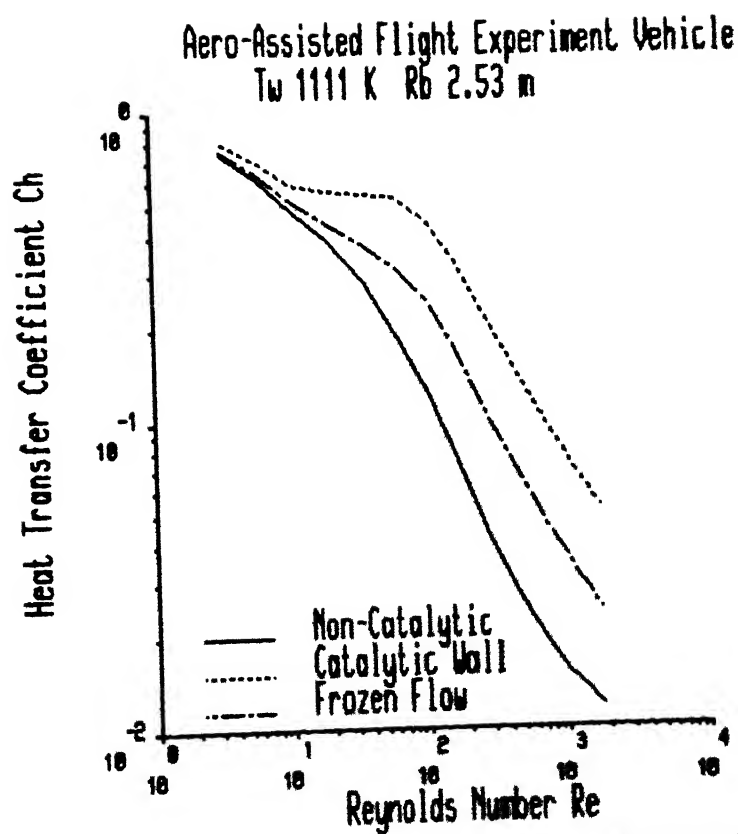


Fig:4.52 Heat Transfer Coefficient for AFE Vehicle

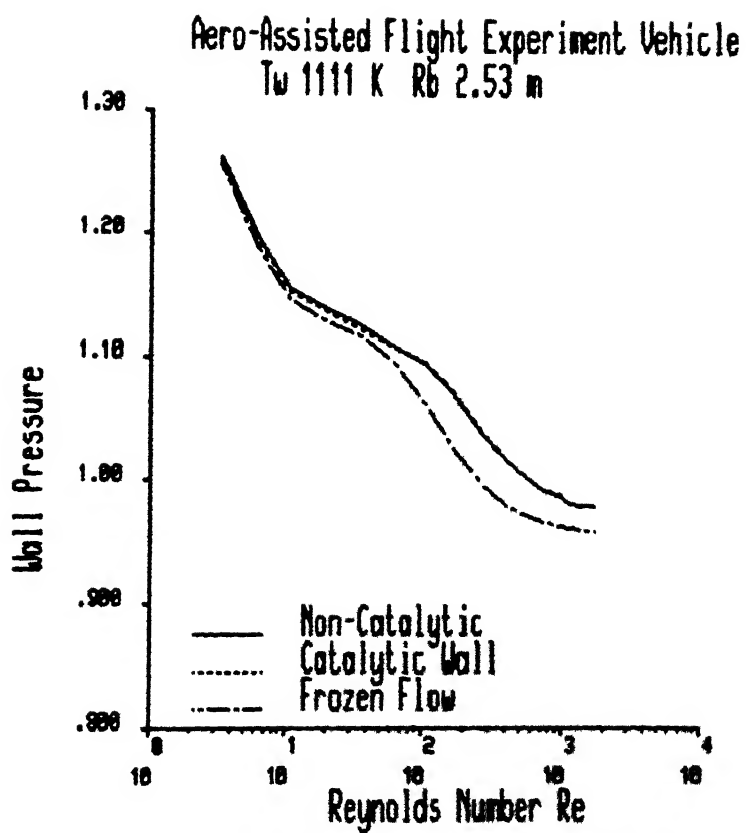


Fig:4.53 Wall Pressure for AFE Vehicle

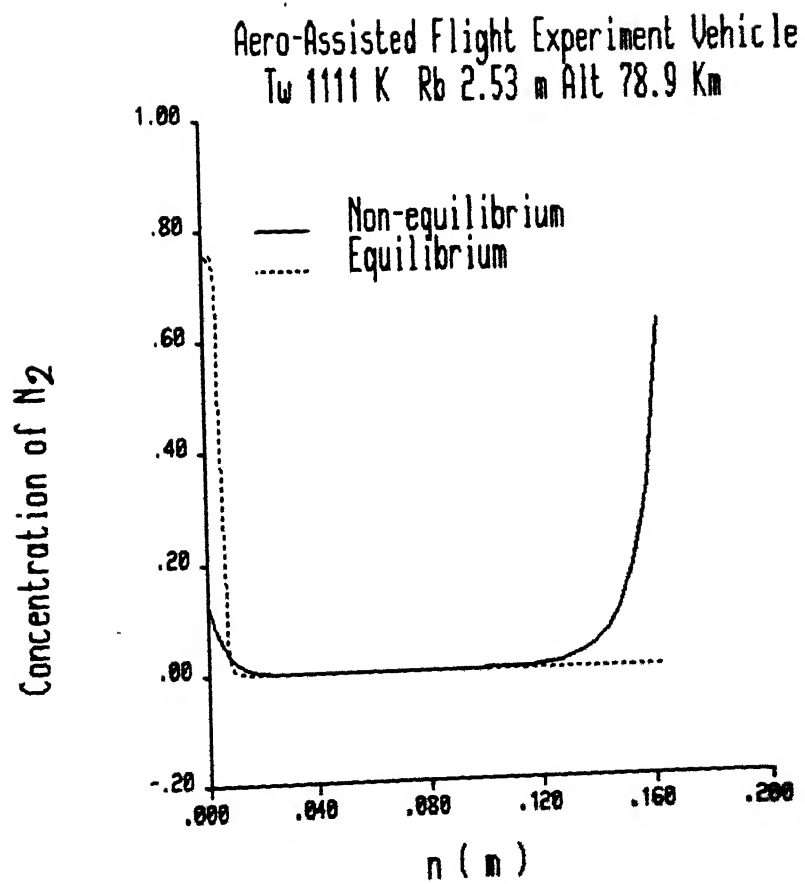


Fig:4.54 Comparison of  $N_2$  Concentration for AFE Vehicle

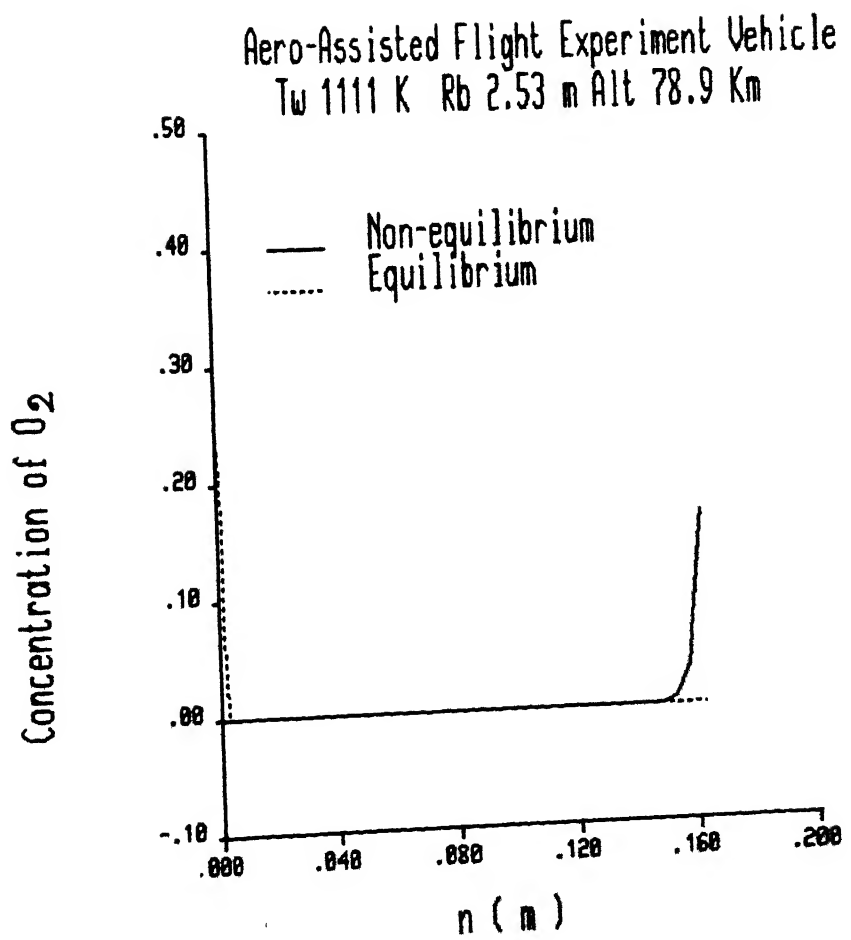


Fig.4.55 Comparison of  $O_2$  Concentration for AFE Vehicle

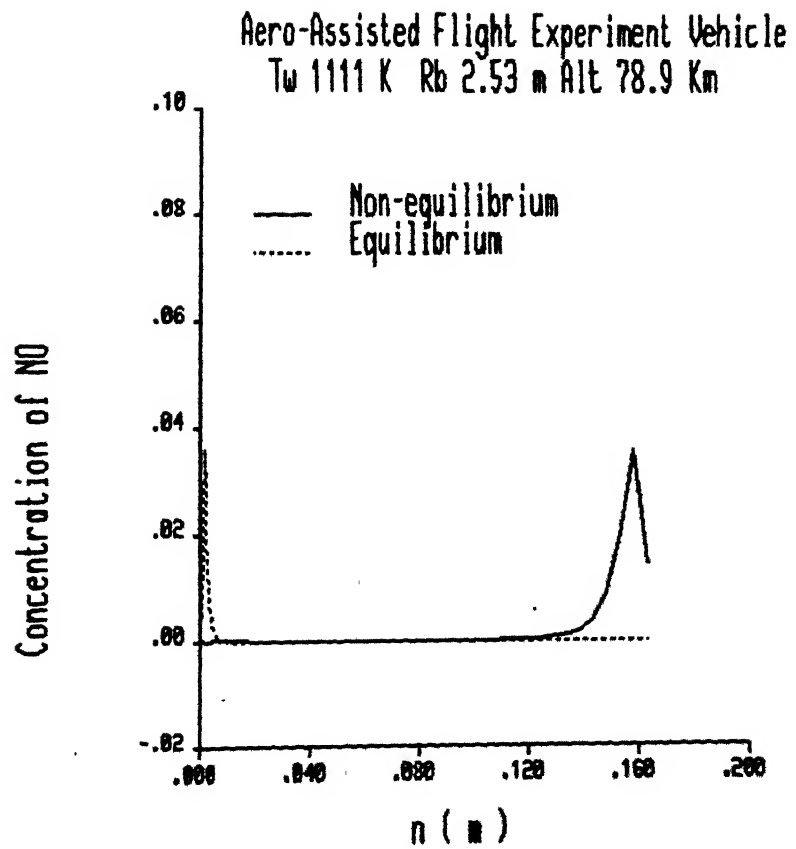


Fig:4.56 Comparison of NO Concentration for AFE Vehicle

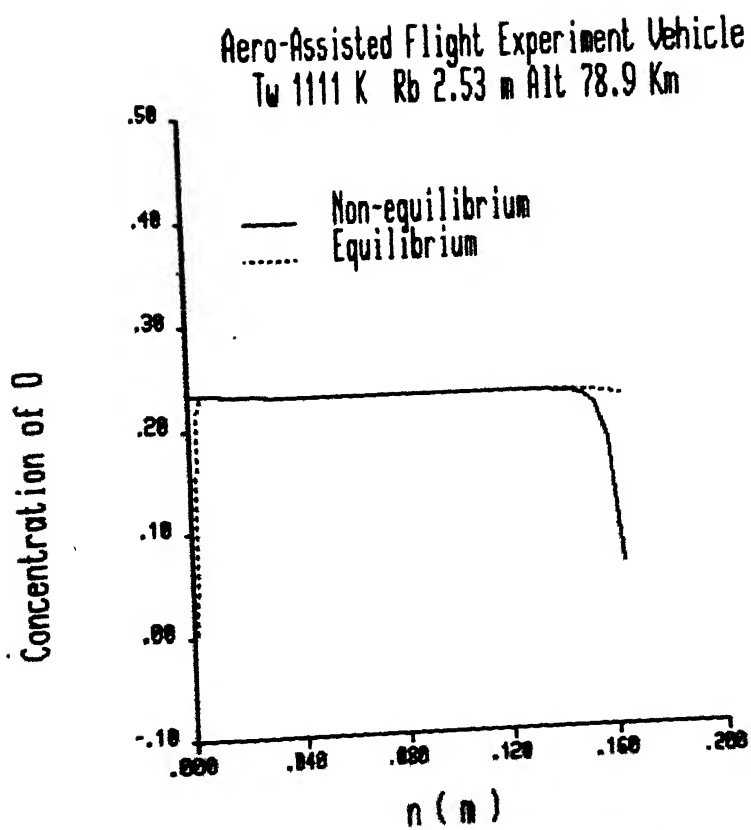


Fig:4.57 Comparison of O Concentration for AFE Vehicle

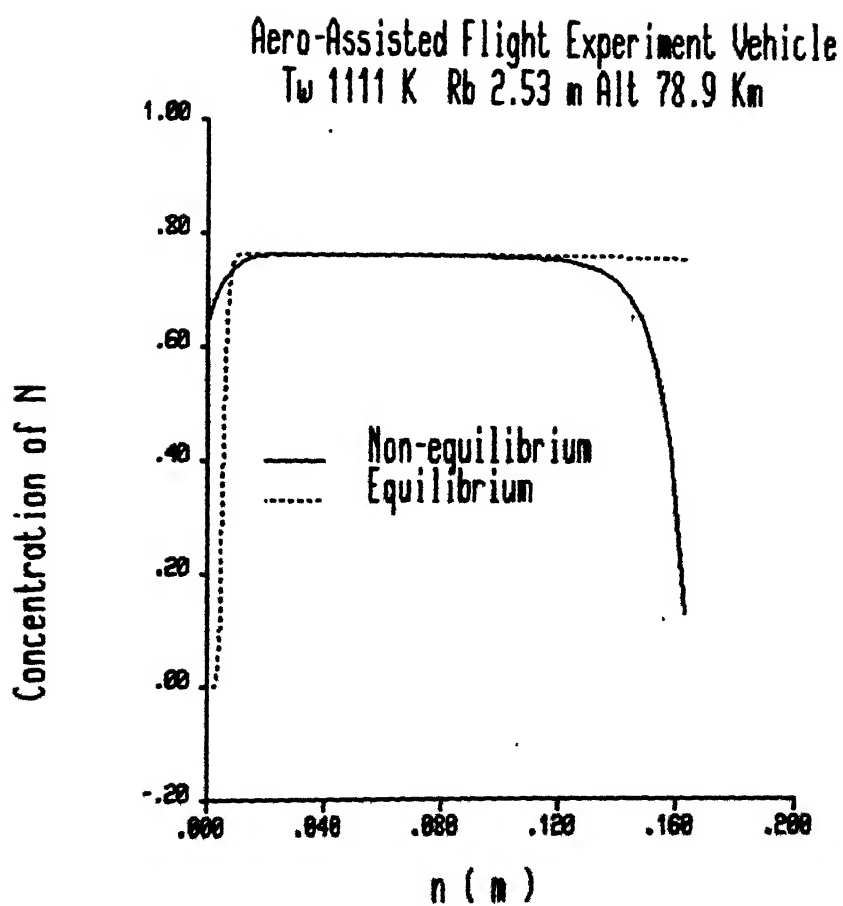


Fig:4.58 Comparison of N Concentration for AFE Vehicle

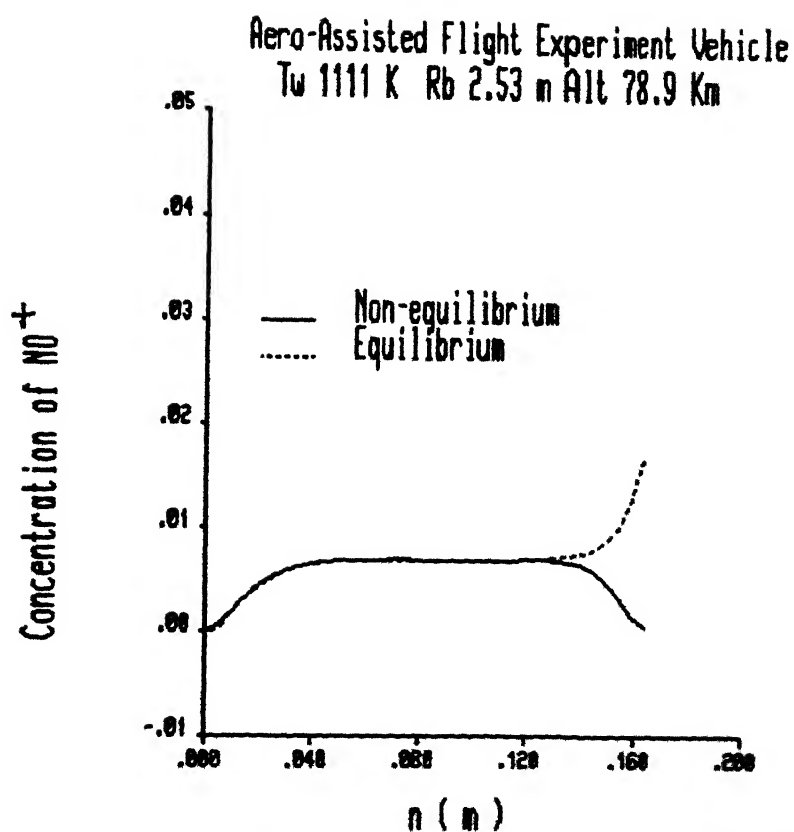


Fig:4.59 Comparison of  $\text{NO}^+$  Concentration for AFE Vehicle



## CHAPTER 5

### CONCLUSIONS

#### 5.1 Introduction

In this chapter, the results of the present investigation are summarised. These results have already been discussed in Chapter 4, where the detailed results of the present work were presented and were compared with other continuum, DSMC and experimental results. The salient features of these results are reiterated here with a view to evaluate how far the questions raised in section 1.4 have been answered. These questions are:

- (i) Is it possible to extend the range of validity of shock layer method by use of full Navier-Stokes equations?
- (ii) How do the chemical reactions within the shock transition zone influence the shock layer flow-field at low Reynolds numbers, where the shock wave is thick?
- (iii) Is it possible to extend the range of Reynolds number for which non-equilibrium computations converge?
- (iv) How to overcome the violation of mass conservation law normally occurring in numerical studies of chemically reacting flows?

- (v) Is it possible to overcome the numerical instability caused by spurious negative concentrations?

The present work is motivated by the fact that most of the continuum analyses for the chemically reacting flow are being carried out by using either VSL/PNS method or merged layer approach. The governing Navier-Stokes equations are simplified in the VSL or PNS method. Certain terms are dropped from Navier-Stokes equations to simplify the governing equations. These terms are not negligible at low Reynolds number range and thus these methods fail to give the correct behaviour of flow structure and surface characteristics at low Reynolds number. This limits the applicability of the VSL and PNS methods. The merged layer method requires the solution of the Navier-Stokes equations from the body surface to the free-stream through the shock, which comes out as the part of the solution. The difficulties associated with the numerical integration of the Navier-Stokes equations make the numerical computations very expensive. Moreover, at higher Reynolds numbers, the shock becomes very thin making it difficult to resolve the shock structure unless a very fine grid is chosen. This limits the applicability of the merged layer method. Moreover, the numerical problems associated with the chemically reacting flow, namely the numerical violation of overall mass conservation due to chemical reactions and instability caused by spurious negative

concentrations, also need to be resolved.

In the present work, full Navier-Stokes equations for chemically reacting flow are integrated in the stagnation zone. The equations are integrated numerically between the body and the shock using surface slip and the shock slip boundary conditions. The important results are briefly discussed in the following sections.

## 5.2 Extension of Validity of Shock Layer Approach with Full Navier-Stokes Equations

It is known that the stagnation point heat transfer rates predicted by Cheng's two thin layer theory agree well with the experimental values even at very low Reynolds numbers. However, experimental investigations by Ahouse and Bogdonoff (1969) on detailed flow field in the stagnation region, Monte Carlo simulation of the flow field at low Reynolds number (Vogenitz and Takata, 1970) raised the doubt on the validity of the two thin layer approach. Ahouse and Bogdonoff (1969) attributed this discrepancy to the failure of continuum approach. This failure was attributed by Jain and Adimurthy (1974) to the thin layer approximations. The present solution, using full Navier-Stokes equations in the shock layer, shows a fairly good agreement with the experimental data and Monte Carlo results as discussed in Chapter 4. The use of full Navier-Stokes equations in the shock layer predicts

following additional features which the VSL model fails to predict even qualitatively .

- (i) Behaviour of the predicted wall pressure agrees well with the experimentally observed behaviour of wall pressure at low Reynolds number.
- (ii) Theoretically predicted recovery factor agrees well with the experimentally observed recovery factor in the low Reynolds number regime.
- (iii) There is a reasonably good agreement between the predicted temperature and density profiles and experimental data.
- (iv) It is also observed that at higher Reynolds number, the computed heat transfer coefficient agrees well with boundary layer prediction for the heat transfer coefficient. However, this phenomenon is also true of shock layer model.

These factors show that the use of full Navier-Stokes equations reproduces many important features of the hypersonic rarefied flow. At the same time at higher Reynolds number, this formulation yields the results which are in good agreement with boundary layer theory predictions.

### 5.3 Influence of Chemical Reactions in Shock Transition Zone on the Flow Field

In the present analysis, derivation of shock slip conditions/post shock conditions assumes an infinitely

thin shock. This tacitly assumes that chemical reactions in the shock transition zone do not influence the post shock chemical composition. The thickness of the shock transition zone increases as the Reynolds number decreases. Due to high temperature in the shock transition zone, the reactions are fast. With increased thickness of the shock transition zone, it is possible that post shock composition will be different from the free stream composition.

Merged layer and DSMC methods solve the flow field through the shock transition zone and thus include the influence of chemical reactions in the shock transition zone on the flow field. It is observed that the computed profiles agree well with the profiles obtained from merged layer analysis and DSMC results. This shows that the influence of chemical reactions in the shock transition zone on the flow field is not significant. The influence of chemical reactions in the shock transition zone, if any, is limited to the neighbourhood of the shock.

#### **5.4 Convergence of Non-Equilibrium Computational Procedure**

The computer code based on present formulation was run for a wide range of free-stream conditions. No convergence problem was noticed for APE trajectory for which

where  $Re_s$  is the Reynolds number based on the post shock conditions. It is observed that non-equilibrium computations capture equilibrium concentrations in most of the shock layer at higher Reynolds number. The upper limit of  $Re_s$  for convergence of non-equilibrium code for viscous shock layer (VSL) model was reported to be 500 by Moss(1971). Thus it is seen that use of full Navier-Stokes equations along with UDR scheme and present treatment of mass production terms has increased the range of Reynolds number for which non-equilibrium analysis converges.

### 5.5 Mass Conservation and Species Concentrations

The violation of mass conservation normally occurring in the numerical studies of chemically reacting flows, is taken care of by considering the elemental mass conservation at each iteration as explained in section 3.4. This treatment of production terms ensures that at each iteration, overall mass is conserved with change in concentration of various species. This treatment also ensures that overall mass is conserved with change in temperature in the presence of chemical reactions.

At any iteration, occurrence of spurious negative concentrations will result in improper estimation of production term. This may lead to breakdown of solution procedure. This is taken care of by specifying the bounds for the concentration of the various species. The

concentrations are forced to be positive at any iteration. An upper limit has been specified for all these concentrations. This upper limit is estimated from the free stream composition of the air.

### 5.6 Some Problems for Further Research

The success of the full Navier-Stokes formulation in the shock layer method in describing the chemically reacting hypersonic flow in the stagnation region of a blunt body, encourages the following extensions to the present work.

- (i) Inclusion of radiative heat transfer effects in the present formulation for blunt body flow problem.
- (ii) Introduction of mass injection
- (iii) Introduction of multi-component diffusion and the influence of thermal and pressure diffusion.
- (iv) Introduction of chemical reaction between gas and surface material.
- (v) Investigation of influence of higher order approximations on the stagnation region.
- (vi) The present solution is limited to the stagnation region of a blunt body. This analysis can be extended to integrate Navier-Stokes equations in the downstream region of the blunt body with present solution taken as initial condition.

## REFERENCES

1. Ahouse, D. R. and Bogdonoff, S. M. (1969), An Experimental Flow Field Study of the Rarefied Blunt Body Problem, AIAA Paper 69-659, AIAA Fluid and Plasma Dynamics Conference, Sanfrancisco, California, June 16-18.
2. Armaly, B. F. and Sutton, K. (1980), Viscosity of Multicomponent Partially Ionised Gas Mixture Associated with Jovian Entry, AIAA Paper 80-1495, AIAA 15th Thermophysics Conference, Snowmass, Colorado, July 14-16 1980.
3. Armaly, B. F. and Sutton, K. (1981), Thermal Conductivity of Partially Ionised Gas Mixtures, AIAA Paper 81-1174, AIAA 16th Thermophysics Conference, Palo Alto, California, June 23-25, 1981.
4. Bhutta, B. A. and Lewis, C. H. (1988), Three Dimensional Hypersonic Nonequilibrium Flows at Large Angle of Attack, AIAA paper 88-2568, AIAA Applied Aerodynamics Conference, Virginia,
5. Bird, G. A. (1966), Aerodynamic Properties of Some Simple Bodies in the Hypersonic Transition Regime, AIAA Journal, Vol. 4, No. 1, pp 55-60.
6. Bird, G. A. (1976), Molecular Gas Dynamics, Clarendon Press, Oxford University, England.
7. Bird, G. A. (1981), Monte Carlo Simulation in an Engineering Context, AIAA Progress in Astronautics and Aeronautics, Rarefied Gas Dynamics, Vol. 74, Part I, Ed. S. S. Fisher, New York, pp 239-255.
8. Bird, R. B., Stewart, W. E. and Lightfoot, E. N. (1960), Transport Phenomena, John Willey and Sons, Inc.,
9. Blottner, F. G. (1964a), Chemical Nonequilibrium Boundary Layer, AIAA Journal, Vol. 2, No. 2, pp 232-240.
10. Blottner, F. G. (1964b), Nonequilibrium Laminar Boundary Layer Flow of Ionised Air, AIAA Journal, Vol. 2, No. 11, pp 1921-1927.



11. Blottner, F.G. (1969), Viscous Shock Layer at the Stagnation Point with Nonequilibrium Air Chemistry, AIAA Journal, Vol. 7, No. 12, pp 2281-2290.
12. Boylan, D.E (1971), Laminar Convective Heat Transfer Rates on a Hemi-Sphere Cylinder in Rarefied Hypersonic Flow, AIAA Journal, Vol. 9, No. 8, pp 1661-1663
13. Brokaw, R.S. (1958), Approximate Formula for the Viscosity and Thermal Conductivity of Gas Mixtures, Journal of Chem. Physics, Vol. 29, No. 2, pp 391-397
14. Brokaw, R.S. (1961), Alignment Charts for Transport Properties Viscosity, Thermal Conductivity and Diffusion Coefficient for Nonpolar Gases and Gas Mixtures at Low Density, NASA TR R-81, 1961
15. Bush, W.B. (1964), On the Viscous Hypersonic Blunt Body Problem, J. Fluid Mech., Vol. 20, Part 3, pp 353-367.
16. Candler, G.V. and MacCormack, R.W. (1988), The Computation of Hypersonic Ionised Flows in Chemical and Thermal Nonequilibrium, AIAA Paper 88-511, AIAA 26th Aerospace Science Meeting, Jan. 11-14, 1988, Reno, Nevada
17. Cheng, H.K. (1961), Hypersonic Shock Layer Theory of the Stagnation Region at Low Reynolds Number., Proc. of the 1961 Heat Transfer and Fluid Mechanics Institute, Ed. R.C. Binder et al, Stanford University Press, pp 161-175.
18. Cheng, H.K. (1966), Viscous Hypersonic Blunt Body Problems and Newtonian Theory, Proceedings of International Symposium on Fundamental Phenomena in Hypersonic Flow, Ed. J.G. Hall, Cornell University Press, Ithaca, New York, pp 90-131.
19. Cheng, H.K. and Chang, A.L. (1964), Aerospace Res. Lab. Rep. No. ARL 64-26.
20. Coleman, G.T., Metcalf, S.C. and Berry, C.J. (1977), Heat Transfer to Hemi-Sphere Cylinders and Bluff Cylinders between Continuum and Free Molecular Flow Limits, Rarefied Gas Dynamics, Ed. J. L. Potter, Progress in Astronautics and Aeronautics, Vol. 51, Part II pp 393-404

21. Davis, R. T. (1970), Numerical Solution of the Hypersonic Viscous Shock Layer Equations, AIAA Journal, Vol. 8, No. 5, pp 843-851.
22. Dellinger, T.C. (1971), Computation of Nonequilibrium Merged Stagnation Shock Layer by Successive Accelerated Replacement Method, AIAA Journal, Vol. 9, No. 2, pp 262-269.
22. Fay, J.A. and Riddell, F.R. (1958), Theory of Stagnation Point Heat Transfer in Dissociated Air, J. Aeronautical Sci., Vol. 25, pp 73-85.
23. Gupta, R.N., Scott, C.D. and Moss, J.N. (1985), Slip Boundary Equations for Multicomponent Nonequilibrium Airflow, NASA TP-2459.
24. Gupta, R.N. and Simmonds, A.L. (1986), Hypersonic Low Density Solution of the Navier-Stokes Equations with Chemical Nonequilibrium and Multicomponent Slip, AIAA Paper 86-1349, AIAA/ASME 4th Joint Thermophysics and Heat Transfer Conference, Boston, Mass, June 2-4.
25. Gupta, R.N. (1987), Constants for Polynomial Approximation of Thermodynamic Data of Gases, Private Communication.
26. Hays, W.D. and Probstein, R.F. (1959), Hypersonic Flow Theory, Academic Press, New York
27. Hendricks, W.L. (1974), Slip conditions with Wall Catalysis and Radiation for Multicomponent Nonequilibrium Gas Flow, NASA TMX-64942.
28. Hickman, R.S. and Giedt, W.H. (1963), Heat Transfer to a Hemi-Sphere Cylinder at Low Reynolds Numbers, AIAA Journal, Vol. 1, pp 665-672.
29. Hirschfelder, J.O., Curtiss, C.F. and Bird, R.B. (1964), Molecular Theory of Gases and Liquids, John Willey and Sons Inc.
30. Ho, H.J. and Probstein, R.F. (1960), The Compressible Viscous Layer in Rarefied Hypersonic Flow, ARL TH-60-132, Aeronautical Research Laboratory, Wright Patterson Airforce Base, Ohio.

31. Jain, A.C. (1968), Hypersonic Flow at Low Reynolds Number Near the Stagnation Point of a Blunt Body, Proc. of the Summer Seminar on Fluid Dynamics, Ed. P.L. Bhatnagar, Mallaris Printers, Bangalore, pp 65-80.
32. Jain, A.C. and Adimurthy, V. (1974), Hypersonic Merged Stagnation Shocks Layer, Part I: Adiabatic Wall Case, pp 242-247, Part II Cold Wall Case, pp 248-254, AIAA Journal, Vol. 12, No. 3
33. Jain, A.C. and Kumar, P. (1986), An Improved Stagnation Point Viscous Shock Layer Flow over a Blunt Body, Proc. of the 15th International Symposium on Rarefied Gas Dynamics, Ed. V. Boffi and C Cercignani, B.G. Teubner, Stuttgart, pp 597-606.
34. Jain, A.C. and Kumar, P. (1987), Numerical Solution of Navier-Stokes Equation for Hypersonic Rarefied Stagnation Point Viscous Layer Flow, Proceeding of the Fifth International Conference on Numerical Methods in Laminar and Turbulent Flows, Ed. C. Taylor, W.G. Habbashi and M.M. Hafez, Vol. 5, Part 2, Pineridge Press, Swansea, pp 1045-1056
35. Jain, A.C. and Prabha, S. (1983), Hypersonic Merged Layer and Viscous Layer at the Stagnation Point of a Blunt Body, Department of Aeronautical Engineering, Indian Institute of Technology, Kanpur.
36. Johnston, K.D. and Hendricks, W.L. (1978), A Numerical Solution of the Navier-Stokes Equations for Chemically Nonequilibrium Merged Stagnation Shock Layer on Spheres and Two Dimensional Cylinders in Air, NASA TP-1227.
37. Kang, S.W. and Dunn, M.G. (1972), Hypersonic Viscous Shock Layer with Chemical Nonequilibrium for Spherically Blunted Cones, Report CAL No. AF-3091-A-1, Cornell Aeronautical Laboratory Inc.
38. Kao, H.C. (1964a), Hypersonic Viscous Flow near the Stagnation Streamline of a Blunt Body: II. Third Order Boundary Layer Theory and Comparison with other Methods, AIAA Journal, Vol. 2, No. 11, pp 1898-1906.
39. Kao, H.C. (1964b), Hypersonic Viscous Flow near the Stagnation Streamline of a Blunt Body: I. A Test of Local Similarity, AIAA Journal, Vol. 2, No. 11, pp 1892-97

40. Kim, M. D. and Lewis, C.H. (1985), Three- Dimensional Nonequilibrium Viscous Flow over the Shuttle Orbiter with Catalytic Surface Effects, Journal Spacecraft and Rockets , Vol. 22, No. 2, pp 97-103.
41. Kim, M. D., Swaminathan, S. and Lewis, C.H. (1984), Three- Dimensional Nonequilibrium Viscous Shock Layer Flow over the Space Shuttle Orbiter, Journal of Spacecraft and Rockets, Vol. 21, No. 1, pp 29-35.
42. Kumar, A. and Jain, A.C. (1975), Nonequilibrium Merged Stagnation Shock Layer at Hypersonic Speeds, Intl. J. Heat Mass Transfer, Vol. 18, pp 1113-1118.
43. Lee, J.H. (1985), Basic Governing Equations for the Flight Regimes of Aeroassisted Orbital Transfer Vehicle, AIAA Progress in Aeronautics and Astronautics, Thermal Design of Aeroassisted Orbital Transfer Vehicle, Ed. Nelson, H.F., Vol. 96, pp 3-53.
44. Lees, L. (1956), Laminar Heat Transfer over Blunt NOsed Bodies at Hypersonic Flight Speeds, Jet Propulsion, pp 259-264.
45. Lenard, M. (1962), Stagnation Point Flow of a Variable Property Fluid at Low Reynolds Number, Cornell Univ., Graduate School of Aerospace Engineering., Report No. AFOSR 2981.
46. Leonard, B.P. (1979), A Stable and Accurate Convective Modeling Procedure Based on Quadratic Upstream Interpolation, Computer Methods in Applied Mechanics and Engineering, Vol. 19, pp 59-98.
47. Levinsky, F.S. and Yoshihara, H. (1962), Rarefied Hypersonic Flow over a Sphere, Hypersonic Flow Research, Ed. F.R. Riddell, Academic Press, New York, pp 81-106.
48. Li, C.P. (1987), Chemistry-Split Technique for Viscous Reactive Blunt Body Flow Computations, AIAA Paper 87-282 AIAA 25th Aerospace Science Meeting, Jan. 12-15, 1987, Reno, Nevada.
49. MacCormack, R.W. (1969), The Effect of Viscosity in Hypervelocity Impact Cratering, AIAA Paper 69-354, AIAA Hypervelocity Impact Conference, April 30- May 2, 1969, Cincinnati, Ohio.

50. Miner, E.W. and Lewis, C.H. (1975), Hypersonic Ionising Air Viscous Shock Layer over Nonanalytic Blunt Bodies, NASA CR-2550.
51. Moss, J.N. (1971), Solution for Reacting and Nonreacting Viscous Shock Layers with Multicomponent Diffusion and Mass Injection, Ph.D. Thesis, Deptt. of Aerospace Engg., Virginia Polytechnic Institute and State University, Blacksburg.
52. Moss, J.N. and Bird, G.A. (1986), Direct Simulation of Transitional Flow for Hypersonic Re-entry Conditions, AIAA Progress in Astronautics and Aeronautics Thermal Design of Aeroassisted Orbital Transfer Vehicles, Ed. H.F. Nelson, Vol. 96, pp 113-139.
53. Moss, J.N., Bird, G.A. and Dogra, V.K. (1988), Nonequilibrium Thermal Radiation for an Aero-assist Flight Experiment Vehicle, AIAA paper 88-0081, 26th Aerospace Science Meeting, Jan. 11-14, 1988, Reno, Nevada.
54. Park, C. (1985), On Convergence of Computation of Chemically Reacting Flows, AIAA Paper 85-247, AIAA 23rd Aerospace Science Meeting, Jan. 14-17, Reno, Nevada.
55. Potter, J.L. and Bailey, A.B. (1964), Pressures in the Stagnation Region of Blunt Bodies in Rarefied Flow, AIAA Journal, Vol. 2, pp 743-745.
56. Prabhu, D.K., Tannehill, J.C. and Marvin, J.G. (1987), A New PNS Code for Chemical Nonequilibrium Flows, AIAA Paper 87-284, AIAA 25th Aerospace Science Meeting, Jan. 12-15, 1987, Reno, Nevada.
57. Probst, R.F. and Pan, Y.S. (1963), Shock Structure and the Leading Edge Problem, Rarefied Gas Dynamics, Supplement 2, Ed. J.A. Laurman, Vol. II, Academic Press, New York, pp 194-211.
58. Roach, R.L. (1982), A Consistent Finite Difference Derivation for the Navier-Stokes Equation, AIAA Paper 82-102, AIAA 20th Aerospace Science Meeting, Jan. 11-14, Orlando, Florida.
59. Rott, N. and Lenard, M. (1959), Vorticity Effects on the Stagnation Point Flow of a Viscous Incompressible Fluid, Journal of Aerospace Sciences, Vol. 26, No. 8, pp 542-543

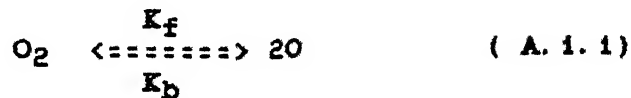
60. Russel, D.A. (1968), Density Disturbance ahead of a Sphere in Rarefied Supersonic Flow, *The Physics of Fluids*, Vol. 11, No. 8, pp 1679-1685.
61. Scott, C.D. (1973), Wall Boundary Equations with Slip and Catalysis for Multicomponent Nonequilibrium Gas Flow, NASA TM X-58111.
62. Sherman, F.S. (1953), New Experiments on Impact Pressure Interaction in Supersonic and Subsonic Rarefied Air Stream, NACA TN-2995.
63. Shidlovskiy, V.P. (1967), Introduction to Dynamics of Rarefied Gases, American Elsevier Pub. Co., pp 60-68.
64. Swaminathan, S., Kim, M.D. and Lewis, C.H. (1983), Effects of Chemical Modeling on Three-Dimensional Non-equilibrium Viscous Shock Layer Flows, AIAA paper 83-1425, AIAA 18th Thermophysics Conference, June 1-3, 1983, Montreal, Canada.
65. Van Dyke, M. (1962), Second Order Compressible Boundary Layer Theory with Application to Blunt Bodies in Hypersonic Flow, *Hypersonic Flow Research*, Ed. F.R. Riddell, Academic Press, New York, pp 37-76.
66. Van Dyke, M. (1963), A Review and Extension of Second Order Hypersonic Boundary Layer Theory, *Rarefied Gas Dynamics*, Supplement 2, Ed. J.A. Laurmann, Vol. II, Academic Press, New York, pp 212-217.
67. Van Dyke, M. (1964a), Perturbation Methods in Fluid Dynamics, Academic Press, New York., pp 77-97.
68. Van Dyke, M. (1964b), Higher Approximations in Boundary Layer Theory, Part 3, Parabola in Uniform Stream, *Journal of Fluid Mechanics*, Vol. 19, Part I, pp 145-159.
69. Van Dyke, M. (1969), Higher Order Boundary Layer Theory, *Annual Review of Fluid Mechanics*, Vol. 1, pp 265-292.
70. Vidal, R.J. and Whittliff, C.E. (1963), Hypersonic Low Density Studies of Blunt and Slender Bodies, *Rarefied Gas Dynamics*, Ed. J. A. Laurman, *Advances in Applied Mechanics*, Vol. 2, Supplement II, Academic Press, New York, pp 343-376.

71. Vogenitz, F.M. and Takata, G.Y. (1970), Monte Carlo Study of Blunt Body Hypersonic Viscous Shock Layer, Rarefied Gas Dynamics, Ed. D. Dini, C. Cercignani and S. Nescilla Proceedings of the International Symposium on Rarefied Gas Dynamics, Pisa, Italy, June 29-July 3, pp 911-918.
72. White, F.M. (1974), Viscous Fluid Flow, McGraw Hill Pub. Co., New York., pp 22-36.
73. Widhopf, G.F. and Victoria, K.J. (1973), On the Solution of the Unsteady Navier-Stokes Equations Including Multi-component Finite Rate Chemistry, Computers and Fluids, Vol. 1, pp 159-184.
74. Williams, F. (1965), Combustion Theory, Addison Weseley Book Co. Inc.

## APPENDIX 1

INFLUENCE OF LINEARISATION OF PRODUCTION TERM

Though the analysis involves multi-component multi-reaction gas mixture, for the sake of developing an understanding of the influence of linearisation of production terms, consider the case of single reaction given by



For this reaction mass production rate is given by

$$w_{\text{O}} = 2 M_{\text{O}} \left[ \rho K_f \frac{C_{\text{O}_2}}{M_{\text{O}_2}} - \rho^2 K_b \left( \frac{C_{\text{O}}}{M_{\text{O}}} \right)^2 \right] \quad (\text{A.1.2})$$

$$w_{\text{O}_2} = - M_{\text{O}_2} \left[ \rho K_f \frac{C_{\text{O}_2}}{M_{\text{O}_2}} - \rho^2 K_b \left( \frac{C_{\text{O}}}{M_{\text{O}}} \right)^2 \right] \quad (\text{A.1.3})$$

Using the fact that  $M_{\text{O}_2} = 2 M_{\text{O}}$ , equations (A.1.1) and (A.1.2) can be written as:

$$w_{\text{O}} = A [ C_{\text{O}_2} - \alpha C_{\text{O}}^2 ]$$

$$(\text{A.1.4})$$



and

$$w_{O_2} = A [ \alpha C_O^2 - C_{O_2} ]$$

( A.1.5 )

where

$$A = \rho K_f$$

$$\alpha = \rho K_b / K_f$$

At this stage, the sum of the two mass production rates is zero, that is:

$$w_O + w_{O_2} = 0$$

( A.1.6 )

whereas, linearisation of the equations ( A.1.4 ) and ( A.1.5 ) yields

$$w_O = A \underline{C_{O_2}} - A \alpha \underline{C_O} C_O$$

( A.1.7 )

$$w_{O_2} = A \alpha \underline{C_O^2} - A C_{O_2}$$

( A.1.8 )

where the underlined terms have taken their values at the previous iteration.

Addition of the two production rate terms gives

$$w_O + w_{O_2} = A ( \underline{C_{O_2}} - C_{O_2} ) + A \alpha \underline{C_O} ( \underline{C_O} - C_O )$$

( A.1.9 )

On applying mass conservation condition

$$C_O + C_{O_2} = 1$$

( A.1.10 )

one gets

$$C_0 - \underline{C_0} = - ( C_{O2} - \underline{C_{O2}} )$$

( A.1.11 )

Finally, equations ( A.1.11 ) and ( A.1.9 ) yield

$$W_0 + W_{O2} = A ( 1 + \alpha \underline{C_0} ) ( \underline{C_{O2}} - C_{O2} )$$

( A.1.12 )

which is non-zero quantity until new and old values of  $C_{O2}$  are identical.

This shows that linearisation of production terms causes net mass production rate to be non-zero. This fact should be taken into account while the details of the solution procedure are being worked out.